

Lecture Notes in Mechanical Engineering

Shailendra Kumar
K. P. Rajurkar *Editors*

Advances in Manufacturing Systems

Select Proceedings of RAM 2020

 Springer

Lecture Notes in Mechanical Engineering

Series Editors

Francisco Cavas-Martínez, Departamento de Estructuras, Universidad Politécnica de Cartagena, Cartagena, Murcia, Spain

Fakher Chaari, National School of Engineers, University of Sfax, Sfax, Tunisia

Francesco Gherardini, Dipartimento di Ingegneria, Università di Modena e Reggio Emilia, Modena, Italy

Mohamed Haddar, National School of Engineers of Sfax (ENIS), Sfax, Tunisia

Vitalii Ivanov, Department of Manufacturing Engineering Machine and Tools, Sumy State University, Sumy, Ukraine

Young W. Kwon, Department of Manufacturing Engineering and Aerospace Engineering, Graduate School of Engineering and Applied Science, Monterey, CA, USA

Justyna Trojanowska, Poznan University of Technology, Poznan, Poland

Lecture Notes in Mechanical Engineering (LNME) publishes the latest developments in Mechanical Engineering—quickly, informally and with high quality. Original research reported in proceedings and post-proceedings represents the core of LNME. Volumes published in LNME embrace all aspects, subfields and new challenges of mechanical engineering. Topics in the series include:

- Engineering Design
- Machinery and Machine Elements
- Mechanical Structures and Stress Analysis
- Automotive Engineering
- Engine Technology
- Aerospace Technology and Astronautics
- Nanotechnology and Microengineering
- Control, Robotics, Mechatronics
- MEMS
- Theoretical and Applied Mechanics
- Dynamical Systems, Control
- Fluid Mechanics
- Engineering Thermodynamics, Heat and Mass Transfer
- Manufacturing
- Precision Engineering, Instrumentation, Measurement
- Materials Engineering
- Tribology and Surface Technology

To submit a proposal or request further information, please contact the Springer Editor of your location:

China: Dr. Mengchu Huang at mengchu.huang@springer.com

India: Priya Vyas at priya.vyas@springer.com

Rest of Asia, Australia, New Zealand: Swati Meherishi
at swati.meherishi@springer.com

All other countries: Dr. Leontina Di Cecco at Leontina.dicecco@springer.com

To submit a proposal for a monograph, please check our Springer Tracts in Mechanical Engineering at <http://www.springer.com/series/11693> or contact Leontina.dicecco@springer.com

Indexed by SCOPUS. All books published in the series are submitted for consideration in Web of Science.

More information about this series at <http://www.springer.com/series/11236>

Shailendra Kumar · K. P. Rajurkar
Editors

Advances in Manufacturing Systems

Select Proceedings of RAM 2020

 Springer

Editors

Shailendra Kumar
Sardar Vallabhbhai National Institute
of Technology
Surat, India

K. P. Rajurkar
University of Nebraska–Lincoln
Lincoln, OR, USA

ISSN 2195-4356

ISSN 2195-4364 (electronic)

Lecture Notes in Mechanical Engineering

ISBN 978-981-33-4465-5

ISBN 978-981-33-4466-2 (eBook)

<https://doi.org/10.1007/978-981-33-4466-2>

© The Editor(s) (if applicable) and The Author(s), under exclusive license to Springer Nature Singapore Pte Ltd. 2021

This work is subject to copyright. All rights are solely and exclusively licensed by the Publisher, whether the whole or part of the material is concerned, specifically the rights of translation, reprinting, reuse of illustrations, recitation, broadcasting, reproduction on microfilms or in any other physical way, and transmission or information storage and retrieval, electronic adaptation, computer software, or by similar or dissimilar methodology now known or hereafter developed.

The use of general descriptive names, registered names, trademarks, service marks, etc. in this publication does not imply, even in the absence of a specific statement, that such names are exempt from the relevant protective laws and regulations and therefore free for general use.

The publisher, the authors and the editors are safe to assume that the advice and information in this book are believed to be true and accurate at the date of publication. Neither the publisher nor the authors or the editors give a warranty, expressed or implied, with respect to the material contained herein or for any errors or omissions that may have been made. The publisher remains neutral with regard to jurisdictional claims in published maps and institutional affiliations.

This Springer imprint is published by the registered company Springer Nature Singapore Pte Ltd. The registered company address is: 152 Beach Road, #21-01/04 Gateway East, Singapore 189721, Singapore

Organizing Committee of Conference RAM 2020

Chairman

Prof. S. R. Gandhi, Director, SVNIT, Surat

Organizing Secretaries

Dr. Shailendra Kumar, SVNIT, Surat

Dr. Harshit K. Dave, SVNIT, Surat

Coordinators

Dr. Amrut S. Mulay, SVNIT, Surat

Dr. Pawan Sharma, SVNIT, Surat

Steering Committee

Dr. R. V. Rao, SVNIT, Surat

Dr. H. K. Raval, SVNIT, Surat

Dr. K. P. Desai, SVNIT, Surat

Dr. A. A. Shaikh, SVNIT, Surat

Dr. T. N. Desai, SVNIT, Surat

Programme Committee

Dr. D. I. Lalwani, SVNIT, Surat
Dr. J. V. Menghani, SVNIT, Surat
Dr. Ravi Kant, SVNIT, Surat
Dr. Dinesh Singh, SVNIT, Surat
Dr. V. D. Kalyankar, SVNIT, Surat
Dr. S. N. Pandya, SVNIT, Surat
Dr. B. N. Sahoo, SVNIT, Surat
Dr. Sumit Khare, SVNIT, Surat

Advisory Committee

Dr. K. P. Rajurkar, Uni. of Nebraska, USA
Dr. Dumitru Nedelcu, Uni. of Iasi, Romania
Dr. Chintan Vaishnav, MIT, USA
Dr. J. P. Davim, Uni. of Aveiro, Portugal
Dr. M. P. Jahan, Miami University, USA
Dr. H. M. A. Hussein, Helwan University, Egypt
Dr. Andrew Y. C. Nee, NUS, Singapore
Dr. Panagiotis Kyratsis, UWM, Greece
Dr. R. Balasubramaniam, BARC Bombay
Dr. Suhas Joshi, IIT Bombay
Dr. J. Ram Kumar, IIT Kanpur
Dr. D. Ravi Kumar, IIT Delhi
Dr. P. M. Pandey, IIT Delhi
Dr. Anupam Agrawal, IIT Ropar
Dr. A. M. Sidpara, IIT Kharagpur
Dr. K. Hariharan, IIT Madras
Dr. G. S. Dangayach, MNIT Jaipur
Dr. Venu Gopal A., NIT Warangal
Dr. P. K. Patowari, NIT Silchar
Dr. Rajiv Kumar Garg, NIT Jalandhar
Dr. P. C. Tewari, NIT Kurukshetra
Dr. Vishal Sharma, NIT Jalandhar
Dr. H. S. Mali, MNIT Jaipur
Dr. Prabhat Ranjan, BARC Bombay
Dr. U. Chandrasekhar, Wipro 3d
Dr. P. K. Jain, IITDM Jabalpur
Dr. R. K. Verma, MMMUT Gorakhpur

List of Reviewers

Dr. H. K. Raval, SVNIT, Surat
Dr. K. P. Desai, SVNIT, Surat
Dr. Shailendra Kumar, SVNIT, Surat
Dr. P. K. Patowari, NIT, Silchar
Dr. T. N. Desai, SVNIT, Surat
Dr. H. K. Dave, SVNIT, Surat
Dr. J. V. Menghani, SVNIT, Surat
Dr. Dinesh Singh, SVNIT, Surat
Dr. M. K. Rathod, SVNIT, Surat
Dr. Arati Mulay, CoE, Pune
Dr. S. N. Pandya, SVNIT, Surat
Dr. A. S. Mulay, SVNIT, Surat
Dr. B. N. Sahoo, SVNIT, Surat
Dr. Pawan Sharma, SVNIT, Surat
Dr. Sudhanshu Kumar, MANIT, Bhopal
Dr. Prabhat Ranjan, BARC, Mumbai
Dr. Piyush Gohil, MSU, Baroda
Dr. V. J. Badheka, PDP, Gandhinagar
Dr. K. P. Mehta, PDP, Gandhinagar
Dr. Vishal John Mathai, AMCoE, Kerala
Dr. M. K. Chudasama, GEC, Dahod
Dr. Dilip B Jani, GEC, Dahod
Dr. Hiesh Panchal, GEC, Patan
Dr. M. P. Sutaria, CHARUSAT, Anand
Dr. J. D. Patel, MEC, Basna
Dr. Ravi Bhatt, CGPIT, Gujarat
Dr. Shakil Kagzi, SNPIT, Umrakh
Dr. K. D. Maniya, CKPCET, Surat
Dr. Abhay Utpat, SVERI, Pandharpur
Prof. J. M. Joshi, VGEC, Chandkheda

Preface

Since 2010, Department of Mechanical Engineering at Sardar Vallabhbhai National Institute of Technology, Surat has been organizing series of conferences on “Recent Advances in Manufacturing”. In order to enable the sharing of knowledge in the areas of Manufacturing technologies, we have organized six national conferences on “Recent Advances in Manufacturing” and now we have planned the International Conference on Recent Advances in Manufacturing (RAM-2020). The Conference is organized to bring the academicians, researchers and practicing engineers for sharing their experiences in the field of advance manufacturing. RAM-2020 will provide the opportunity for networking among participant institutes/organizations/industries to systematically confront the challenges in mutual areas of interest to advance manufacturing technology in these areas.

The proceedings volumes are published in the Springer series Lecture Notes in Mechanical Engineering in two volumes, viz. Volume 1—Advances in Manufacturing Processes and Volume 2—Advances in Manufacturing Systems. We acknowledge the academic support from Prof. Dumitru Nedelcu and Prof. K. P. Rajurkar while editing the volume 1 and 2 respectively. We are also thankful to Ms. Priya Vyas and her team at Springer Nature for timely publication of these volumes.

As the entire world is facing the threat from corona pandemic, the international as well as interstate travel is restricted. However, we have tried our best to carve out a comprehensive schedule, keynote speakers, oral presentations in both online and offline mode, all of which will facilitate stimulating insightful discussions within the research community. In spite of such a pandemic situation, 60 participants have presented their findings and exchanged ideas related to manufacturing domain.

We are thankful to the conference organizing committee members, the advisory committee members, the reviewers, session chairs and the volunteers, without whose generous contributions this conference would not number of presentations and number of participants.

Most of all, we thank the participants for enriching the international conference with their active participation.

Dr. Shailendra Kumar
Organizing Secretary, RAM-2020
Surat, India

Dr. Harshit K. Dave
Organizing Secretary, RAM-2020
Surat, India

Contents

1	Computational Design and Digital Fabrication	1
	Panagiotis Kyratsis, Anastasios Tzotzis, and Athanasios Manavis	
2	Development of Macro Program for Improving Machining Characteristics of Logarithmic Spiral on CNC Machining Center	17
	Vratraj Joshi, Bhavin Desai, Shalin Marathe, Keyur Desai, and Harit Raval	
3	Automatic Feature Recognition (AFR) of the Inclined Cross-Hole in Hollow Cylinders	25
	Abdullah D. Ibrahim, Sabreen A. Abdelwahab, H. M. A. Hussein, and Ibrahim Ahmed	
4	Grey Relational Multi-decision Analysis of SS304 Bead Characteristics Processed in Wire Arc Deposition Process for Additive Manufacturing	33
	D. T. Sarathchandra and M. J. Davidson	
5	Optimizing the Defocused CO₂ Laser Microchanneling Process Using Grey Relational Analysis	43
	Shashi Prakash	
6	Selection of Multi-point Diamond Dresser for Grinding Process Using Grey Relation Analysis	53
	V. V. Pansare, V. S. Gadakh, and S. S. Patil	
7	Development of Integrated Versatile Paper, Plastic and Aluminum Waste Sorting and Disposal System	63
	Sharada Gavade, Soham Kulkarni, Shivani Mohite, and Kiran Bhole	
8	Development of Machining Fixture to Improve Machining Lead Time of Helical Gearbox Case	75
	Hardik Beravala, Rohan Pandey, Shubham Samudre, and Jayesh Parpiyani	

9	Design and Development of Robust Fixture to Perform Friction Stir Welding/Processing on Conventional Vertical Milling Machine	83
	Jainesh Sarvaiya and Dinesh Singh	
10	Design of Gripper and Selection of Robotic Arm for Automation of a Pick and Place Process	95
	Vijesh Shah, Nandkumar Gilke, Vilas Dhore, Chandrashekhar Phutane, and Bhavisha Kondhol	
11	Utilization of Stone Industry Waste as Filler for Sustainable Development of Aluminum Alloy Composites: A Thermo-Mechanical and Mechanical Characterizations	109
	Vikash Gautam, Amar Patnaik, and I. K. Bhat	
12	Performance Improvement of OEM Brake Caliper by Manufacturing with Design Changes	123
	Mauli Mirajkar, Parvathidevi Gurubaran, P. Jeevan Sunny, Armugasunder Konar, and P. K. Ambadekar	
13	Development of Novel Abrasive Media Using Granite Dust Powder Waste for Finishing Applications	139
	Ankit Soni, Jai Kishan Sambharia, and Sandesh Trivedi	
14	Enhancement of Electric Hybrid Vehicle	157
	Dhyey R. Savaliya, Vaibhav M. Dholariya, Uttam B. Khunt, Abhishek Singh, Monik M. Dholariya, and Jenish H. Patel	
15	Extraction of Phenolic Compounds from the Waste of <i>Borassus flabellifer</i>: A Step Toward Waste Valorization	169
	Akshay Y. Bageshwar and Meghal A. Desai	
16	Use of Sustainable Practices in Cement Production Industry: A Case Study	181
	Vishal Naranje, T. V. S. Chidambaram, Rajeev Bhushan Garg, and B. D. Bachchhav	
17	Analysis, Modeling and Experimental Study of Stretching Stress in the Design of Pressure Sensor	193
	Shrinkhla Ghildiyal, R. Balasubramaniam, and Joseph John	
18	On Numerical Modeling and Flow Analysis of Piston Bowl Geometry of a Compression Ignition Engine	203
	Bridjesh Pappula, Geetha Narayanan Kannaiyan, and Seshaiiah Turaka	
19	FEM-Based Thermal Modeling for Analyzing ECDM Process	213
	Manoj Kumar, R. O. Vaishya, and N. M. Suri	

20 Designing and Analyzing the Different Parameters of Pulp Removal Machine 227
 Chiraya Hans Wilson and Bobby K. George

21 Fabrication and Analysis of Apparatus for Measuring Stored Renewable Hydrogen Energy in Metal Hydrides 241
 Rohan Kalamkar, Vivek Yakkundi, and Aneesh Gangal

22 Investigation of Wind Loads on Utility-Scale Seasonal Tilt Solar PV Power Plants 251
 Syed Abdul Mateen and Kiran S. Bhole

23 Application of Neural Network to Predict Printability of Polycaprolactone Using FDM 263
 Rahul Narkhede, Ravi Teja Karumuri, Ashish R. Prajapati, and Harshit K. Dave

24 ANFIS-Based Prediction Model for Tool Wear Criteria During Orbital Electrical Discharge Machining of Ti6Al4V 277
 Naisarg H. Sagathiya, Ashish R. Prajapati, Keyur P. Desai, and Harshit K. Dave

25 Evaluation of Metal Foam of Al6061 + MgO Using PM Route 293
 Rahul Rathod, Bhupesh Goyal, Prashantsingh Tomar, and Akash Pandey

26 Mechanical and Wear Characterization of Epoxy Resin-Based Functionally Graded Material for Sustainable Utilization of Stone Industry Waste 303
 Aakash Sharma and Vikash Gautam

27 Acoustic Emission System for Monitoring Mechanical Behavior During Ultrasonic Metal Welding 319
 Vijay Dodiya, Sarthak Bhavsar, Naman Kansara, Nikhil Murarka, Keyur P. Desai, Harshit K. Dave, and Himanshu V. Patel

28 Analysis of Enablers of Humanitarian Supply Chain Management 329
 Sachin Agarwal and Ravi Kant

About the Editors

Dr. Shailendra Kumar is currently Professor and Head at the Department of Mechanical Engineering, S. V. National Institute of Technology, Surat, India. He is graduated in Production Engineering from Regional Institute of Technology, Jamshedpur (Presently NIT Jamshedpur) and Ph.D. from Maharshi Dayanand University, Rohtak, Haryana, India. His broad area of research is manufacturing. He is especially interested in AI applications in sheet metal forming, additive manufacturing, conventional and non-conventional machining, and CAM. More than 160 papers published in reputed journals and conferences are at his credit. He has completed several research projects funded by Indian Govt. agencies including Dept. of Sc. & Tech. (DST), Naval Research Board (NRB), MHRD, SERB; and also worked as Co-Principle Investigator in one Int. project of NPST, Kingdom of Saudi Arabia, Riyadh. He is also the recipient of Young Scientist Award of DST, Govt. of India.

Dr. K. P. Rajurkar is currently a Distinguished Professor at the Department of Mechanical & Materials Engineering, College of Engineering, University of Nebraska – Lincoln, Nebraska, USA. He obtained his B.E. (Mechanical Engineering) from Jabalpur University and M.S. and Ph.D. from Michigan Tech. His major areas of research interests include modeling and analysis of manufacturing processes, and systems sensing and control of traditional and non-traditional macro, micro and nano manufacturing processes. He holds a patent on cryogenically cooled tool machining and is the author of more than 120 refereed publications. He was awarded the Society of Manufacturing Engineers (SME) Gold Medal in 2009 and the M. Eugene Merchant Manufacturing Medal of ASME/SME in 2018. Recognized as a research leader, he was president of the North American Manufacturing Research Institute of SME (NAMRI/SME) in 1998-99. He is also the recipient of Distinguished Service Award, North American Manufacturing Research Institution, Society of Manufacturing Engineers (SME) in 2011.

Chapter 1

Computational Design and Digital Fabrication



Panagiotis Kyratsis, Anastasios Tzotzis, and Athanasios Manavis

Introduction

The advent of more sophisticated and advanced computer-aided design (CAD) software has increased the productivity of the design engineers. Commercial CAD software are now filled with functions that were not available in the past decades. One such is the parametric modeling. With proper utilization of the application programming interface (API), it is possible to take advantage of the parametric modeling to develop simple macros or complete applications that can support design, assembly, manufacturing and engineering documentation.

Kim et al. [1] described an end-mill design process based on the cutting simulation method. This method was used to obtain the machined shape of an end-mill by using Boolean operations between a given grinding wheel and a cylindrical workpiece. This research was implemented using a commercial CAD system with API function programming. Tapoglou [2] presented a novel simulation model that enables accurate prediction of important aspects of the chips produced during power skiving. The simulation model was embedded on a CAD environment and through the simulation code, the virtual simulation of the manufacturing process was realized. A similar study was carried out by Dimitriou et al. [3]. The authors described a simulation method of gear hobbing, based on virtual kinematics of solid models representing the cutting tool and the work gear. An algorithm has been developed and embedded in a commercial CAD environment that can be used to generate realistic chips. The algorithm is supported by a universal and modular code as well as by a user-friendly graphical interface. Roberto and Osorio-Gómez [4] proposed a method to search the optimal sequence of assembling for a product, by comparing different

P. Kyratsis (✉) · A. Tzotzis · A. Manavis
Department of Product and Systems Design Engineering, University of Western Macedonia,
50100 Kila Kozani, Greece
e-mail: pkyratsis@uowm.gr

sequences extracted in automatic mode from a 3D CAD model. In addition, this method allows the manufacturer to analyze and study the optimal assembly sequence without the direct use of a CAD system. Oancea and Haba [5] presented a software tool which allows the user to obtain the manufacturing and the cutting data for each process from the manufacturing sequence of rotational parts, by combining computer-aided production planning (CAPP), CAD and computer-aided manufacturing (CAM) modules. The authors used the programming resources of a commercial CAD software to develop their software tool. Mok et al. [6] developed an effective reuse and retrieval system that can easily register modeled standard parts using a simple graphic user interface. Open API and a commercial CAD solution were used for the purpose. The system was applied to standardize mold bases and mold parts and it consists mainly of three kinds of module: the standard part module, the parts-list module and the retrieval-system module. Similar techniques were applied for measuring and verification purposes. García-Hernández et al. [7] developed a software application for measuring gears and described its implementation using general-purpose spreadsheet software that calculates the probe positions and direction of measurement. Finally, studies where CAD-based programming was used for computational design purposes are available in the literature as well. Teodor et al. [8] designed dedicated software for computing polynomial approximation and the axial section of the gear hob. The profiling method of the gear hub uses the Bezier approximation polynomials. Similar approaches were followed for parametrically automated 3D design and manufacturing [9, 10], as well as for simulating manufacturing processes [11, 12].

Computational design is a new and continuously progressing technology. Furthermore, parametric modeling offers a number of opportunities for novelty and better solutions. In the past, unusual geometries were extremely difficult to be modeled and manufactured. In addition, today there are various tools available and the designers' perspective is widely affected. The idea is to design complicated geometries based on textual programming languages. Leitão and Santos [13] described that the computational design principles open new horizons in what we call novel design forms. Specifically, generative design (another term for computational design technique) is a modern methodology of using textual programming to create and modify shape, geometry and ornamentation.

According to Killian [14] computational design approach allows automation of the design procedures and extension of the standard features of CAD applications, and therefore overstepping their limitations. Krause [15] defined that computational design allows immediate generation of large number of design alternatives. In addition to geometric approach of final alternatives of the same product or structure that are produced via computational design way, Casale et al. [16] described that the study of geometry is oriented to concept, formal and expressive control, and built form. Moreover, Chen and Pottmann [17] defined that the critical analysis of the geometric shape goes through the problems of its virtual representation—also in parametric form—and finally transforms it into a physical object with simple prototyping equipment.

Malakuczi [18] used parametric applications to generate structures and deals that digital fabrication tools can lead to new opportunities in many product typologies

across the material culture. On the other hand, designers are able to use textual programming languages to develop CAD-based applications that are focused on unique geometric models. Textual programming languages allow control within a software (i.e. Python™ commands and structures joined with Rhino™ via RhinoScriptSyntax module). Lopez and Leitão [19] cite that a programming language is a formal medium for expressing ideas and not just a way to get a computer to perform operations. Furthermore, in a textual programming language, programs are described using a linear sequence of characters. Especially, the current paper includes a case study that is developed by using RhinoScriptSyntax™ module that includes module containing functions that perform various operations on Rhino™. The library of functions is about geometry, commands, document objects and application methods.

According to Viny et al. [20] all functions are returned as simple Python™ variables due to the ease of design processing. Kyratsis et al. [21] used the methodology of computational design which is based on textual programming language in order to generate forms in 3D space. The main reason of this procedure aims on designing innovative structures for CNC laser cutting and engraving applications. The presented paper is based on the computational design technology together with the use of CNC laser cutting and engraving techniques for the material of wood using a CAD-based application (Rhino™) via textual programming language (Python™ and RhinoScriptSyntax™ module).

Even though modern CAD solutions are enriched with capabilities, the need for automated functionalities is still high. In the present paper, two case studies related to the implementation of the CAD-based programming resources are being presented. Firstly, an interactive tool developed via the API of SolidWorks™ is being introduced. This tool combines several engineering aspects in one simple graphical interface. For example, the automatic creation of typical design features such as fillet, chamfer and hole, and the rapid production of the standardized engineering drawings. Finally, a CAD-based application for automatic generation of complex 3D geometries [22] was developed with the aid of Python™ programming language and Rhino™ for the representation of the CAD geometries.

Multi-feature Generation Tool

Design of User Interface

The selection of topology objects, such as vertices, edges and faces, is an integral part of every CAD-based process. Hence, for automating the topology selection procedure, the basis for utility of CAD-based applications can be established. In the present paper, an effort is made to combine certain functionalities of SolidWorks™ by using the API. The goal is to develop an all-around application that can support the user during routine design tasks. Specifically, the presented application can be used to automatically create standard CAD features such as fillet, chamfer, pattern and

hole with minimal effort. In addition, multiple selection schemes (i.e. selection of all available edges/faces, selection of specified edge/face) can be automated. Moreover, it is possible to expand the functionalities of the application by adding the proper code with VBA™.

The application of user-interface is divided into four tabs. Figure 1.1a illustrates the first tab that is related to the topology selection. Users can choose the objects on which the preferred features will be applied. The type of topology object as well as the ID of an object can be set. Figure 1.1b depicts the second tab that contains several options that are required for setting three basic design features (fillet, chamfer and hole). In addition to the aforementioned features, it is possible to automatically create circular patterns also, based on custom or standard properties (Fig. 1.1c). Finally,

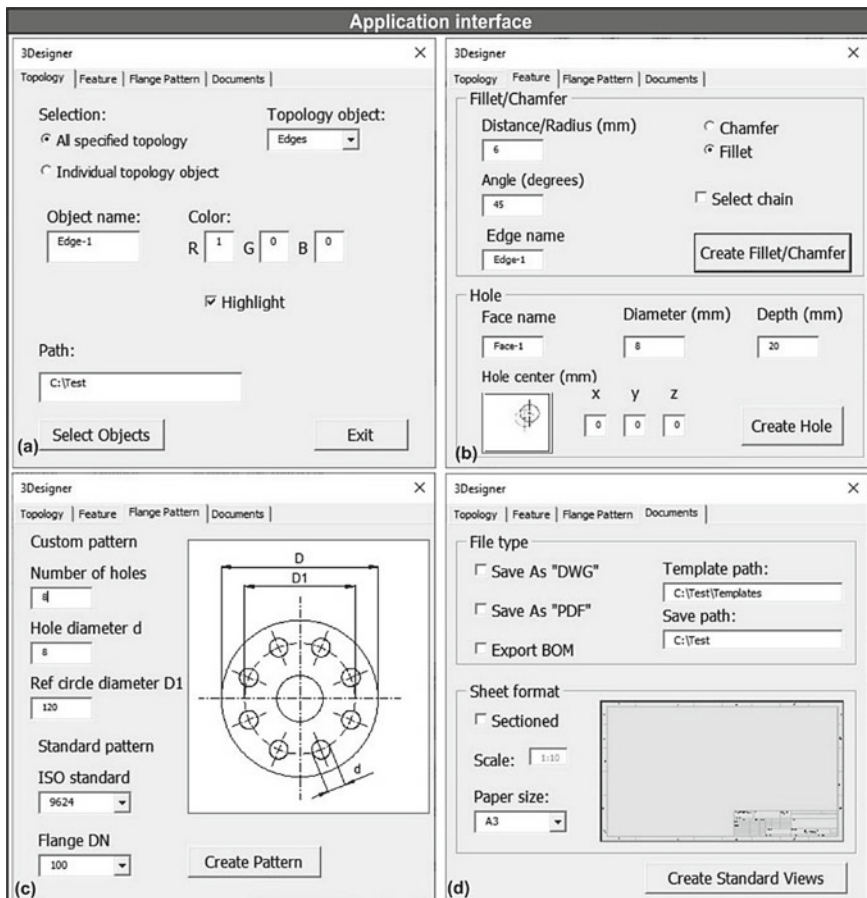


Fig. 1.1 The user-interface: topology selection tab (a), feature creation tab (b), pattern creation tab (c) and documents creation tab (d)

via the fourth tab (Fig. 1.1d) users can produce standardized engineering documents such as three-view drawings, sectioned view drawings and assembly documents.

The input of the values and the selection of the options are all performed with the aid of the user-interface which is the bridge between the user and the CAD system [23–25].

Programming via SolidWorks™ API

Programmatically, the code of the tool is divided into three main modules. The topology selection module is the first one. The code of this module is responsible for the connection of the application tool to an open part or assembly document so that access to available solid bodies can be established. This way it is possible to locate the user-specified topology object (i.e. face, edge, vertex) by traversing all available objects with a “For” loop. However, prior to locating the preferred topology entities, the code changes the default ID of each one of these objects according to the one specified by the textbox entitled “Object name” (see Fig. 1.1a) and then stores them to an array for future use. That is, if a part contains 20 edges then they will be renamed to “Edge” plus a number from 1 to 20 as suffix. Finally, the corresponding entities are selected depending on the user preferences. In addition, the selected entities can be colored according to the chosen RGB combination (see Fig. 1.1a) in order to facilitate the visualization of the selection procedure in complex parts or large assemblies.

The second module is the one related to the feature creation. First, the corresponding topology objects (edges or faces) are selected since they are already named. Then, for the case of the hole feature only, an appropriate sketch is inserted on the selected face, based on the input values (see Fig. 1.1b). Finally, a fillet feature, a chamfer feature or a hole feature is applied on the selected objects according to the user’s preferences. Additionally, it is possible to apply a specific fillet feature to a chain of edges instead of applying it multiple times. On top of that, this module contains extra code for the automatic creation of flange patterns (see Fig. 1.1c). User can choose between customized or standardized patterns according to the dimensions given by the input fields or the commercial ISO standards, respectively. The steps followed in the pattern creation slightly differ to the ones taken in the aforementioned features (fillet, chamfer and hole creation). At first, the main cylindrical face of the part is recognized and selected, and consequently a new sketch is inserted. This sketch contains the reference construction circle and the hole profile. Lastly, the flange pattern is applied.

The last module contains the program for the automatic production of the engineering documents. A new drawing document is created and formatted according to the input specifications (scale and paper size) as shown in Fig. 1.1d. Finally, the document is prepared (standard three-view drawing) and saved in the following file types: PDF and DWG. Optionally, user may select to add a sectioned view of the part or the assembly to the drawings. Moreover, a bill of materials (BOM) is automatically prepared in the case of an open assembly document, which the user may

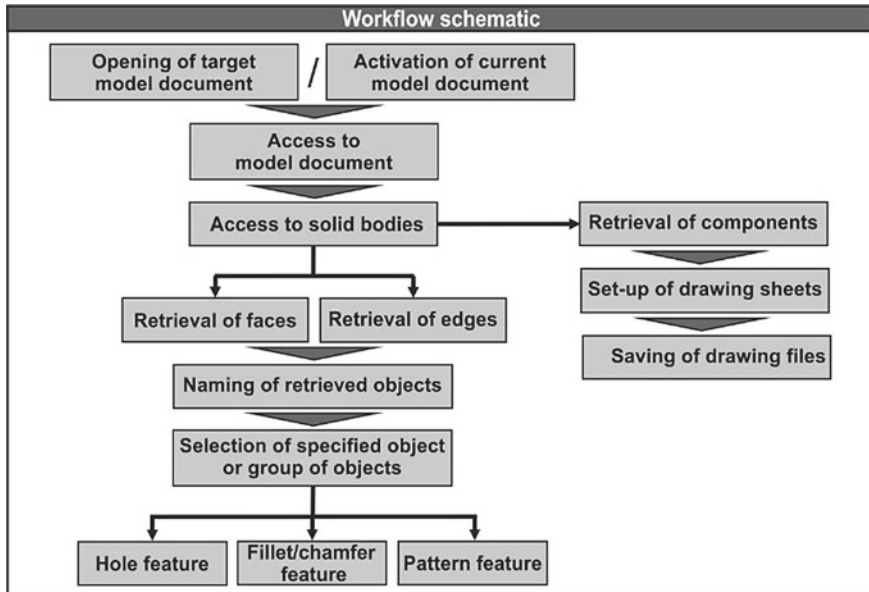


Fig. 1.2 The workflow of the application tool

export as a spreadsheet. All the files are saved in a folder where the original part or assembly exists, but the user may choose otherwise by just slightly altering the code.

Figure 1.2 summarizes the steps followed during the execution of each of the tool's functions.

According to the schematic (Fig. 1.2), the "OpenDoc6" and the "ActiveDoc" API methods are required to open an existing model document and activate it respectively, which is the first step of the workflow. If there is no document active, a message will warn the user. Next, the "GetBodies2" method as well as the "GetFaces" and the "GetEdges" methods are implemented in order to gain access to the solid bodies of the model and hence to the topology objects that are available in the bodies. Depending on whether the model document is a part or an assembly, the method must be called via the appropriate interface (i.e. IPartDoc, IComponent). To retrieve the topology objects a "For" loop is used that traverses all objects, changes their names and stores them to an array. The method for changing the names of the objects is the "SetEntityName". The name is a combination of a user-specified prefix and a numeral as suffix which is generated by a counter. Subsequently, the selection of the desired entities is realized with the "GetEntityByName" and the "Select4" methods. The first method is the one that gets the entity, whereas the latter is the one that selects and marks the entity. The "GetMaterialPropertyValues2" and the "SetMaterialPropertyValues2" methods are used for the object coloring option.

The methods "InsertFeatureChamfer" and "FeatureFillet3" are employed to insert the chamfer and fillet features, respectively, on the preferred topology object. The feature parameters (fillet radius, angle and width of chamfer) are set via the input

fields (see Fig. 1.1b) which are connected to the corresponding variables. Similarly, the creation of holes that is performed with the “FeatureCut4” method requires the set of several parameters, such as the hole diameter, the depth of cut and the center of the cut profile. The design of the flange pattern is achieved with the “FeatureCircularPattern5” method. The input fields illustrated in Fig. 1.1c define the diameter of the reference circle, the diameter of the holes and the number of the holes for the customized flange option. The creation of a standardized pattern is performed with the same method and the data are dictated by the combo-box. In both cases, a cylindrical face must be present in the active model document. Thus, the object selection procedure is not defined by the user preferences, rather it is pre-defined. In other words, the code uses the “GetSurface” method and a “For” loop to traverse all faces of the solid bodies found in the model, in order to find and get any cylindrical surface for the pattern to be applied. If no cylindrical face is found, the pattern feature cannot be completed. With respect to the circle sketch that describes the hole profile, the “CreateCircleByRadius” method is used. The implementation of this method requires the set of the radius and the center of the circle.

The methods used in the engineering drawings production procedure (fourth tab) are the following. The “OpenDoc6” is required to open the target assembly document. Creation and setup of a new drawing document are performed with the “NewDocument” and the “SetupSheet6” methods, respectively. The input fields (see Fig. 1.1d) are connected to variables that define the template path for the drawing documents, the save path and the folder where the target assembly resides. In addition to these settings, the user must define the sheet size and the scale. It is possible to change the name of the sheet and the margins by modifying the corresponding code. The sheets of the drawing document are created with the “NewSheet4” method and a “For” loop which follow the two previous methods. The loop is needed to traverse all the components that comprise the target assembly. The number of sheets created by the “NewSheet4” method depends on the number of components found. The insertion of the standard three-view of the model is realized with the “CreateDrawViewFromModelView3” methods, whereas the placement of the basic annotations (i.e. dimensions) is done with the “InsertModelAnnotations3” method. The model views are pre-defined and are placed on the paper space according to the default values given by SolidWorks™ based on the paper size. It is possible to configure the three variables that represent the coordinates X, Y and Z of the placement location, to change the location. On the other hand, the annotations cannot be changed because they solely depend on the annotations the user included during the design process of each part. In order to place the numbering balloons on each of the components, the “CreateAutoBalloonOptions” method is employed. This method creates an array that stores the preferences (i.e. shape, size) for the balloons. Lastly, these preferences are applied to the balloons, which are then inserted to the drawing with the “AutoBalloon5” method. Furthermore, the standard data of the assembly that are used to create the BOM are extracted with the “CreateMassProperty” method, whereas the custom properties (i.e. weight, material) can be associated to the BOM with the utilization of the “InsertBomTable3” method. Finally, the “SaveAsText2” method is used to

export the BOM as a spreadsheet and the “SaveAs” to save the drawing documents to the preferred file type (PDF, DWG).

Table 1.1 summarizes the most important SolidWorks™ API methods and properties that were used in this study. The presented application tool demonstrates the possibilities that derive from the programming of a CAD system via its API.

The implementation of the previously mentioned API methods was used for the development of the presented application tool. The following code snippet (Fig. 1.3) presents the use of a “For” loop in order to traverse and name all faces in the solid bodies of a model so that the selection process can be facilitated. Additionally, two check structures (“If–Then–Else” statements) are included so that the selection of an individual face or the selection of all available faces can be achieved. Similar strategies were used in the work of Kyratsis [26].

Textual Programming for Computational Design Application

Computer-aided design applications based on textual programming languages offer a great number of opportunities to the user/designer. The design methodology used via computational design prompts toward very unusual geometries and someone can argue that these are extremely difficult to be manufactured. Furthermore, the usage of a computational design application is crucial nowadays—due to the evolution of design methodologies (i.e. digital fabrication tools, virtual and augmented reality applications, CNC laser cutting and engraving techniques). Fortunately, new technologies offer new possibilities in the design and manufacturing industry.

The proposed case study presents a CAD-based application for automatic development of special 3D geometries with the aid of Python™ as a main textual programming language and Rhino™ for the CAD-based representations of geometries. Figure 1.4 illustrates the workflow for the automated creation of 3D entities. The recommended procedure consists of a series of steps that complete CAD-based applications. First, the user creates two different types of objects by using Rhino™ tools: a primitive geometry (i.e. sphere, cube, cylinder, cone, pyramid, etc.) and a plane.

All dimensions of these designed elements are up to the users’ choice. The main mechanism of the application is: the plane will cut the initial geometry to a certain number of flat layers. Thereafter, the user inserts specific numerical values for the parameters (Rhino™ command line) that determine the final form of the 3D structure. The proposed variables of the application are: step (number of cuts from plane on the primitive object), count (number of surface layers) and thickness (layers extrusion).

Python™ programming language is the main tool that a designer uses for the application development. Specifically, the designer imports the *rhinoscriptsyntax module* to the Rhino™ software. The combination between Python™ and Rhino™ deals with a great number of advantages in CAD-based application development. Some of the commands used for the script are presented in Table 1.2. Furthermore, a complete script of the proposed CAD-based application is presented in Table 1.3.

Table 1.1 SolidWorks™ API methods and properties used in the study

API method/property	Explanation	Return value
OpenDoc6	Opens an existing document	Newly loaded model document
ActiveDoc	Connects to the currently active document	Model document
GetBodies2	Gain access to the bodies in the currently active part	Array of bodies
GetFaces	Gets all the faces on the body	Array of faces on the body
GetEdges	Gets the edges for the selected body	Array of edges
SetEntityName	Sets the name of the entity	True/false
GetEntityByName	Gets an entity (face, edge, vertex) by name	Entity
Select4	Selects an entity and marks it	True/false
GetMaterialPropertyValues2	Gets the material property values for the selected component	Material properties
SetMaterialPropertyValues2	Sets the material property values for the selected component	–
InsertFeatureChamfer	Inserts a chamfer	Pointer to the IFeature object
FeatureFillet3	Creates the specified fillet feature for selected edges or faces	IFeature
FeatureCut4	Creates a cut extrude feature	Cut extrude feature
GetSurface	Gets the surface referenced by this face	Underlying surface for this face
CreateCircleByRadius	Creates a circle based on a center point and a specified radius	Sketch segment for the circle
FeatureCircularPattern5	Inserts a circular pattern feature	Circular pattern feature
CreateMassProperty	Obtains mass property information about one or more solid bodies in the document	IMassProperty object

(continued)

Table 1.1 (continued)

API method/property	Explanation	Return value
InsertBomTable3	Inserts a BOM table in a part or assembly document	BOM table annotation
SaveAsText2	Saves a table to a text data file	True/false
SaveAs	Saves the active document to the specified name in the specified format	True/false
NewDocument	Creates a new document based on a specified template	Newly created document
SetupSheet6	Sets up the specified drawing sheet	True/false
NewSheet4	Creates a new drawing sheet in the current drawing document	True/false
CreateDrawViewFromModelView3	Creates a drawing view on the current drawing sheet using the specified model view	Pointer to the newly create IView object
InsertModelAnnotations3	Inserts model annotations into the current drawing document in the currently selected drawing view	Array of inserted IAnnotation objects
CreateAutoBalloonOptions	Creates an object that stores auto balloon options	IAutoBalloonOptions
AutoBalloon5	Automatically inserts BOM balloons in selected drawing views	Array of INotes

Figure 1.5 presents four alternative design for the object of sphere that it is user's choice. The final results of this procedure are that the application creates a number of alternatives cuts of the selected object. The development of these different patterns emphasizes the creation of family morphologies. The alternative morphologies are (based on numerical values of proposed parameters from user's point of view):

- Alternative design (A): Step = 4, Count = 50 and Layer's Thickness = 1
- Alternative design (B): Step = 7, Count = 50 and Layer's Thickness = 2
- Alternative design (C): Step = 2, Count = 50 and Layer's Thickness = 0.5
- Alternative design (D): Step = 2, Count = 80 and Layer's Thickness = 0.5.


```

Sub main()
Set swApp = Application.SldWorks
Set swModel = swApp.ActiveDoc
Set swPart = swModel

FaceCounter = 1

vBodies = swPart.GetBodies2(swAllBodies, False)
For i = 0 To UBound(vBodies)
Set swBody = vBodies(i)
vFaces = swBody.GetFaces
  For j = 0 To UBound(vFaces)
Set swFace = vFaces(j)
Set swEnt = swFace
Debug.Print swPart.SetEntityName(swEnt, "Face" & FaceCounter)
FaceCounter = FaceCounter + 1
  Next j
Next i
Debug.Print FaceCounter

If OptionButton2.Value = True Then
swPart.ClearSelection2 True
Set swFace = swPart.GetEntityByName(UserForm1.Face_TB.Text, _ swSelFACES)
Set swEnt = swFace

  If swEnt Is Nothing Then
MsgBox "Face " & Face_TB.Text & " does not exist." _
  & vbCrLf & "Please select another."
Exit Sub
  Else
swEnt.Select4 True, swSelectData
  End If
End If

If OptionButton1.Value = True Then
Set swFace = swBody.GetFirstFace
swPart.ClearSelection2 True
Do While Not swFace Is Nothing
Set swEnt = swFace
swEnt.Select4 True, swSelectData
Set swFace = swFace.GetNextFace
Loop
End If
End Sub

```

Fig. 1.3 Code snippet of automatic topology selection with SolidWorks™ API

The results of these alternative choices by the user are:

- Alternative design (A): a *medium* density of individual layers
- Alternative design (B): a *low* density of individual layers
- Alternative design (C): a *high* density of individual layers
- Alternative design (D): an *extremely* high density of individual layers.

The presented structure is based on the computational design technology together with the use of CNC laser cutting and engraving techniques for the material of wood. Laser cutting is a technology widely used in the manufacturing industry. Especially, in the wooden products production, designers create computer models based on textual programming languages of the appropriate geometry for each component, and after their cut, they are assembled in a specific manner with an aim to reach the intended geometry.

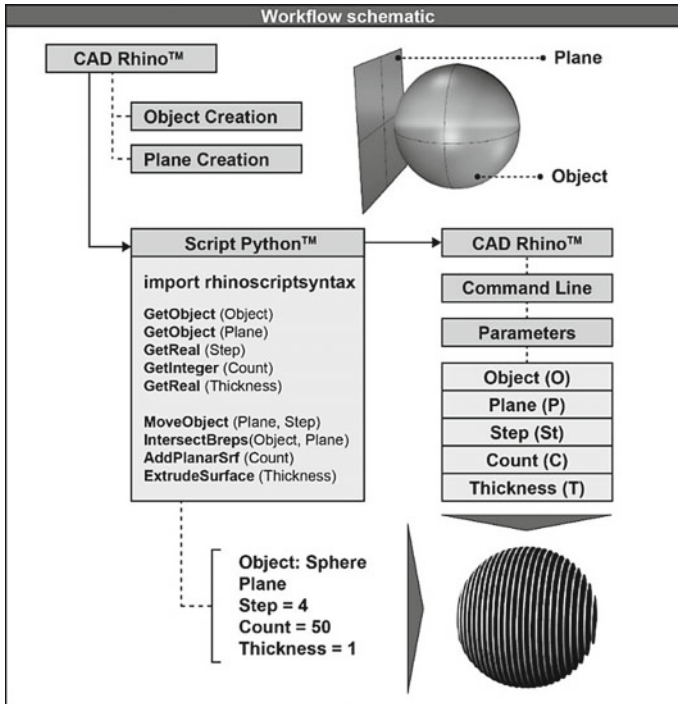


Fig. 1.4 The workflow of CAD application based on textual programming

Table 1.2 Script commands for the computational design application

Command	Usage
GetObject	Inserts plane, object
GetReal	Inserts values for step and thickness
GetInteger	Inserts values for count
MoveObject	Moves plane
IntersectBreps	Creates segments
AddPlanarSrf	Creates segment surface
ExtrudeSurface	Extrudes surfaces

The final produced structure deals with the main concept of wooden applications for architectural and product design purposes (i.e. wooden toy puzzles, portable architectural kiosks, etc.). The selected material for the product is wood, which is very fashionable nowadays, because it combines both quality and cost-effectiveness. The main idea is the use of cut wood based on the design principles offered by the computational design technology. The different components can be produced in short production times and these production times can be kept to a minimum. The curves used in the proposed design are well placed with high aesthetics. Finally, the

Table 1.3 Complete textual programming script for application

Python™ Module for Python™

```
import rhinoscriptsyntax as rs
```

Defeminations

```
def MyCut( obj , cutter , step , count , thickness ):
    listCrvs = []
```

“Cutting the Object” Mechanism

```
for i in range(1,count):
    cutter = rs.MoveObject( cutter , [step,0,0] )
    Intersect = rs.IntersectBreps( obj , cutter )
    listCrvs.append( Intersect )
rs.DeleteObject( obj )
rs.DeleteObject( cutter )
curve = rs.AddLine( [0,0,0] , [thickness,0,0] )
```

Layers extrusion

```
for crv in listCrvs:
    if crv == None:
        continue
    else :
        #print crv
        srf = rs.AddPlanarSrf( crv )
        rs.ExtrudeSurface( srf , curve )
        rs.DeleteObject( crv )
rs.DeleteObject( curve )
```

User’s choices (design parameters)

```
obj = rs.GetObject( "select object:")
cutter = rs.GetObject( "select cutter:")
step = rs.GetReal( "step = " , 4 ) # real numbers "rs.getReal()"
count = rs.GetInteger( "count = " , 50 )
thickness = rs.GetReal( "thickness = " , 1 , 0 , step )
MyCut( obj , cutter , step , count , thickness )
```

different types of shapes from the proposed application are a family of prototypes with an aim to explore aesthetics and technical characteristics from the designers’ point of view.

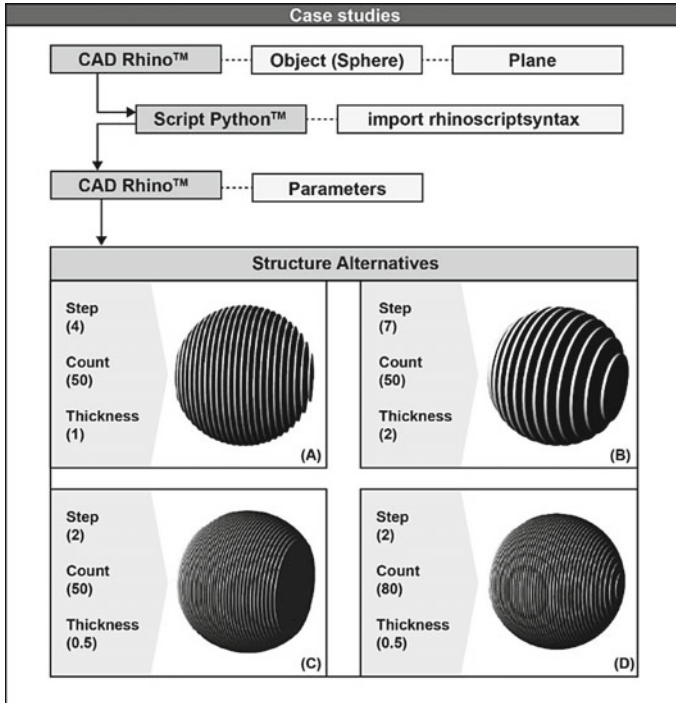


Fig. 1.5 A series of case studies of CAD application based on textual programming

Conclusions

The implementation of the SolidWorks™ API and the programming with the Rhino syntax module is being presented in this paper. Two distinct tools have been developed that can provide assistance to design engineers during the product development phase.

The programming resources used in the presented case studies are the SolidWorks™ API under VBA coding and Rhino™ 3D tools with Python™ programming language.

In general, the following conclusions can be drawn:

- The possibilities that derive from the utilization of CAD-based programming tools are vast.
- It is possible to design user-interfaces to accommodate the functionalities of the developed tools.
- In addition, CAD systems can be connected to other type of software such as MS™ Excel™.
- Most of the standard CAD-based operations can be automated.
- Special 3D entities can be automatically generated for use with 3D printing or 2D CNC operations that otherwise would require a lot of time and effort to design.

Furthermore, the value of such tools increases as the complexity of the system or product under development increases.

References

1. Kim J, Park J, Ko TJ (2008) End mill design and machining via cutting simulation. *Comput Des* 40:324–333. <https://doi.org/10.1016/j.cad.2007.11.005>
2. Tapoglou N (2019) Calculation of non-deformed chip and gear geometry in power skiving using a CAD-based simulation. *Int J Adv Manuf Technol* 100:1779–1785. <https://doi.org/10.1007/s00170-018-2790-3>
3. Dimitriou V, Vidakis N, Antoniadis A (2007) Advanced computer aided design simulation of gear hobbing by means of three-dimensional kinematics modeling. *J Manuf Sci Eng Trans ASME* 129:911–918. <https://doi.org/10.1115/1.2738947>
4. Roberto V, Osorio-Gómez G (2012) Assembly planning with automated retrieval of assembly sequences from CAD model information. *Assem Autom* 32:347–360. <https://doi.org/10.1108/01445151211262410>
5. Oancea G, Haba S-A (2016) Software tool used in CAPP/CAM systems for rotational parts. *Sci Bull Ser C Fascicle Mech Tribol Mach Manuf Technol* 30
6. Mok H-S, Kim C-H, Kim C-B (2011) Automation of mold designs with the reuse of standard parts. *Expert Syst Appl* 38:12537–12547. <https://doi.org/10.1016/j.eswa.2011.04.040>
7. García-Hernández C, Gella-Marín RM, Huertas-Talón JL, Berges-Muro L (2016) Algorithm for measuring gears implemented with general-purpose spreadsheet software. *Measurement* 85:1–12. <https://doi.org/10.1016/j.measurement.2016.02.013>
8. Teodor V, Popa I, Popa C et al (2009) Algorithm for gear hub tool profiling by Bezier polynomial approximation. *The Rotary Helical Screw Compressor Case*
9. Anghel Drugarin CV, Stroia M (2017) Computer-aided manufacturing of 3D workpieces. *ANALELE Univ “EFTIMIE MURGU” REȘIȚA ANUL XXIV, NR 1, 2017* 1453–7397 24:41–46
10. Tzivelekis CA, Yiotis LS, Fountas NA, Krimpenis AA (2015) Parametrically automated 3D design and manufacturing for spiral-type free-form models in an interactive CAD/CAM environment. *Int J Interact Des Manuf* 11:223–232. <https://doi.org/10.1007/s12008-015-0261-8>
11. Kyratsis P, Tapoglou N, Bilalis N, Antoniadis A (2011) Thrust force prediction of twist drill tools using a 3D CAD system application programming interface. *Int J Mach Mach Mater* 10:18–33. <https://doi.org/10.1504/IJMMM.2011.040852>
12. Garcia-Hernandez C, Gella-Marín RM, Huertas-Talón JL, Efkolidis N, Kyratsis P (2016) WEDM manufacturing method for noncircular gears using CAD/CAM software. *Strojniški Vestn-J Mech Eng* 62:137–144. <https://doi.org/10.5545/sv-jme.2015.2994>
13. Leitão A, Santos L (2011) Programming languages for generative design—visual or textual? *Respect Fragile Places* (29th eCAADe conference proceedings), pp 549–557
14. Kilian A (2006) Design innovation through constraint modeling. *Int J Archit Comput* 4:87–105. <https://doi.org/10.1260/147807706777008993>
15. Krause J (2003) Reflections: the creative process of generative design in architecture. *Gener Arts Conf* 14
16. Casale A, Valenti GM, Calvano M, Romor J (2013) Surfaces: concept, design, parametric modeling and prototyping. *Nexus Netw J* 15:271–283. <https://doi.org/10.1007/s00004-013-0146-8>
17. Chen HY, Pottmann H (1999) Approximation by ruled surfaces. *J Comput Appl Math* 102:143–156. [https://doi.org/10.1016/S0377-0427\(98\)00212-X](https://doi.org/10.1016/S0377-0427(98)00212-X)
18. Malakuczi V (2019) Computational by Design, towards a co-designed material culture. A design tool. *Des J* 22:1235–1248. <https://doi.org/10.1080/14606925.2019.1594989>

19. Lopes J, Leitão A (2011) Portable generative design for CAD applications. *Integr Through Comput—Proc 31st Annu Conf Assoc Comput Aided Des Archit ACADIA 2011* 196–203
20. Viny A, Dabholkar A, Cardoso Llach D (2018) Two design experiments in playful architectural adaptability. *Nexus Netw J* 20:25–39. <https://doi.org/10.1007/s00004-017-0350-z>
21. Kyratsis P, Manavis A, Gianniotis P, Ghiculescu D (2019) A non-conventional methodology for interior product design using conceptual design principles and parametric tools. *Nonconv Technol Rev Tehnol Neconv* 23
22. Tzintzi V, Manavis A, Efkolidis N, Dimopoulos C, Kakoulis K, Kyratsis P (2017) Conceptual design of jewellery: a space-based aesthetics approach. *MATEC Web Conf* 112. <https://doi.org/10.1051/mateconf/201711207025>
23. Tzotzis A, Garcia-Hernandez C, Huertas-Talon J-L, Tzetzis D, Kyratsis P (2017) Engineering applications using CAD based application programming interface. In: *MATEC web of conferences*, p 7
24. Kyratsis P, Gabis E, Tzotzis A, Tzetzis D, Kakoulis K (2019) CAD based product design: a case study. *Int J Mod Manuf Technol* 11:88–93
25. Kyratsis P, Tzotzis A, Tzetzis D, Sapidis N (2018) Pneumatic cylinder design using cad-based programming. *Acad J Manuf Eng* 16:107–113
26. Kyratsis P (2020) Computational design and digital manufacturing. *Int J Mod Manuf Technol* 12:82–91

Chapter 2

Development of Macro Program for Improving Machining Characteristics of Logarithmic Spiral on CNC Machining Center



Vratraj Joshi, Bhavin Desai, Shalin Marathe, Keyur Desai, and Harit Raval

Introduction

In the field of CNC machining, many algorithms are proposed to improve productivity. Literature related to machining of curved tool path, and algorithm development is studied in the present work. Kalidaas et al. [1] suggested that mathematical model can be developed to optimize and correlate the process parameters with surface roughness. Parameshwari et al. [2] identified surface finish as quality attribute and is assumed to be directly related to productivity. The milling parameters evaluated were cutting speed, feed rate and depth of cut. Omirou et al. [3] developed an algorithm to generate motion that use real-time interpolation. Rough pass and finish pass are applied to control surface quality. Abbas et al. [4] described that an algorithm may be required to develop user-defined cycle. Fitter et al. [5] discussed that parametric representation has become a standard form of computer-aided geometric design to define various industrial profiles. Free-form curves are represented mathematically as parametric curves to make them more computers compatible. Boujelbene et al. [6] suggested that explicit function is used, while second-order continuous tool path comprising arc and straight line segments can be compared with first-order continuous tool path. Tseng et al. [7] observed that the final surface produced may lack smoothness due to interpolation of line segments. Yang et al. [8] reported that parametric interpolator is favorable in the machining of free-form geometry. The linear interpolator has the advantages of simplicity. Farouki et al. [9] formulated explicit

V. Joshi (✉)

R. N. G. Patel Institute of Technology – RNGPIT, Bardoli – Navsari Road, Isroli, Afwa, Bardoli, Surat, Gujarat 394620, India
e-mail: vkj.fetr@gmail.com

B. Desai · S. Marathe · K. Desai · H. Raval

Department of Mechanical Engineering, S.V. National Institute of Technology, Surat, Gujarat 395007, India

function with the compact part program. Sata et al. [10] defined the numerically controlled tool path. From the literature, it is noted that geometrical data of the cutter path is stored in a CAD model and transformed to CAM to machine the curve. Various algorithms have been developed to decrease data volume, part program preparation time and to attain shape flexibility. Inspiring from the literature, it is decided to develop algorithm for logarithmic spiral curves in the present work.

In the present work, MACRO programming is attempted and compared with the conventional part programming approach considering linear interpolation. It is a flexible programming method, where planar curve can be expressed by any mathematical parametric equation that can be machined using MACRO programming. In the present work, MACRO and conventional programming techniques for machining curved shape with continuously changing radius (logarithmic spiral) are studied and compared. Explicit function is used while programming with MACRO interpolator. Commands for CNC machining can be developed that convert motion trajectory from the desired path. CNC Fanuc controller can prepare MACRO programming to be executed by preparatory codes. It can utilize conditional and logical loops, arithmetic variables and operators. For parts with similar design, a MACRO programming can be developed to reduce part programming time. A subprogram is helpful to machine parts having similar operations. Workpiece variables such as dimensions, holes, threads and slots can be changed frequently. Tool position coordinates are not needed to be changed every time as and when the part is changed; hence a single MACRO program is more suitable for a same part family. It helps in reducing duplication by using the commands such as GO TO, IF [condition] THEN [do something condition], EQ [equals], NE [not equals], GT [greater then], LT [Less then], + , - , *, /, SIN, COS, TAN, ATAN, SQRT and ABS.

Machining of Logarithmic Spiral

A logarithmic spiral, also known as equiangular spiral or growth spiral, is a self-similar spiral curve which often appears in nature. The curve was described by Descartes and investigated by Jacob Bernoulli, who mentioned the curve as “the marvellous spiral”. Equation (2.1) is an equation for the radius of the spiral curve. It shows that radius “ r ” varies with variation in angle “ θ ” [11].

$$r = ae^{b\theta} \quad (2.1)$$

$$\left. \begin{aligned} X &= r \cos \theta \\ Y &= r \sin \theta \end{aligned} \right\} \quad (2.2)$$

Equation (2.1) provides radius “ r ” of the spiral curve for the value of “ θ ” that varies at regular interval. X and Y coordinates are calculated at various points on curved geometry using logarithmic spiral function. The values of X and Y coordinates of

the cutter location points are required to machine the curve. From Eq. (2.2), it is cleared that the values of X and Y coordinates are dependent on the value of “ r ” and as per Eq. (2.1). Figure 2.1a–c shows interpolation, simulation and actual machining of logarithmic spiral. Positions of X and Y coordinates can be changed by varying the value of variable “ θ ” for the given “ a ” and “ b ” because of value of radius “ r ” is dependent on variable “ θ ”. So, by varying the value of “ θ ”, the values of X and Y coordinates can be obtained as mentioned in Eq. (2.2) from the polar value of the radius “ r ”.

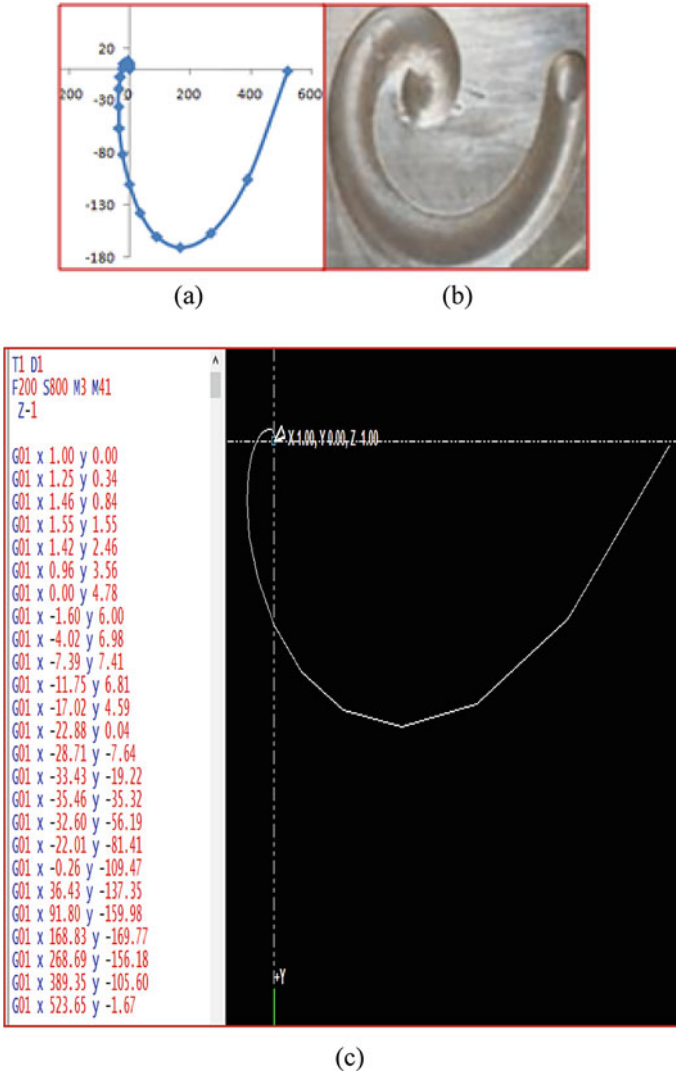


Fig. 2.1 a–c Simulation and actual machining of logarithmic spiral

Table 2.1 Assigning MACRO address

MACRO address	Variable	Description	Initial value
#101	a	Constant	1
#102	b	Constant	1
#103	Θ	Initial angle	0
#104	r	Polar coordinates	1
#105	X	X coordinates of cutter location points	1
#106	Y	Y coordinates of cutter location points	0

Logarithmic spiral is interpolated with MACRO programming. Angular increment starts from initial value “0°” and ends at “360°” with the increment of 3.6°. It means the total calculated cutter location points are determined by dividing the subtraction of maximum value and minimum value of angle with the step size [i.e., $(360-0)/3.6 = 100$]. Drawing logarithmic spiral in AutoCAD with measuring cutter location points takes more time. Table 2.1 shows the variables stored at various MACRO addresses and the detailed MACRO program is reported in annexure.

Results and Discussion

Conventional programming and MACRO programming are compared for length and size of program, as well as for program writing and execution time. It is noted that program writing time includes time required for drawing the logarithmic spiral and feeding the program. Comparison between conventional and MACRO programming methods for the machining of the logarithmic spiral is shown in Table 2.2. In the present work, time for drawing logarithmic spiral with 100 cutter location points for each quadrant in AutoCAD is 2652 s.

Time for feeding X and Y coordinates is 1133 s. Cutter tool path is driven by equation in case of MACRO programming. No drawing is required in that case. Hence, program feeding time (i.e., 231 s) is quiet less. Machine feed is taken as 100 mm/min,

Table 2.2 Comparison of conventional and MACRO programming

			Conventional programming	MACRO programming
Length (words)			540	57
Size (KB)			14	0.38
Time (s)	Program writing	Drawing	2652	0
		Feeding	1133	231
	Program execution		32	67
	Total		3817	298

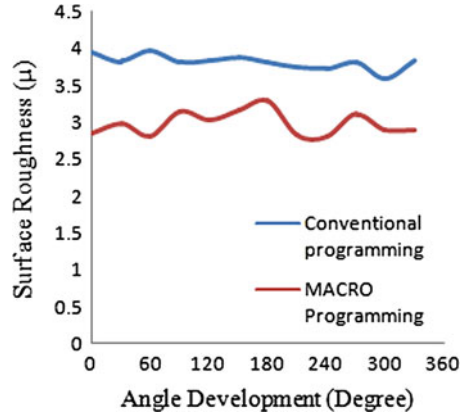
and hence program execution time to cut the curve by conventional programming is 32 s. The processor has to calculate X and Y coordinates for every cutter location (CL) points in case of MACRO programming. So, the program execution time is 67 s. It is more than double of the time for machining done by conventional programming. Total time including program writing (i.e., drawing and feeding) and program execution time for the conventional method to cut the logarithmic spiral is quite high (i.e., 3817 s) compared to MACRO programming method (i.e., 298 s). The program size of conventional programming is 14 KB and the length is 540 words. While for MACRO programming, the program size is 0.38 KB and the length is 57 words. These are the additional advantages of MACRO programming. The logarithmic spiral is machined by conventional and MACRO programming methods to examine surface quality, with the help of SURFTEST (SJ-210 Mitutoyo). The workpiece is marked clockwise at 30° at 12 positions ($360^\circ/120$) of the test piece to measure surface quality. Table 2.3 shows the surface roughness of logarithmic spiral (i.e., variable curvature) machined by conventional and MACRO programming.

The average value of surface roughness is lesser for MACRO programming method ($2.992 \mu\text{m}$) compared to conventional programming method ($3.811 \mu\text{m}$). For conventional programming, number of cutter location (CL) points determines the programming length. As length of MACRO programming is equation driven, it is less compared to conventional programming. Some duration of time is needed to execute the program by processor to calculate coordinates of cutter location (CL) points as per the equation; sufficient time to change the direction according to curvature region of the tool path is availed to the machine, which results in the less fluctuation of cutting force. It reduces the tool overdrive and improves the surface quality. Figure 2.2 indicates a comparison of the average surface roughness for both programming methods.

Table 2.3 Measurement of surface roughness

Surface roughness (μ)			
S. No.	Conventional programming	MACRO programming	Difference
1	3.951	2.848	1.066
2	3.827	2.974	0.853
3	3.973	2.811	1.162
4	3.822	3.144	0.678
5	3.83	3.036	0.794
6	3.879	3.158	0.721
7	3.806	3.288	0.518
8	3.751	2.829	0.921
9	3.729	2.809	0.92
10	3.814	3.111	0.703
11	3.581	2.904	0.677
12	3.829	2.905	0.924
Avg.	3.811	2.992	

Fig. 2.2 Surface roughness in machining of logarithmic spiral



Coordinates of cutter location (CL) points are calculated by the processor. Hence, cutter stops for a while. It enhances surface quality while machining the curve using MACRO programming method. As shown in Fig. 2.2, surface roughness is less in the case of logarithmic spiral machined with MACRO programming compared to conventional programming.

Conclusion

CAD software is not required while curved geometry is machined with MACRO programming because the curve is represented by the mathematical equation. And hence, sufficient time is availed by processor to calculate the cutter location (CL) coordinates. Tool is stopped for a while at the previous point while the next point is calculated. Enough time to follow the direction according to curvature of the tool path is provided to the processor. Cutting force fluctuation is less and good surface finish is achieved. Conventional and MACRO programming are prepared for the curved shape motion of the tool but cutting force leads tool in the tangential direction. It results in cutting force fluctuation. Owing to that, surface roughness is more for conventional programming compared to MACRO programming methods.

Annexure

MACRO programming for Logarithmic spiral.

M03 S2000 (Spindle clockwise rotation).

G01 Z0 F1000 (Air cutting).

G01 Z-2.0 F50 (Tool mark at center).

#101 = 0 (Initial value of θ).

N10.
 #102 = 2 (Initial value of k).
 #103 = cos [#101] (Value $\cos \theta$).
 #104 = sin [#101] (Value $\sin \theta$).
 #105 = cos [#101*#102] (Value of $r = \cos(k\theta)$).
 #106 = #105*#103 (Finding value of $x = r \cos \theta$).
 #107 = #105*#104 (Finding value of $y = r \sin \theta$).
 N30.
 G01 X#106 Y#107 Z = -0.4 F100.

References

1. Kalidass S, Palanisamy P (2013) Prediction and optimization of surface roughness for end milling operation using artificial neural networks and genetic algorithm. *J Manuf Eng* 8(1):028–037
2. Parameshwari PSD (2014) Prediction of process parameters in cnc end milling of UNS C34000 medium leaded brass. *J Manuf Eng* 9(1):036–044
3. Omirou SA (2004) CNC interpolation algorithm for boundary machining. *Robot Comput Integr Manuf* 20(3):255–264
4. Abbas AT, Megahed SM (2005) A general algorithm for drilling holes lying in a matrix. *Comput Integr Manuf* 21:235–239
5. Fitter HN, Pandey AB (2014) Comparison of parametrically programmed machining with CAM system machining for C_0 continuity Bezier curves based on various parameters. *Procedia Eng* 97:1167–1177
6. Boujelbene M, Moisan A, Tounsi N, Brenier B (2004) Productivity enhancement in dies and molds manufacturing by the use of C_1 continuous tool path. *Int J Mach Tools Manuf* 44:101–110
7. Tseng YJ, Chen Y-D (2000) Three dimensional biarc approximation of freeform surfaces for machining tool path generation. *Int J Prod Res* 38:4739–4763
8. Yang DCH, Tom K (1994) Parametric interpolator versus linear interpolator for precision CNC machining. *Comput Aided Des* 26:225–234
9. Farouki RT, Manjunathaiah J, Yuan G (1999) G codes for the specification of Pythagorean hodograph tool paths and associated federate functions on open architecture CNC machines. *Int J Mach Tools Manuf* 39:123–142
10. Sata T, Kimura F, Okada N, Hosaka M (1981) A new method of CNC interpolation for machining the sculptured surface. *Ann CIRP* 30:369–372
11. Archibald RC (1918) The logarithmic spiral. *Am Math Monthly* 25:189–193

Chapter 3

Automatic Feature Recognition (AFR) of the Inclined Cross-Hole in Hollow Cylinders



Abdullah D. Ibrahim, Sabreen A. Abdelwahab, H. M. A. Hussein,
and Ibrahim Ahmed

Introduction

Feature is a specific shape or another property of a part which helps the designer in reasoning about a part by associating knowledge [1]. Interpreting the geometrical CAD data automatically (feature recognition) of manufacturing features is insufficiently applied in real industry yet. Many researches on automatic feature recognition have proposed algorithms to recognize the combined and interacting machining features [2], but these algorithms are not often compatible with all CAD systems [3–5]. Most of these algorithms belong to three main groups of approaches, namely graph-based, hint-based and volumetric decomposition [6].

To facilitate an interface between various CAD/CAM systems, a neutral format for representation is required. There are various neutral files, such as STEP, DXF, IGES, and STL files. The international standard ISO 10303-203 is a definition of

A. D. Ibrahim (✉)

Senior Lab Engineer, Process and Product Development Department, American University in Cairo (AUC), Cairo, Egypt

e-mail: AbdullahDosoqy@yahoo.com

S. A. Abdelwahab

Production Technology Department, Faculty of Technology and Education, Helwan University, Cairo, Egypt

e-mail: engsabreenabdallah@gmail.com

H. M. A. Hussein

Mechanical Engineering Department, Faculty of Engineering, Helwan University, Cairo, Egypt

e-mail: hmahuss@hotmail.com

I. Ahmed

Automotive Technology Department, Faculty of Technology and Education, Helwan University, Cairo, Egypt

e-mail: Ilmahmed1968@yahoo.co.uk

STEP model data [7], and it is an internationally recognized neutral file format that is suitable for most of the commercial CAD software; it also comprises coordinates data that are easy to extract and geometric dimensioning and tolerancing data correlated to the part.

Recognition of a cross-hole feature can be achieved when B-Spline-Curve-With-Knots exist in the neutral file STEP AP-203. Inclined cross-holes can pass or offset from the axis of the cylinder, and it might also pass through or be blind [8].

This paper proposes an AFR system for inclined cross-hole in hollow cylinders, in which the SolidWorks software is used to draw the part and save it as a STEP AP-203 file format. For extracting and recognizing the inclined cross-hole feature, a tailor-made software is developed using Visual Basic programming language.

Literature Review

For AFR, various approaches have been developed and implemented. This review is focused on the researches closely related to the proposed system described in this paper as follows:

Nagi [9] has developed a system for extracting features from prismatic parts manufactured by milling operation. The input file to the system is in format of STEP AP-203, and the output is in STEP AP-224 format for defining the geometry and topology of a part.

Shunmugam et al. [10] has proposed a developed feature recognition system. The author used that system in recognizing the orthogonal features. For representing the part 3-D model, the module of feature recognition considers STEP AP-203 file format. Face adjacency graph and volume subtraction techniques were considered for feature recognition.

Sivakumar and Dhanalakshmi [11] have proposed a system for extracting manufacturing features from STEP AP-203 file of cylindrical parts. The geometrical and dimensional information of features are extracted by using the process of feature extraction. The extracted information is stored in a text file and then the logic rules are used for analyzing the data of turning features.

Malleswaria and Sarcar [12] have presented a new software for feature recognition of cylindrical parts that used a neutral file STEP as an input. This software analyzed different entities and strings and in the neutral file and extracted geometrical, topological and dimensional data of surfaces such as centre of circles, radius of the circles, the surfaces type, and axis coordinates of surface. This software has interpreted and evaluated the data exacted in terms of manufacturing process and recognized features for the turned parts. The software used rule-based technique during feature recognition process.

The above AFR review illustrates that the researchers have used different methodologies for recognizing machining features depending on the neutral file STEP AP-203 to represent the part 3D model and to recognize the machining features. So, using STEP file format is needed to represent the model data of the part, and it also helps in CAD/CAM systems integration. Thus, the current research is proposing a system for recognizing the inclined cross-hole features in hollow cylinders that is representing in the neutral file STEP AP-203, and a tailor-made software is used for extracting and recognizing the inclined cross-hole based on rule-based reasoning.

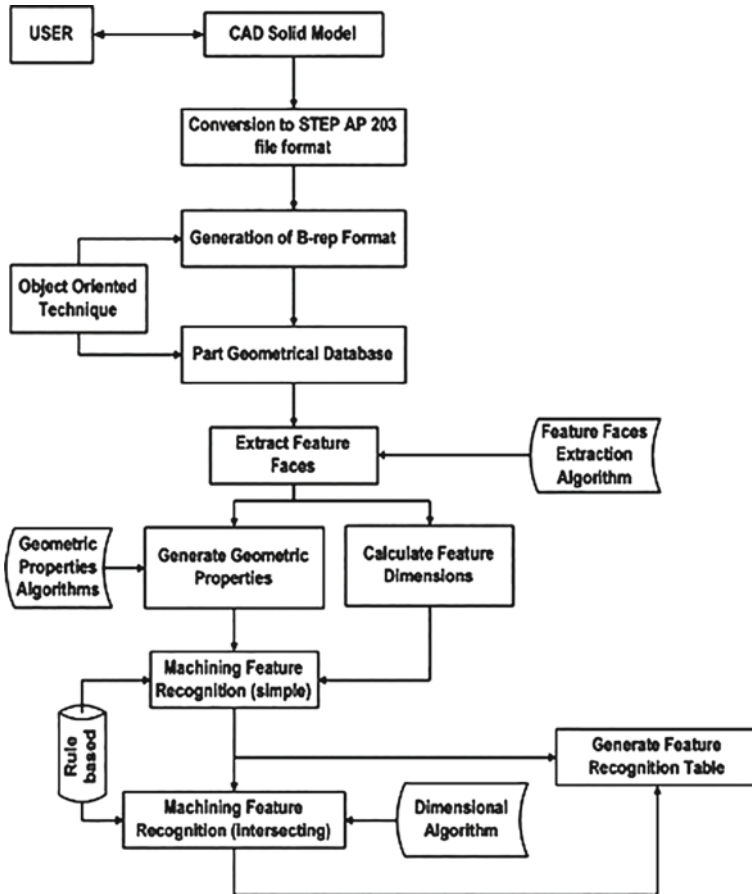


Fig. 3.1 The architecture of the current system [13]

Architecture of the Current System

The current system has been built by linking SolidWorks software to Visual Basic. The drawing is sent to the Visual Basic as a neutral file STEP AP-203. Then, the Visual Basic shows the part on a special screen through a tailor-made software which is installed on it. The software can extract and recognize the inclined cross-hole feature based on rule-based reasoning. Figure 3.1 shows the architecture of the current system [13].

Data Extraction and Feature Recognition

The object-oriented approach is used to extract data from the input file. Visual Basic extracts the data of the part and the technique of B-Reb is used to represent the part's

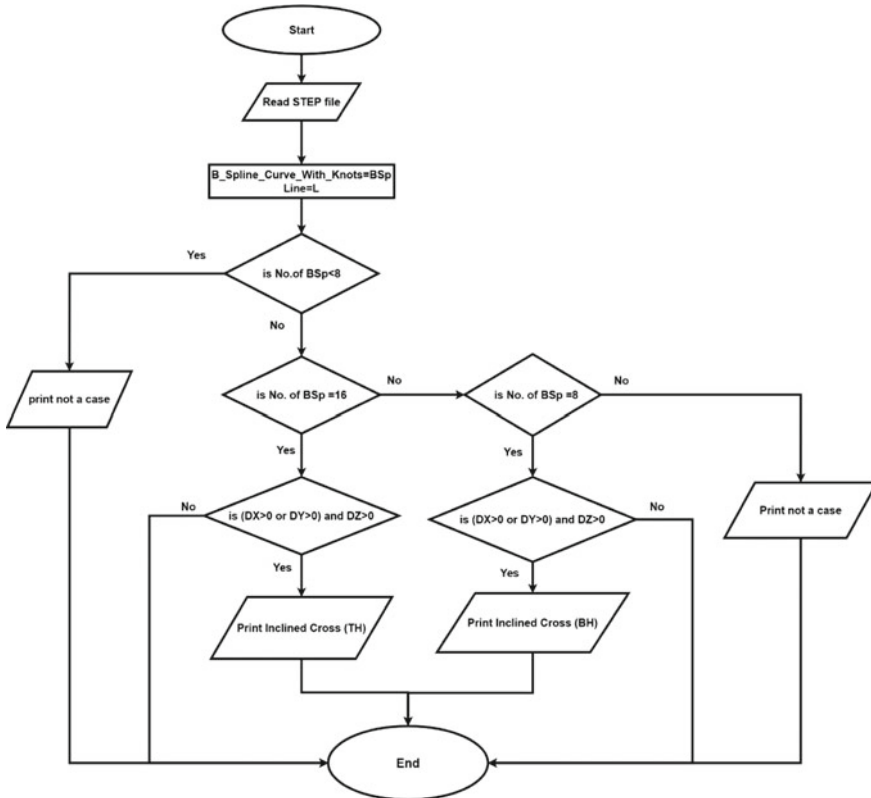


Fig. 3.2 Flowchart of AFR of inclined cross-holes in hollow cylinders

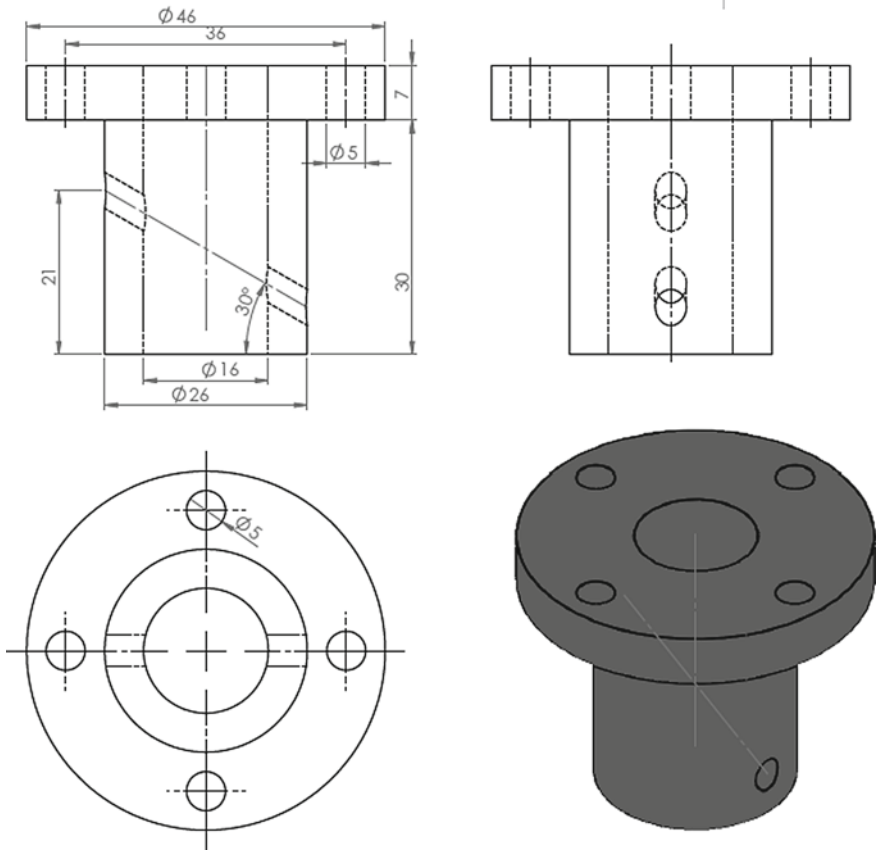


Fig. 3.3 Drawing and isometric of the part

geometrical structure and specify the orientation type of all faces from the database of B-Rep which includes the geometrical and topological information.

Figure 3.2 shows a flowchart of AFR of inclined cross-holes in hollow cylinders.

Validation of the Developed Methodology

The developed methodology is validated through a case study. The part drawing is prepared by using SolidWorks software and it is saved in STEP AP-203 file format.

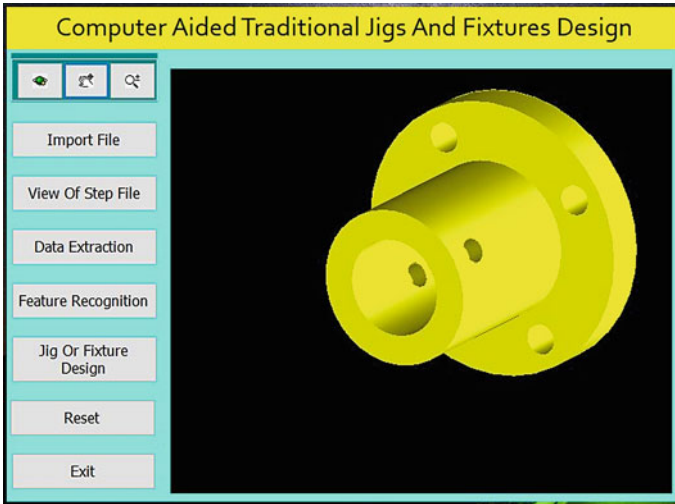


Fig. 3.4 Drawing of part on software screen

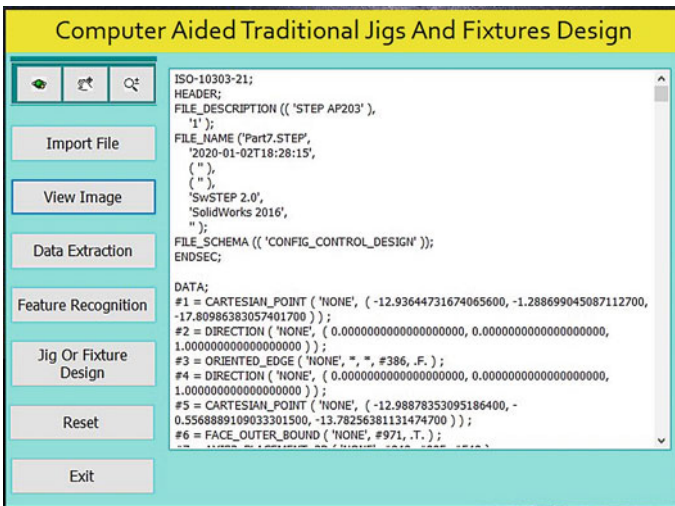


Fig. 3.5 STEP AP-203 file of the part

Then, a tailor-made software which is installed on Visual Basic is used to extract model part data from part drawing file and to extract inclined cross-hole feature.

Recognition of the Inclined Cross Through Hole

Figure 3.3 shows the drawing and isometric of a cylindrical part, and recognition of the inclined cross through hole will be done through the following steps:

Face Number	Face Name	Face Radius
1	generated cylinder	8
2	generated cylinder	13
3	PLANE	0
4	PLANE	0
5	PLANE	0
6	PLANE	0
7	PLANE	0
8	PLANE	0
9	generated cylinder	2.5
10	generated cylinder	2.5
11	generated cylinder	23
12	generated cylinder	2.5
13	generated cylinder	2
14	generated cylinder	2.5
15	generated cylinder	2
16	generated cylinder	13
17	generated cylinder	2.5
18	PLANE	0
19	PLANE	0
20	generated cylinder	2.5
21	PLANE	0
22	PLANE	0
23	PLANE	0
24	PLANE	0
25	PLANE	0
26	PLANE	0
27	generated cylinder	2
28	generated cylinder	23
29	generated cylinder	2
30	generated cylinder	2.5
31	generated cylinder	8
32	generated cylinder	2.5

Fig. 3.6 Report of the extracted data

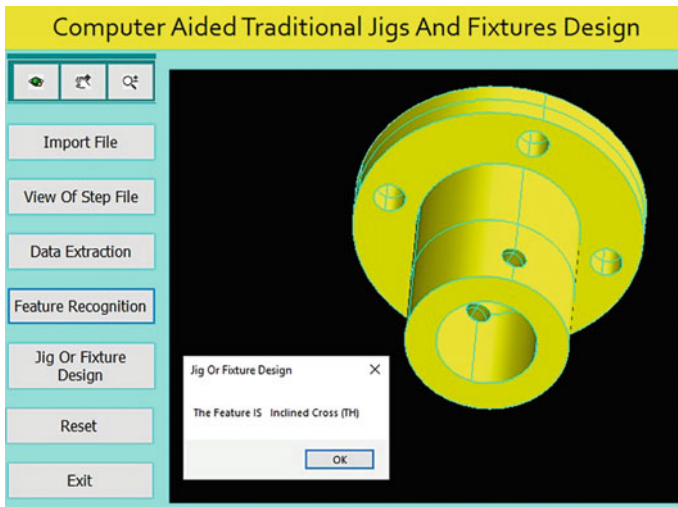


Fig. 3.7 AFR of an inclined cross blind hole

- The drawing and isometric of a cylindrical part prepared using SolidWorks software is shown in Fig. 3.3. The file is saved in STEP AP-203 file format.
- The tailor-made software which is installed on Visual Basic platform is used to extract the part data from the part file and compare these data with the rules of feature recognition. Figure 3.4 shows the part on the screen of tailor-made software.

Figure 3.5 depicts the file of cylindrical part and Fig. 3.6 shows the report of extracted data.

Feature recognition of an inclined cross through hole is shown in Fig. 3.7.

Conclusion

The present paper proposes a new simple approach for automatic feature recognition of inclined cross-holes in hollow cylinders using a tailor-made software which is installed on Visual Basic platform. This software links SolidWorks software to Visual Basic and shows the part on special screen. The software extracts data of the part geometry from STEP AP-203 file and recognizes the inclined cross-holes in hollow cylinders. Validation of the proposed methodology has been done using a case study.

References

1. Shah J, Mantyla M (1995) Parametric and feature-based CAD/CAM. A Wiley-Interscience Publication, Wiley, New York
2. Chang P, Chang C (2000) An integrated artificial intelligent computer-aided process planning system. *Int J Comput Integr Manuf* 13(6):483–497
3. Liu S (2004) Feature extraction and classification for rotational parts taking 3D data files as input. *J Chin Inst Ind Eng* 21(5):432–443
4. Sunil VB, Agarwal R, Pande S (2010) An approach to recognize interacting features from B-Rep CAD models of prismatic machined parts using a hybrid (graph and rule based) technique. *Comput Ind* 61:686–701
5. Kamarani A, Abuel Nasr E (2010) Engineering designing and rapid prototyping. Springer, Berlin, p 231
6. Han JH, Pratt M, Regli WC (2000) Manufacturing feature recognition from solid models: a status report. *IEEE Trans Robot Automat* 16(6):782–796
7. STEP Application Protocol (AP) 203 editions 1 & 2, Configuration Controlled 3D Designs of Mechanical Parts and Assemblies, ISO10303 1994, (2007) & (2009)
8. Vangipurapu NM (2013) Automatic feature recognition for rotational components from STEP files. Unpublished PHD thesis, Andhra University, College of Engineering, India
9. Bhandarkar MP, Nagi R (2000) STEP-based feature extraction from STEP geometry for agile manufacturing. *Comput Ind* 41:3–24
10. Rameshbabu V, Shunmugam MS (2009) Hybrid feature recognition method for setup planning from STEP AP-203. *Robot Comput-Integr Manuf* 25:393–408
11. Sivakumar S, Dhanalakshmi V (2013) A feature-based system for CAD/CAM integration through STEP file for cylindrical parts. *Indian J Eng Mater Sci* 20:21–26
12. Malleswari VN, Valli PM, Sarcas MMM (2013) Automatic recognition of machining features using STEP files. *Int J Eng Res Technol* 2
13. Khan A, Abouel Nasr E, Al-Ahmari A, Mian S (2018) Integrated process & fixture planning: theory and practice. Taylor & Francis, Routledge, Boca Raton

Chapter 4

Grey Relational Multi-decision Analysis of SS304 Bead Characteristics Processed in Wire Arc Deposition Process for Additive Manufacturing



D. T. Sarathchandra and M. J. Davidson

Introduction

Wire and arc additive manufacturing (WAAM) belongs to the directed energy deposition process which uses electrical arc as energy source and wire as feedstock. WAAM can be attained by processes like gas metal arc welding (GMAW) [1], gas tungsten arc welding (GTAW) [2], and plasma arc welding (PAW) [3]. There are numerous advantages for WAAM over laser-assisted and plasma-assisted additive manufacturing processes, in terms of the capital cost of machines and material flexibility. Cold metal transfer (CMT) process is considered as the advancement of the GMAW process with lower heat input and spatter as compared to other arc welding methods [4]. The key factor involved in CMT technology is the automatic wire feed controller. The reciprocated wire feed mechanism was incorporated with an electrical process in which arc initiation and short circuiting will be synchronized by the electrical controller. In the present work, austenitic stainless steel of grade SS304 was used for experimental studies. Austenitic stainless steels have been widely used as nuclear structural materials for reactor coolant piping, valve bodies, spacer column assembly, control rod drive mechanism, and vessel internals because of their excellent mechanical properties, good mechanical properties and corrosion resistance at high temperature and high pressure environment [5, 6]. Many input factors contribute directly or indirectly to the material characteristics. These include input power, weld speed, wire feed rate, stand-off distance, inert gas flow rate, path planning, deposition strategies, and so on. The present study considers the effect of input power in terms of current, weld speed, and stand-off distance on the clad bed properties such as bead shape and size, and depth of penetration.

D. T. Sarathchandra (✉) · M. J. Davidson
National Institute of Technology Warangal, Warangal 506004, India
e-mail: sarathchandradongari@gmail.com

Grey relational analysis (GRA) was proposed by Deng in 1989. The grey relational assessment is a technique of evaluating the degree of similarity between the sequences through grading. The grey relation evaluation concepts have drawn significant interest among researchers. Some researchers worked to optimize the multi-objective optimization using GRA [7].

Therefore, this study presents a multi-objective optimization of CMT bead characteristics using the GRA method coupled with RSM. The RSM examines an adequate estimate of input and output variables and determines the optimum operating conditions for a function being studied or a segment of the factor field that meets the operational requirements. Three parameters, namely current, weld speed, and stand-off distance, are selected to run the experiment. The grey relational analysis is applied to evaluate the single bead characteristics for the development of additive manufacturing structures.

Materials and Methods

Experiments were conducted on Fronius-made manual CMT machine TPSI 320I model, attached with in-house developed three-axis manual-controlled workstation. While experimenting, welding torch was held stationary in a vertical position through which filler wire feeding is done on the system at a fixed angle, while the table bed will have three-axis motions. Argon gas with a flow rate of 10 l/min was used as a shielding gas that was supplied from the cylinder. The schematic diagram of the CMT process was shown in Fig. 4.1. Commercially available stainless steel 304 filler wire of 1.2 mm diameter was used for deposition. The chemical composition of the wire which was certified is as shown in Table 4.1. Mild steel of size $250 \times 250 \times 10$ mm was used as the substrate for deposition. Before the cladding, mild steel plates are sandblasted over the surface and cleaned to dry to avoid contaminations.

Fig. 4.1 Schematic diagram of WAAM system with CMT configuration

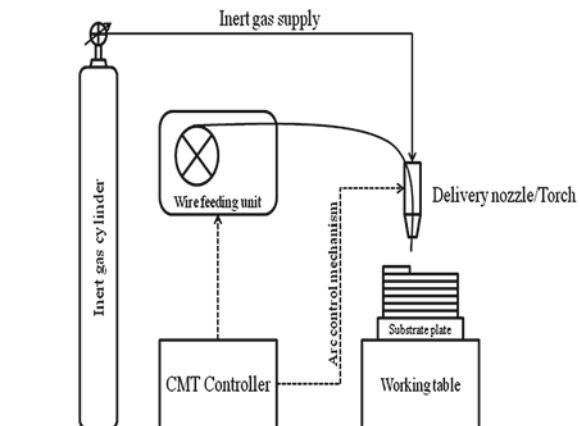


Table 4.1 Chemical composition of SS304

Cr	Ni	Mn	Mo	Cu	Al	Si	P	Co	N	C	Fe
17.61	8.85	3.97	0.008	1.17	0.015	0.49	0.01	0.11	0.05	0.06	Bal.

Response Surface Method

Input current (*I*), welding speed (*S*), and stand-off distance (*D*) are observed to be the most affecting process parameters on bead characteristics. Parameter ranges were identified by conducting trial experiments. Based on trial experiments and literature research, current, stand-off distance, and weld speed are found to be important parameters for experimental design. Table 4.2 shows the experimental design condition as per the central composite experimental design for three parameters and three-level response surface designs.

Table 4.2 Experimental design and corresponding responses

Experimental conditions				Response matrix		
Experiment	Current in A	Standoff distance in mm	Weld speed in m/min	Bead width (mm)	Bead height (mm)	Penetration (mm)
1	90	4	0.4	3.901	3.217	1.197
2	100	5	0.3	4.732	3.732	1.794
3	100	5	0.3	5.164	3.734	1.419
4	90	4	0.2	5.637	4.072	1.253
5	100	5	0.3	5.082	3.179	1.711
6	100	5	0.3	4.833	3.531	3.531
7	110	4	0.2	2.696	2.371	0.767
8	110	6	0.4	4.477	3.123	1.739
9	90	6	0.2	2.653	1.935	0.786
10	90	6	0.4	3.858	3.680	1.134
11	110	4	0.4	2.281	1.592	0.872
12	110	6	0.2	5.912	3.868	1.775
13	83.67	5	0.3	4.133	2.778	1.281
14	116.33	5	0.3	5.209	3.194	1.711
15	100	5	0.46	4.425	2.351	1.481
16	100	3.36	0.3	4.643	2.951	1.668
17	100	5	0.3	4.655	2.896	1.679
18	100	5	0.3	4.901	3.397	1.840
19	100	6.63	0.3	4.803	3.062	1.940
20	100	5	0.14	3.332	1.898	0.858

Grey Relational Analysis

For both consumers and manufacturers, quality and profitability are critical. The objective of real-time situations is multi-objective in nature. Hence it is essential to convert a multi-optimization problem into a single-objective function through statistical approaches. Grey relational analysis is one of them. The procedure followed in GRA is:

1. Normalize the data obtained from experiments from zero to one
2. Grey relational coefficients has to be evaluated from the normalized data
3. Obtain overall grey relational grade (GRG).

From the GRG whichever the experimental condition has got Rank 1 is considered to be the optimal setting that satisfies all the objective functions.

The characteristics equations for normalizing the minimization and maximization problems are obtained by using Eqs. (4.1) and (4.2).

$$x_i^*(k) = \frac{\max(x_i^o(k)) - x_i^o(k)}{\max(x_i^o(k)) - \min(x_i^o(k))} \quad (4.1)$$

$$x_i^*(k) = \frac{x_i^o(k) - \min(x_i^o(k))}{\max(x_i^o(k)) - \min(x_i^o(k))} \quad (4.2)$$

where $x_i^*(k)$ is the sequence data after normalization; $x_i(k)$ is actual response value; $\max(x_i^o(k))$ its maximum value, and $\min(x_i^o(k))$ is the minimum value of the generated data.

After normalization matrix obtained from the experimental data, grey relational coefficients are obtained to estimate the relationship between normalized data and actual data and is calculated using Eq. (4.3)

$$\xi(k) = \frac{\Delta_{\min} + \xi \Delta_{\max}}{\Delta_{o_i}(k) + \xi \Delta_{\max}} \quad (4.3)$$

where $\Delta_{o_i}(k)$ is deviation sequence and is calculated as $|x_i^*(k) - x_i^o(k)|$; ξ is the distinguished coefficient and the value is ranging between 0 and 1. In general, 0.5 is used.

The next step is to obtain the grey relational grade (GRG) and is defined as

$$\gamma_i = \frac{1}{n} \sum_{k=1}^n w_k \xi_i(k) \quad (4.4)$$

where w_k is the weight factor, which is selected based on the priorities.

Results and Discussion

SS304 single beads were successfully deposited on a mild steel substrate as shown in Fig. 2a. The samples were cut in the middle and extracted from the plate. The micrographs of the samples are depicted in Fig. 2b. The bead characteristics such as bead width, bead height, and penetration were observed from the micrographs through 3D optical microscope (Make: QASMO optical microscope DIC polarizer, Model: QX4RT) at 1000 μm scale. However, for additively layered structures smooth, flat, and thin layers are recommended for the deposition of successive layers. Hence, the maximum bead width, minimum bead height, and minimum penetration are the desired objectives for the present study. Figure 4.3 shows the bead geometry measurements which are obtained from the micrographs. The RSM experimental design and corresponding observations are tabulated in Table 4.2. The experiments were randomly conducted to ensure the results are free from the experimental bias.

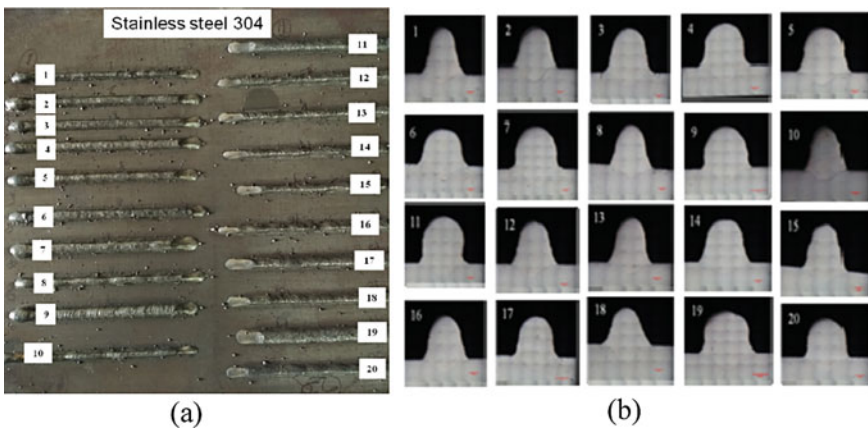


Fig. 4.2 a SS304 beads deposited on mild steel substrate plate, b macro images of bead profiles

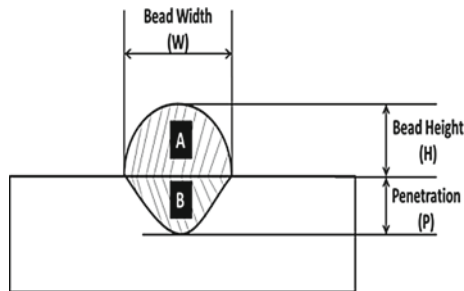


Fig. 4.3 Schematic diagram of weld bead characteristics

In the present study, penetration has given higher weightage than bead width and bead height. The weights are given as 0.4, 0.3, and 0.3 for penetration bead width and bead height, respectively. For any additive manufacturing process, interfacial characteristics and bonding between the layers play an important role in the fabrication process. The interfacial characteristics depend on the penetration of the successive layers. Hence in the present study penetration has given more weightage than bead width and height. The grey relational analysis to find out the grey relational grade with normalization data and grade coefficients is presented in Table 4.3. The GRG represents the grade value combined with all the three objectives. From Table 4.3 it is observed that experiment no 11 has rank 1 with the highest grade of 0.754. Hence this condition can be treated as an optimal parameter setting that satisfies all three objectives. Different parameter settings can be obtained with different weightage combinations, and all this depends on the desired performance and application.

Figure 4.4 shows the effects plots for combined GRA grade for the single-bead deposition. From the plots, it is observed that GRA grade decreases with current and stand-off distance up to a cut-off limit and then increased, whereas GRA grade increases with weld speed. The same has been revealed in ANOVA. MINITAB software is used to perform ANOVA for the GRA results. Table 4.4 shows the ANOVA for the combined GRA grade. From the analysis, current and weld speed are significant in predicting the experimental variation for multiple bead characteristics performance. From the analysis it is found that current is the most significant parameter than the other parameters because it has higher contribution.

Conclusions

Grey relational analysis was applied to response surface design experiments to evaluate the multi-objective performance of bead characteristics deposited by the cold metal transfer process. The deposition characteristics, namely bead width, bead height, and penetration, are considered for the present study. The weights used in the analysis can be changed with process requirements.

From the GRA analysis, the simultaneous objective of maximum bead width, minimum height, and minimum penetration is observed at 110 Amperes current, 4 mm/min weld speed, and 0.4 mm stand-off distance. Any specific performance measure can be adjusted so that the other performance metrics satisfy the minimum requirement.

Since additive manufacturing process mostly relays on interfacial characteristics of single beads, the study on bead characteristics bead width height, and penetration will affect the layer height, surface roughness, and interfacial characteristics. Hence, the multi-objective criteria have to be followed to develop the AM process from the welding process. Further, the present results give an idea on the combined performance of bead characteristics which may help the conversion of single bead deposition into a multi-pass multi-track deposition which tends to be an additive manufacturing process.

Table 4.3 GRA analysis data

S. No.	Normalization matrix			Deviation sequence matrix			GRA coefficient matrix					Rank
	Bead width	Bead height	Penetration	Bead width	Bead height	Penetration	Bead width	Bead height	Penetration	Combined GRA grade		
1	0.446	0.345	0.844	0.554	0.655	0.156	0.474	0.433	0.763	0.577	11	
2	0.675	0.137	0.628	0.325	0.863	0.372	0.606	0.367	0.574	0.521	19	
3	0.794	0.136	0.764	0.206	0.864	0.236	0.708	0.367	0.679	0.594	9	
4	0.924	0.000	0.824	0.076	1.000	0.176	0.868	0.333	0.740	0.656	5	
5	0.771	0.360	0.658	0.229	0.640	0.342	0.686	0.439	0.594	0.575	12	
6	0.703	0.218	0.000	0.297	0.782	1.000	0.627	0.390	0.333	0.439	20	
7	0.114	0.686	1.000	0.886	0.314	0.000	0.361	0.614	1.000	0.692	4	
8	0.605	0.383	0.648	0.395	0.617	0.352	0.559	0.447	0.587	0.537	18	
9	0.102	0.862	0.993	0.898	0.138	0.007	0.358	0.783	0.986	0.737	3	
10	0.434	0.158	0.867	0.566	0.842	0.133	0.469	0.373	0.790	0.569	13	
11	0.000	1.000	0.962	1.000	0.000	0.038	0.333	1.000	0.929	0.772	1	
12	1.000	0.082	0.635	0.000	0.918	0.365	1.000	0.353	0.578	0.637	6	
13	0.510	0.522	0.814	0.490	0.478	0.186	0.505	0.511	0.729	0.596	8	
14	0.806	0.354	0.658	0.194	0.646	0.342	0.721	0.436	0.594	0.585	10	
15	0.590	0.694	0.742	0.410	0.306	0.258	0.550	0.620	0.659	0.615	7	
16	0.651	0.452	0.674	0.349	0.548	0.326	0.589	0.477	0.605	0.562	15	
17	0.654	0.474	0.670	0.346	0.526	0.330	0.591	0.487	0.602	0.564	14	
18	0.722	0.272	0.612	0.278	0.728	0.388	0.642	0.407	0.563	0.540	16	
19	0.695	0.407	0.576	0.305	0.593	0.424	0.621	0.458	0.541	0.540	17	
20	0.289	0.877	0.967	0.711	0.123	0.033	0.413	0.802	0.938	0.740	2	

Fig. 4.4 Main effect plot for combined GRA grade

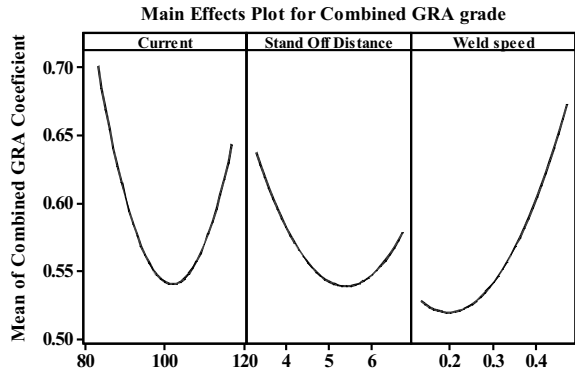


Table 4.4 ANOVA for combined GRA grade

Source	DF	Adj SS	Adj MS	F-value	P-value	Remarks
Regression	3	7.2373	2.41243	272.29	0.000	
Current	1	0.07206	0.07206	8.13	0.011	Significant
Stand-off distance	1	0.00156	0.00156	0.18	0.680	Non-significant
Weld speed	1	0.04977	0.04977	5.62	0.030	Significant
Error	17	0.15061	0.00886			
Lack-of-fit	12	0.13085	0.0109	2.76	0.135	
Pure error	5	0.01976	0.00395			
Total	20	7.38792				

Acknowledgements The authors would like to acknowledge “Welding Research Cell, SVCE, Sri Perumbudur”, for their support in the smooth conduction of experiments.

References

1. Xiong J, Li R, Lei Y, Chen H (2018) Heat propagation of circular thin-walled parts fabricated in additive manufacturing using gas metal arc welding. *J Mater Process Technol* 251:12–19. <https://doi.org/10.1016/j.jmatprotec.2017.08.007>
2. Ma Y, Cuiuri D, Li H, Pan Z, Shen C (2016) The effect of postproduction heat treatment on γ -TiAl alloys produced by the GTAW-based additive manufacturing process. *Mater Sci Eng A* 657:86–95. <https://doi.org/10.1016/j.msea.2016.01.060>
3. Lin J, Lv Y, Liu Y, Sun Z, Wang K, Li Z, Wu Y, Xu B (2017) Microstructural evolution and mechanical property of Ti-6Al-4V wall deposited by continuous plasma arc additive manufacturing without post heat treatment. *J Mech Behav Biomed Mater* 69:19–29. <https://doi.org/10.1016/j.jmbbm.2016.12.015>
4. Ge J, Lin J, Lei Y, Fu H (2018) Location-related thermal history, microstructure, and mechanical properties of arc additively manufactured 2Cr13 steel using cold metal transfer welding. *Mater Sci Eng A* 715:144–153. <https://doi.org/10.1016/j.msea.2017.12.076>

5. Xu J, Chen J, Duan Y, Yu C, Chen J, Lu H (2017) Comparison of residual stress induced by TIG and LBW in girth weld of AISI 304 stainless steel pipes. *J Mater Process Technol* 248:178–184. <https://doi.org/10.1016/j.jmatprotec.2017.05.014>
6. Lee HT, Jeng SL (2001) Characteristics of dissimilar welding of alloy 690 to 304L stainless steel. *Sci Technol Weld Join* 6:225–234. <https://doi.org/10.1179/136217101101538811>
7. Deng JL (1989) Introduction to Grey system theory. *J Grey Syst* 1:1–24

Chapter 5

Optimizing the Defocused CO₂ Laser Microchanneling Process Using Grey Relational Analysis



Shashi Prakash 

Introduction

CO₂ lasers are commonly used for cutting different materials in industries. Though high-power CO₂ lasers are used for machining almost all sort of materials, low-power CO₂ lasers are particularly useful for polymeric materials. Many of these polymeric materials are used in microfluidic devices as a substrate material. Although glass and silicon have been the first choice for such devices, transparent polymers such as polymethyl methacrylate (PMMA) have evolved as an efficient alternative to these materials. Fabricating microchannels on glass and silicon are not only difficult but also time-consuming, leading to costly microfluidic devices. Also, many a times, clean room is the essential requirement apart from extremely costly fabricating process [1]. Microchannel fabrication on PMMA substrates has resulted in great improvement in the development of cost-effective and portable microfluidic devices. A CO₂ laser-based fabrication method takes a fraction of time and cost when compared to other fabricating methods, such as wet etching, lithography, and micromilling. A CO₂ laser is at least ten times cheaper than other microfabricating equipment used such as wet etching, excimer lasers, and femtosecond lasers [2]. PMMA is a transparent polymeric material. It is also used as a substitute material for glass in applications subjecting to low heating requirements. PMMA is often used in drug delivery systems and bio-implants as it possesses a good degree of bio-compatibility [3]. PMMA can be machined using excimer lasers [4], femtosecond lasers [3], as well as hot embossing [5] with a good surface finish. However, these devices are not only costly but take large amount of time. With a CO₂ laser, a whole PMMA-based microfluidic device can be built in less than 45 min [6]. A CO₂ laser-based processing

S. Prakash (✉)

School of Engineering & Applied Science, Ahmedabad University, Ahmedabad, Gujarat, India

e-mail: shashi.prakash@ahduni.edu.in

may not require post-processing if parameters are used optimally [7]. PMMA as a material has high degree of absorptivity with infrared beams combined with low heat capacity and low heat conductance, which results in clean and effective laser cutting [8].

Although CO₂ laser beams are Gaussian in shape, but this does not limit the laser to produce only Gaussian shape microchannels. In a recent attempt [9], authors were able to fabricate microchannels with rectangular and U cross-sections. With a low-power CO₂ laser, microprocessing can be done using direct cutting method (vector cutting) as well as raster cutting method [10]. However, both the methods produce rough surface when focused processing is done and the resulting devices may not be usable in many applications. Although there are various post-processing and in situ processing such as multi-pass processing [11] available for producing improved surface roughness, defocused processing can produce microchannels with least time and in single-pass processing [12]. Although defocused processing results in improved surface roughness, increased beam width also results in larger microchannel width and lower microchannel depth which may not be desirable for many microfluidic devices. Hence, an optimization problem can be evolved amicably. Previously, the authors have used desirability function-based multi-objective optimization process for the similar defocused problem [7]. Many optimization methods can be applied, including traditional as well as evolutionary methods such as genetic algorithm, particle swarm algorithm (PSO), and so on. Many optimization methods have been recently developed and that requires significant computation facilities. In this regard, simple optimization methods can be proved to be very effective which do not require computation facilities and can be carried out on simple spreadsheet like software. Grey relational analysis (GRA) is an effective method for multi-objective problems. GRA coupled with Taguchi's design was used earlier for optimizing the microchanneling process with Nd:YAG laser [13]. Application of GRA can also simplify the optimization process in laser defocused processing. Therefore, in this work, GRA has been used in defocused CO₂ laser processing for optimizing the input parameters, namely energy deposition and defocused distance for obtaining better surface finish, minimizing width and heat-affected zone (HAZ) and increasing microchannel depth.

Experimentation

Full Factorial Design

A 60 W CO₂ laser (make Universal) was used to create microchannels on PMMA substrates in defocused condition. Beam diameter at focusing plane was measured using standard method as deliberated in reference [14]. Beam diameter was found to be 237 μm . Five different defocusing planes were chosen for experimentation 1 mm apart from each other below the focusing plane. Using more than 5 mm of

defocused distance was found to be more than acceptable limit as beam divergence at more than 5 mm of defocusing resulted in excessive microchannel widths. Figure 5.1 shows different defocusing planes considered in this experiment. It shows different defocusing planes below the focusing planes considered in this experiment. Figure 5.2 shows typical output parameters resulting from microchanneling processes [15]. This includes microchannel width, depth, surface roughness, and heat-affected zone (HAZ).

Apart from defocusing distance, ratio of beam power to scanning speed was selected as another input parameter to be termed as energy deposition (J/mm) [12]. Energy deposition was varied at five different levels based on various pilot experiments, viz., 0.1, 0.15, 0.2, 0.25, and 0.3 J/mm. These parameters were selected so as to keep microchannel width less than 500 μm which is most suitable for most of the microfluidic devices [1]. Totally 25 experiments were performed according to full factorial design as indicated in Table 5.1. Width, depth, and HAZ were measured using Olympus optical microscope (STM6) while surface roughness was measured using Zygo 3D profilometer and Mitutoyo surface roughness tester.

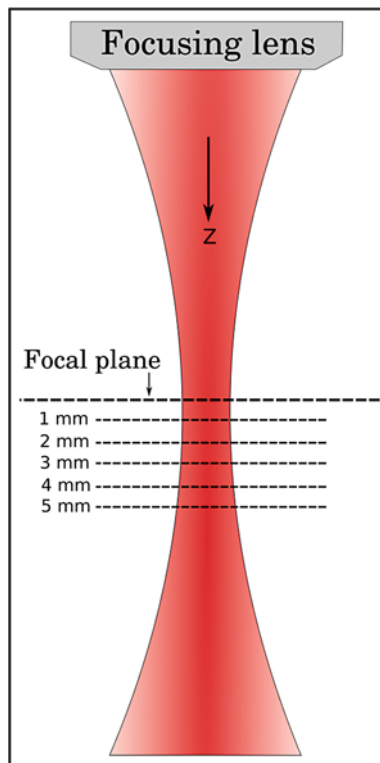


Fig. 5.1 Defocused planes considered in this research work, 1 mm apart from each other [7]

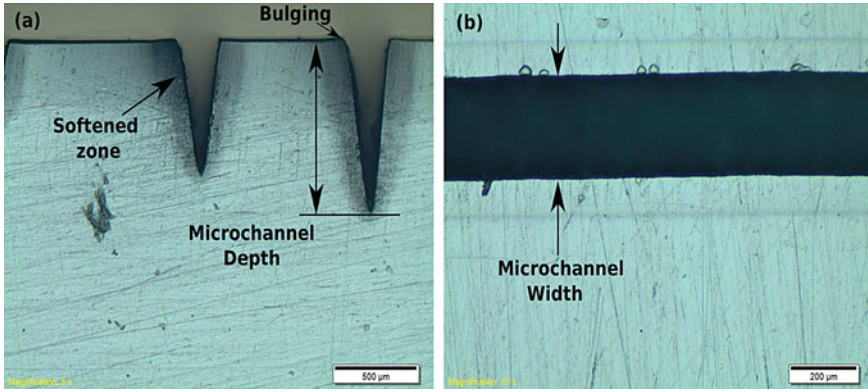


Fig. 5.2 Output parameters of a laser microchanneling process on PMMA [15]

Beam Diameter at Different Defocusing

Beam diameter was measured using an optical microscope (STM-6, Olympus). Microchannel width, depth, and heat-affected zone (HAZ) were also measured using this microscope. Beam diameter at focusing plane was found to be 237 μm . Beam diameter at different defocusing can be determined using Eq. 5.1.

$$w = w_1 \left[1 + \left(M^2 \frac{\lambda(z)}{\pi w_1^2} \right)^2 \right]^{\frac{1}{2}} \quad (5.1)$$

where w denotes beam radius at distance z from the focusing plane, w_1 is beam radius at new surface, M^2 represents beam quality parameter, and λ represents wavelength of laser beam. Surface roughness of the microchannel walls was measured using Zegage Zygo profilometer and stylus-based Mitutoyo surface roughness tester. Surface roughness measurements were taken at three different locations and their average value was used. Beam diameter at different planes are given in Table 5.2.

Grey Relational Analysis (GRA)

Grey relational analysis deals with information level between 0 and 1. Output parameters are normalized between these two levels. Normalization of data is also called grey relational generation. Using these normalized data, grey relational coefficient (GRC) was calculated. Grey relational coefficient denotes the relationship between actual results and desired output results. After calculating GRCs, grey relational grade (GRG) is calculated by averaging the GRCs corresponding to each parameter. The overall performance characteristics depend upon grey relational grade. This

Table 5.1 Experimental design and responses

Exp. no	Process parameters		Responses (μm)			
	E (J/mm)	d (mm)	W	D	SR	HAZ
1	0.3	3	351	542	0.68	104
2	0.2	5	430	245	0.07	108
3	0.15	2	269	300	1.96	85
4	0.2	2	282	390	1.67	87
5	0.2	1	247	492	4.92	85
6	0.1	5	337	110	0.08	100
7	0.3	1	279	705	3.7	94
8	0.1	2	252	187	2.12	78
9	0.15	3	310	255	1	92
10	0.1	3	278	164	1.1	80
11	0.25	5	445	334	0.09	110
12	0.2	4	370	300	0.26	101
13	0.2	3	329	340	1.1	96
14	0.15	1	240	355	4.44	80
15	0.25	4	390	385	0.18	106
16	0.15	4	343	235	0.37	95
17	0.3	4	404	450	0.15	114
18	0.25	2	297	524	1	97
19	0.25	3	340	454	0.87	98
20	0.3	5	465	385	0.1	120
21	0.1	1	212	237	6.67	76
22	0.3	2	302	620	1.3	100
23	0.15	5	365	185	0.1	102
24	0.1	4	319	135	0.5	90
25	0.25	1	267	600	3.36	90

E energy deposition, *d* defocusing distance, *W* microchannel width, *D* microchannel depth, *SR* surface roughness, *HAZ* heat affected zone

Table 5.2 Beam diameter at different defocusing distances

Defocus distance (mm)	Beam diameter ((μm)
0	237
1	251.93
2	292.193
3	349.12
4	415.93
5	488.58

process converts multi-objective optimization process into single-objective optimization process. The input parameters corresponding to highest grey relational grade results in optimal set of parameters. In grey relational generation, lower the better (LB) or higher the better (HB) criterion may be used depending upon desirable output parameter. In case of lower the better characteristics, normalized values may be determined using Eq. 5.2.

$$x_i(k) = \frac{\max y_i(k) - y_i(k)}{\max y_i(k) - \min y_i(k)} \quad (5.2)$$

In case of higher the better characteristics, GRC may be determined using Eq. 5.3.

$$x_i(k) = \frac{y_i(k) - \min y_i(k)}{\max y_i(k) - \min y_i(k)} \quad (5.3)$$

Grey relational coefficient can be calculated using Eq. 5.4.

$$\xi_i(k) = \frac{\Delta_{\min} + \psi \Delta_{\max}}{\Delta_{0i}(k) + \psi \Delta_{\max}} \quad (5.4)$$

where

$$\Delta_{0i} = \|x_0(k) - x_i(k)\|$$

Here the value of Ψ is set to be 0.5, the quantity used in most situations.

$$\begin{aligned} \Delta_{\min} &= \forall j^{\min} \in i \forall k^{\min} \|x_0(k) - x_j(k)\|; \\ \Delta_{\max} &= \forall j^{\max} \in i \forall k^{\max} \|x_0(k) - x_j(k)\|; \end{aligned}$$

After calculating GRCs, grey relational grade (GRG) can be obtained by averaging the values of GRCs.

$$\gamma_i = \frac{1}{n} \sum_{k=1}^n w_i \xi_i(k) \quad (5.5)$$

where w_i is weightage provided to i th response parameter and n is the number of response outputs. In this work, each parameter has been considered to be of equal importance, hence same weightage is provided to each output parameter. Output parameters related to largest GRGs represent most optimum solution.

Results and Discussion

The normalized values of output parameters, GRCs and GRGs, are calculated using Eqs. 5.2, 5.3, 5.4, and 5.5 and given in Table 5.3. Since five levels of input parameters have been used in this work, GRGs for these five levels of input parameters have been separately calculated as given in Table 5.4. In this table, the input parameter levels corresponding to highest GRGs represent most optimum values. Energy corresponding to 0.3 J/mm and defocus distance of 1 mm was found to be most optimum combination of input parameters according to grey relational analysis. Output response values corresponding to this level of input parameters are 279, 705, 3.7, and 94 μm for width, depth, surface roughness, and HAZ values, respectively.

Table 5.3 Normalized results and grey relational coefficients for process response values

Normalized values				GRC				GRG
W	D	SR	HAZ	W	D	SR	HAZ	
0.4506	0.7261	0.9076	0.3636	0.4765	0.64604	0.84399	0.440	0.602
0.1383	0.2269	1.0000	0.2727	0.3672	0.39274	1.0000	0.407	0.542
0.7747	0.3193	0.7136	0.7955	0.6894	0.42349	0.63584	0.710	0.615
0.7233	0.4706	0.7576	0.7500	0.6438	0.48571	0.67347	0.667	0.617
0.8617	0.6420	0.2652	0.7955	0.7833	0.58276	0.40491	0.710	0.620
0.5059	0.0000	0.9985	0.4545	0.503	0.33333	0.99698	0.478	0.578
0.7352	1.0000	0.4500	0.5909	0.654	1.0000	0.476	0.550	0.670
0.8419	0.1294	0.6894	0.9545	0.7598	0.36481	0.61682	0.917	0.665
0.6126	0.2437	0.8591	0.6364	0.5635	0.39799	0.78014	0.579	0.580
0.7391	0.0908	0.8439	0.9091	0.6571	0.3548	0.76212	0.846	0.655
0.0791	0.3765	0.9970	0.2273	0.3519	0.44503	0.99398	0.393	0.546
0.3755	0.3193	0.9712	0.4318	0.4446	0.42349	0.94556	0.468	0.570
0.5375	0.3866	0.8439	0.5455	0.5195	0.44906	0.76212	0.524	0.564
0.8893	0.4118	0.3379	0.9091	0.8188	0.45946	0.43025	0.846	0.639
0.2964	0.4622	0.9833	0.3182	0.4154	0.48178	0.96774	0.423	0.572
0.4822	0.2101	0.9545	0.5682	0.4913	0.38762	0.91667	0.537	0.583
0.2411	0.5714	0.9879	0.1364	0.3972	0.53846	0.97633	0.367	0.570
0.6640	0.6958	0.8591	0.5227	0.5981	0.62173	0.78014	0.512	0.628
0.4941	0.5782	0.8788	0.5000	0.4971	0.54239	0.80488	0.500	0.586
0.0000	0.4622	0.9955	0.0000	0.3333	0.48178	0.99099	0.333	0.535
1.0000	0.2134	0.0000	1.0000	1.000	0.38863	0.33333	1.000	0.680
0.6443	0.8571	0.8136	0.4545	0.5843	0.77778	0.72848	0.478	0.642
0.3953	0.1261	0.9955	0.4091	0.4526	0.36391	0.99099	0.458	0.566
0.5771	0.0420	0.9348	0.6818	0.5418	0.34294	0.88472	0.611	0.595
0.7826	0.8235	0.5015	0.6818	0.697	0.73913	0.50076	0.611	0.637

Table 5.4 GRGs corresponding to different levels of input parameters

Parameters	Levels					
	Denotes	-2	-1	0	1	2
Energy	E	0.6038	0.5938	0.5826	0.5966	0.6346*
Defocus	D	0.6492*	0.6334	0.5974	0.578	0.5534

These values can be further improved utilizing ANOVA analysis. However, GRA can be efficiently used to find the most optimum set of input parameters out of experimental runs. Hence, GRA has been found to be a very powerful and efficient tool for multi-objective optimization process.

CO₂ laser-based microchanneling processes are used widely by researchers belonging to different streams and orientation. Owing to its simplicity, it can be used by academicians and researchers without using the computational facilities and with the application of spreadsheets only.

Although other methods like genetic algorithm, artificial bee colony algorithm, and so on can also be used to optimize defocused microchanneling process, GRA has inbuilt simplicity which can be applied without running the long codes.

Conclusion

CO₂ laser-based microchanneling process is mostly used in the fabrication of microfluidic chips. It is one of the most used fabrication process across the microfluidic industries and research labs. However, the process generates rough surface at the microchannel walls due to sharp intensity gradient within the beam spot diameter. Defocused processing can be successfully used for reducing the surface roughness of the microchannel walls. However, enhanced surface finish due to defocused processing comes at a cost of larger microchannel widths which may adversely affect the application of microfluidic chips. In order to contain the microchannel width within acceptable limit, GRA-based optimization process was applied in this research work. When increasing the defocusing distance, microchannel width also increases. Defocused processing also improves surface finish of the microchannel. The larger the defocusing distance, the lower is the surface roughness of the microchannel. Even the small amount of defocus can improve the surface finish of the microchannel wall significantly. Experiment number 7 corresponding to 0.3 J/mm of deposited energy and 1 mm of defocusing distance was found to be most optimum solution out of all the conducted 25 experiments.

References

1. Prakash S, Kumar S (2015) Fabrication of microchannels: a review. *Proc Inst Mech Eng Part B: J Eng Manuf* 229(8):1273–1288
2. Fu L-M, Ju W-J, Yang R-J, Wang Y-N (2012) Rapid prototyping of glass-based microfluidic chips utilizing two-pass defocused CO₂ laser beam method. *Microfluidics Nanofluidics* 14(3):479–487
3. Fernandez-Pradas JM, Florian C, Caballero-Lucas F (1999) Femtosecond laser ablation of polymethyl-methacrylate with high focusing control. *Appl Surf Sci* 278:185–189
4. Chang T-C, Molian PA (1999) Excimer pulsed laser ablation of polymers in air and liquids for micromachining applications. *J Manuf Process* 18:1–17
5. Mathur A, Roy SS, Tweedie M (2009) Characterisation of PMMA microfluidic channels and devices fabricated by hot embossing and sealed by direct bonding. *Curr Appl Phys* 9(6):1199–1202
6. Lounsbury JA, Karlsson A, Miranian DC, Cronk SM, Nelson DA (2013) From sample to PCR product in under 45 minutes: a polymeric integrated microdevice for clinical and forensic DNA analysis. *Lab Chip* 13:1384–1393
7. Prakash S, Kumar N, Kumar S (2016) CO₂ laser microchanneling on polymethylmethacrylate (PMMA) at different defocusing. In: 6th international & 27th all India manufacturing technology, design and research conference (AIMTDR-2016)
8. Prakash S, Acherjee B, Kuar AS, Mitra S (2013) An experimental investigation on Nd:YAG laser microchanneling on polymethyl methacrylate submerged in water. *Proc Inst Mech Eng Part B: J Eng Manuf* 227(4):508–519
9. Prakash S, Kumar S (2017) Fabrication of rectangular cross-sectional microchannels on PMMA with a CO₂ laser and underwater fabricated copper mask. *Opt Laser Technol* 94:180–192
10. Prakash S, Kumar S (2018) Pulse smearing and profile generation in CO₂ laser micromachining on PMMA via raster scanning. *J Manuf Processes* 31:116–123
11. Prakash S, Kumar S (2017) Experimental investigations and analytical modeling of multi-pass CO₂ laser processing on PMMA. *Precis Eng* 49:220–234
12. Prakash S, Kumar S (2016) Experimental and theoretical analysis of defocused CO₂ laser microchanneling on PMMA for enhanced surface finish. *J Micromech Microeng* 27(2):025003
13. Acherjee B, Prakash S, Kuar AS, Mitra S (2014) Grey relational analysis based optimization of underwater Nd: YAG laser micro-channeling on PMMA. *Procedia Eng* 97:1406–1415
14. Prakash S, Kumar S (2015) Profile and depth prediction in single pass and two-pass CO₂ laser microchanneling process. *Int J Precis Eng Manuf* 16(2):1–10
15. Prakash S, Kumar S (2015) Fabrication of channels on transparent PMMA using CO₂ laser (10.6 μm) for microfluidic applications: an experimental investigation. *J Micromech Microeng* 25(3):361–366

Chapter 6

Selection of Multi-point Diamond Dresser for Grinding Process Using Grey Relation Analysis



V. V. Pansare, V. S. Gadakh , and S. S. Patil 

Introduction

Grinding is one of the oldest manufacturing processes and has been used since the Stone Age to accomplish such tasks as creating hunting tools. Because of the growing demand for higher productivity at reduced cost, manufacturing industries require that the grinding process should run more effectively with reduced lead time to achieve an acceptable level for grinding conditions. The goal of the grinding process is to produce parts with maximum surface finish and accuracy on hard components.

Dressing is an operation performed on the grinding wheel surface in order to reform the wheel, which occurs after losing its original shape through wear. The purpose of dressing is to remove the glazed and loaded surface from the grinding wheel, for improving the cutting ability of the grinding wheel during the process. Generally dressing has crucial effect on wheel performance with respect to the surface finish and grinding ratio in subsequent grinding process produced on the workpiece. There are mainly two categories of multi-point diamond dressers: (1) natural (ND) and (2) synthetic dresser. Natural diamond dresser is again classified into grit and

V. V. Pansare (✉)

Department of Mechanical Engineering, Amrutvahini College of Engineering, SPPU, Pune, Maharashtra 422608, India

e-mail: pansareviraj3@gmail.com

V. S. Gadakh

Department of Production Engineering, Amrutvahini College of Engineering, SPPU, Pune, Maharashtra 422608, India

e-mail: vijay.gadakh@avcoe.org

S. S. Patil

Department of Production Engineering, Sinhgad College of Engineering, Vadgaon Bk., SPPU, Pune, Maharashtra 411041, India

e-mail: sanjayspatil70@gmail.com

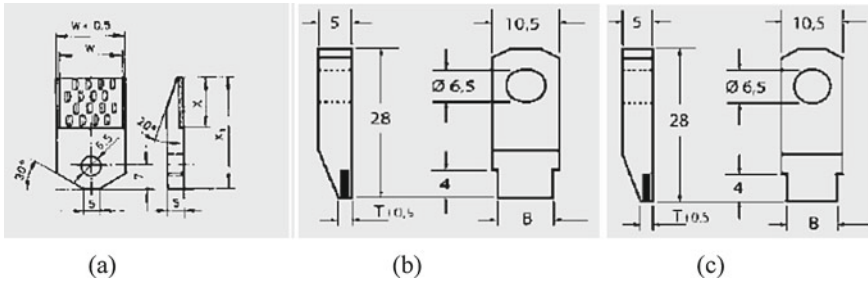


Fig. 6.1 Types of multi-point dressers. **a** Needle blade with natural diamond dresser, **b** MCD needle blade dresser, **c** CVD needle blade dresser [1]

needle types, whereas synthetic dressers are classified into chemical vapor deposition (CVD) type multi-point diamond dresser and monocrystalline diamond (MCD) type dressers. The detail of each dresser type is shown in Fig. 6.1.

Needle blade with natural diamond dressers are useful for angular plunge/straight and profile dressing of specially fused Al_2O_3 , all Al_2O_3 and sintered Al_2O_3 grinding wheels with 46–80 grit size. MCD needle blade dressers are preferably used for profiling, sintered Al_2O_3 , SiC and straight dressing of hard grinding wheels. Similarly, CVD needle blade dressers are mostly preferred for special fused Al_2O_3 and sintered Al_2O_3 grinding wheels and high-precision straight dressing of Al_2O_3 [1].

Fritsche and Bleicher [2] have produced active grain stack model which provides information of grinding wheel structure and interaction of different layers with each other. Patil and Bhalerao [3] reported that for getting good surface finish dressing parameters play an important role in CNC cylindrical angular grinding machine. Choi et al. [4] developed generalized process models for cylindrical plunge grinding process. It is reported that their models can predict performances at different conditions of grinding process. Jiang et al. [5] produced a mathematical model to predict the ground surface roughness and topography by considering grinding, wear and dressing variables. Sinha et al. [6] selected optimal dressing parameters depending on grit size of wheel. It is reported that optimum range of dressing depth and dressing lead for a specific grit size grinding wheel significantly influences the ground product quality as well as the prime grinding attributes like grinding forces. Hecker and Liang [7] developed a mathematical model to predict surface roughness of ground parts. Liu et al. [8] presented a kinematic simulation study using single-point diamond dresser to predict the surface roughness in grinding process with the help of different abrasive grain shapes.

From the reported literature and industrial survey, it is observed that majority of the papers dealt with process parameter optimization using different well-established algorithms, either for grinding process-related parameters or developed some models to predict the performances. Very few literatures discussed about single-point diamond dresser in grinding process; however, literature lacks in terms of multi-point diamond dresser for grinding process. Hence, the purpose of present work is

to select best multi-point diamond dresser in cylindrical plunge grinding process for getting better surface finish.

Experimental Procedure

The present work illustrates the selection of best multi-point diamond dresser in cylindrical plunge grinding process. The effect of grinding process parameters such as grinding feed rate, dressing cross feed rate and dressing depth of cut on surface finish (SR), maximum grinding ratio (GR) and optimum power (P) were considered using the Taguchi method. In Taguchi method, it is required to consider all design aspects which affect the variation of functional characteristics of the product from target values. The Taguchi method is a popular optimization method as it reduces the number of experiments [9].

Experiments were performed on CNC angular head grinding machine (Model: AHG 60X300) with EN31 cylindrical workpiece material and grinding wheel (Specification: 38A60K8VT3) was employed. A L_9 orthogonal array was used as per Taguchi design with three trials [9]. A large number of trials were performed to find out the working range of grinding parameters using Taguchi's single parameter approach. The working range of the grinding parameters chosen is shown in Table 6.1.

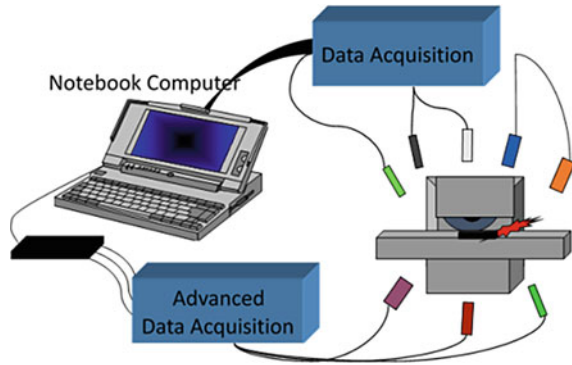
During experimentation plunge and wet grinding were considered along with the depth of grinding $300\ \mu\text{m}$, and the wheel speed and workpiece speed of 1250 rpm and 100 rpm, respectively. Soluble oil was used as lubricant while different types of multi-point diamond dressers, namely natural (Order # 69014185757), MCD (Order # 66260392047) dresser and CVD (Order # 66260336093) dresser were used.

The workpiece surface roughness was measured using Mitutoyo SJ-410. For grinding power measurement, field instrument system (FIS) unit was used, as shown in Fig. 6.2. For grinding ratio measurement, the material removal volume and wheel wear volume were found out. But it is a complex task to measure the material removal volume. For that specially made graphite sheets were taken for the impressions of the grinding wheel after the grinding operation. The graphite sheets were mounted using the bolts on the dresser fixture. The dimension of graphite sheet is $70 \times 35 \times 3\ \text{mm}$. The graphite sheets were observed under the microscope (Make: Metatech, Model: MVH-1) for finding the change of initial diameter and final diameter. The

Table 6.1 Grinding factors working range with their levels

S. No.	Factors	Symbol	1	2	3
1	Dressing depth of cut	$D\ (\mu\text{m})$	10	20	40
2	Dressing cross feed rate	$C\ (\text{mm}/\text{min})$	60	80	120
3	Grinding feed rate	$\text{FR}\ (\text{mm}/\text{min})$	0.6	1.2	2.4
4	Dresser	d	ND	MCD	CVD

Fig. 6.2 Process of power measurement with field instrument system



grinding ratio can be calculated as:

$$\text{Grinding ratio} = \frac{MR}{WR} = \frac{\frac{\pi}{4} \times \Delta D_m^2 \times L}{\frac{\pi}{4} \times \Delta d_w^2 \times L} = \frac{\Delta D_m^2}{\Delta d_w^2}$$

where L is the specimen length as 40 mm, ΔD_m and Δd_w are the difference between initial and final diameter of the work material; and initial and final diameter of the grinding wheel, respectively.

GR, SR and P were evaluated for all the different types of dressers and are presented in Table 6.2. In this work, SR and P are non-beneficial attributes, where smaller values are desirable, whereas GR is beneficial attribute, where maximum values are preferable. The values of SR and P are normalized as per the following Eq. (6.1).

$$x_i^*(k) = \frac{\max x_i^0(k) - x_i^0(k)}{\max x_i^0(k) - \min x_i^0(k)} \tag{6.1}$$

Table 6.2 Surface roughness, power and grinding ratio

Run	D	C	FR	d	GR	Avg. SR	Power (kW)
1	1	1	1	1	10.02	0.146	1.48
2	1	2	2	2	6.66	0.294	2.42
3	1	3	3	3	9.60	0.548	5.06
4	2	1	2	3	9.59	0.354	3.99
5	2	2	3	1	7.70	0.194	3.01
6	2	3	1	2	9.16	0.271	1.16
7	3	1	3	2	9.99	0.388	4.34
8	3	2	1	3	7.85	0.252	1.46
9	3	3	2	1	7.36	0.176	2.31

Table 6.3 Normalized values of the responses

GR	SR	P
1.0000	1.0000	0.9179
0.0000	0.6318	0.6769
0.8750	0.0000	0.0000
0.8720	0.4826	0.2744
0.3095	0.8806	0.5256
0.7440	0.6891	1.0000
0.9911	0.3980	0.1846
0.3542	0.7363	0.9231
0.2083	0.9254	0.7051

Similarly, the value of GR is normalized as per the following Eq. (6.2).

$$x_i^*(k) = \frac{x_i^0(k) - \min x_i^0(k)}{\max x_i^0(k) - \min x_i^0(k)} \tag{6.2}$$

where $i = 1$ to $9, k = 1$ to $n; n$ is the performance measure, and i is the trial number. Table 6.3 shows the normalized values. The grey relational coefficient (GRC) [$\xi_i(k)$] is determined as follows:

$$\xi_i(k) = \frac{\Delta_{\min} + \zeta \Delta_{\max}}{\Delta_{0i}(k) + \zeta \Delta_{\max}} \tag{6.3}$$

Note that larger-the-better is achieved when $x_i(k) = x_0(k)$, that is, when $x =$ reference.

Here, $x_0^*(k)$ denotes the reference sequence; $x_j^*(k)$ indicates the comparability sequence; $\zeta \in [0 - 1]$ is the distinguishing coefficient; 0.5 is widely accepted; $\Delta_{0i} = \|x_0^*(k) - x_i^*(k)\|$ is the difference in absolute value between $x_0^*(k)$ and $x_j^*(k)$; $\Delta_{\min} = \min_{\nabla j \in i} \min_{\nabla j \in k} \|x_0^*(k) - x_j^*(k)\|$ is the smallest value of Δ_{0i} ; $\Delta_{\max} = \max_{\nabla j \in i} \max_{\nabla j \in k} \|x_0^*(k) - x_j^*(k)\|$ is the largest value of Δ_{0i} . After calculating GRCs, the grey relational grade (GRG) is obtained as:

$$\gamma_i = \frac{1}{n} \sum_{k=1}^n \xi_i(k) \tag{6.4}$$

where γ_i is the GRG and ‘ n ’ is the number of output characteristics. The GRC and the related GRG for every experimental run are determined and shown in Table 6.4. The maximum value of GRG shows optimal grinding parameters.

Table 6.4 Grey relational coefficient, grade and rank

GR	SR	P	GRG	Ranking
1.0000	1.0000	0.8590	0.9530	1
0.3333	0.5759	0.6075	0.5056	8
0.8000	0.3333	0.3333	0.4889	9
0.7962	0.4914	0.4079	0.5652	7
0.4200	0.8072	0.5132	0.5801	6
0.6614	0.6166	1.0000	0.7593	2
0.9825	0.4537	0.3801	0.6054	5
0.4364	0.6547	0.8667	0.6526	3
0.3871	0.8701	0.6290	0.6288	4

Table 6.5 Mean GRG at each level

Factors	Mean GRG			Difference
	1	2	3	
D	0.5090	0.6969*	0.4608	0.2361
C	0.5915*	0.5748	0.5003	0.0913
FR	0.6887*	0.5165	0.4615	0.2271
d	0.6001*	0.5079	0.5587	0.0922

*Indicates the optimal setting

Optimal Setting of Grinding Parameters

At each level the mean value of GRG is determined. The maximum value GRG shows the better output characteristics. The mean GRG and the optimal level of the grinding parameter are shown in Table 6.5. Further a graph is plotted (Fig. 6.3), as per the highest GRG value for each parameter in Table 6.5, and the optimal level of the grinding factors is $D_2C_1FR_1d_1$.

Analysis of Variance

ANOVA is used to study the factors that significantly influence the quality measures. ANOVA (Table 6.6) results show that the dressing depth of cut and grinding feed rate are the significant grinding parameters that affect the multiple performance measures. Moreover, dressing cross feed rate and type of diamond dresser are less significant grinding process factors due to minimum values of percentage contribution. From the experiments, the optimal level parameter is $D_2C_1FR_1d_1$. The mean value of GRG

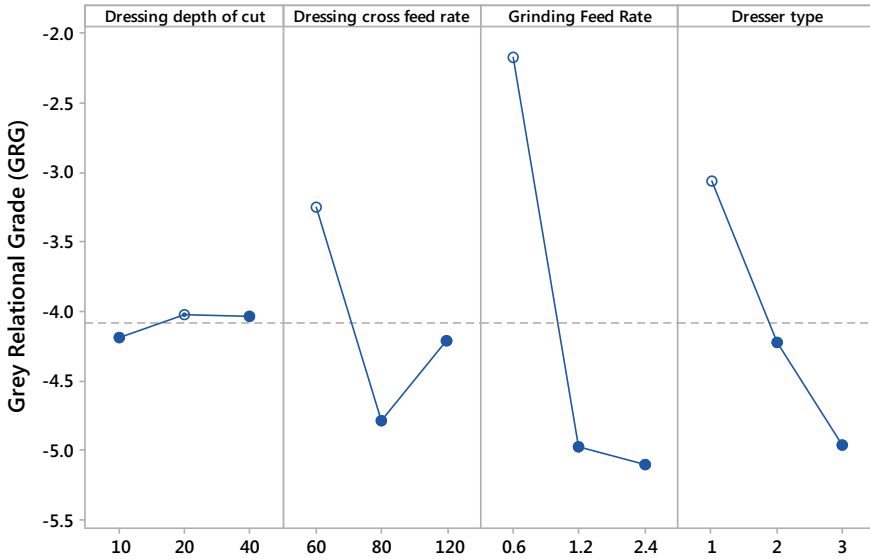


Fig. 6.3 Main effect of grey relational grade (GRG)

Table 6.6 ANOVA for the means

Factors	DoF	Adj SS	Adj MS	Contribution (%)
D	2	0.0933	0.0466	45.63
C	2	0.0141	0.0070	6.92
FR	2	0.0842	0.0421	41.18
d	2	0.0127	0.0063	6.25
Total	8	0.2045		100

DoF degrees of freedom; Adj SS adjusted sum of square; Adj MS adjusted mean square

of the grinding parameter at respective level is taken from Table 6.4 and the predicted value of GRG is calculated as 0.953.

Confirmation Tests

The experimental validation at optimal setting of grinding parameters was done. The natural type dresser, dressing cross feed rate 60 mm/min, dressing depth of cut 20 μm and grinding feed rate 0.6 mm/min were fixed; the achieved mean surface finish, power and grinding ratio are 0.153 μm, 1.49 kW and 9.96, respectively. The validated experimental results with value of GRG are given in Table 6.7.

Table 6.7 Grey relation grade values

Level setting	Optimum grinding parameter	
	Predicted	Experimental
GR		9.98
SR		0.153
P		1.49
Grey relational grade	0.9387	0.9431

Conclusion

The Taguchi-based grey relational analysis is applied to find out the cylindrical grinding process parameters. Multiple performance measures are reported in this paper and the following conclusions are drawn:

- The optimal level of the dressing depth of cut is 20 μm , dressing cross feed rate 60 mm/min, and grinding feed rate 0.6 mm/min when natural type dresser is used.
- In this investigation the dressing depth of cut is an important factor that contributes ~46% to the overall contribution.
- Dressing depth of cut and grinding feed rate are the significant grinding factors that affect the multiple performance measures.
- Dressing cross feed rate and type of diamond dresser are less significant grinding factors due to least percentage contribution.

Acknowledgements This research work was supported by Saint-Gobain. The authors are thankful to Mr. Anurag Doshi, Saint-Gobain who gives us insight and expertise that greatly helped the research.

References

1. Tools D, Wheels W (2010) diamond tools for dressing grinding. Dressing tools
2. Fritsche A, Bleicher F (2015) Evaluating and influencing dressing results by changing the grain size distribution based on statistical and experimental investigations. In: Seliger G, Yusof NM (eds) *Procedia CIRP*, 12th global conference on sustainable manufacturing—emerging potentials. Elsevier B.V., pp 718–723
3. Patil SS, Bhalerao YJ (2017) Ranking of vitrified grinding wheel parameters by using analytical hierarchical process (AHP) for surface roughness of work piece in grinding operation. In: International conference on advances in mechanical, industrial, automation and management systems (AMIAMS). IEEE, pp 185–188
4. Choi TJ, Subrahmanya N, Li H, Shin YC (2008) Generalized practical models of cylindrical plunge grinding processes. *Int J Mach Tools Manuf* 48:61–72. <https://doi.org/10.1016/j.ijmachtools.2007.07.010>
5. Jiang JL, Ge PQ, Bi WB et al (2013) 2D / 3D ground surface topography modeling considering dressing and wear effects in grinding process. *Int J Mach Tools Manuf* 74:29–40. <https://doi.org/10.1016/j.ijmachtools.2013.07.002>

6. Sinha MK, Setti D, Ghosh S, Rao PV (2014) An investigation into selection of optimum dressing parameters based on grinding wheel grit size. In: Dixit US, Narayanan RG, Sankar MR (eds) 5th international & 26th all India manufacturing technology, design and research conference (AIMTDR 2014), 12–14 Dec 2014, IIT Guwahati, Assam, India, pp 1–6
7. Hecker RL, Liang SY (2003) Predictive modeling of surface roughness in grinding. *Int J Mach Tools Manuf* 43(43):755–761. [https://doi.org/10.1016/S0890-6955\(03\)00055-5](https://doi.org/10.1016/S0890-6955(03)00055-5)
8. Liu Y, Warkentin A, Bauer R, Gong Y (2013) Investigation of different grain shapes and dressing to predict surface roughness in grinding using kinematic simulations. *Precis Eng* 37:758–764. <https://doi.org/10.1016/j.precisioneng.2013.02.009>
9. Nikalje AM, Kumar A, Srinadh KVS (2013) Influence of parameters and optimization of EDM performance measures on MDN 300 steel using Taguchi method. *Int J Adv Manuf Technol* 69:41–49. <https://doi.org/10.1007/s00170-013-5008-8>

Chapter 7

Development of Integrated Versatile Paper, Plastic and Aluminum Waste Sorting and Disposal System



Sharada Gavade, Soham Kulkarni, Shivani Mohite, and Kiran Bhole

Introduction

Totally 40% of waste remain uncollected today [1]. Waste disposal is important from many aspects of life. Emphasis is given globally on the effective waste management. Recycling of waste is one of the important activities. Technology has developed a lot in the field of recycling things. Figure 7.1 shows the typical supply chain of recycling systems in India. The chain starts with waste pickers which pass the waste to Kabadiwallah and then further to traders and finally to recyclers. Numbers of methods are available to recycle our waste.

The following subsections summarize the developments in recycling of waste and the potential gap in the waste management.

Previous Developments

Biddinika et al. [2] have made efforts to design a shredder for household plastic waste whose output is meant to be used for pyrolysis technology for producing liquid oil. It is a great technology but this technology is unable to answer the unsolved question of flow of uncollected waste to the recycling plant. Many more works like Akash et al. [3], Sudhakara et al. [4] and Atadious [5] have designed various types of cost-effective, portable shredders and so on, but when it comes to the installation of such infrastructure in the areas where the waste pickers cannot reach and there is various

S. Gavade (✉) · S. Kulkarni · S. Mohite · K. Bhole
Sardar Patel College of Engineering, Andheri (West), Mumbai 400058, India
e-mail: shardagavade@gmail.com



Fig. 7.1 Supply chain of present waste recycling system

type of waste available, the following points fall under the unaddressed issues of above systems.

- No provision for sorting different types of waste.
- Focus area only plastics.
- Industry-oriented design.
- Cannot be used to install eateries canteens.
- Lack of aesthetics and user orientation.

There are also various options available in the market typically called as ‘Plastic Bottle Reverse Vending Machine’. Zeleno, Europack, Avanti, and so on are few of them. Generally, these machines are meant to dispose only plastic bottles but few of them like Zeleno also have a facility to dispose of aluminum or steel cans in addition to plastic bottles. Presently, the cost of such machines goes around Rs. 5 lakh which is not affordable to many of the organizations to install. The reason why these machines remain idle even after installing lies in the selection of the installation areas. Following are the reasons mentioned with respective areas:

Railway stations and bus stand: Waste pickers collect lots of PET bottles from this area. When this machine is installed at such a place, it threatens the livelihood of these waste pickers. This provokes them to harm and damage such types of reverse vending machines. Hence, when these machines are installed waste pickers make them ill functional in some or the other way and hence the purpose of such machines is not served in these public places.

Office spaces: Many of the office spaces already have a mechanism to dispose of their waste. The collected waste is given to vendors which further sell it to the recyclers. This is true about big companies only. But, in small offices this system doesn’t work and even they may not afford a machine of high initial cost for waste disposal.

Research Gap

There are machines which shred only waste water bottles. There is no facility which incorporates shredding of other available wastes such as aluminum cans or crushing of paper cups and tetra packs. This mixed waste gets piled up in bins consuming more storage space. Further, it is dumped on dumping grounds. As there are lots of efforts involved in segregating this dumped waste, it is hardly segregated and recycled. Instead of regular dumping bins, if one introduces a machine where the dumped waste is segregated on the basis of its type, either for PET plastic bottle, aluminum can, paper cup or tetra pack, then either it is crushed or shredded. This is a very simple step toward liquefying the flow of waste for recycling purposes. As waste accumulation is one of the major concerns it needs to be focused. The waste is not getting recycled within the time which it should be. Hence more and more waste are getting accumulated on the earth. This research study is hence devoted toward

1. Increasing ease of collecting the waste
2. Automatically sorting it
3. Processing of waste (crushing or shredding to reduce the volume)
4. Storing waste temporarily.

The major question is not about recycling but about the facility to collect the waste. If the waste is cut into small pieces and then stored, it will occupy comparatively less space. Further before cutting if it is sorted according to different types then processed and then stored separately it can be sent directly to their recycling plants. This will hence reduce the time gap between waste generation and recycling and will eventually reduce the percentage of waste accumulation. Focus on the areas where the traditional recycling chain is broken typically in areas such as predominantly small eateries, food courts, college canteens and big housing societies (where waste pickers cannot enter or are not allowed to enter). Segregating all types of recyclable wastes generated in such areas and further processing to reduce its volume and storing separately is considered. This study is set to provide a low-cost solution, further, increasing the flow and speed of recyclable waste in the recycle chain.

Efforts should be made to introduce such a machine which can incorporate the facility of identifying the different types of common wastes such as polyethylene terephthalate (PET) water, soft drinks and juice bottles, aluminum cans, paper cups and tetra packs. Further crush it or both crush and shred and then temporarily store to avoid further sorting and make the continuous flow of waste. Figure 7.2 depicts the major areas discussed in the problem statement.

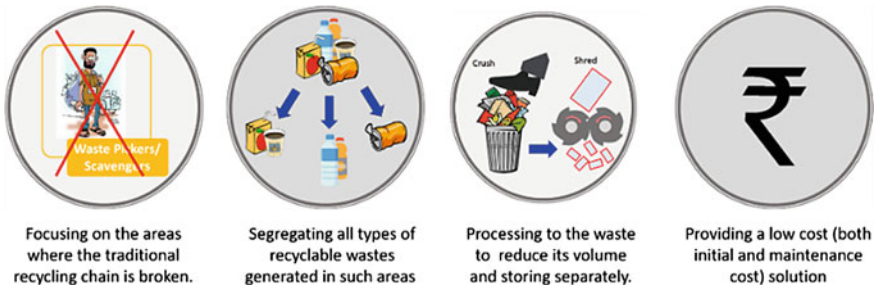


Fig. 7.2 Typical areas of problem addressed in the proposed study

Proposed Methodology of Sorting

Capacitive Sensors: Sensor-Based Sorting

Change in capacitance with change in dielectric constant because of different types of materials like metals, plastic and paper. This sensor can detect the target based on the permittivity value of each material [6]. The main components of a capacitive sensor consist of plates, oscillator, threshold detector and output circuit. The plate of the sensor acts as one of the plates of the capacitor while target waste material acts as another plate.

The air between these two plates acts as a dielectric material. According to capacitance principle, the capacitance increases with decrease in the distance between the plates and vice versa. Capacitance sensor is capable of detecting any material having dielectric constant greater than air. Figure 7.3 shows the setup for the capacitive-type sensors. Table 7.1 indicates the dielectric values of paper and plastic.

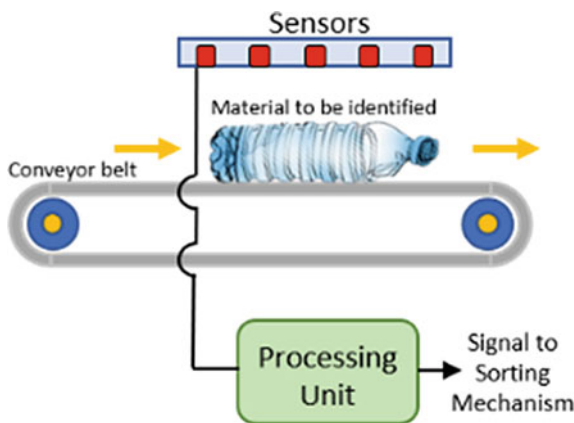


Fig. 7.3 Setup for capacitive sensor for waste sorting

Table 7.1 Value of dielectric constants of waste material considered in the study

Materials	Dielectric value (ϵ)
Paper	3.60–3.85
Plastics	3.00–4.00

Inductive and Light Sensor: Sensor-Based Sorting

The inductive sensors are used to detect whether the waste fed to the machine is metallic or not.

Figure 7.4 shows the waste segregation algorithm using inductive and light sensor. In case of metal proximity sensor, on approach of metal the eddy current is inducted in the approached metal. This inductive eddy current changes the magnetic field produced by inductive proximity sensor. This change in magnetic field is stimuli for the sensor. Depending on this principle, the decision is taken whether it is an aluminum can or a plastic/paper. Hence then what remains is sorting paper and plastics. The general observation regarding PET bottles is that they are usually transparent. Hence a light sensor can be used to segregate opaque paper cups, tetra packs and transparent PET bottles.

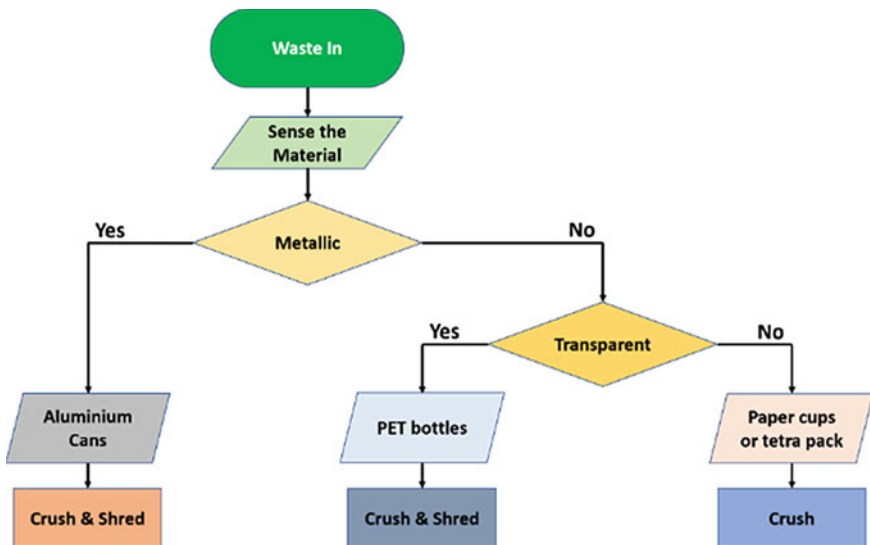


Fig. 7.4 Waste segregation algorithm based on inductive and light sensor

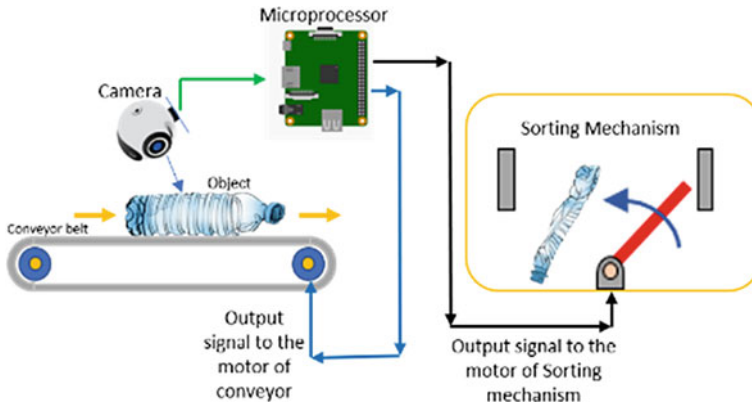


Fig. 7.5 Block diagram of image processing system for waste sorting

Image Processing-Based Sorting

To make this sorting system more reliable and fool-proof instead of using sensors the technology of image processing can also prove to be useful. This process of image processing involves feeding the data to the microprocessor in terms of images. The algorithm then carries out the function of setting the parameters to determine the object (the output based on the input data, i.e. various images). Various types of images of the targeted waste are fed as inputs. A robust algorithm gives the required output for identification of the type of waste; whether a PET bottle, aluminum can, paper cups or any unwanted material which is to be rejected [7].

The waste fed into the machine goes onto the conveyor. The camera clicks its picture and sends this data to the microprocessor. The microprocessor then based on the algorithm identifies what type of waste it is. Based on that it sends the output signal to the motors of the conveyor and sorting mechanism—defining the direction of rotation to carry out the sorting process. Figure 7.5 shows the block diagram of this image processing unit. Selection of the best method for the sorting will be done using evaluation matrix or decision matrix method. This part of work is under study.

System Details

Construction Details

- Bi-directional conveyor: The function of the conveyor is to move waste forward inside the machine and to reject the unwanted waste.
- Sensing mechanism: It may consist of sensors or image processing technology to identify the type of material of the waste.

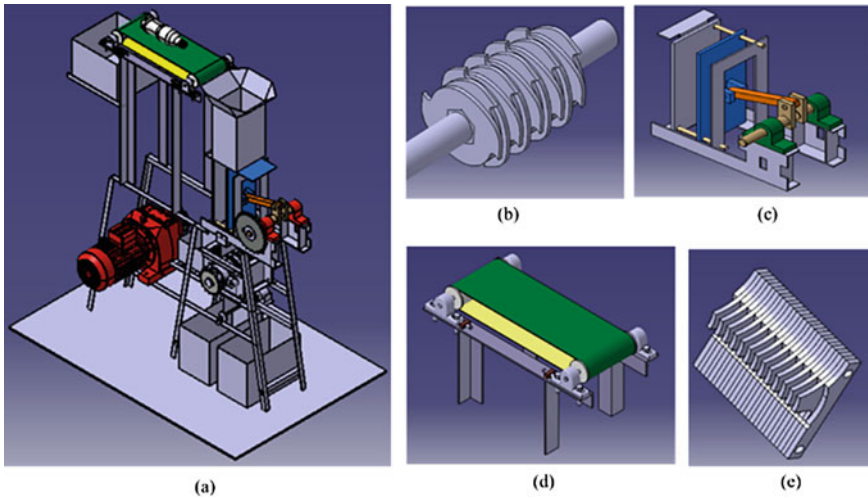


Fig. 7.6 a CAD assembly of machine; b CAD model of rotary shredder assembly; c CAD model of crusher; d CAD model of bi-directional conveyor belt; e CAD model of fixed blades assembly

- **Electronic unit:** Electronic unit consists of microprocessor, relays and other electronic components. Function of electronic unit is to receive the input signals from the sensing mechanism, amplify, process it to generate an output signal to actuate bi-directional conveyor, the sorting mechanism, crusher and shredder.
- **Crusher:** Crusher is the main processing part of the system. Reciprocating crusher used to crush the waste bottles, paper cups and cans.
- **Sorting mechanism:** This is a flap separator which separates crushed paper from plastic and aluminum before entering the shredder unit. And further another mechanism fitted after shredder segregates plastic and aluminum flakes.
- **Shredder:** The function of shredder is to shred the waste into fine flakes so as to reduce its volume.

Figures 7.6 shows the 3D CAD parts developed for the machine in CATIA V5 software. CATIA V5 software is used for design and development of machine. CATIA V5 is used because it provides multiple workbenches like part design, product design, drafting, assembly and so on, which were necessary for this work.

Working of System

The user has to insert the waste into the machine through the opening provided at the front panel of the machine and then press the start button above it. The panel of the machine is as shown in Fig. 7.7a. The type of waste inserted into the machine will be identified by the sensing mechanism on the conveyor itself. Once the waste type is

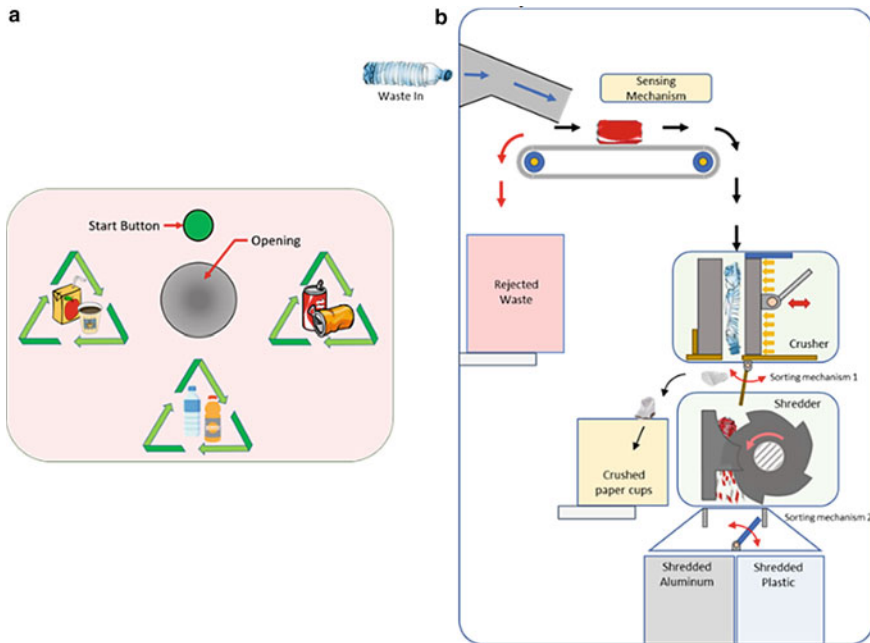


Fig. 7.7 **a** Front panel of machine showing various options for user; **b** block diagram of proposed versatile waste sorting and disposal machine

identified, the necessary input data is sent to the sorting mechanism by the electronic unit. If any unwanted waste is inserted into the machine it will be discarded. For discarding, the conveyor motor will move in the opposite direction, thus dumping the unwanted waste in a separate bin. If the targeted waste material is sensed on the conveyor belt, then the motor of the conveyor belt starts rotating and the waste is taken forward to the next processing stage (Crusher). The motive of the crusher is to compact the targeted waste.

Paper waste after crushing directly goes to the storage bins as the sorting mechanism 1 sorts it out. But crushed plastic and aluminum is fed to the shredder unit. After shredding the sorting mechanism 2 does the work of taking this shredded waste into the respective bins. At a time one waste item will be processed in machine, until waste is stored in bins. Before completing one cycle no other waste is processed.

Paper waste after crushing directly goes to the storage bins. But crushed plastic and aluminum are fed to the shredder unit. After crushing the sorting/separating mechanism does the work of taking this shredded waste into the respective bins. The block diagram of the machine is as shown in Fig. 7.7b.

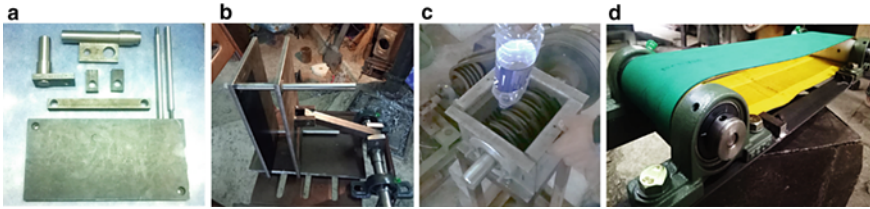


Fig. 7.8 a Components of crusher, b crusher, c shredder, d conveyor

Design and Fabrication

Detailed manual design calculations were done for all the parts. Maximum shear stress theory was used for the same. All static and dynamic loadings were considered while designing the components. Design data book by V. B. Bhandari was referred for this purpose.

The fabrication of current work is under development stage. Various parts like shredder, crusher and conveyor are manufactured. Thus up to 60% of the total system is fabricated up till now.

The general manufacturing procedure is as follows:

- Generation of drawings of the parts to be manufactured
- Estimation of material required for manufacturing
- Procurement of the material
- Machining of the material to the required dimension
- Assembly of the parts using welding, and detachable assembly is done using nuts and bolts.

To manufacture each component a sequence of operations was selected. This sequence was decided by considering the availability of manufacturing resources such as machines and tools and the process sheets were made for the same. Figure 7.8 shows the actual photographs of the manufactured parts.

Cost Estimation

This study focuses on providing an affordable solution for the target areas of this work in predominantly eateries, food courts, college canteens and big housing societies. The available options in the market cost about 5 lakh (INR) and are hardly affordable and suitable for the above-mentioned locations. Hence our effort is to reduce this cost in all possible ways while maintaining the required functions of this infrastructure. Cost estimate for developing the prototype consists of basic costs required for manufacturing machine components such as material cost, cost incurred in procurement of raw material, machining cost and cost of bought out parts. This cost estimate is

prepared at normal working conditions and the actual costing may vary at the time of manufacturing but there won't be much difference. The initial cost of the machine development is Rs. 66,000 (sorting mechanism considered for calculation is image processing-based sorting). The running cost of the machine would be Rs. 10 per hour of waste to be processed. Cost estimate is done on the basis of past experiences of various stakeholders involved in this process.

Energy Aspects and Impact on Environment

There are many possible ways to channelize the collected waste to resolve the energy issues. Starting with PET bottles, which have the possibility of being off here and there if bins are not around, technologies have been developed to use these waste plastic bottles for making useful fuel. The technique of pyrolysis [8] which consists of decomposition of plastics at higher temperature will convert it to fuel. This fuel can be used for various purposes. Researches have proved that this fuel made out of plastics has higher calorific value and on burning produces less harmful emissions. Continuing with the topic of aluminum waste, only 5% of energy is necessary to recycle plastic than that of making a new one [9]. Target areas defined in this paper are the areas where even if the waste is collected it all ends up on the landfills [10, 11]. But locally people burn this waste which causes a lot of air pollution because of the content of plastics in it.

To study the impact on the environment a survey of waste generation of our own college campus—Bhavans campus, Andheri (West) Mumbai was carried out. The wet waste is used to form compost but the dry waste is taken away by the BMC (Brihanmumbai Municipal Corporation). Figure 7.9a shows weekly plastic usage of various canteens and mess. Figure 7.9b shows PET bottles are the major contributors to this dry plastic waste.

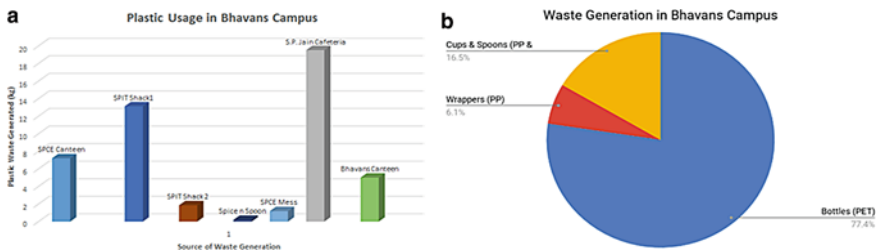


Fig. 7.9 **a** Plastic usage per week (classification by cafeteria); **b** waste generation per week (classification by plastic type)

Conclusion

Design and fabrication of novel versatile waste sorting and crushing system can be carried out to improve the waste supply chain with the following points:

- Collecting sorted common waste like paper cups, aluminum cans and PET bottles at initial stage avoids mixing of waste and saves further sorting time.
- Crushing paper cups reduces its volume up to 65%.
- Crushing and shredding aluminum cans and PET bottles reduces its volume up to 50% [12].
- Due to reduced volume of waste, more amount of waste can be easily stored in machine.

Acknowledgements The authors are thankful to Dr. Nilesh Raykar, Prof. D. N. Jadhav, Mr. Panchal and Mr. Desmond for their guidance in the component designing phase and manufacturing.

References

1. Souro DJ (2000) Urban residential solid waste management in India. Sage Publications, Inc., Public Works & Policy. <https://doi.org/10.1177/1087724X0044006>
2. Muhammad KB, Mochamad S, Arip NH, Zahrul M, Fumitake T (2017) Technology for public outreach of fuel oil production from municipal plastic wastes. ScienceDirect, Energy Procedia 142. <https://doi.org/10.1016/j.egypro.2017.12.424>
3. Akash BP, Christina, Darshan KS, Manoj (2019) Plastic waste management by mechanical Shredder Machin. In: IJARIE-ISSN(O) 5(2):2395–4396
4. Sudhakara R, Thunga R (2018) Design and development of mini plastic shredder machine. In: ICAAMM IOP Publishing, IOP Conf Ser: Mater Sci Eng. <https://doi.org/10.1088/1757-899X/455/1/012119>
5. Atadious D, Oyejide OJ (2018) Design and construction of a plastic shredder machine for recycling and management of plastic wastes. Int J Sci Eng Res 9(5):1379–1385
6. Irfana KA, Muhammad M, Hassan B (2016) Application of capacitance proximity sensor for the identification of paper and plastic from recycling materials. Res J Appl Sci Eng Technol 12(12):1221–1228
7. Zhaokun W, Binbin P, Yanjun H, Guanqun S (2019) Classification for plastic bottles recycling based on image recognition. Waste Manage 88:170–181
8. Chunfei W, Paul TW (2010) Pyrolysis–gasification of plastics, mixed plastics and real-world plastic waste with and without Ni–Mg–Al catalyst. Fuel 89:3022–3032
9. Aurora LD, José IR, Isabel P, Sol LA, Maximina R (2020) Zero-waste process for the transformation of a hazardous aluminum waste into a raw material to obtain zeolites. J Cleaner Prod 255. <https://doi.org/10.1016/j.jclepro.2020.120178>
10. Fávoro SL, Freitas AR, Ganzerli TA, Pereira AGB, Cardozo AL, Baron O, Muniz EC, Giroto EM, Radovanovic E (2013) PET and aluminium recycling from multilayer food packaging using supercritical ethanol. J Supercrit Fluids 75:138–143

11. Green JAS (2007) Emerging trends in aluminum recycling. Aluminium recycling and processing for energy conservation and sustainability. ASM International, Materials Park, Ohio, pp 147–154
12. Oluwatobi IO, Damilola AO, Olawale OO (2019) Development of shredding and washing machine for polyethylene terephthalate (PET) bottles pelletizer. Int J Eng Sci Appl 3(2):102–109

Chapter 8

Development of Machining Fixture to Improve Machining Lead Time of Helical Gearbox Case



Hardik Beravala , Rohan Pandey, Shubham Samudre, and Jayesh Parpiyani

Introduction

In the competitive market, customer satisfaction is the main pillar of any manufacturing industries. It is important to have regular orders from customers to maintain a position in the competition. The manufacturing industries must fulfil three basic requirements of the customer, which are mainly on-time delivery, good quality and reduced price. High takt time, delay work, increased ideal time, lack of standardization in the work and so on are the major reasons for customer dissatisfaction. When a business delivers good service with on-time delivery at a reduced rate, the customer's order is always with better quality. It is also critical that the industry focuses on issues designed to boost income, growth and market stability. The lean management techniques like Poka Yoke, 5 s, visual management, cause and effect diagram, Judoka and so on have been used effectively in manufacturing to achieve delivery of products on time. Lean tools are effectively applied in various fields of engineering and medical applications [1–3]. Rajenthira kumar and Siva applied lean manufacturing techniques to identify unwanted activities and improved the cycle time in the construction equipment manufacturing industry [1]. The major seven wastes of lean manufacturing, that is, unwanted activities were identified, and the cycle time was improved by 63% through the value stream mapping technique. Nowotarski et al. proposed a methodology based on lean management on the construction site [3]. It was reported that the application of lean tools effectively reduced the time and cost in the column concreting, storage area management and scaffolding ordering operations. Jiagin et al. improved the performance of a closed manufacturing cell by the reduction in the product setup times [4]. Feldmeth and Mülle designed the lean

H. Beravala (✉) · R. Pandey · S. Samudre · J. Parpiyani
Department of Production Engineering, Birla Vishvakarma Mahavidyalaya, Vallabh Vidyanagar,
Gujarat 388120, India
e-mail: hsberawala@bvmengineering.ac.in

manufacturing system based on lean principles proposed by the Toyota production system applicable in the assembly design [5].

The work and time study techniques have been proven scientific approach to improve the efficiency of manufacturing and service factor utilization. Duran et al. applied time study method in the glass manufacturing industry [6]. It was reported that by the implementation of time study technique, the productivity of the plant was increased by 53%. Al-Saleh et al. performed motion and time study at the motor vehicle periodic inspection (MVPI) station to reduce the bottleneck in the inspection point with the help of the simulation software [7]. The suggested method showed the reduction in the bottleneck and improvement of 175% in the inspection capacity.

Siva et al. applied the current state value stream mapping technique to identify the bottleneck in the manufacturing of filter drier [8]. A fixture was developed which raised the production of filter drier from about 16% and reduction of bottleneck process time about 37%. Eyer et al. extended the EOQ model to the EMQ model to reduce the setup cost in the fluctuating variable lead time environment in the manufacturing industry [9]. Dong et al. gave the importance to select the locating elements and identification of locating surfaces for the workpiece positioning in the fixture design [10]. Bejlegaard et al. proposed a generic architecture design methodology for the design of reconfigurable fixtures for positioning of 14 different sub-components in one single reconfigurable fixture for the assembly operation [11]. The reconfigurable design of fixtures reduced the requirement of multiple fixtures and resulted in the reduction in the tooling cost. Wu et al. designed and manufactured a fixture to machine jet engine blade [12]. The proposed clamping-sequence method in the fixture effectively reduced the local maximum deformation of the blade. In addition, the system stiffness is increased by 20 Hz and the clamping force increased by 200 N. Baraiya et al. developed a fixture for finishing of ring-shaped cylindrical aluminum alloy workpiece [13]. The fabricated fixture can finish the inner, outer and side surface of a ring at the same time. The maximum percentage improvement in surface roughness by 36, 37 and 27% in the inner, outer and side surface was reported, respectively. There were few attempts conducted to improve geometrical control by the fixture design in the machining of thin-walled structure [14–16]. Fei et al. developed the fixture which provided support to the workpiece back surface by its simultaneous motion with the milling cutter during machining of tin-walled workpiece [14]. The motion of fixture with respect to cutter reduced the elastic deflection and improved the geometrical accuracy of thin-walled structure during the machining. The literature shows that the fixture helps to reduce the lead time and improve the quality of the product.

The gearbox manufacturing industry produced mainly casted helical gearboxes that were used in the desired speed ratio to transmit rotational motion. These gearboxes have a size of 500 mm × 1300 mm × 700 mm. The manufacturing of casted gearboxes starts with the machining of gearbox cases and other individual parts such as shafts and helical gears. The machining of the gearbox case begins with the pre-production inspection of the delivered gearbox cases and then marking the center line on the gearbox cases followed by the machining on a horizontal machining center. To extract burrs and chips from the body, the machined component is disassembled,

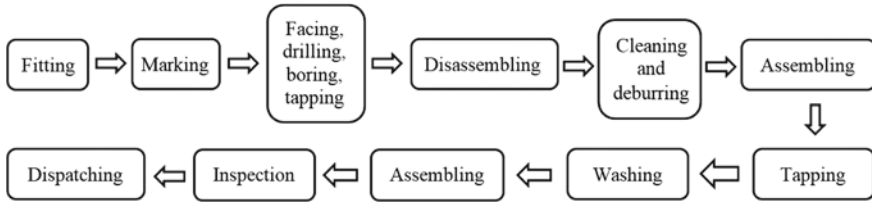


Fig. 8.1 Operation sequence of helical gearbox case

followed by tapping and drilling. The gearbox case body is then washed in the workstation, followed by post-inspection, and finally the gearbox is dispatched to the main assembly department. The common manufacturing process steps for such gearbox cases are shown in Fig. 8.1. The average machining lead time of a helical gearbox case as per the present operation sequence was found to be 570 min.

In order to improve the production rate, the industry wanted to reduce the average machining lead time. Hence, in the present research work, a lean manufacturing tool, namely value stream mapping technique, was used to identify the waste in the machining of the helical gearbox case. After identifying the waste, appropriate corrective actions were incorporated and the performance of operation was compared.

Value Stream Mapping of Existing Method of Clamping the Gearbox Case

The helical gearbox case was machined at the vertical machining center (HMT, Mazak FH10800). The gearbox case was clamped on the machine table with the help of strap clamp as shown in Fig. 8.2. Before clamping it should ensure that the gearbox case must be aligned to the machine table. This setup consumed an average of 40 min. In single setup, surface A and surface B should be machined (refer Fig. 8.2). However, due to the present method of clamping gearbox case allowed facing of surfaces A and B, while the surface C was hindered by the clamps. Hence, all the

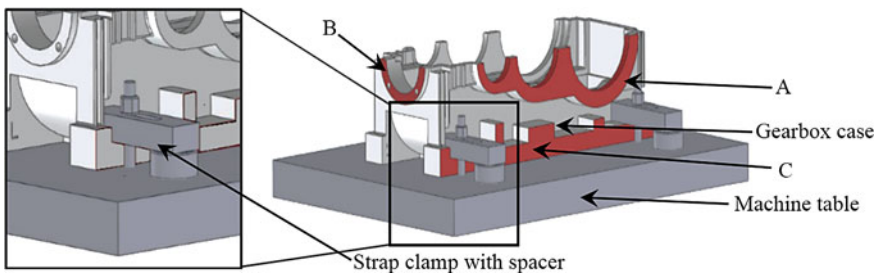


Fig. 8.2 Helical gearbox case clamp on machine table using strap clamp

three sides cannot be machined in single setup. Therefore, the machining of surface C required another setup. In the second setup, gearbox case body was to be revolved and clamped for the rest of the part to be machined. This setup consumed an average of 50 min. This second setup took a longer time as compared to the first one because of the lower face it needed to change the orientation and realignment of the gearbox case with respect to machine table. In order to machine the faces A, B and C, it required two setups to facing the single gear casing and it consumed an average of about 120 min. Every time a component is loaded on the machine, the operator does the setting manually which includes initial clamping, dialing the component, final clamping, zero offset and so on. From the detailed study by the value stream mapping technique of the existing process of gearbox case manufacturing, it was found that the manual setting of the component onto the machine contributed to about 40% of non-value-added time. It resulted in the loss of productivity of the machine and hence it makes difficult to achieve the production target of 625 gearbox cases per month. In order to reduce the lead time, it was required to develop the fixture which allowed facing surfaces A, B and C in a single setup.

Development of Machining Fixture

The main objective for the development of the fixture was not only to allow the gearbox case to be aligned with CNC machine axes but also to allow two surfaces to be faced in one setup. Machining fixture consists of the main body, spacer pin and support in two quantities each. Figure 8.3 shows the different assembly components of machining fixture. The main body, spacer and support were made from cast iron. The fixture's main body was clamped on the machine table. Its main function was to provide the clamping of the gearbox case during facing operation. The spacer provided the location to the gearbox case from its pre-machined diagonal holes with

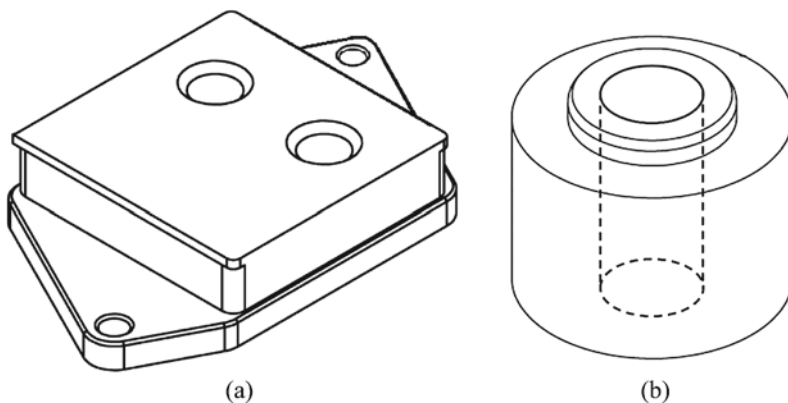


Fig. 8.3 Schematic diagram of **a** fixture main body and **b** spacer pin

respect to machine axis. The fixture lifted the gearbox case about 100 mm from the machine table so that it was possible to machine the surfaces A, B and C in a single setup. Figure 8.4 shows the mounting of gearbox case on the fixture assembly, and the location is provided by the fixture to the gearbox case as per the 3-2-1 location system. As shown in Fig. 8.4b, spacer provided the location to the gearbox casing with the help of locators 2, 5 and 6 at the pre-machined hole P and locators 3, 7 and 8 at the pre-machined hole R. The support provided the location with the help of locators 1 and 4 near the hole O and S, respectively. Rest of the degree of freedom is restricted by the M20 fasteners which provided the clamping force 9 and 10 at the holes P and R, respectively.

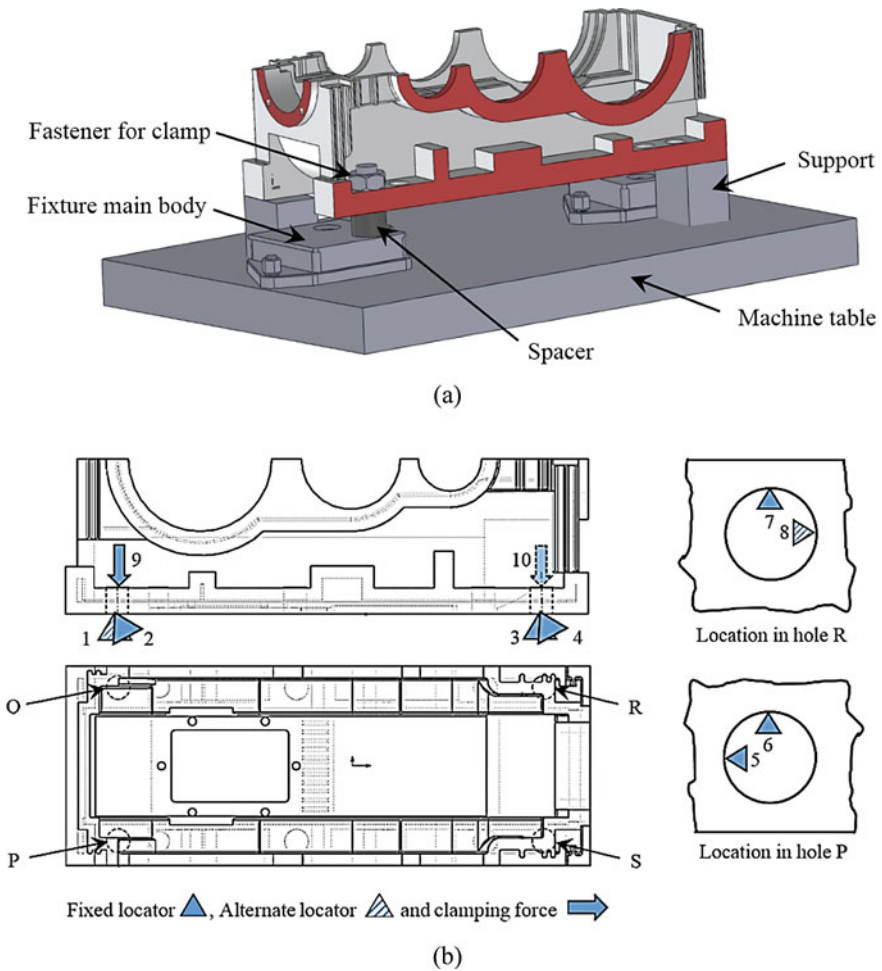


Fig. 8.4 Gearbox case **a** mounting on the fixture assembly, **b** location system provided by the fixture

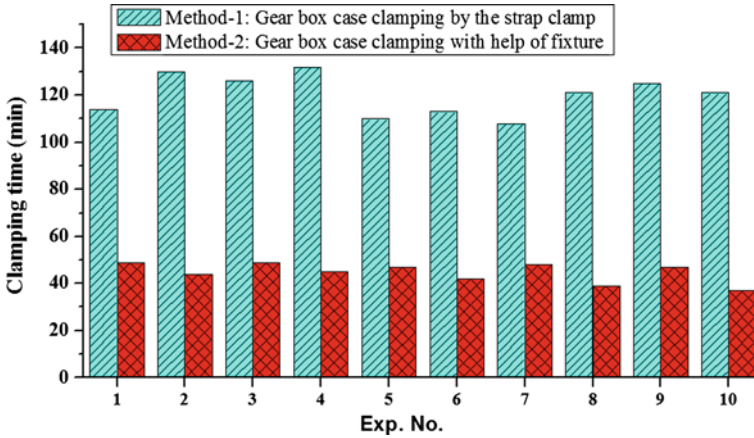


Fig. 8.5 Comparison of both methods of clamping gearbox case

The experimentation was performed by time study method in order to compare the performance of the fixture with respect to the previous method of clamping of the gearbox case. In this method, both methods measured the time consumed for loading, positioning and clamping the gearbox case. It was performed out by an industry's machinist, helper and crane operator.

Results and Discussion

The experimental results are graphically plotted and shown in Fig. 8.5. The comparison of the clamping methods for the gearbox case shows that the average setup time of 120 min is reduced to 45 min by the fixture. Thus, with the aid of newly developed fixture, the setup time for machining the gearbox case reduced by about 62.5%. This was because the new fixture allowed surfaces A, B and C to be facing in a single setup. Moreover, in earlier gearbox case clamping by the strap clamps, the fixture eliminated the multiple setups for facing three surfaces. The developed fixture saved 75 min of production lead time per gearbox case. Hence, it resulted in the reduction of machining lead time for the helical gearbox case and achieved the production target of 625 helical gearbox cases per month.

Conclusions

The present paper focused on reduction in the machining lead time for helical gearbox case. The clamping of the gearbox case by strap clamps on the machine table increased additional 120 min of non-value-added time. It leads to cause high takt time, delay work, increased ideal time and the output target was difficult to achieve. The new fixture was developed to replace the existing method of clamping

of the gearbox case by the strap clamps. The experimental results show that the lead time for the case was reduced from 120 to 45 min with the aid of the fixture, which saves 62.5% of non-value-added time in gear case machining. It also eliminates multiple setups for the machining of a gearbox case. The developed fixture therefore helps in improving productivity and cycle time. This considerable saving in takt time is directly proportional to the reduction in the cost of production and contributes to customer satisfaction by cost reduction and on-time delivery. In the future, the proposed fixture design can be applicable to other size gear box cases. In addition, the flexibility of fixture can be improved by adding specific bores used for mounting the upcoming new series of similar gearbox cases.

References

1. Rajenthirakumar D, Mohanram PV, Harikarthik SG (2011) Process cycle efficiency improvement through lean: a case study. *Int J Lean Thinking* 2(1):46–58
2. Susie T, Lee L, Polancich S, Pilon B (2019) The Application of the Toyota production system LEAN 5S methodology in the operating room setting. *Nurs Clin N Am* 54:53–79
3. Nowotarski P, Paslawski J, Matyja J (2016) Improving construction processes using lean management methodologies—cost case study. *Proc Eng* 161:1037–1042
4. Yang J, Deane RH (1993) Setup time reduction and competitive advantage in a closed manufacturing cell. *Eur J Oper Res* 69:413–423
5. Feldmeth M, Mülle E (2019) Influences between design characteristics of lean manufacturing systems and implications for the design process. *Procedia Manuf* 39:556–564
6. Duran C, Cetindere A, Aksu YE (2015) Productivity improvement by work and time study technique for earth energy-glass manufacturing company. *Procedia Econ Financ* 26:109–113
7. Al-Saleh K (2011) Productivity improvement of a motor vehicle inspection station using motion and time study techniques. *J King Saud Univ-Eng Sci* 23(1):33–41
8. Siva R, Prabhakaran M, Rishikesh S, Santhosh AK, Sangeetha M (2020) Lead time reduction through lean techniques on filter drier component by modifying fixture design—case study. *Mater Today: Proc.* <https://doi.org/10.1016/j.matpr.2020.01.221>
9. Coates ER, Sarker BR, Ray TG (1996) Manufacturing setup cost reduction. *Comput Ind Eng* 31(1/2):111–114
10. Dong X, DeVries WR, Wozny MJ (1991) Feature-based reasoning in fixture design. *CIRP Ann* 40(1):111–114
11. Bejlegaard M, ElMaraghy W, Brunoe TD, Andersen AL, Nielsen K (2018) Methodology for reconfigurable fixture architecture design. *Manuf Sci Technol* 23:172–186
12. Wu D, Wang H, Peng J, Zhang K, Yu J, Zheng X, Chen Y (2019) Machining fixture for adaptive CNC machining process of near-net-shaped jet engine blade. *Chin J Aeronaut* 33(4):1311–1328
13. Baraiya R, Babbar A, Jain V, Gupta D (2020) In-situ simultaneous surface finishing using abrasive flow machining via novel fixture. *J Manuf Processes* 50:266–278
14. Fei J, Lin B, Xiao J, Ding M, Yan S, Zhang X, Zhang J (2018) Investigation of moving fixture on deformation suppression during milling process of thin-walled structures. *J Manuf Processes* 32:403–411
15. Calabrese M, Primo T, Prete AD (2017) Optimization of machining fixture for aeronautical thin-walled components. *Procedia CIRP* 60:32–37
16. Do MD, Son Y, Choi HJ (2018) Optimal workpiece positioning in flexible fixtures for thin-walled components. *Comput Aided Des* 95:14–23

Chapter 9

Design and Development of Robust Fixture to Perform Friction Stir Welding/Processing on Conventional Vertical Milling Machine



Jainesh Sarvaiya  and Dinesh Singh 

Introduction

Friction stir welding and processing (FSW/P) is a solid-state process that coalesces metal below its melting point under extreme strain applied by the high strength non-consumable rotating tool [1]. The relative motion between the rotating tool and workpiece produces very high undesirable forces, like axial force, welding/processing force, and torque force during processing [2–4]. Figure 9.1 shows the schematic diagram of various forces acting during FSW/P. It is very crucial for the work plate to be rigidly fixed while processing. A very slight displacement in the work plate can create an adverse effect on the qualities of the material. The issue is during the plunging stage of friction stir welding (FSW), a rotating tool applies lateral force on a workpiece abutted joint that increases the gap between the workpiece interfaces. This separating force between two work plates is only observed in FSW but not in friction stir processing (FSP) as it has a single work plate. However, very high torque and axial force are noted at the initial stage of tool–workpiece interaction. Also, the loose-fitting of a workpiece in the fixture is associated with safety concerns, while FSW/P, a minor casualty, may lead to tragic accidents.

The FSW/P process can be described in three stages: (a) plunging stage, (b) dwelling stage, and (c) translational stage. After the plunging stage, peak forces on the tool stabilize with the generation of heat and increases the flowability of material [5]. Therefore, the fixture has to resist more severe stresses during the plunging stage than dwelling and translation stages. Thus, while designing FSW/P fixture,

J. Sarvaiya (✉) · D. Singh
Department of Mechanical Engineering, Sardar Vallabhbhai National Institute of Technology,
Surat, Gujarat 395007, India
e-mail: jainesh.nit@gmail.com

D. Singh
e-mail: dineshsinghmed@gmail.com

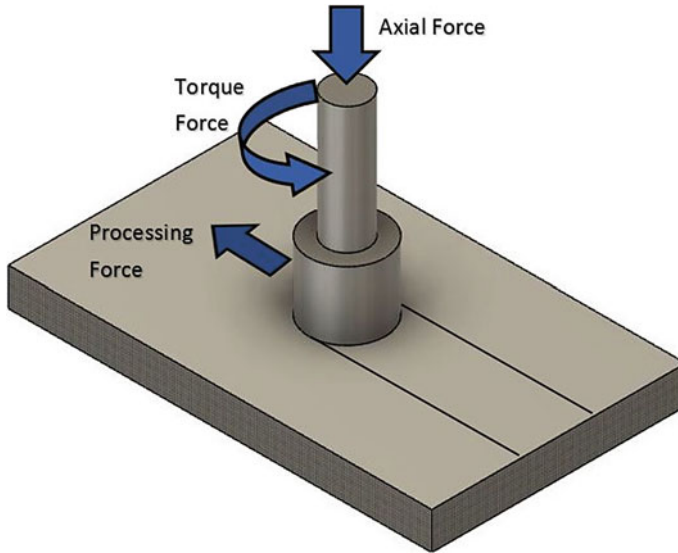


Fig. 9.1 Various forces acting during FSP

peak forces generated during the plunging stage must be considered. The success of FSW/P is directly or indirectly dependent on the design of the fixture, clamping device, and material used. Nowadays, companies are specially manufacturing the FSW/P type of machine that has an inbuilt accessory of fixture and clamping devices [6–8]. But such kind of machines requires a very high cost of investments. Thus, it is necessary to construct an economical fixture for the FSW/P in a universal vertical milling machine design in such a way that it withstands high forces and hold the workpiece rigidly. Moreover, it is possible to modify a conventional vertical milling machine for FSW/P through a suitable design fixture and clamping device [9–12].

Parida et al. [13] developed a fixture and clamping system that securely holds the workpiece. It also eliminates the formation of a gap between the joint and reduces job switching time with a cost-effective strain gauge-based force measuring dynamometer. Richter-Trummer et al. [14] studied the effect of different clamping forces on the distortion and residual stress developed in the abutted FSW joint. It was observed that lower distortion and a more uniform residual stress distribution is produced through the thickness due to higher clamping forces. Ramnath et al. [15] designed and analyzed three FSW fixture materials, that is, cast iron (C45), die steel (D4), and tool steel and hard alloy (H20) by ANSYS software. The outcome of this analysis deduced that C45 steel material is also successfully used as a fixture material in place of D4 and H20 materials. Further, it noticed that the design of a wedge shape at the corner of the fixture reduces the stress concentration. Ahmed and Saha [16] developed and proposed an FSW fixture for joining a thin sheet of aluminum alloy by using a lever-type clamping system and asbestos as a cover plate to reduce heat loss. The feasibility of the fixture is successfully established by FSW of 0.5 mm

thin AA 6061-T6 sheets at five different tool travel speeds. Fratini et al. [17] have specially designed an inbuilt cooling system in a backplate of FSW fixture and choice of materials to overcome the shortcomings of welding of titanium alloy sheets. In this present work, a fixture and the clamping system is designed and developed to overcome the problem of fixture rigidity that securely holds a workpiece and fixture to the milling bed during processing. It also reduces the job shifting time and easy installation on conventional vertical milling machine bed. The unavailability of an expensive company made FSW/P machine motivated to design and develop a fixture that modifies traditional vertical milling machines into the FSW/P machine.

Design and Development of a Fixture

The adequately developed fixture has shown high efficiency in carrying out FSW/P operations in the conventional vertical milling machine. While designing FSW/P fixture, the following are the points that should be considered: (a) Backplate should be reasonably thick relative to the thickness of the work plates to be processed or welded. (b) The chosen material should have a low thermal conductivity that maintains a sufficiently high temperature to promote the work material plasticization and flow. (c) It is necessary to clamp from the top so that work plates should not lift from their position during processing. (d) The longitudinal and transverse movement of the work plate should be restricted. (e) In the case of FSW, for smooth welding, its joint should be kept intact to reduce the gap between the plates. The fixture has four main components: fixture plate, locating device, clamping device, and the support plate.

Component of a Fixture

Fixture plate. It is the core part of the fixture with a size 320×280 mm and a thickness of 22 mm under which is a rectangular recess of size 280×100 mm with a depth of 8 mm to facilitate the setting of a workpiece. The corner point of this recess has a circular blind hole of diameter 8 mm that helps in proper accommodation and proper alignment of a rectangular workpiece. Sliding slot recess in the X and Y directions are also provided to locate the workpiece in their position (see Fig. 9.2).

Locating device. It is a device that correctly positions and restricts the movement of a workpiece in a lateral and longitudinal direction. It helps in the accommodation of workpiece if any little variation in shape and size.

Sliding plate in X direction: It accommodates the workpiece if there is any variation in length. The half circular-cut gives run out of space for the FSP tool at the end stage of the process. The slotted hole helps in X direction movement and can be tightened

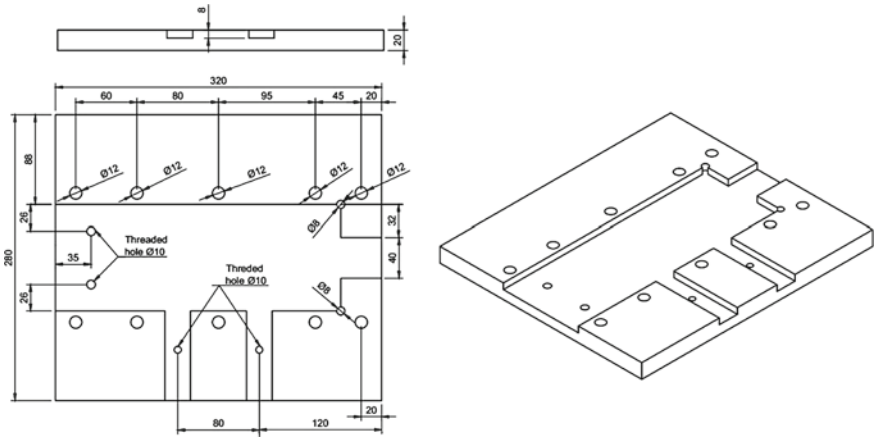


Fig. 9.2 Fixture plate with recess for the accommodation of workpiece (all dimensions in mm)

in that position using the Allen bolt. The dimension of the sliding plate is shown in Fig. 9.3a.

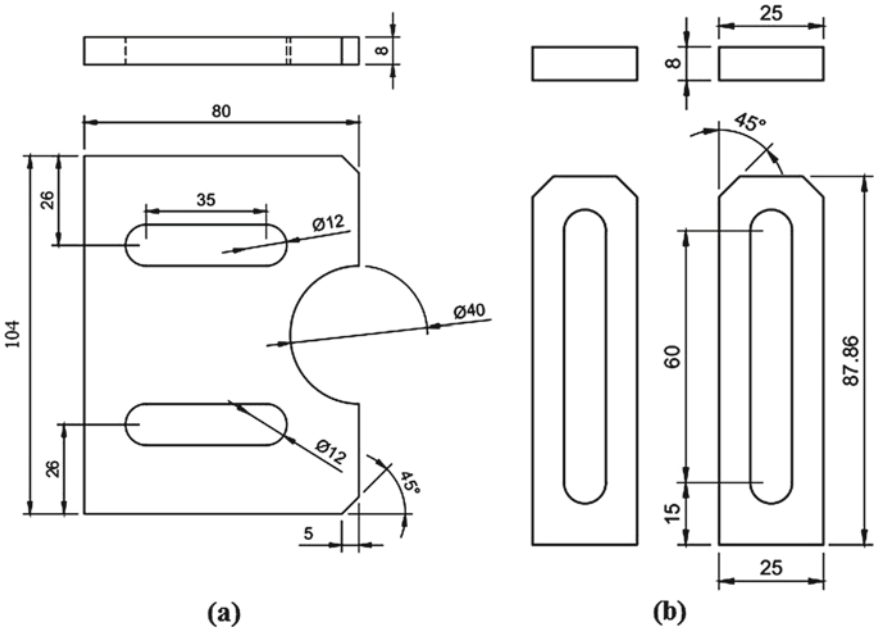


Fig. 9.3 Sliding plate to constraint workpiece movement in a X direction and b Y direction (all dimensions in mm)

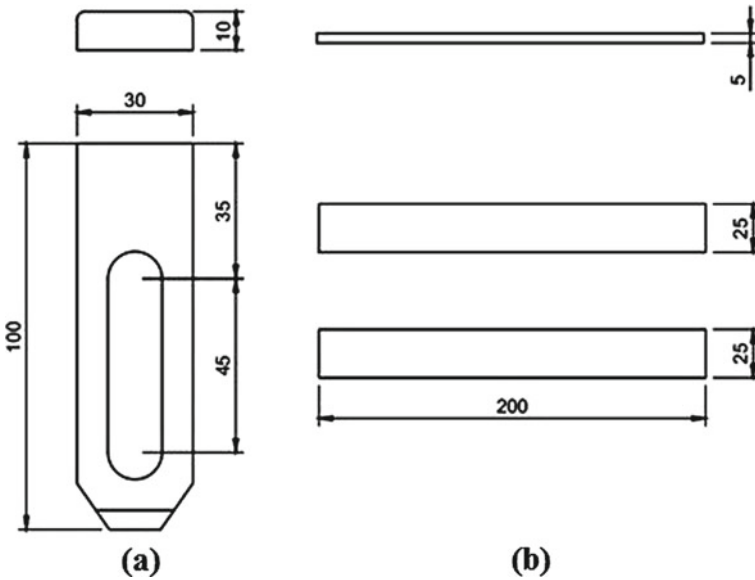


Fig. 9.4 **a** Clamping device and **b** the support plate (all dimensions in mm)

Sliding plate in Y direction: It accommodates the workpiece if there is any variation in width. The slotted hole helps in movement in Y direction and can be tightened in that position using the Allen bolt (see Fig. 9.3b).

Clamping device. The purpose of clamping is to hold the workpiece accurately in the fixture and to ensure that the work should not be displaced under processing forces. The clamping device design should be such that the operating time is as minimum as possible. Thus, tightening of Allen bolt in clamping quickly and directly fixed to the T-slot nut in vertical milling machine bed, which further ensures the rigidity of the workpiece with fixture. The shape and size of the clamp are shown in Fig. 9.4a.

Support plate. It uniformly distributes the clamping forces on a workpiece. It kept between the workpiece and the clamp, made up of the same material as that of the fixture. Thus, it restricts the upward movement of a workpiece, and results in negligible distortion during and after the processing work material. The dimension of the support plate is shown in Fig. 9.4b.

The complete diagram of the fixture and its various parts is shown in Fig. 9.5. The fixture and all its parts are fabricated at M/s. Keytex Machines (Surat, India) within acceptable dimensional tolerance after finalizing the drawing. The final fabricated FSW/P fixture is easily installed on the milling machine bed T-slot with the help of ten Allen screws of size M12 × 1.25. However, the provision of four extreme holes (at the start and the end of processing) rigidly holds the fixture with milling bed even after relaxing the clamping bolt (see Fig. 9.6). For the sliding plates, two Allen

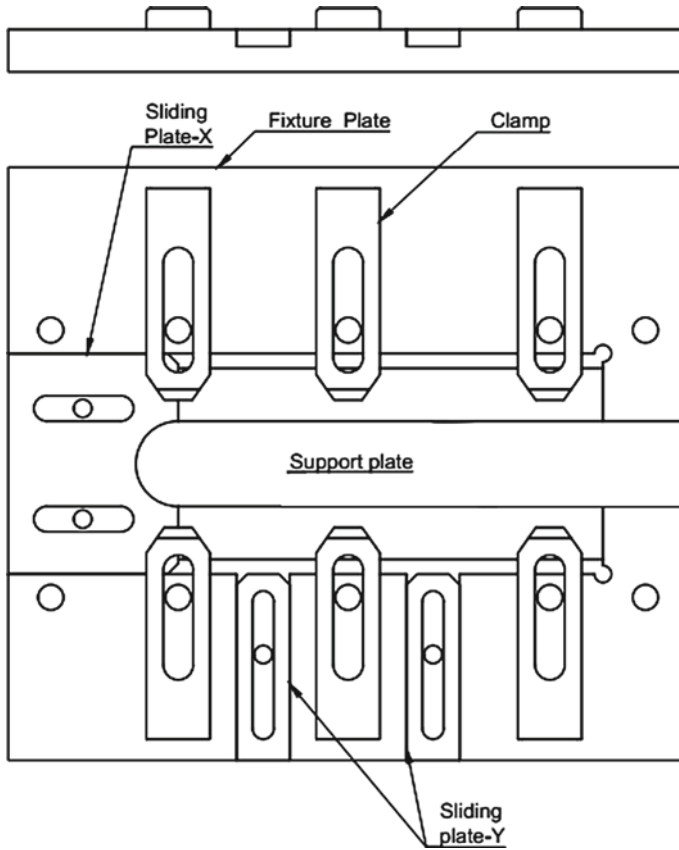


Fig. 9.5 The complete diagram of the fixture and its parts

screws of size $M10 \times 1.25$ are used. Table 9.1 shows the bill of material of designed and fabricated FSW/P fixture.

Heat Treatment of the Fixture Plate

Surface hardening is a process that has a sort of techniques like carburizing, nitriding, carbonitriding, and so on through which wear resistance of component is improved without affecting the ductility of an interior part that gives toughness [18]. The combination of surface hardness for wear resistance and toughness to internal part for impact resistance is useful in applications like gear teeth, cam, shaft, bearing, tools, dies, and automotive clutch plates. The material used for manufacturing fixture is medium carbon steel (C45 steel). It is also designated according to ASTM A29 grades AISI 1045 steel. The chemical composition and material properties are shown

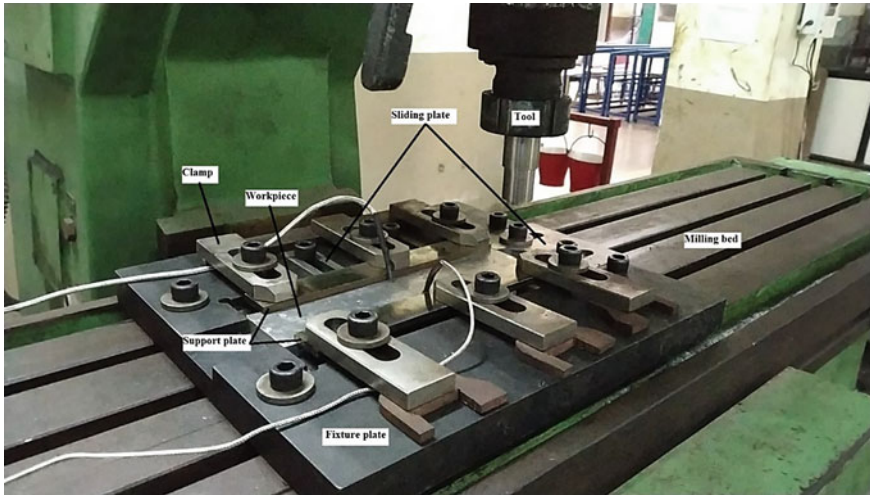


Fig. 9.6 Final fabricated fixture installed on the vertical milling machine bed

Table 9.1 Bill of material

Item No.	Parts	Size (mm)	Material	Quantity
1	Workpiece	200 × 100 × 8	Aluminum alloy	1
2	Fixture/baseplate	320 × 280 × 22	C45 (surface hardened)	1
3	Sliding plate (X direction)	104 × 80 × 8	C45	1
4	Sliding plate (Y direction)	100 × 30 × 10	C45	2
5	Support plate	200 × 25 × 5	C45	2
6	Allen screw	M12 × 1.25	Carbon steel	10
7	Allen screw	M10 × 1.25	Carbon steel	4
8	T-slot nut	–	C45	10

in Tables 9.2 and 9.3, respectively. Its hardness increased by heating it in the furnace between 820 and 950 °C with coke (at austenite with its high solubility of carbon) hold until temperature is uniform throughout the section. So, at this temperature, carbon diffused into the surface and provided a hardness of more than 55 HRC. Thus, this method improves the resistance to surface indentation, fatigue, and wear. Figure 9.6 shows the fixture plate appears black after surface hardening due to carbon diffusion during the hardening process.

Table 9.2 Chemical composition of C45 steel

Element	C	Fe	Mn	P	S
Content (wt %)	0.42–0.50	98.51–98.98	0.60–0.90	≤0.040	≤0.050

Table 9.3 Physical and mechanical properties

Properties	Density	Young's modulus	Poisson's ratio	Yield strength	Ultimate tensile strength
Values	7.87 g/cc	200 GPa	0.33	310 MPa	565 MPa

Testing of Fixture

Finite Element Analysis (FEA) of the Fixture Plate

The mechanism of force action in FSW/P is similar to that of face milling cutting operation. For FEA under static conditions, three maximum forces, such as axial force, transverse/processing force, and torque force generated during the plunging stage are considered. The boundary conditions applied are similar to actual situations. During FSP, the fixture/base plate is fixed to the milling machine bed with a T-slot nut and Allen screws. Therefore, the boundary conditions for the fixture plate is kept fixed in all three directions. All interfaces between the workpiece and fixture plate are kept in sliding contact. The vertical upward movement of a workpiece is restricted due to the clamping device. The results are calculated based on the assumption of linear response to the stress.

Steps of FEA analysis. Following are the steps for the FEA of designed and developed FSW/P fixture:

1. Selection of “Study static stress” from various simulation applications.
2. Selection of fixture material (i.e., AISI 1045) and workpiece material (i.e., AA 6061).
3. Meshing is the most crucial part of the simulation process, where intricate geometries are segregated into simple elements that can be used as discrete local approximations of the larger component. The meshing influences the accuracy, convergence, and speed of the simulation. The smaller the mesh size, the higher the accuracy, but it increases the time to solve. The mesh element type used is a solid tetrahedral with 24,750 elements with 41,802 nodes (see Fig. 9.7).
4. Apply boundary conditions for the FSP fixture model.
5. Application of loads such as vertically downward force due to the FSP tool, torque force generated due to the rotating moment of a tool and horizontal force due to processing speed. Based on the Trimble et al. [4] observation of force measurement during friction stir welding Al alloy, the maximum forces during the plunging stage were taken into consideration for stress analysis. The considered load for static stress analysis is 20 kN for a vertically downward force, 2 kN for a horizontal force, and 60 Nm for a torque force.

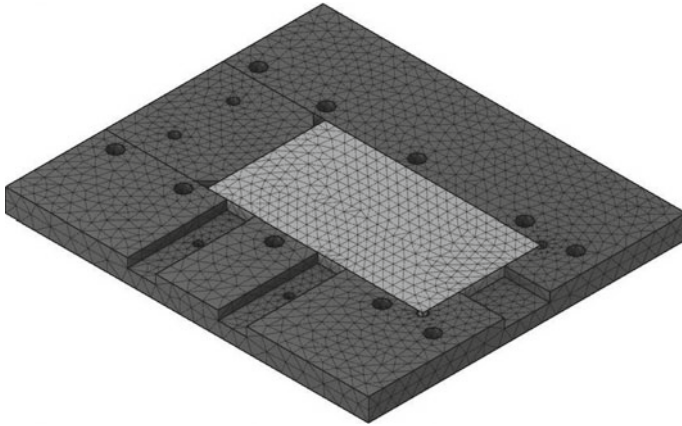


Fig. 9.7 The meshing of the fixture model

- 6. Solving the fixture model once it verifies the feasibility of the proposed model and its constraint.

FEA result. Von-Mises stress plot obtained after solving the fixture model, as shown in Fig. 9.8. When all three combined loads applied, the maximum Von-Mises stress was 7.248 MPa, which is lower than the yield strength of fixture material. Therefore, no failure is possible as the factor of safety is 15. The list of the result generated in terms of factor of safety, stress, displacement, reaction force, strain, and the contact pressure is shown in Table 9.4.

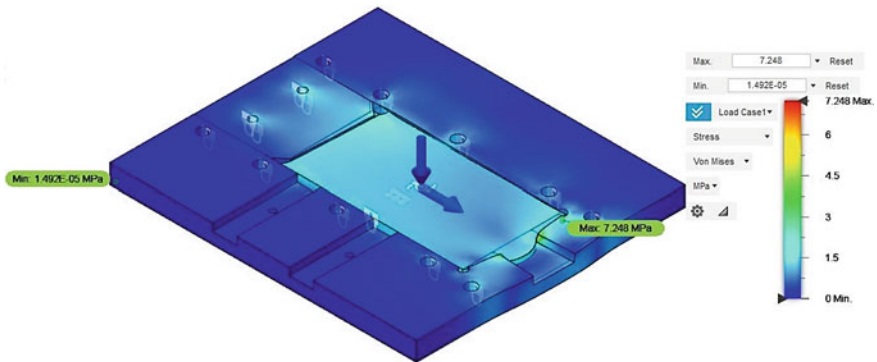


Fig. 9.8 Fixture model stress analysis

Table 9.4 Result summary with its minimum and maximum values

Name	Minimum	Maximum
<i>Safety factor</i>		
Safety factor	15	15
<i>Stress</i>		
Von Mises	1.492×10^{-05} MPa	7.248 MPa
<i>Displacement</i>		
Total	0 mm	0.001298 mm
<i>Reaction force</i>		
Total	0 N	45.69 N
<i>Strain</i>		
Equivalent	1.108×10^{-10}	6.23×10^{-05}
<i>Contact pressure</i>		
Total	0 MPa	8.044 MPa

Experimentation Through a Fixture

The fabricated FSW/P fixture is also experimentally validated on a traditional vertical milling machine of M/s. Batliboi company model number BFV-5 (see Fig. 9.6). The sample prepared with the help of the fixture has no defect, smooth surface finish, and have no distortion. During FSP, lesser vibration and no lateral and longitudinal displacement of the workpiece is observed as it is firmly held by fixture and clamping devices (see Fig. 9.9).



Fig. 9.9 Experiment setup

Conclusion

In this paper, the FSW/P fixture is designed and analyzed with the help of Autodesk Fusion 360 (Education License). Further, the robustness of the fixture and clamping device is validated with experimentation. From the result static stress analysis, it can be perceived that maximum stress generated is 7.248 MPa, the maximum displacement is 0.001298 mm, and the maximum reaction force is 45.69 N, which is within an acceptable tolerance. The stress concentration factor is observed negligibly on the fixture model, which ensures the rigidity of the fixture. The higher factor of safety imparts high failure strength, which is able to bear a higher load without failure. It is also experimentally validated that negligible vibration and no displacement in any direction is observed during FSP. The samples prepared were free from defects, and thus, the proposed fixture design is suitable for the FSW/P process.

References

1. Mishra R, Ma Z, Charit I (2003) Friction stir processing: a novel technique for fabrication of surface composite. *Mater Sci Eng A* 341:307–310
2. Hussein SA, Izamshah R (2015) Generated forces and heat during the critical stages of friction stir welding and processing. *J Mech Sci Technol* 29:8–13
3. Rai R, De A, Bhadeshia HKDH, DebRoy T (2011) Review: friction stir welding tools. *Sci Technol Weld Joining* 16:325–342
4. Trimble D, Monaghan J, O'Donnell GE (2012) Force generation during friction stir welding of AA2024-T3. *CIRP Ann-Manuf Technol* 61:9–12
5. Atharifar H, Lin D, Kovacevic R (2009) Numerical and experimental investigations on the loads carried by the tool during friction stir welding. *J Mater Eng Perform* 18:339–350
6. Sharma A, Sharma VM, Sahoo B, Pal SK, Paul J (2019) Effect of multiple micro channel reinforcement filling strategy on Al6061-graphene nanocomposite fabricated through friction stir processing. *J Manuf Processes* 37:53–70
7. Yang K, Li W, Xu Y, Yang X (2019) Using friction stir processing to augment corrosion resistance of cold sprayed AA2024/Al₂O₃ composite coatings. *J Alloy Compd* 774:1223–1232
8. Dinaharan I, Sathiskumar R, Murugan N (2016) Effect of ceramic particulate type on microstructure and properties of copper matrix composites synthesized by friction stir processing. *J Mater Res Technol* 5:302–316
9. Elangovan K, Balasubramanian V (2008) Influences of tool pin profile and tool shoulder diameter on the formation of friction stir processing zone in AA6061 aluminium alloy. *Mater Des* 29:362–373
10. Salekrostam R, Besharati Givi MK, Asadi P, Bhemmat P (2010) Influence of friction stir processing parameters on the fabrication of SiC/316L surface composite. *Defect Diffus For* 297–301:221–226
11. Alidokht SA, Soleymani S, Assadi H (2011) Microstructure and tribological performance of an aluminium alloy based hybrid composite produced by friction stir processing. *Mater Des* 32:2727–2733
12. Barmouz M, Besharati Givi MK, Seyfi J (2011) On the role of processing parameters in producing Cu/SiC metal matrix composites via friction stir processing: investigating microstructure, microhardness, wear and tensile behavior. *Mater Charact* 62:108–117
13. Parida B, Vishwakarma SD, Pal S (2015) Design and development of fixture and force measuring system for friction stir welding process using strain gauges. *J Mech Sci Technol* 29:739–749

14. Richter-Trummer V, Suzano E, Beltrão M, Roos A, Dos Santos JF, De Castro PMST (2012) Influence of the FSW clamping force on the final distortion and residual stress field. *Mater Sci Eng A* 538:81–88
15. Ramnath BV, Elanchezian C, Rajesh S, Prakash SJ, Kumar BM, Rajeshkannan K (2018) Design and development of milling fixture for friction stir welding. *Mater Today Proc* 5:1832–1838
16. Ahmed S, Saha P (2018) Development and testing of fixtures for friction stir welding of thin aluminium sheets. *J Mater Process Technol* 252:242–248
17. Fratini L, Micari F, Buffa G, Ruisi VF (2010) A new fixture for FSW processes of titanium alloys. *CIRP Ann-Manuf Technol* 59:271–274
18. Dossett J, Totten GE (2013) Introduction to surface hardening of steels. *ASM Handbook* 4:389–398

Chapter 10

Design of Gripper and Selection of Robotic Arm for Automation of a Pick and Place Process



Vijesh Shah, Nandkumar Gilke, Vilas Dhore, Chandrashekhar Phutane, and Bhavisha Kondhol

Introduction

The process of enclosing a product to preserve it for storage, sale, distribution, and use is packaging. The term packaging also means designing, producing, and evaluating of packages. In other words, packaging can also be described as the system of pre-processing of goods for transportation, storage, sales, and the end consumer. The packaging is used to contain, protect, and preserve the product to be transported, informs, and sold [1]. The packaging industry valued for 3.65 billion USD is estimated to be valued at 5.96 billion USD by 2024 with the compound annual growth rate (CAGR) of 8.52%, within the forecast period of 2019–2024 [2]. Packaging in the pharmaceutical and cosmetic industry is one of the highly regulated processes with only minor variations in detail from region to region. Its main objectives are to protect products from climatic or biological reactions, chemical or physical contamination, and at the same time also being economical. It must also

V. Shah (✉) · N. Gilke · V. Dhore
Department of Mechanical Engineering, K.J.Somaiya College of Engineering Vidyavihar,
Mumbai 400077, India
e-mail: vijesh.shah@somaiya.edu

N. Gilke
e-mail: nandkumargilke@somaiya.edu

V. Dhore
e-mail: vilasdhore@somaiya.edu

C. Phutane · B. Kondhol
Design Engineer, Elmach Packaging India Pvt. Ltd., Bhiwandi 421302, India
e-mail: cpphutane@gmail.com

B. Kondhol
e-mail: bkondhol080394@gmail.com

provide stability to the product throughout its shelf life [3]. Some common factors that are included along packaging in the pharmaceutical and cosmetic industry are the safety of the consumer, to assure the production efficiency through shelf life, avoidance of possibility of packaging products into the product itself, restrain of contamination to a product via environmental factors like oxygen, heat, moisture, and microbial contamination and maintain sterility [4, 5].

The packaging is often involved in dispense, apply, and use of the product. The packaging industry is a continuously evolving sector with a gradual increase in demand for high-speed packaging for various materials. These increasing demands can be achieved by modifying the system or machine with the incorporation of an industrial robot in the line of operation. The integration of an industrial robot and industry can be broadly divided into three categories, viz., product handling, assembly, and finishing processes. Term material handling refers to the conveying of material, in components, or as a whole product form, from one place to another. Assembly includes the combining of two or more components into one component or part, or a whole congregated product. These operations typically include a series of pick and place operations along the processing line [6]. The trend of automation is still moving toward the path of assembly of components converting tedious manual work into automation. Compared to manual assembly, automated assembly especially leads to higher quality production and stabilization. Modified versions of the technology are also expanding into the manual work areas of the assembly. Compared to manual assembly, automated assembly lines lead to better performance and stability [7]. A system for the automatic inspection of foreign matter into the product and custom-built hardware for the transportation of the product, agitation of particles, capturing of the image, and its analysis is designed by [8]. The machine vision guides the robot to see the location and direction of the angle for each product, while at the same time inspecting the material to prevent damage of the product to be handled. The machine vision from the camera is faster than human observation, and the robot selects faster than human hands. The application of the vision-guided robots in the food packaging industry is reviewed by [9]. A new system that can grasp multiple products with the help of a designed end effector mounted on the robot to place it precisely inside the package is designed to improve the speed and efficiency of the pre-existing packaging system.

System Design

Selection of Robot

A mechatronic system which can assist or replace human operator to carry out a variety of physical tasks is considered as a robot [10]. In terms of effectiveness, there are three main benefits of using a robot. The first is the success rate, repetition,

accuracy, and speed of the process. Second is that a robot can work in harsh environmental conditions without breakdown and with the same efficiency. Finally, IR is very flexible. They can be customized to a variety of products in many processes [11]. To achieve superior quality and improved productivity the industries are moving from the current state of automation to robotization. The speed of the picking and placing of the parts is increased along with the production rates with the help of robotic automation [12]. The operation of pick and place can be performed with the same flexibility by the robot system as a human operator due to modular design [13]. Industrial pick and place robots are classified into three different categories majorly Cartesian, Delta, and SCARA. The problem of finding a robot configuration for multigrasp assembly is solved with the help of an algorithm by [14].

The newly designed and developed prototype can achieve and sustain very high speed and acceleration, and to achieve smooth and rigorous behavior throughout the work envelope and in every direction [15]. Table 10.1 shows the comparison between different types of robots and their perks. In our application, the most suited one is SCARA as we have to mount our robot on the pre-existing machine, and SCARA provides multiple mounting options. Also, it is fairly accurate which is good as we

Table 10.1 Comparison of different robots

SCARA	Cartesian	Delta
SCARA possesses a higher accuracy than Delta that is of up to 10 microns or 0.01 mm	The basis for the accuracy of the Cartesian robot is linear actuators. The main determinant for the accuracy is the type of actuators used and the drive mechanism. The mathematics involved in the kinematics is simpler since the control system has to move only in XYZ direction. So Cartesian robots are excellent for accuracy	SCARA robots are more accurate than Delta
The SCARA may be suitable for mounting or controlling power, but has a separate envelope and the speed range is not so high	For some applications with substantial loads or repetitions, a Cartesian robot may be the ideal solution	Delta is not good with force requirements like insertion applications. It is best suited for the conveyor tracking application
SCARA robot can either be mounted on a ceiling, wall, or floor as per the requirement. In addition, the form factor could interfere when they are placed right over the conveyor. Even though they have cylindrical work envelope still they are not quite around themselves	The mounting of the Cartesian robots is in the fashion of the gantry system as the movement of the robot is in Cartesian coordinates. Although it may be a cheaper solution but the time required to set up and integration is more along with the space requirement	The biggest challenge of Delta robots is that it needs a sturdy overhead structure

Table 10.2 Comparison of different SCARA robot

Property	Dobot	Estun	Make-A
Payload	3 kg	3 kg	3 kg
Range	400 mm	400 mm	400 mm
J1	±130°	±132°	±132°
J2	±131°	±141°	±141°
J3 (mm)	0–150	0–150	0–180
J4	±360°	±360°	±360°
J1	600°/s	600°/s	720°/s
J2	600°/s	600°/s	720°/s
J1 + J2 (mm/s)	6000	6000	7200
J3 (mm/s)	1100	1060	1100
J4	2600°/s	2250°/s	2600°/s
Cycle Time	0.45 s		0.44 s
Comparison	20° less reach at J2 and 30 mm at J3 than Make-A	30 mm less reach at J3 than Make-A	
	Slower by 120°/s at J1 and J2 than Make-A	Slower by 120°/s at J1 and J2, 350°/s at J4 than Make-A	
	1200 mm/s slower at J1 + J2 than Make-A	1200 mm/s slower at J1 + J2, 400 mm/s at J3 than Make-A	

have to place the product into a pre-formed cavity. The flexibility and agility of the SCARA robot are demonstrated by [16].

Thus, from the above comparison Table 10.2, it was easy enough to select the make and model for the SCARA to be used which is Make-A.

The above three figures, Figs. 10.1, 10.2, and 10.3 show the comparison of three different make of SCARA robots in different fields of range speed and payload at different axis.

Fig. 10.1 Angular reach comparison of SCARA

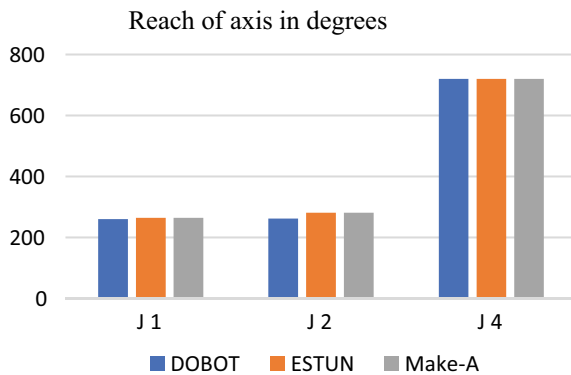


Fig. 10.2 Comparison of speed at base and shoulder of SCARA

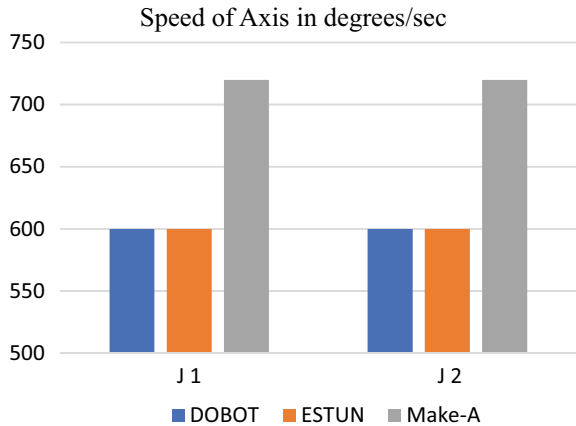
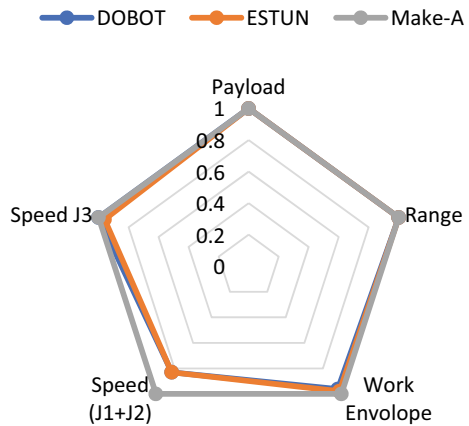


Fig. 10.3 Comparison of parameters of various SCARA



Design of End Effector

A device that can be attached to the wrist of the robot and enabling it to perform a special task is called end effector. The end effector is the part of special-purpose tooling for a robot [17]. To achieve a commercial pick-and-place process, it needs low-cost gripper, high speed, and reliability [18]. MEMS microgripper is used for the effective pick-and-place techniques that integrate both gripping and releasing of micro-objects by [19]. For the designing of the gripper, we have to consider multiple criteria. More grasping contact in the workpiece can be provided with the use of resilient pads in the gripper. The interchangeability of the replaceable pads/cups can also be employed for holding different work part sizes. A wide range of applications can be handled by robotic vacuum grippers and are suitable for picking up irregular as well as products that are made up of a variety of materials smooth as well as porous like cardboard, glass, plastic, and even sheet metal [20]. End effector comprising

combined gripping action by electromagnetic as well as a vacuum that is used to pick the object also rotate along the axis in required orientation is designed and developed by [21].

Different Types of Products to Be Handled

The product to be handled comes in various shapes, curvatures, and materials to strongly hold the product suction cups, or vacuum grippers are selected which can sturdily hold the product by getting wrapped around it up to some extent. Various shapes of the products are displayed in Fig. 10.4a–e. Table 10.3 shows various dimensions, masses, and materials possible to be handled by the designed gripper.

Selection of Components for End Effector

The payload of the selected SCARA is 3 kg; however, the optimum cycle speed is achieved when it is kept under 2 kg according to the details available from various robot manufacturers. Although the maximum payload capacity of a robot may be different, every robot works at the optimum speed for a payload lower than the maximum payload in our case which is 2 kg. Therefore, to achieve this condition a polymeric material with a density almost the one-third of aluminum is selected for the end effector.

Since there is a difference in the position of components at pickup point and placing point, a pneumatic cylinder is required to provide a stroke of 3 mm.

Round-shaped suction cups are selected for the application since it helps to grasp the object coming in any orientation pre-calibrated by the operator. The diameter of the cup has to be selected based on the minimum dimension of the product which is generally a width instead of a length in most of the elongated products.

Vacuum grippers are needed to handle the product; thus, it needs a mounting plate or bar to space it according to the distance between products.

The vacuum generator needs to generate the required amount of vacuum.

Pneumatic fittings need to be selected according to the selected pneumatic components.

A cylinder stopper needs to be designed as a standard pneumatic cylinder is not available in a stroke of 3 mm.

Holding Force Calculation

$$F_{TH} = \frac{w}{\mu} \times (g + a) \times S \dots [17] \quad (10.1)$$

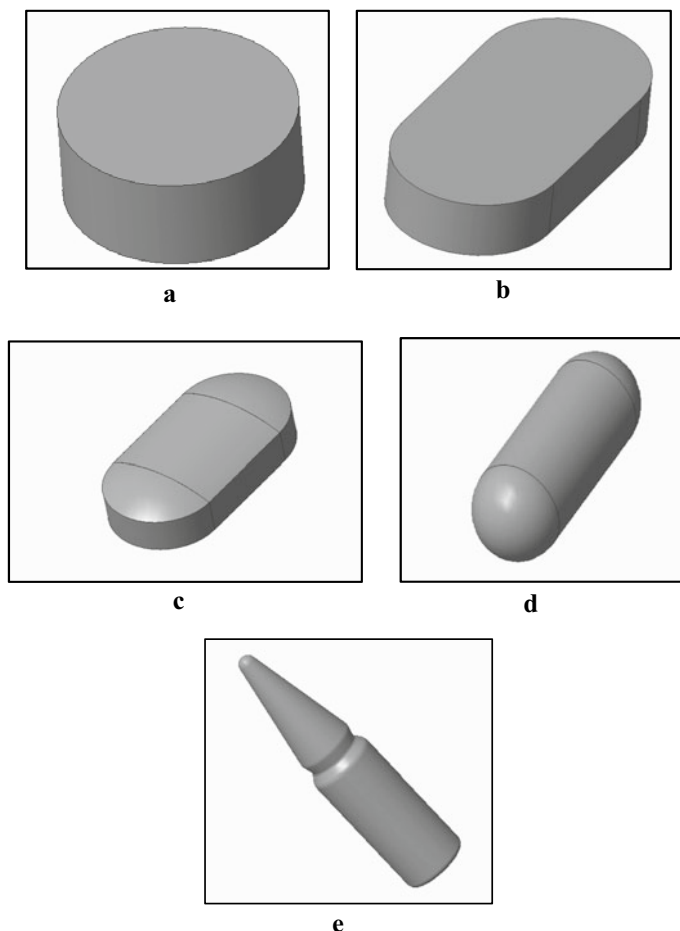


Fig. 10.4 **a** Flat round, **b** Flat elongated, **c** Convex shaped, **d** Cylindrical shaped, **e** Cylindrical container

Table 10.3 Product characteristics

Product	Dimension	Weight	Material
Flat round	$\Phi 10 \text{ mm} \times 7 \text{ mm}$ thickness	0.1–0.5 g	Metal, glass, gelatine, compressed powder in solid form, plastic, color cake (water color), wood, chocolate, non-porous food products, etc.
Flat elongated	$\Phi 10 \text{ mm} \times 9 \text{ mm long} \times$ 6 mm thickness	0.15–0.6 g	
Convex shaped	$\Phi 10 \text{ mm} \times 9 \text{ mm long} \times$ 8 mm thickness	0.15–0.6 g	
Cylindrical shaped	$\Phi 3.5 \text{ mm}—\Phi 7.5 \text{ mm}$ Long 2.6–16.5 mm	0.25–0.4 g	
Cylindrical container	$\Phi 10 \text{ mm}—\Phi 17 \text{ mm Ht}$ 25–48 mm	2–15 g	

F_{TH} = Theoretical holding force [N]

w = Weight [kg]

Weight of the single product = 0.2 g (Since the trials will be performed on the dummy cylindrical-shaped product weighing 0.2 g per piece)

Weight of 40 products = $40 \times 0.2 = 8$ g

g = Acceleration due to gravity [9.81 m/s^2]

a = Acceleration [m/s^2] of the robot

μ = Friction coefficient.

The coefficient of friction between workpiece and suction pad is very important [17].

- Oily surfaces: $\mu = 0.1$
- Moist or wet surfaces: $\mu = 0.2-0.4$
- Glass, stone, plastic (dry): $\mu = 0.5$
- Wood and metal: $\mu = 0.5$
- Rough surface: $\mu = 0.6$
- Sandpaper (dry): $\mu = 0.1-1.0$.

Holding forces: Theoretic holding force always has to be higher than the calculated holding force. To overcome external factors that were not considered during designing recommended safety factor of 2 is considered.

S = Factor of safety.

$$F_{TH} = \left(\frac{8}{1000 \times 0.6} \right) \times (9.81 + 65.45) \times 2$$

$$= 2.006 \text{ N}$$

Volume to Be Vacuumed Per Min

$$\text{Volume in end effector} = \left(\frac{\pi}{4} \right) \times \left(\frac{4}{1000} \right)^2 \times 300 \times 4 = 15.07 \text{ ml} \quad (10.2)$$

$$\text{Volume in tube} = \left(\frac{\pi}{4} \right) \times \left(\frac{4}{1000} \right)^2 \times 2000 = 25.13 \text{ ml}$$

Volume in suction cup = 6.53 ml

Total volume = 46.73 ml

Total volume \times FOS (2) \times no. of cycles = $46.73 \times 2 \times 60 = 5607.6 \text{ ml/min}$

Thus, vacuum generator must generate vacuum at the rate of more than 5.6 l/min.

In the above calculations, 300 represents the total length of the connecting hole to connect each suction cup to provide vacuum through a single generator, 2000

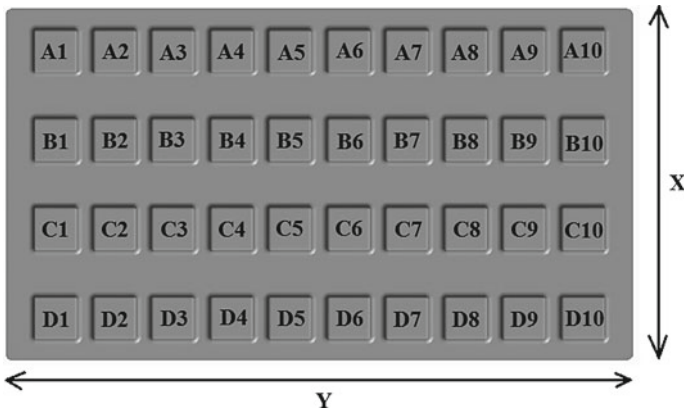


Fig. 10.5 Product placement positioning

represents the length of the connecting tube from the location of the vacuum generator to the gripper, and 4 is the inner diameter of the hole and the tube.

Required Product Placement

The product is required to be placed in a particular array in which a total of 40 products will be picked and placed at the same time, where the horizontal as well as the vertical distance between the products is needed. Figure 10.5 shows the placing positions of all the 40 products.

End Effector

The model consists of all the pneumatic connections; also, the weight is equally distributed and the part is symmetric which is shown in Figs. 10.6 and 10.7. The center of gravity of the end effector is along the shaft axis of the robot. Possible slots are provided to reduce the weight and bring under 2 kg. A pneumatic cylinder is used to provide the stroke to overcome the relative difference in pick-and-place position. The more compact version of the pneumatic cylinder was selected to even further reduce the weight.

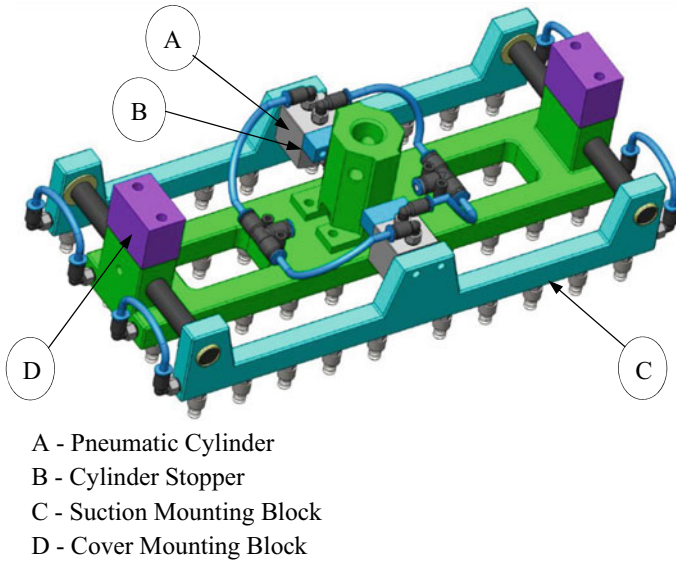


Fig. 10.6 Top view of end effector

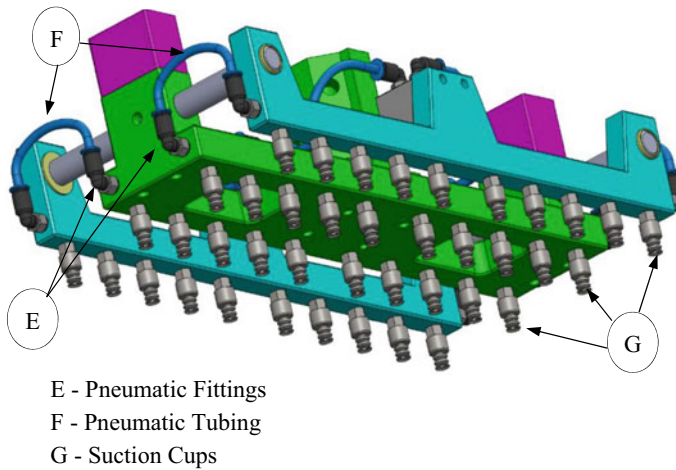


Fig. 10.7 Bottom view of the end effector

Robot Cycle Time Diagram

The timing of the cycle performed by the Make-A SCARA robot is depicted in Fig. 10.8. The time required for the particular functions to be performed is calculated

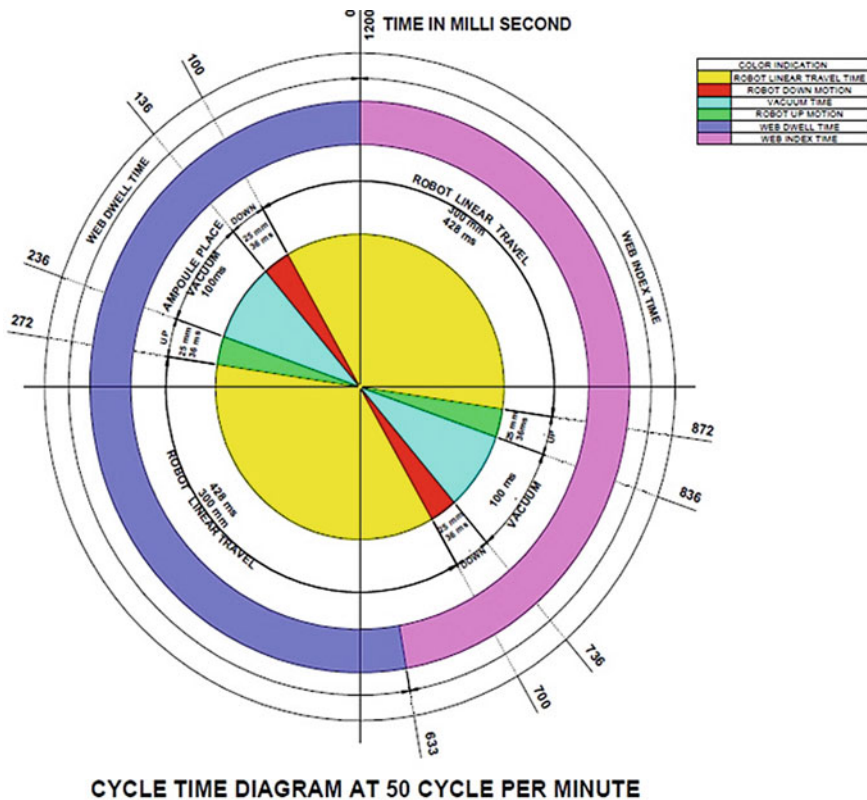


Fig. 10.8 Cycle time diagram of robot

based on the combined speed of the joints of the robot and the functioning time of the pneumatic components.

Results and Conclusions

In this project, the machine component design is one of the important tasks carried out with the help of CAD software, SolidWorks 2019. The software helps in easy iterations and optimization of the design component to reduce the overall development time of components or systems. The design of end effector and product design is carried out with the aid of CAD. End effector with vacuum grippers is designed which is well suited for handling objects efficiently and delicately. This work provides an insight into the various steps considered in the selection of a robot for the task of pick-and-place operation in the packaging industry. The selection is based on the various key factors like mounting options, space utilization, versatility,

speed, work envelope, and cycle time of the robot. As suction cups are available in a variety of sizes, it can be selected according to the dimension of the product. They are perfectly suited for handling of variety of materials like glass, wood, gelatin, and so on, including food compliant materials like chocolates. The integration of a robot in the packaging system helps to increase the speed of the feeding process of the machine with higher reliability and versatility. The current system without the integration of robotics runs at the cycle speed of 30 cycles per minute. With the integration of robotic feeding using the SCARA robot, it is expected to achieve the speed of 50 cycles per minute. The total expected increment in output is by 800 products per minute considering 20 cycles per minute with 40 products per cycle.

References

1. Soroka (2002) Fundamentals of packaging technology. Institute of Packaging Professionals. ISBN 1-930268-25-4
2. <https://www.marketsandmarkets.com/Market-Reports/bag-in-box-market-147350286.html>: 8th October 7:58 pm
3. Subramanian K (2017) Impact of packaging in self service marketing. *Int J Sci Prog Res (IJSPPR)* 93:60–66
4. Kunal M, Akhilesh D, Kumar S (2012) Recent trends in pharmaceutical packaging: a review. *Int J Pharm Chem Sci* 1(3):1282–1292
5. Yam KL (ed) (2010) *The Wiley encyclopedia of packaging technology*. Wiley, pp 205–216. ISBN 978-0-470-08704-6. <https://doi.org/10.1002/9780470541395>
6. Bader Farah, Rahimifard S (2020) A methodology for the selection of industrial robots in food handling. *Innov Food Sci & Emerg Technol* 64:102379. <https://doi.org/10.1016/j.ifset.2020.102379>
7. Vagaš Marek (2016) The assembly of electric socket at automated workplace with SCARA robot. *Appl Mech Mater* 844:25–30. <https://doi.org/10.4028/www.scientific.net/amm.844.25>
8. Ge et al (2017) A system for automated detection of Ampoule injection impurities. *IEEE Trans Autom Sci Eng* 14(2):1119–1128. <https://doi.org/10.1109/TASE.2015.2490061>
9. Connolly C (2007) ABB high-speed picking robots establish themselves in food packaging. *Ind Robot* 34(4):281–284. <https://doi.org/10.1108/01439910710749591>
10. Wang L, Nee AYC (2009) Collaborative design and planning for digital manufacturing. <https://doi.org/10.1007/978-1-84882-287-0>, <https://doi.org/10.1007/978-1-84882-287-0>
11. Bader F, Rahimifard S (2018) Challenges for industrial robot applications in food manufacturing. In: *Proceedings ISCSIC'18*, pp 1–8. ACM Digital Library. <https://doi.org/10.1145/3284557.3284723>
12. Sentil Kumar S (2015) Design of pick and place robot. *Int J Adv Res Electr, Electron Instr Eng* 4(6)
13. Brantmark H, Hemmingson E (2001) FlexPicker with PickMaster revolutionizes picking operations. *Ind Robot* 28(5):414–420. <https://doi.org/10.1108/EUM000000005844>
14. Dogar M, Spielberg A, Baker S et al (2019) Multi-robot grasp planning for sequential assembly operations. *Autonom Robot* 43:649–664. <https://doi.org/10.1007/s10514-018-9748-z>
15. Nabat V, de la O. Rodriguez M et al (2005) Very high-speed parallel robot for pick-and-place. In: *IEEE/RSJ international conference on intelligent robots and systems*, Edmonton, Alta., pp 553–558. <https://doi.org/10.1109/IROS.2005.1545143>
16. Nagehauthuri A, Kuruganty S, Shaur A (2002), Introduction of mechatronics concepts in a robotics course using an Industrial SCARA robot equipped with a vision sensor. *Mechatronics* 12:183–193. [https://doi.org/10.1016/S0957-4158\(01\)00059-9](https://doi.org/10.1016/S0957-4158(01)00059-9)

17. Sharma A (2015) Design study of end effector. *Int J Eng Adv Technol*, 4(3). ISSN: 2249-8958
18. Blanes C, Mellado M, Ortiz C, Valera A (2011) Technologies for robot grippers in pick and place operations for fresh fruits and vegetables. *Span J Agric Res* 9:1130–1141. <https://doi.org/10.5424/sjar/20110904-501-10>
19. Zhang Y, Chen BK, Liu X, Sun Y (2010) Autonomous robotic pick-and-place of micro-objects. *IEEE Trans Robotics* 26(1):200–207. <https://doi.org/10.1109/TRO.2009.2034831>
20. <https://robotiq.com/products/vacuum-grippers-> 4th December 2019 6:15 pm
21. Gore K, Gray C (1996) Pick-and-place tool for vacuum and magnetic coupling. United States Patent USOO5865487A 23

Chapter 11

Utilization of Stone Industry Waste as Filler for Sustainable Development of Aluminum Alloy Composites: A Thermo-Mechanical and Mechanical Characterizations



Vikash Gautam, Amar Patnaik, and I. K. Bhat

Introduction

Rapid development of industries and urbanization of place as well as rise in the living standards of people is the root cause for the arise of a major problem of solid wastes. Industrialization is the necessity of developing countries to boost up nation's economy. Simultaneously, it is the root cause for the generation of a huge quantity of waste that led toward serious problem related to health or environmental pollution. Therefore, wastes are seemed to be a by-product of growth in industries. The waste products increase with the increasing demand for raw materials in industries and conventional resurfaces are diminishing day by day. Wastes occupy the land distorting its fertility, and simultaneously increase the cost of waste disposal. The developing countries like India need to make effort for minimization of these solid wastes and simultaneously recycle of the waste or utilization of waste in different areas. At the same time, the need for sustainable development program has all amplified the need to reuse the materials that were once regarded as wastes. Over recent decades, innovative research works have been carried out to explore all possible

V. Gautam (✉)

Mechanical Engineering Department, Swami Keshvanand Institute of Technology, Jaipur 302025, India

e-mail: Gautam.mnitj@gmail.com

A. Patnaik

Mechanical Engineering Department, Malaviya National Institute of Technology, Jaipur 302017, India

I. K. Bhat

Vice Chancellor at Manav, Rachna University, Faridabad, Haryana 121004, India

methods for utilization of waste materials in wide range. Till now wastes generated through industrialization and urbanization have been used in many places as alternative aggregates in embankment, road, pavement, and building construction.

Various solid wastes are generated by the industries such as copper slag, alumina, fly ash, cement by pass dust (CBPD), cement klin dust, and rice husk. Copper slag is a by-product of copper ores obtained during the matte smelting and refining of copper [1, 2]. Sehi et al. [3] reported that copper slag is used in the manufacturing of cement and concrete, and Satpathy et al. [4] use copper slag as filler material in glass-epoxy composites for improvement in wear resistance properties. Similarly, red mud is the by-product of alumina obtained from bauxite by the Bayer's process. Red mud is used as a partial substitute of clay in ceramics products like bricks, tiles, and so on; it is also used in soils for treatment of iron-deficient soils [5–7]. Geetha et al. [8] reported the synthesis of red mud reinforced Al356 alloyed composites. Similarly, Mahata et al. [9] confirmed the fabrication of aluminum titanate–mullite composite from red mud rich in titanium. Fly ash is generated by coal combustion, and is composed of fine particles that are driven out of the boiler with the flue gases. Fly ash has been used as spherical filler for the production of lightweight high-strength concrete as well as fly ash reinforced metal or polymer composites [10, 11]. Rice milling generates a by-product know as husk. Alaneme et al. [12] reported the synthesis of rice husk ash reinforced Al–Si alloy composites and observed the effect of reinforcement on mechanical properties. Similarly, Narasaraju et al. [13] confirmed the synthesis of rice husk and fly ash reinforced hybrid Al–Si alloy composites and its mechanical properties. Again Debnath et al. [14] reported the adhesive and wear behavior of rice-husk-filled glass/epoxy composites.

Stone sector industries produce a huge amount of slurry by cutting or polishing of marble and granite slab. The waste marble slurry is converted into low-grade gypsum which is used in cement and fertilizer industries. The waste granite slurry is used in construction industries. Granite slurry or dry powder is a mixture of different oxides (SiO₂, Al₂O₃, etc.), and its chemical composition is presented in Table 11.1 [15]. Granite slurry is widely used in construction industries as a substitute of cement [16]. Granite powder has significant mechanical properties reported in Table 11.2 [15]. Kukshal et al. [17] evaluated the mechanical and fracture behavior of SiC-reinforced A356 alloy composites fabricated through liquid stir casting technique. Mechanical characterization results show that the hardness, tensile strength, and flexural strength

Table 11.1 Chemical composition of aluminum alloy 5083 [15]

Element	Al	Si	Fe	Cu	Mn	Mg	Zn	Ti	Cr
wt%	Balance	0.4	0.4	0.1	0.4–1	4.0–4.9	0.25	0.15	0.25

Table 11.2 Chemical composition of granite powder [15]

Element	SiO ₂	Al ₂ O ₃	K ₂ O	Na ₂ O	CaO	FeO	Fe ₂ O ₃	MgO	TiO ₂	MnO
wt%	72.04	14.42	4.12	3.69	1.82	1.68	1.22	0.71	0.30	0.05

of A356 alloy are enhanced by the addition of micro SiC particulates. However, the stress intensity factor was not of much effect with increment in crack length irrespective of particulate content. Similarly, in another study with alumina particles with the same alloy composite, the experimental result shows that the increment in alumina content in A356 alloy significantly affects the tensile strength, flexural strength, fracture strength, and Young's modulus [18]. Again, Gangwar et al. [19] examined the effect of TiO₂ particulate on mechanical properties of A380 alloy. The mechanical characterization results depicted that increment of titania particulates in A380 alloy enhanced the hardness and tensile strength, whereas the flexural strength is shown in reverse trend. Okayasu et al. [20] examined the effect of silicon nitride on mechanical properties of aluminum alloy. They reported that an increment of silicon nitride particulates in aluminum alloys degrades the bending strength of alloyed composites. Similar observation was also reported by Anilkumar et al. [21]. They showed the effect of fly ash content and particle size on mechanical properties of aluminum alloy. The experimental results show that the increment in fly ash particles into aluminum alloy enhanced compression strength, flexural strength, tensile strength, and hardness. On the other side, increment in fly ash particle size shows decrement in compression strength, tensile strength, flexural strength, and hardness of aluminum alloy. These composites materials were used in different fields, such as automobile, wind turbine, and structural building construction.

The present research work is focused on the gainful utilization of stone industry waste as filler. The chemical composition of granite powder shows that it is a mixture of different hard abrasive particles, such as alumina, silica, and iron oxides. These hard ceramic particles impart good strength and low thermal expansion coefficient at high temperature. A series of granite-reinforced aluminum alloy composites is fabricated through liquid stir casting technique. In composite series the aluminum alloy 5083 is mixed with different weight fractions (0, 2, 4, and 6 wt% granite particulate powder) of granite powder. Thereafter, physical, mechanical, fracture, and thermo-mechanical properties are determined for granite powder reinforced aluminum alloy composites.

Materials and Methods

In the present research work, we used aluminum alloy 5083 as matrix material and waste granite particulate powder as reinforcement. The mechanical properties and chemical composites of granite powder are presented in Tables 11.1 and 11.2 [15]. The designed formulations are fabricated using high-temperature vacuum casting machine (Fig. 11.1). A sequence of activities performed for fabrication are listed as follows:

1. The graphite crucible is preheated (about 200 °C) first to prevent oxidation of base material (i.e. aluminum alloy) and its easy melting.



Fig. 11.1 High-temperature vacuum casting machine and cast iron mold

2. Thereafter pieces of base material are put inside the crucible. Further, the crucible is heated till 650 °C. This melts the base material.
3. The reinforcing phase (i.e. granite powder) is added to the molten base alloy slowly and a mechanical stirrer at 400 rpm is used to mix the ingredients at least for 5 min. To ensure proper wettability between ingredients 1 wt% magnesium powder is added to the mixture. This step continues for another 10 min. Thus, homogeneity in the mixture is ensured.
4. Now plunger is opened so that the molten metal is automatically poured into the molds (made of rectangular stainless steel) for solidification. The mold is kept in the room for around 20 min so as to achieve proper curing.
5. When the room temperature of casting is obtained, the specimen samples are prepared as per the characterization or testing methods with the help of diamond cutter.

Characterization Methods

In physical characterization the effect of reinforcement on density and void content is evaluated. Theoretical density is calculated by Agarwal and Broutman [22] who proposed formula for experimental density by water dispersion principle. Void content is difference in ratio of theoretical and experimental. In mechanical characterization flexural, hardness, impact, and fracture tests were carried out.

Flexural strength is measured according to ASTM standard E290 using the universal testing machine (UTM) provided by Aimil Ltd., India. ASTM E290 standard configures that the cross-head speed should be maintained 1 mm/min during the test. The span length is taken as 40 mm during that test with sample dimension of $60 \times 10 \times 10 \text{ mm}^3$, respectively. Micro-hardness test is carried out using Vicker's hardness tester according to ASTM standard E-9.

ASTM E-23 standard was used to evaluate the impact strength using impact tester. The test specimen size as per the standard is $64 \times 12.7 \times 3.2 \text{ mm}^3$ with depth of notch 10.2 mm. Thermo-mechanical properties were carried out using dynamic mechanical analyzer provided by Perkin Elmer-8000. The test was conducted in the temperature range of 30–250 °C at constant frequency (1 Hz) under three-point bending configuration. A roller supported load point applied a static force of 1 N uniformly on the middle of material and to inhibit friction effects. The sample size for dynamic mechanical analysis test is $27.5 \times 10 \times 1.5 \text{ mm}^3$. The span length was kept 25 mm during the three-point bending test.

ASTM E-399 is used to evaluate stress intensity factor using universal testing machine provided by Aimil Ltd., India. Fracture test is conducted in mode-I condition with different crack lengths. These crack lengths were prepared in the middle of specimen using wire electrical discharge machine. After test, breaking load and stress intensity factor is determined using Eqs. 11.1 and 11.2 for different crack lengths samples.

$$K1 = \frac{P}{B\sqrt{W}}\gamma(\beta) \quad (11.1)$$

$$\gamma(\beta) = \frac{\sqrt{2} \tan \frac{\pi a}{2W}}{\cos \frac{\pi a}{2W}} \left[0.75 + 2.02 \left(\frac{a}{W} \right) + 0.37 \left(1 - \sin \frac{\pi a}{3W} \right)^3 \right] \quad (11.2)$$

whereas K is the stress intensity factor, P is maximum load (stress), B is thickness of specimen, W is width of specimen and a is crack length. $\gamma(\beta)$ = function of crack length and specimen width.

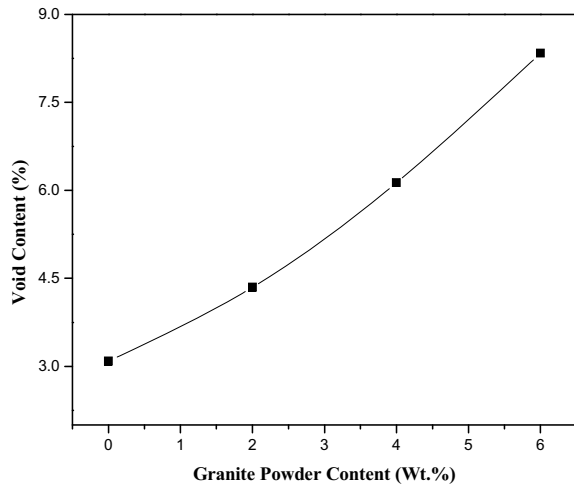
Results and Discussion

Effect of Granite Reinforcement on Density and Void Content

The physical and mechanical properties of a particulate-reinforced metal alloyed composites were dependent on the weight ratio of matrix and reinforcement materials. These properties were strongly affected by proper distribution of reinforcement material in composites and interface bonding between matrix and reinforcement materials. The void plays a vital role to examine the mechanical properties of a composite. The voids act as stress concentration point which leads toward early deformation under

Table 11.3 Theoretical/experiment density and void content with composites designation

Designations	Measured density (g/cc)	Theoretical density (g/cc)	Voids content (%)
5083 GD-0	2.12	2.18	2.75
5083 GD-2	2.23	2.32	3.87
5083 GD-4	2.35	2.48	5.24
5083 GD-6	2.45	2.62	6.49

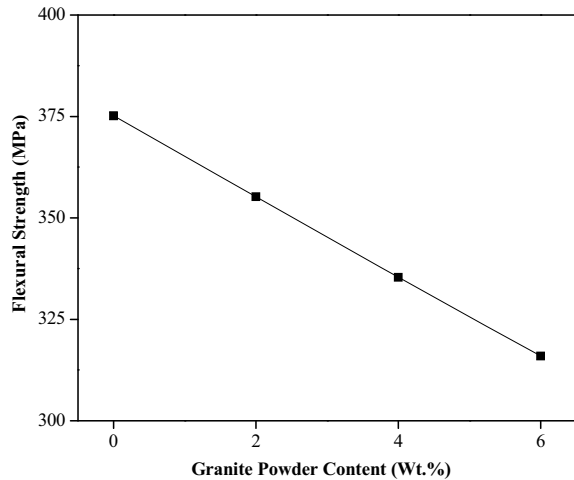
Fig. 11.2 Effect of granite powder reinforcement on void content of composites

the loading condition. The knowledge of void content was desirable for estimation of the quality of the composites. It was understandable that a good composite should have fewer voids. Table 11.3 shows the theoretical and experimental density with void content of granite powder reinforced aluminum metal alloy composites. It was observed from Fig. 11.2 that void content was increased with the addition of granite powder in alloy matrix material. The possible reason might be attributed to the fact that lower density may be attributed to insufficient bonding at the interface of matrix and ceramic particulates that left voids. The agglomeration of particulates while solidifying may have created intra-particulate voids because of insufficient bonding with matrix material. The possible error may be the fabrication methodology which resulted in voids contents [23].

Effect of Granite Reinforcement on Flexural Strength

Flexural strength of granite powder filled 5083 aluminum alloy composites is shown in Fig. 11.3. From Fig. 11.3 it was clearly observed that incorporation of granite powder into base matrix led to decrement in flexural strength of composites and the

Fig. 11.3 Effect of granite powder reinforcement on flexural strength of composites

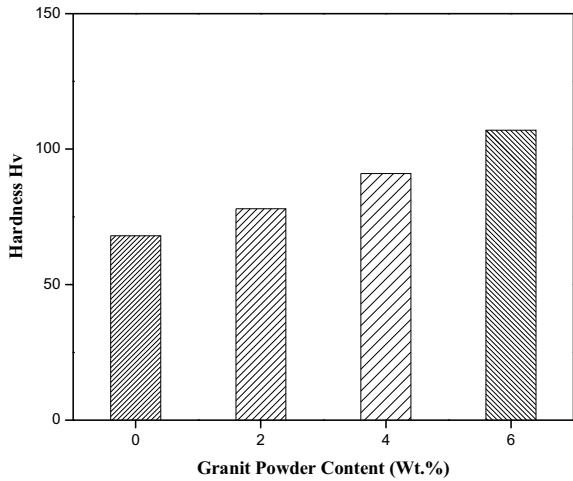


decrement rate was less. The flexural strength of aluminum alloy 5083 decreased up to ~19% after incorporation of granite particulate into base matrix. The maximum flexural strength 375.13 MPa and minimum flexural strength 315.93 MPa were obtained for 0 and 6 wt% granite-reinforced aluminum alloyed composites, respectively. From the analysis it was observed that the flexural strength decreases up to 5% by 2 wt% granite particulate incorporation into base matrix. It further decreased up to 6% on further addition of 2 wt% granite particulate and further decreased up to 6% on further addition of 2 wt% granite particulate into base matrix. The possible reason behind the degradation of flexural strength with incorporation of granite particulate into base matrix may lead to poor strength between the matrix and filler material, hence decreased the effectiveness of stress transfer between them [24–26].

Effect of Granite Reinforcement on Hardness

Figure 11.4 shows the hardness variation for granite powder reinforced aluminum alloy composites. From the graph it was observed that hardness is increased with the incorporation of granite powder into 5083 aluminum alloy. The hardness of pure 5083 aluminum alloy was found as 68 Hv, and after addition of 2 wt% granite powder it increased linearly ~12%. On further addition of 2 wt% granite powder it increased ~14%. On further addition of 2 wt% granite powder increased ~15% and the hardness was found to be 107 Hv. The reason behind the increment in hardness after addition of granite powder into base matrix may be that the granite powder was a mixture of different hard oxides. These hard oxides were dispersed into base matrix homogeneously and that would impart strength to base matrix. Similar results were reported by Park et al. [27] and Hunt et al. [28] for particulate-reinforced metal matrix composites.

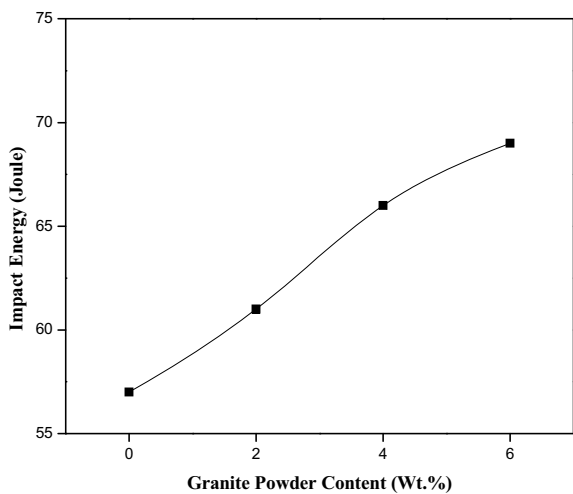
Fig. 11.4 Effect of granite powder reinforcement on hardness of composites



Effect of Granite Reinforcement on Impact Energy

Impact energy variation with reinforcement for 5083 aluminum alloy was presented in Fig. 11.5. From the graph it was observed that addition of granite particles improves the absorption of impact energy for aluminum alloy composites. The amount of energy absorption improved from 57 to 69 joules by incorporation of granite powder into base matrix. The percentage increase in impact energy from 2 to 6 wt% granite powder filled aluminum alloy composites were ~6, ~8, and ~4%, respectively. The possible reason behind the enhancement in impact energy may be the presence of hard abrasive particles in granite particulate which impart energy to soft matrix material.

Fig. 11.5 Effect of granite powder reinforcement on impact strength of composites

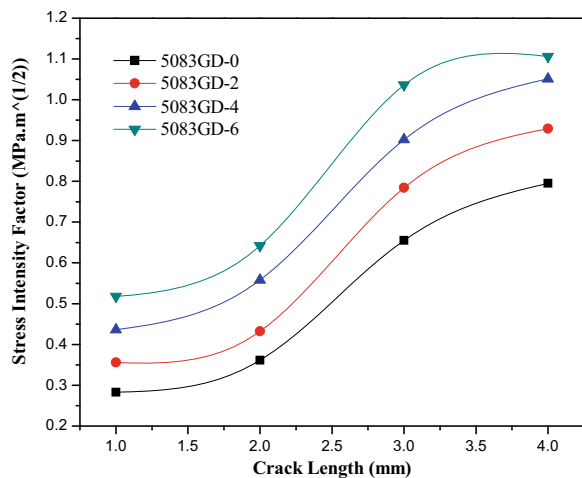


These hard particles were responsible for the increment in the dislocation pile up and there was a restriction to the plastic flow. These results were in accordance with those obtained by Seah et al. [29], Sharma et al. [30], Kataih [31], which reported similar findings for particulate-filled metal matrix composites.

Effect of Granite Reinforcement on Stress Intensity Factor

The values of mode I stress intensity factors (SIFs) are calculated for granite powder filled aluminum alloy composites shown in Fig. 11.6. Figure 11.6 shows the variation of stress intensity factor with increment in granite particulate into 5083 aluminum alloy, as well as with increment in crack length. From the graph it is clearly observed that the stress intensity factor magnitude enhances with increment of granite particulate into 5083 aluminum alloy. The minimum stress intensity magnitude is obtained for 0 wt% granite-filled aluminum alloy composite and maximum stress intensity magnitude is obtained for 6 wt% granite-filled alloy composite. This may attribute to enhancement of interfacial bonding between matrix-particulates. In the literature it was reported that the magnitude of stress intensity factor is affected by several factors such as: the mechanical properties of the matrix and reinforcement, crack length, and loading conditions. The adhesion strength between the matrix and the reinforcement plays a significant role in determining the stress intensity factor at different crack lengths [32–36]. From the graph it was clearly depicted that the stress intensity factor magnitude is directly proportional to crack length. The crack growth behavior is significantly affected by several factors such as matrix material and reinforcement material. The amount of reinforcement material, their size and shape also affect the crack growth behavior. Hence, it was very difficult to conclude a specific cause, specifically particulate-filled alloy composites [32–36].

Fig. 11.6 Effect of granite powder reinforcement on stress intensity factor



Effect of Granite Reinforcement on Thermo-Mechanical Properties

Thermo-mechanical analysis of composites has been carried out to know the visco-elastic response of composites. To check the visco-elastic response the following properties were characterized, such as storage modulus (E'), loss modulus (E''), and damping factor ($\tan \delta$). These properties act as a function of temperature. The variation of E' , E'' , and $\tan \delta$ are shown in Fig. 11.7a–c. Storage modulus (E') is known as the stiffness of visco-elastic material. Storage modulus (E') undergoes a consistent decay with increasing temperature in the range of 29–250 °C irrespective of the compositions. Figure 11.7a shows the variation of storage modulus (E') for granite particulate-reinforced aluminum alloyed composites. Figure 11.7a reveals that the storage modulus decays with increment in temperature, and a maximum decay in storage modulus was observed for 6 wt% granite powder reinforced composites. On the other hand, minimum decay in storage modulus is observed for granite particulate reinforced aluminum alloyed composites. The decay in storage modulus magnitude depends on the incorporation of granite powder particle as particle incorporated into base matrix enhanced stiffness of composites. The increase in E' in such cases may be ascribed to thermally induced phase transformations, leading to hardening of the composites. Similar observations are reported by Patnaik et al. [37] and Zang et al. [38] for particulate-reinforced metal alloy composites.

The loss modulus for granite particulate powder reinforced aluminum alloyed composites is shown in Fig. 11.7b. The graph reveals that with the increase in temperature, loss modulus magnitude is enhanced in the order of 6 wt% granite powder >4 wt% granite powder >2 wt% granite powder >0 wt% granite powder, respectively. Granite filler reinforcement was the main cause for proper flow of stress across the interface.

The damping factor ($\tan \delta$) indicates the amount of energy recovered in terms of mechanical damping or internal friction in visco-elastic system. The variation in $\tan \delta$ of the composites as a function of temperature is shown in Fig. 11.7c for granite particulate powder reinforced aluminum alloyed composites. It is observed that the damping factor is directly proportional to temperature. High damping factor was obtained for granite powder reinforced composites when stiffness starts to decrease. The decrement in stiffness leads to the debonding between particulate and matrix material. The maximum damping factor is observed for 6 wt% granite powder and minimum for 0 wt% granite powder, respectively, for granite powder reinforced aluminum alloyed composites. Similar results were reported by Cox et al. [39] and Licitra et al. [40] for damping behavior of metal matrix composites.

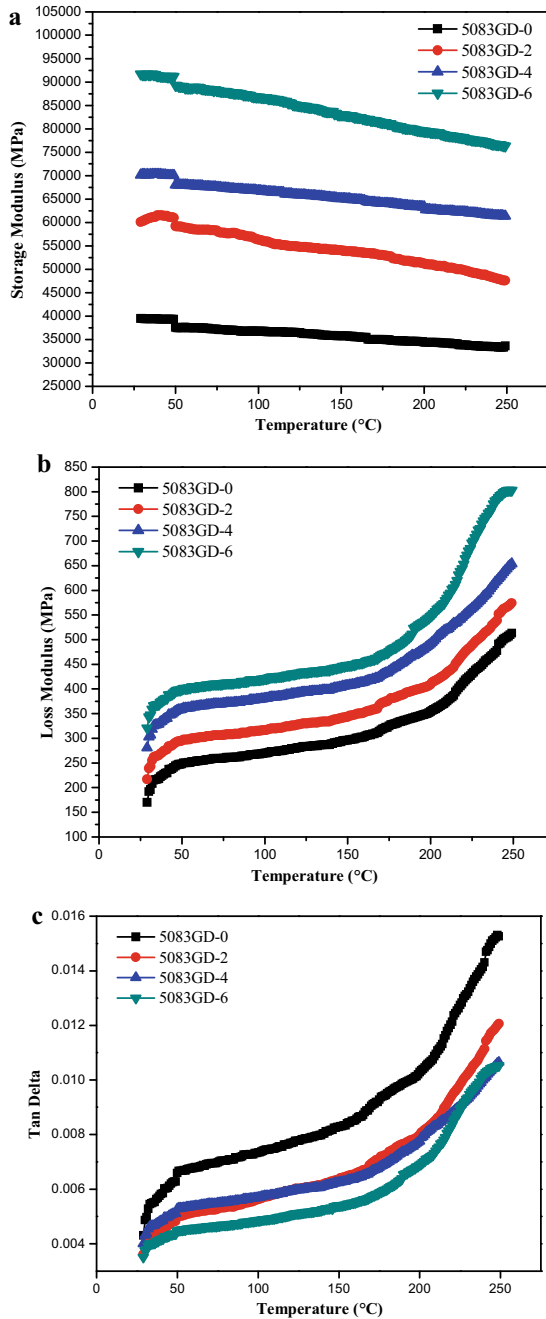


Fig. 11.7 a Variation of storage modulus with temperature for granite particulate powder reinforced aluminum alloyed composites, b variation of loss modulus with temperature for granite particulate powder reinforced aluminum alloyed composites, c variation of tan delta with temperature for granite particulate powder reinforced aluminum alloyed composites

Conclusion

This work shows that the stone industry waste, like granite powder, can be gainfully used as a potential cost-effective filler material for particulate-filled metal matrix composites. This work opens up a new avenue for value-added utilization of a solid industrial waste like granite powder. The following conclusions were drawn on the basis of fabrication and experimental results:

1. The granite powder filled aluminum metal matrix composites were fabricated successfully using stir casting technique with different weight fraction of filler material. Density and void test shows that density and void content of fabricated composites are enhanced with the incorporation of granite filler into 5083 aluminum alloy.
2. The addition of granite filler into 5083 aluminum alloy leads to the degradation of flexural strength. However, the maximum and minimum flexural strength was observed for unfilled aluminum alloy and 6 wt% granite powder reinforcement aluminum alloy composites.
3. Hardness and impact energy enhanced with the incorporation of granite filler into 5083 aluminum alloy. The maximum hardness and impact strength was found for 6 wt% granite powder aluminum alloy composites.
4. The magnitude of stress intensity factor enhanced with increment of granite filler into 5083 aluminum alloy as well as increment in crack lengths. However, 6 wt% granite powder filled composites shows maximum magnitude of stress intensity factor and unfilled aluminum alloy shows minimum stress intensity factor.
5. The visco-elastic properties of 5083 aluminum alloy were significantly altered by incorporation of granite filler in base matrix.

References

1. Biswas AK, Davenport WG (2003) Extractive metallurgy of copper. Pergamon Press, New York, p 518
2. Pati PR, Satapathy A (2015) Development of wear resistant coatings using LD slag premixed with Al_2O_3 . *J Mat Cycl Waste Manag* 17:135–143
3. Shi C, Meyer C, Behnood A (2008) Utilization of copper slag in cement and concrete resources. *Conserv Recycle* 52:1115–1120
4. Biswas S, Satapathy A (2010) Use of copper slag in glass-epoxy composites for improved wear resistance. *Waste Manag Res* 28:615–625
5. Patel M, Padhi BK, Vidyasagar P, Pattnaik AK (1992) Extraction of titanium dioxide and production of building bricks from red mud. *Res Ind* 37(3):154–157
6. Summers RN, Guise NR, Smirk DD (1993) Bauxite residue (red mud) increases phosphorus retention in sandy soil catchments in Western Australia. *Fertil Res* 34(1):85–94
7. Satapathy A, Mishra SC, Ananthapadmanabhan PV, Sreekumar KP (2007) Development of ceramic coatings using redmud—a solid waste of alumina plants. *J Sol Waste Techn Manag* 33(2):48–53
8. Geetha B, Ganesan K (2014) Optimization of tensile characteristics of Al 356 alloy reinforced with volume fraction of red mud metal matrix composite. *Procedia Eng* 97:614–624

9. Mahata T, Sharma BP, Nair SR, Prakash D (2000) Formation of aluminium titanate–mullite composite from bauxite red mud. *Mater Mat Trans B* 318:551–553
10. Sarajaadevi M, Murugesan V, Rengaraj K, Anand P (1998) Utilization of fly ash as filler for unsaturated polyester resin. *J Appl Poly Sci* 69:1385–1391
11. Sharma KK, Swaroop S, Thakur DS (1993) Recycling of LD slag through sinter route on direct charging in blast furnace at Bhilai Steel Plant. In: *Proceedings of national seminar on pollution control in steel industries*, pp 72–79
12. Alaneme KK, Akintunde IB, Olubambi PA, Adewale TM (2013) Fabrication characteristics and mechanical behavior of rice husk ash-alumina reinforced Al-Mg-Si alloy matrix hybrid composites. *J Mater Res and Tech* 2(1):60–67
13. Narasaraju G, Raju DL (2015) Characterization of hybrid rice husk and fly ash-reinforced aluminium alloy (AlSi10Mg) Composites. *Mater Toda Proceed* 2:3056–3064
14. Debnath K, Dhawan V, Singh I, Dvivedi A (2014) Adhesive wear and frictional behavior of rice husk filled glass/epoxy composites. *J Prod Eng* 17(1):21–26
15. Gautam V, Patnaik A, Bhat IK (2015) Thermo-mechanical and fracture characterization of uncoated, single and multilayer (SiN/CrN) coating on granite powder filled metal alloy composites. *Silic* 8:133–143
16. Kala TF (2013) Effect of granite powder on strength properties of concrete. *Inter J Eng Sci* 2(12):36–50
17. Kukshal V, Gangwar S, Patnaik A (2013) Experimental and finite element analysis of mechanical and fracture behavior of SiC particulate filled A356 alloy composites: Part I. *J Mat Des Appl* 229:91–105
18. Kukshal V, Gangwar S, Patnaik A (2013) Experimental and finite element analysis of mechanical and fracture behavior of Al₂O₃ particulate-filled A356 alloy composites: part II. *J Mat Des Appl* 229:64–76
19. Okayasu M, Hitomi M, Yamazaki H (2009) Mechanical and fatigue strengths of silicon nitride ceramics in liquid aluminum alloys. *J Eur Ceram Soc* 29:2369–2378
20. Gangwar S, Patnaik A (2013) A study on the physical and mechanical properties of TiO₂ filled A380 alloy composites. *Inter J Comp Mat* 3:69–72
21. Anilkumar HC, Hebbar HS, Ravishankar KS (2011) Mechanical properties of fly ash reinforced aluminium alloy (al6061) composites. *Inter J Mech Mat Eng* 6:41–45
22. Agarwal BD, Broutman IJ (1990) *Analysis and performance of fiber composites*, 2nd edn. Wiley, New York
23. Turk A, Durman M, Kayali ES (2007) The effect of manganese on the microstructure and mechanical properties of zinc-aluminium based ZA-8 alloy. *J of Mater Sci* 42:8298–8305
24. Chu S, Wu R (1999) the structure and bending properties of squeeze-cast composites of A356 aluminium alloy reinforced with alumina particles. *Comp Sci and Tech* 59:157–162
25. Abdullah Y, Razak Y, Daud RS, Harun M (2009) Flexural strength and fracture studies of Al-Si/SiC_p composites. *IJMME* 4:109–111
26. Qu Z, He R, Wei K, Pei Y, Fang D (2015) Pre-oxidation temperature optimization of ultra-high temperature ceramic components: flexural strength testing and residual stress analysis. *Cera Inter* 41(3):5085–5092
27. Park BG, Crosky AG, Hellier AK (2008) High cycle fatigue behaviour of microsphere Al–Al₂O₃ particulate metal matrix composites. *Comp: Part B* 39:1270–1279
28. Seah KHW, Sharma SC, Girish BM, Kamath R, Satish BM (1997) Mechanical properties and fractography of cast lead/quartz particulate composites. *Mater and Des* 18(3):149–153
29. Sharma SC (1997) Mechanical properties and fractography of cast lead/quartz particulate composites. *Mater Des* 18:149–153
30. Kataiah GS, Girish DP (2010) The mechanical properties and fractography of aluminium 6061-TiO₂ composites. *Int J Pharm Stud Res* 1:17–25
31. Papakyriacou M, Mayer HR, Stanzl SET, Groschl M (1995) Near-threshold fatigue crack growth in Al₂O₃ particle reinforced 6061 aluminium alloy. *Fat Frac Eng in Mater struc* 18(4):477–487

32. Levin M, Karlsson B (1991) Influence of SiC particle distribution and prestraining on fatigue crack growth rates in aluminium AA6061-SiC composite material. *Mater Sci and Tech* 7:596–607
33. Kumai S, Yoshida K, Higo Y, Nunomura S (1996) Effects of dendrite cell-size and particle distribution on the near-threshold fatigue-crack growth-behavior. *Acta Mater* 44(6):2249–2257
34. Somekawa H, Kim HS, Singh A, Mukai T (2007) Fracture toughness in direct extruded Mg-Al-Zn alloys. *J Mater Res* 22:2598–2607
35. Hemanth J (2001) Fracture toughness and wear resistance of Aluminum-boron particulate composites cast using metallic and non metallic chills. *Mater Des* 23:41–50
36. Zong BY, Zhang F, Wang G, Zuo L (2007) Strengthening mechanism of load sharing of particulate reinforcements in a metal matrix composite. *J Mater Sci* 42:4215–4226
37. Patnaik A, Mamatha TG, Biswas S, Kumar P (2012) Damage assessment of titania filled Zinc-aluminum metal matrix composites in erosive environment: a comparative study. *Mater and Des* 36:511–521
38. Zhang JM, Perez RJ, Wong CR, Lavernia EJ (1994) Effects of secondary phases on the damping behavior of metals, alloys and metal-matrix composites. *Mater Sci Eng* 13:325–389
39. Cox J, Luong DD, Shunmugasamy VC, Gupta N, Strbik OM, Cho K (2014) Dynamic and thermal properties of aluminum alloy A356/silicon carbide hollow particle syntactic foams. *Meta* 4:530–548
40. Licitra L, Luong DD, Strbik OM, Gupta N (2015) Dynamic Properties of alumina hollow particle filled aluminum alloy A356 matrix syntactic foams. *Mater Des* 66:50–55

Chapter 12

Performance Improvement of OEM Brake Caliper by Manufacturing with Design Changes



Mauli Mirajkar, Parvathidevi Gurubaran, P. Jeevan Sunny, Armugasunder Konar, and P. K. Ambadekar

Abbreviations

W_T	Weight transfer
W	Mass
H	Height of center of gravity
L	Wheel base
g	Acceleration due to gravity
μ	Coefficient of friction b/w surface and tyre
W_{FD}	Front dynamic load
W_{RD}	Rear dynamic load
B_{FF}	Braking force front
B_{TF}	Braking torque front
B_{FR}	Braking force rear
B_{TR}	Braking torque rear
F_{mc}	Force on master cylinder
A_{mc}	Area of piston master cylinder

M. Mirajkar · P. Gurubaran (✉) · P. Jeevan Sunny · A. Konar · P. K. Ambadekar
Department of Mechanical Engineering, SIES Graduate School of Technology, Navi Mumbai,
India

e-mail: parvathidevi.guru@gmail.com

M. Mirajkar

e-mail: mauli.mirajkar16@siesgst.ac.in

P. Jeevan Sunny

e-mail: jeevansunny@yahoo.co.in

A. Konar

e-mail: skonar121306@gmail.com

P. K. Ambadekar

e-mail: pkaspa2018@gmail.com

P_{Mc}	Pressure on master cylinder
F_{p1}	Pedal force
$F_{caliper}$	Force on caliper
F_{disc}	Force on disc

Introduction

The foremost function of a braking system is to slow down a vehicle by conversion of its kinetic energy into heat through friction. In a hydraulic braking system, brake fluid generally containing ethylene glycol is used to transmit the pressure from the actuating mechanism to the braking mechanism. When the brake pedal in a hydraulic system is pressed the pushrod connected to it exerts force on the pistons inside the master cylinder (Fig. 12.1). This causes the fluid inside the reservoir to flow into the pressure chamber, resulting in an escalation in pressure of the entire hydraulic system. This forces the fluid to flow through the hydraulic lines or brake hose toward the caliper, thereby displacing the pistons of the caliper. The pistons of the caliper then apply force on the brake pads, pushing them against the rotating disc. The friction generated between the pads and the disc produces a braking torque which slows down the vehicle. Heat generated due to friction is either dissipated through vents and channels in the discs via convection or is conducted through the pads. When the brake pedal is released the springs in the master cylinder assembly return the piston back into its position. This action relieves the hydraulic pressure on the caliper and produces suction to the caliper piston causing it to move back into its casing and allowing the brake pads to release the disc. Brake caliper are of two types, namely floating and fixed. In a floating caliper (Fig. 12.2) the piston is on the inboard side of the caliper and the caliper is mounted on a guiding pin acting as a cylindrical

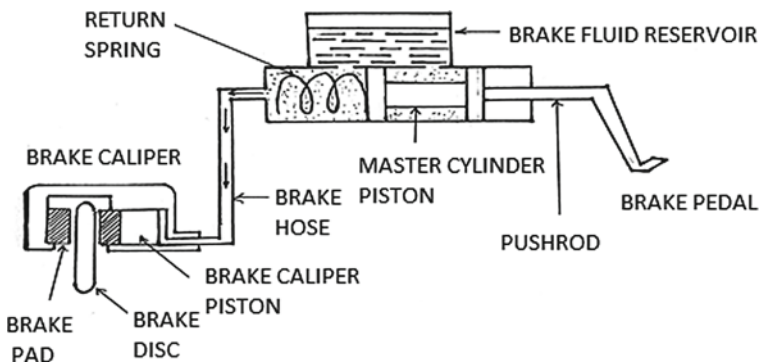
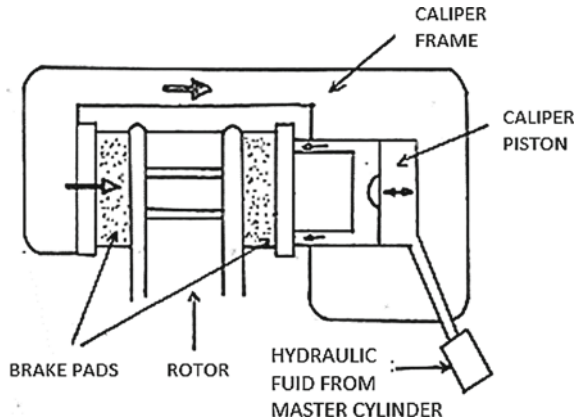


Fig. 12.1 Working of hydraulic disc braking system

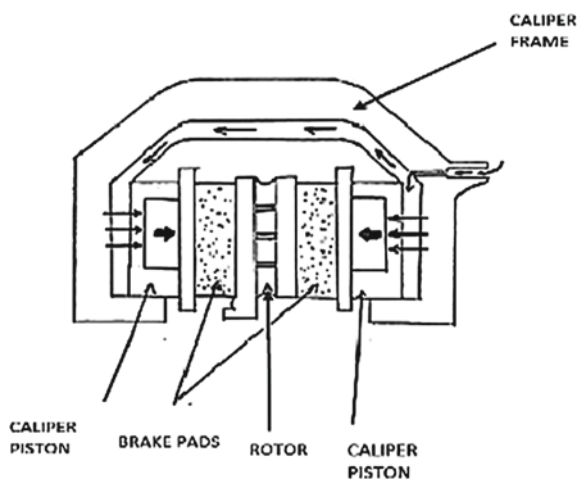
Fig. 12.2 Floating caliper



support. In a fixed caliper (Fig. 12.3) pistons are present on both sides of the disc and can be directly fixed to the mountings on the uprights.

The different components of a floating caliper are shown in Fig. 12.4 in order to explain the modifications in the design explicitly. The primary component of a caliper is the frame of the brake caliper which provides the function of casing all the components of caliper, viz., the piston, seals, brake pads, and bleeding screw in their position and enabling relative motion between them for effective working of the braking system. The banjo bolt is a hollow perforated bolt which transfers the brake fluid from the brake hose into the brake caliper. The caliper piston seal performs the dual function of sealing the piston bore and retracting the caliper piston after brakes are applied. The dust boot prevents the entry of any dust or foreign substance inside the caliper. The design of the seal groove assembly of a brake caliper highly influences the braking performance of the caliper. A bleed screw is a component

Fig. 12.3 Fixed caliper



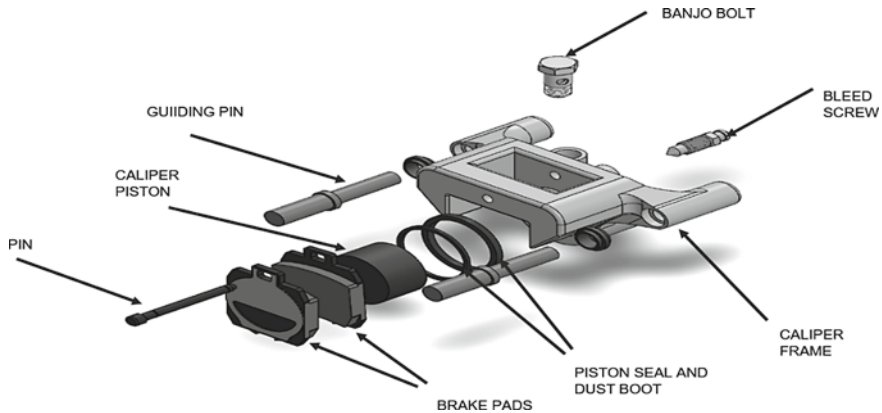


Fig. 12.4 Components of floating caliper

which is used to create a temporary opening in a closed hydraulic system facilitating the removal of air or any other substance from the hydraulic system through the differences in pressure and density.

In order to have high-performance braking system, it is essential to have an efficiently functioning brake caliper. The efficiency of a brake caliper depends upon few parameters as explained further. The piston diameter should be sufficiently large to produce the required braking force. The hydraulic pressure generated inside the brake caliper should be high enough to ensure that adequate amount of force is applied on the brake pads. The pressure generated should not be lost due to leakages inside the caliper so that there is no pressure loss leading to inadequate clamping action. Removal of air from the hydraulic system is necessary because the presence of air bubbles in the brake system reduces the hydraulic pressure that is developed within the system due to the compressed air. Also, the bleeding screw hole in the caliper should open out at the topmost point of the bore to ensure complete removal of air from the hydraulic system.

The literature was studied to identify the presence of above-mentioned work. Phad et al. [1] studied the design and conducted optimization of brake caliper for the system for maximum performance. Anwana and Cai [2] demonstrated the caliper seal groove design and also established the mechanics behind the deformation of rubber confined to the prescribed boundaries of the seal groove. The force and friction analysis of disc brake and rotor was studied by Mishra et al. [3]. It helps to understand the force and also the amount of friction on the disc brake, and therefore, estimates the efficiency of the disc brake. Maleque and Rahman [4] explained the automotive brake mechanism and suggested that the widely used material is cast iron for the brake rotor. The author emphasized on the substitution of cast iron products by other lightweight materials. An idea to design a brake caliper which is lightweight and provides adequate braking torque required for efficient clamping over the brake disk of the vehicle in hostile racing environments was presented by Bokade and Jade [5]. Khairnar et al. [6] made predictions regarding the critical performance

parameters by taking into consideration the geometric design parameters for the seal groove design. Pishdad [7] focused on the optimization and analysis regarding a heavy-duty caliper and applications of asymmetric designs. According to Limpert [8] the braking force is the most important aspect. The clamping force generated should always be more than the required braking force to slow the vehicle down completely. The research of Amrish [9] was to analyze the different classifications of brake rotors. Brake rotor analysis includes the steady-state thermal analysis and the structural analysis regarding the same. This paper studies the heat dissipation and clamping force based on material variation for drilled disk rotor type brake disk (Negi et al. [10]) after initial testing of the braking setup and its implementation on the vehicle. The overall adjustability of the braking system meets the design goals of possessing better and responsive braking system. The other design objective of achieving minimum stopping distance was also achieved through the redesigned braking system. Doumiat et al. [11] suggested the normal forces and lateral load transfer estimation for the vehicle's safety experimental test. This study introduces the estimated wheel to ground contact normal forces, and also the load transfer effect. The method of testing is proposed based on the dynamic behavior of a vehicle. Vasseljen [12] explained the braking loads developed by a vehicle under sudden deceleration and related thermal analysis for the brake disk to sustain the high temperatures. Also, the integration methods between the caliper and uprights assembly are used for improving in-wheel packing. Grześ [13] aimed to take consideration regarding the temperature fields of the disc rotor during short and emergency braking conditions. This study concluded that in the domain of time the rotating speed of disc along with contact pressure with respect to specific material properties intensely affects the disc brake temperature fields. Pohane and Choudhari [14] discussed the use of finite element model to calculate static structural analysis and transient state analysis. A three-dimensional model of the brake pad and the disc would be required for the aforementioned analysis. Blumberg and Neto [15] explained the methodology for the analysis of the caliper in ANSYS software. This study uses the meshing parameters, regions to be constrained, and the input parameters for the static analysis.

On the basis of literature survey and practical understanding, certain drawbacks of original equipment manufacturer (OEM) caliper have been identified. The bleed screw of the caliper positions downward in direction when mounted on the right side of the vehicle. This increases the difficulty to remove the air bubbles present inside the hydraulic braking system and some air bubbles would remain at the top, and during the bleeding process complete air cannot be removed which causes inefficient braking. Generally, the automobile companies manufacture brake caliper for the left side and the right side separately. This adds up to the machining cost and time for the manufacturing of two separate designs of caliper. Additionally, the fluid entry passage of a brake caliper from the brake hose consists of an intricately drilled pathway which is inclined to all X , Y and Z axes which makes the drilling process complicated and expensive. Further, due to the complicated geometry of the fluid entry passage, there are high chances of fluid leakage in the caliper leading to failure of the braking system. Also, in such calipers the fluid has to travel a longer distance to reach the caliper piston bore which increases the time taken for clamping action. Importantly,

the OEM calipers have standard piston diameters which does not have the provision of using varying diameter pistons. Due to these problems the braking efficiency of a vehicle is reduced and hence desirable performance like lesser stopping distance and stopping time are not achieved.

The primary objective of this study is to reduce the chances of leakages in the brake caliper and in the braking system and achieve lesser stopping distance and stopping time. The designed brake caliper is intended to have reduced weight with simplified design and geometry in order to decrease the unsprung mass of the vehicle. Also, the proposed study aims to design a caliper such that it can provide intermediate piston diameters according to the working pressure of the fluid and the braking force required to stop the vehicle. The remaining paper is organized as follows: material selection is discussed in Sect. 2, methodology in Sect. 3 and design in Sect. 4. The results are presented and analyzed in Sects. 5, and 6 describes the discussion of the results.

Material Selection

The selection of material is crucial in order to meet the objectives. The caliper housing material must be rigid enough to sustain all the forces that would occur on it. Also, the material should have a lesser strength to weight ratio to make the caliper lighter. To maintain the required strength in the component aluminum 7075 T6 was selected for the housing with properties as provided in Table 12.1.

The caliper piston material selected was aluminum alloys as the thermal conductivity of aluminum is high ranging between 200 and 250 W/mK. This leads the heat to be transmitted through the piston which was generated due to the friction between rotor and friction pads, causing a fall in disc temperature. Pistons can also be made of titanium or phenol formaldehyde, but are not preferred because of their high cost compared to aluminum. To have a safe and efficiently functional braking system, it is necessary to have brake pads or friction materials with high coefficient of friction which is independent of temperature effects, velocity, pressure, wear, ambient conditions and corrosion. The friction material also has to be environment-friendly and of low cost. To satisfy these parameters we selected OEM metal composite brake pads with properties as shown in Table 12.2.

The piston seal is placed inside the bore of the caliper, and the factors like its compatibility with brake fluid, operating temperature range, fluid pressure sustainability range, hardness, working conditions, tensile strength, compressibility and failure modes are crucial considerations. Various materials available for seals are

Table 12.1 Properties of aluminum 7075 T6

Mechanical properties	Yield strength	Modulus of elasticity	Poisson's ratio
Values	503 MPa	71.7 GPa	0.33

Table 12.2 Brake pad properties

Modulus in compression	830 MN/m ²
Ultimate shear strength	11 N/m ²
Thermal conductivity	5796 Nm/hkm
Brinell hardness	14
Friction coefficient	0.35
Unit pressure	0.35–5.2 MN/m ²

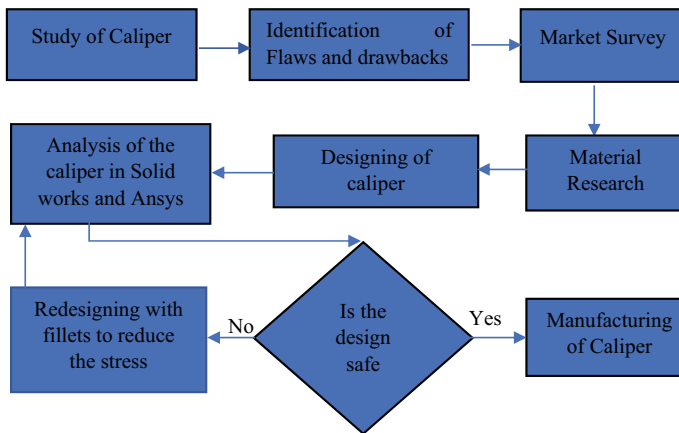


Fig. 12.5 Methodology of proposed system

thermoplastic elastomers, rubber, rigid thermoplastics, and so on. Considering the properties of the brake fluid, rubber is the best suited material for the seals. It can operate up to 150 bar and can work within the range of −40 to 130 °C having tensile strength up to 13 MPa.

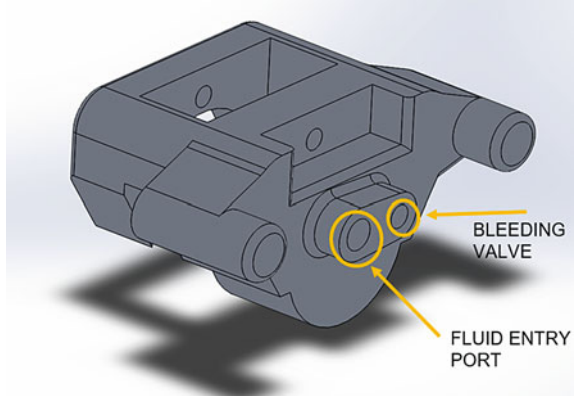
Methodology

The methodology followed to implement the proposed system is shown in Fig. 12.5.

Design

The 3D model of a caliper as shown in Fig. 12.6 is created using the software SolidWorks 2016. The fluid entry port of the caliper is introduced directly into the bore of the caliper piston with a horizontally drilled pathway parallel to X-axis in order to simplify the geometry of the fluid entry port. The bleeding valve is positioned

Fig. 12.6 CAD model of caliper



in the center to ensure that the bleed screw will not position in the downward direction irrespective of its mounting position. The caliper is designed in such a way that it can accommodate a piston bore of diameter ranging from 28 to 38 mm.

Results and Analysis

Calculations

The following calculations are done for designing the brake system. These calculations validate that the caliper design meets the necessary requirements. While braking, the generated braking torque on the rotor must be greater than the torque on the wheel due to weight transfer for efficient braking action.

Calculation of braking torque requirement:

$$\text{Weight transfer: } W_T = (H/L) * (W/g) * \mu * g$$

$$\text{Dynamic load: Front } W_{FD} = \text{Front Static load} + W_T$$

$$\text{Rear } W_{RD} = \text{Rear Static load} - W_T$$

$$\text{Required braking force and torque: } B_F = \mu_g * W_{FD} \quad (12.1)$$

$$B_T = B_F * \text{wheel diameter} \quad (12.2)$$

Calculation of generated braking torque: $F_{mc} = F_{p1} * \text{pedal ratio}$

$$P_{Mc} = F_{mc} / A_{mc}$$

$$P_{mc} = P_{caliper}$$

$$F_{caliper} = P_{caliper} * A_{caliper}$$

Generated braking force and torque: $F_{disc} = \mu_{pad} * F_{caliper}$ (12.3)

$$B_{TF} = F_{disc} * Radius_{disc}$$
 (12.4)

The braking torque that we get from Eq. (12.4) must be greater than that of the braking torque from Eq. (12.2) for effective braking action.

Design calculations were carried out for an ATV vehicle having kerb weight 250 kg. The parameters like static load of vehicle, wheel base, height of center of gravity are required for designing. Table 12.3 presents the design input variables. The master cylinder selected is Bosch tandem master cylinder having a bore diameter of 19.07 mm. The comparison of braking torque for above calculations is presented in Table 12.4.

The caliper designed has a piston diameter of 32 mm which produces sufficient torque necessary to stop an ATV of kerb weight 150 kg. But the caliper is designed in such a way that it can have a maximum of 38 mm diameter piston bore. Hence

Table 12.3 Design input parameters

Parameters		Value
Weight of vehicle (including driver's weight)		250 kg
Static load	Front	103.5 kg
	Rear	116.5 kg
Wheel base		54 inch
CG height		19.97 inch
Coefficient of friction between tires and road surface		1
Pedal ratio		8:1
Master cylinder bore diameter		19.07 mm
Disc diameter	Front	165 mm
	Rear	180 mm
Coefficient of friction between the pad and the disc		0.35
Pedal force		300 N
Caliper piston diameter		32 mm

Table 12.4 Comparison of braking torque for above calculations

Braking torque	Required braking torque (Nm)	Generated braking torque (Nm)
Front	265.275	343.00
Rear	100.85	413.910

Table 12.5 Braking torque (Nm) of motorcycle

Master cylinder bore diameter (mm)	Caliper piston diameter (mm)			
	30	32	34	38
12.7	535.6811	609.486	688.05258	859.4705
15.87	343.0519	390.3169	440.63117	550.4078
19.07	237.5814	270.3148	305.16005	381.1861
25.4	133.9203	152.3715	172.01314	214.8676

Table 12.6 Braking torque (Nm) of car

Master cylinder bore diameter (mm)	Caliper piston diameter (mm)			
	30	32	34	38
12.7	468.7209	533.3003	602.046	752.0367
15.87	300.1705	341.5273	385.55227	481.6068
19.07	207.8837	236.5254	267.01505	333.5378
25.4	117.1802	133.3251	150.5115	188.0092

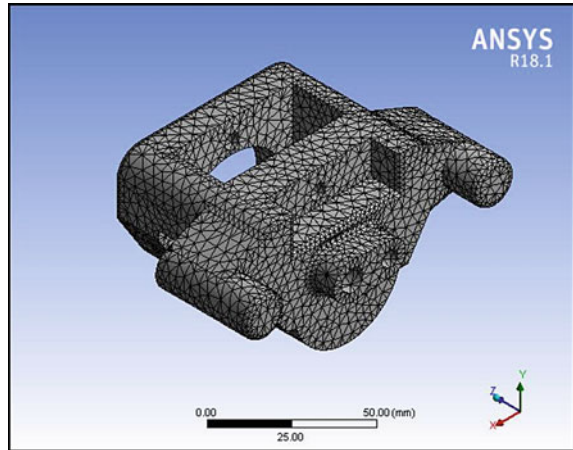
it can produce greater torque which is enough to stop a vehicle of maximum kerb weight of 1000 kg. Tables 12.5 and 12.6 show the required braking torque to stop a vehicle and the braking torque provided by the designed caliper. Design calculations for motorcycle of kerb weight of 180 kg and braking torque of 360–400 Nm are shown in Table 12.5. Whereas calculations for a car of kerb weight of 1000 kg and a braking torque between 800 and 600 Nm are shown in Table 12.6.

Analysis

In order to do analyze, the following properties of material were given as input to the software. The analysis of the CAD model of the caliper is done by varying the values of force and pressure. Software Ansys 18.1 is used to study the static structural analysis of the CAD model.

Material: Al 7075 T-6
 Density: 2700 kg/m³
 Young's modulus: 72 GPa

Fig. 12.7 Meshing of caliper



Ultimate tensile strength: 590 MPa.

Figure 12.7 shows the meshing of the caliper, and by using the default settings mesh quality (i.e., a coarse mesh with element size = 4 mm) 0.619 was obtained.

The body of the caliper is subjected mainly to two loads that are: (a) Force on the caliper due to the pressure applied at the back of the piston and (b) force on the caliper body due to clamping. Considering vehicle mass as 250 kg, weight distribution of 45% at front and 55% at rear, pressure force of piston area of 8.4 MPa, clamping force of 3000 N at the end of opposite pad and having a fixed support at the two mounting positions.

The design of caliper has FOS 2.1, total deformation is 0.9 mm, minimum equivalent stress is 0.02536 MPa. The results obtained from the analysis with ANSYS Workbench are as shown in Figs. 12.8 and 12.9.

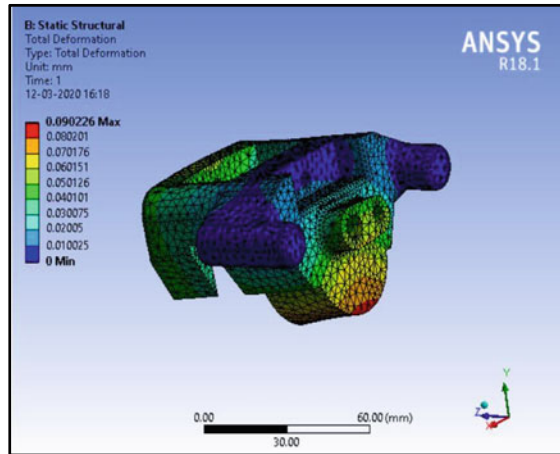
After designing we machined the caliper with CNC machining. The machined caliper is then set up in a front/rear split brake system on a BAJA ATV for bleeding. The other brake components used are:

- Master cylinder—Bosch TMC (19.07 mm bore diameter, 30 mm stroke length)
- Brake hose—Stainless steel braided Teflon brake hose (5 mm inner diameter)
- Brake disc—SS 420 (front diameter 165 mm, rear diameter 180 mm)
- Pedal—Al 7075 pedal ratio 8:1.

Iterations

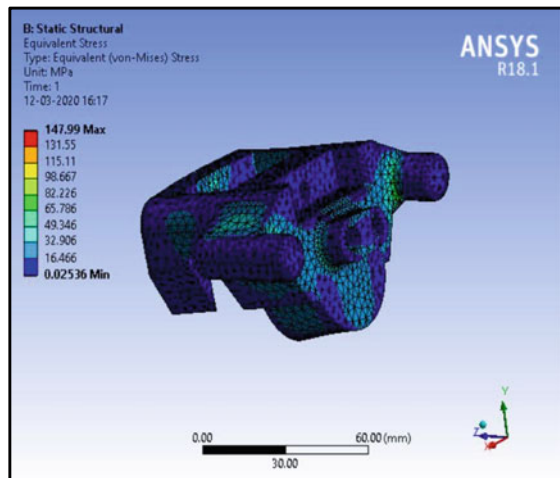
Several iterations were made to overcome the drawbacks faced during the bleeding of the caliper.

Fig. 12.8 Deformation



Total Deformation is 0.9 mm

Fig. 12.9 Equivalent stress



Min Equivalent stress is 0.02536 M Pa

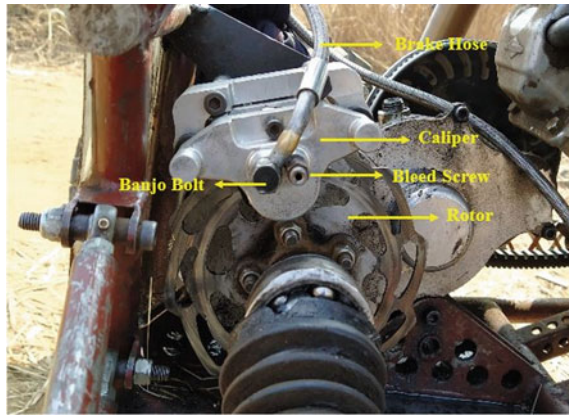
Iteration 1:

The oil leaked from the piston bore during the bleeding process. This was because the oil seal rings could not properly accommodate the seal grooves. Hence the oil seal rings did not perform its function of preventing the oil leakage. Also, another function of the seal is to retract the piston backwards, which was not performed due to improper machining of the grooves.

Result: Improper clamping action.

Action Taken: Machining of grooves with proper tolerances.

Fig. 12.10 Caliper mounted on gearbox (inboard braking)



Iteration 2:

After designing the grooves with adequate tolerances, there were no leakages in the caliper. Also, the new caliper is designed such that the movements of brake pads are guided properly for clamping of the discs. Figure 12.10 shows the final design of caliper in rear inboard braking system of an ATV.

After bleeding the brake system, the vehicle was tested to run 150 ft on concrete surface for validating the stopping distance.

Discussion

In the modified vehicle, custom brake caliper mountings can be incorporated based on upright assembly for different types of vehicle. Compactness of the model can be achieved so that in-wheel packing is easier and no hindrance to other subsystems is formed. According to the total curb weight of the vehicle, the modifications for the piston bore according to standard piston diameter can be adjusted. Just by keeping the main design as the same on each caliper and just by varying the piston diameter the caliper can be used for every type of vehicle segment (SUV, Hatchback, etc.). Taking into consideration the weight transfer of the vehicle, a compact brake disk having lesser diameter can be employed. By this method the required braking force can be achieved and excess forces are not developed so that it can lock the wheel immediately and cause the vehicle to skid. Also, as the system is made compact the total assembly weight is made less. By this, the unsprung mass of the vehicle at each individual wheel is reduced and the vehicle performance is not compromised. Furthermore, the handling characteristics of vehicle is not compromised when vehicle goes into bumps and droops. The bleed screw positioning is made such that complete air bubbles trapped in the system can be evacuated easily. And flow of air bubbles out of the system is faster so that bleeding process can be faster and clamping performance of the caliper is improved.

Material selected is Al-7075 T-6 for the caliper and SS-420 for brake disk. The specific gravity as well as cost is less and the performance is enhanced as lightweight assembly is designed. Also, the material chosen has good corrosion resistance and thus has longer lifespan. The proposed model is thus better than the available OEM and offers many benefits. The brake caliper bleed screw has been positioned upwards to facilitate easier for bleeding process. The piston diameter can be varied according to the required braking force for complete braking. The weight of the redesigned caliper is lesser than the OEM caliper of the same piston diameter. Due to the reduced weight of the caliper, the unsprung mass of the vehicle also reduces. This indirectly increases the stability of the vehicle. By using this caliper model, the time required for assembly of caliper is reduced.

Conclusion

The design goal of the caliper model is to improve the braking efficiency of the system by making design changes in the geometry of the banjo valve and bleed screw valve. By employing a seal groove which has perfect tolerance the brake fluid won't exit the main piston chamber which would reduce the chances of leakage in the caliper. By using aluminum 7075-T6 as the standard material for manufacturing, the overall weight of the assembly would reduce, which would make the unsprung mass of the vehicle to reduce and the vehicle performance would not be restrained. The lightweight and compact design helps in improving the vehicle performance and stability. Based on the mounting points for the caliper on the vehicle upright, the caliper system can be easily modified so that serviceability is made easy and is less time-consuming. The simplified design of the caliper enables easy assembly and disassembly of the component. The calculated stopping distance of the vehicle was validated by testing it on concrete surfaces. The stopping distance achieved was 2.9 m. The designed caliper is suitable to be used in any motorcycle or any lightweight four-wheeler. This caliper can be easily used in any BAJA SAE vehicle due to its compliance with the design of the vehicle. In the proposed model the designed caliper can only be used for a vehicle with maximum kerb weight of 1000 kg. Beyond this weight, the caliper will be incapable of providing complete braking. With the designed caliper, a maximum of 38 mm piston diameter can be achieved. The caliper is manufactured with the process of CNC machining which is a relatively expensive process. The CNC machining does not ensure proper groove geometry to be machined in the caliper frame. This causes improper retraction of the piston by the seal. The piston seals are available only in diameter as per the OEM caliper diameter. Hence, there are no seals available for piston diameters other than the standard ones. This causes a problem in having the desired piston diameters of the caliper. With further modifications in caliper, like changing the dimensions of the caliper or increasing the number of pistons, the caliper can be used for heavier vehicles. With further advent in the manufacturing process due to mass production, the designed brake caliper can be die-casted. This process provides more strength to the caliper, reduces

the machining cost and ensures proper seal groove geometry. Further, an electronic brake distribution (EBD) system can be used to vary the amount of force applied on each wheel. Hence, providing adequate clamping action in each wheel.

References

1. Phad D, Auti T, Joshi R (2015) Design and analysis of a Brake Caliper. *Int J Automob Eng Res Dev* 5(5):1–10
2. Anwana OD, Cai H, Chang HT (2002) Analysis of brake caliper seal-groove design. *SAE Trans* 111:1316–1324
3. Mishra YH, Deulgaonkar VR, Makasare PA (2015) Design and optimization of disc brake rotor (for two wheeler). *Int Eng Res J* 288–300
4. Maleque MA, Dyuti S, Rahman MM (2010) Material selection method in design of automotive brake disc. In: Ao SI, Len Gelman and David WL Hukins and Andrew Hunter Korsunsky AM (eds) *The 2010 international conference of computational intelligence and intelligent systems. Proceedings of the world congress on engineering WCE London, UK, 3:2322–2326*
5. Bodake A, Jade A (2018) Optimisation of hydraulic brake caliper of all-terrain vehicle. *Int J Sci Eng Res* 9(12):523–530
6. Khairmar HP, Phalle VM, Mantha SS (2017) Frictional coefficient depending on active friction radius with BPV and BTV in automobile disc braking system. *Int J Eng, Sci Technol* 9(3):41–50
7. Pishdad AR (2012) *Advanced design of brake calipers*. Politecnico di Milano, Italy
8. Limpert R (2011) *Brake design and safety, Edition III*. SAE International
9. Amrish PN (2016) Computer aided design and analysis of disc brake rotors. *Adv Automob Eng* 5(2):1–13
10. Negi V, Deshmuk N, Deshpande A (2017) Design of braking system of BAJA vehicle. *Int J Adv Eng Res Dev* 4(11):1059–1064
11. Doumiati M, Victorino A, Charara A, Lechner D (2009) Lateral load transfer and normal forces estimation for vehicle safety: experimental test. *Veh Syst Dyn: Int J Veh Mech Mobil* 47(12):1511–1533
12. Vasseljen B (2018) Brake caliper design for a formula student race car-on behalf of revolve NTNU. NTNU
13. Grześ P (2009) Finite element analysis of disc temperature during braking process. In: Viadero F, Ceccarelli M (eds) *New trends in mechanism and machine science* 3(4):36–42
14. Pohane R, Choudhari RG (2011) Design and finite element analysis of disc brake. *Int J Eng Res Ind Appl* 4(1):147–151
15. Blumberg R, Neto NF (2010) Design of high performance automotive brake caliper using ANSYS. Paper presented at ANSYS South American conference and esss users meeting, Atibaia SP, Brazil, 19–22 Oct 2010

Chapter 13

Development of Novel Abrasive Media Using Granite Dust Powder Waste for Finishing Applications



Ankit Soni, Jai Kishan Sambharia, and Sandesh Trivedi

Notations and Abbreviations

SiC	Silicon carbide
SR	Surface roughness
PAG	Polymer abrasive gel
MRR	Material removal rate
FEM	Finite element method
AFM	Abrasive flow machine
ANOVA	Analysis of variance
AFF	Abrasive flow finishing
TGA	Thermo gravimetric analysis
R-AFF	Rotational abrasive flow finishing
SDAFM	Self-deformable abrasive flow media
FTIR	Fourier transform infrared spectroscopy
FESEM	Field emission scanning electron microscopy
ΔR_a	The average roughness of a surface
ΔR_p	Max profile peak height
ΔR_q	Root mean square deviation of the profile

A. Soni · J. K. Sambharia (✉) · S. Trivedi
Mechanical Engineering Department, Engineering College Ajmer (an Autonomous Institution of Govt. of Rajasthan), Ajmer, Rajasthan 305025, India
e-mail: jsambharia@gmail.com

A. Soni
e-mail: ankitsoni6655@gmail.com

S. Trivedi
e-mail: sandeshtrivedi@ecajmer.ac.in

ΔR_z The difference between the tallest “peak” and the deepest “valley” in the surface

Introduction

Marble is widely used in the construction and building materials since ancient times. Disposal of this waste either in the form of powder or aggregates is causing environmental problems worldwide. It is well known that there are two sources of waste generation: One, waste generated from quarries, and two, from processing plants [1]. Further, two more types of wastes are generated through processing plants: solid waste and semisolid waste or slurry [2]. Frame sawing with diamond blades is a widely used machining technique especially by small-scale industries, in which water is widely used as a coolant and the powder generated blends with water form viscous slurry [3].

The granite dust powder produced by marble and granite industries causes a lot of environmental pollution and health problems. In the present work, the same industrial waste is used as the base material for the development of abrasive media which is further used in finishing application. So, abrasive flow machine (AFM) is a finishing process widely used to finish difficult profiles and passage. AFM generates uniform profile and accurate results on a remarkable range of finishing operations. The abrasive media flow through the workpiece in which a very small amount of material is removed by abrasive media. Abrasive media is comprised of a base material, abrasive particles, and rheological additives. Plasticizers are mixed with the base material to improve the viscous properties of abrasive media. Moreover, the abrasives are the key in abrasive media, used as aluminum oxide, silicon carbide, cubic boron nitride, and synthetic diamond. Other constituents of media are seeded oil, Aloe barbadensis Mill, and Cyamopsis tetragonoloba powder. The media is tested on rheological properties like critical strain, viscosity, shear stress, critical temperature, and yield stress. The nomenclature of developed media is shown in Fig. 13.1.

The desirable properties of AFM media are as follows:

Porosity: It is the proportion of the void volume of void spaces to the mass volume of the material.

Low adhesion to the workpiece: It is an important property of the abrasive media. The abrasive media should not stick to the workpiece surface.

Permeability: The media should have greater permeability to absorb abrasive and capability to hold it for longer duration as possible. These properties of the base can be improved by adding additives.

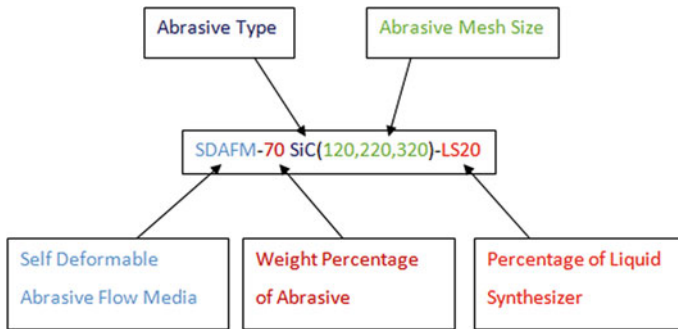


Fig. 13.1 Nomenclature of self-deformable abrasive flow media (SDAFM)

Literature Review

In the current decade, hybridizing of AFF process with other non-conventional processes has opened up new vistas for finishing complicated and difficult shapes, which would have been otherwise impossible with another machining process. In the same context, Jain et al. [4] analyzed the variables of the abrasive flow machine process using the finite element method (FEM) for finishing external surfaces. Kar et al. [5] developed a new AFM media and characterized for fine finishing and are used in the abrasive flow machine process. Shankar et al. [6] provided the rotary motion to the workpiece to enhance the performance of AFF and compared the abrasive flow finishing (AFF) and rotational abrasive flow finishing (R-AFF) processes to evaluate their performance in terms of change in MRR and surface roughness. Gorana et al. [7] analyzed the cutting forces during the finishing process and predict the surface roughness produced during the AFM process. Singh et al. [8] improved MRR and surface roughness by applying a magnetic field around the workpiece in abrasive flow machine. Sambharia et al. [9] characterized an alternatively developed polymer abrasive gel (PAG) and characterized using TGA, FTIR, and FE-SEM. Davies et al. [10] conducted experiments using high viscosity, medium viscosity, and low viscosity poly borosiloxane-based media, with SiC abrasive mesh size (60 and 100) for finishing mild steel dies. Mali et al. [11] used fabricated abrasive flow machine to the finished machined cylindrical surface of the aluminum-based metal matrix composite workpiece. Cheema et al. [12] developed efficient, cost-effective, and environment-friendly media. Magnetically assisted AFM process had improved the surface finish on non-ferrous material, and less number of cycles was used for the same MRR when compared with simple AFM. Agrawal et al. [13] synthesized abrasive media at varying temperatures and concentrations from experimental results; they found that the viscosity of the abrasive media decreases with increases in the percentage of abrasive concentration. From the literature, it is found that very less studies have been reported for synthesization and characterization of the environmentally friendly media. Also, few studies have been reported for internal polishing of complex surfaces using friendly and sustainable media. So, the environmental

footprint of any commercial activity can't be neglected. Efforts are to be done to make the AFM process environmentally friendly for the cost factor. These industries are still following the manual finishing methods for their parts and are unsuitable for complicated surfaces. Today, the primary challenge in industries is availability of low cost and environmentally friendly media. Many researchers worked on the development of fixture and tooling for the part which varies in geometrical size and shape. But still research work on the development of tooling and fixture for complex part shape is required so that the mass production can be increased and the cost of surface finish can be reduced.

Materials and Method

Experimental Equipment

The vacuumized abrasive flow setup (VAFS) is used, which consists of hopper, media pressurizing equipment, motor, tooling, and workpiece. High-precision weighing machine is used to measure the quantity of material for media synthesization. FTIR spectrum 2 (Perkin Elmer) is used for estimations of bonding of media particles in the range of $4100\text{--}400\text{ cm}^{-1}$ for liquid and solid samples. This instrument is used for identifying functional groups and characterizing covalent bonding information. The operational functional groups are identified as IR charts at different wave numbers. FESEM with EDS Nova Nano FE-SEM 450 is used that gives ultra-high-resolution characterization and provides precise, true nanometer-scale data. It gives a resolution of 1.6 nm at 1 kV and $<1\text{ nm}$ at 15 nm. FESEM is a scientific instrument that uses a beam of a dynamic electron to observe objects on a fine scale. The SURFTTEST SJ-210 is a user-friendly surface roughness measurement instrument used for surface roughness test. It is used to view surface roughness waveforms. Rheology test is used to measure a rheological parameter of a fluid variation of viscosity of the fluid by varying temperature as well as varying the shear rate and shear stress given the effect on viscosity of the fluid. Rheolab QC of Anton Paar make equipment is used for rheological study of developed media.

Material

The granite dust powder, gel (Aloe barbadensis Mill and Cyamopsis tetragonoloba powder), SiC abrasives, and high flash point oil are used for the preparation of self-deformable abrasive flow media (SDAFM). The gel has low flow property and does not stick on the workpiece surface during polishing.

The constituents of media are: as a base material—granite dust powder; plasticizer—high flash point oil; abrasive—silicon carbide (120, 220, 320), carrier—gel (Aloe barbadensis Mill and Cyamopsis tetragonoloba powder). The following combinations for SDAFM samples are prepared -

1. Granite dust powder + gel + high flash point oil + SiC (120)
2. Granite dust powder + gel + high flash point oil + SiC (220)
3. Granite dust powder + gel + high flash point oil + SiC (320).

Synthesization Procedure

The media composition is varied by adding the percentage of all contents that affects the media property, abrasive concentration, and the viscosity of media. Initially, as per the required amount of abrasive, granite dust powder is mixed with gel using a mixer machine. In the next step, plasticizer is mixed as per the procedure as mentioned in Fig. 13.2.

The self-deformable abrasive flow media (SDAFM) used granite dust powder, high flash point oil, Aloe barbadensis Mill, and Cyamopsis tetragonoloba powder with silicon carbide particles as abrasives. The SDAFM is synthesized by blending abrasive of various mesh sizes (120, 220, 320) semisolid media with various weight percentages whose viscosity could be changed by the amount of liquid synthesizer. Three different sample images of different mesh sizes are shown in Fig. 13.3. The percentage of ingredients of media has been calculated by the formula

$$\% \text{ of the particle ingredients} = \frac{\text{weight of particular ingredients}}{\text{total weight of the compound}} * 100 \quad (13.1)$$

The components of media with their quantity are listed in Table 13.1.

The gudgeon pin shown in Fig. 13.4 is used as a workpiece for experimentation, which is normally a forged short hollow bar made of a steel alloy of high quality and hardness that found usefull for connecting the connecting bar and piston.

Step 1	<ul style="list-style-type: none"> • Measure required amount of granite dust powder. • Put measured quantity into bowl
Step 2	<ul style="list-style-type: none"> • Measure gel • Mix With granite dust powder.
Step 3	<ul style="list-style-type: none"> • Measure required amount of high flash point oil. • Mix with step 2 mixture.
Step 4	<ul style="list-style-type: none"> • Measured abrasive (silicon carbide 120). • Mix with step 3 mixture.

Fig. 13.2 Synthesis method of media

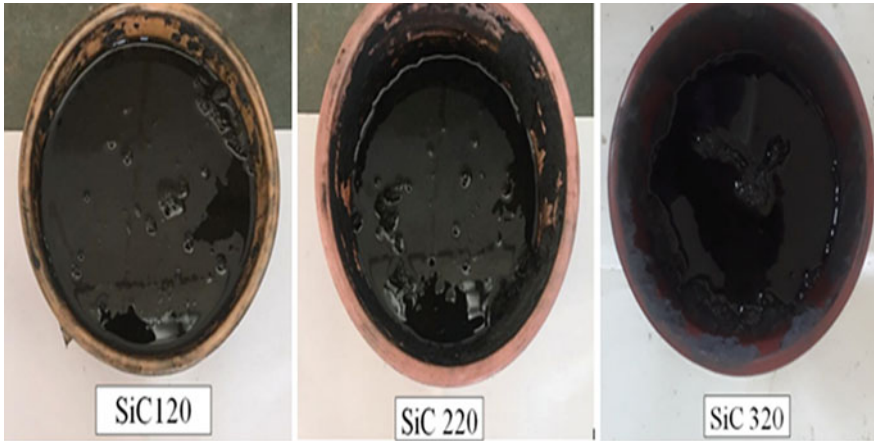


Fig. 13.3 Self-deformable abrasive flow media image

Table 13.1 VAFS parameter with variables

S. No.	Parameters	Variables
1.	Base material	Granite dust powder (50 g)
2.	Carrier	Gel (Aloe barbadensis Mill and Cyamopsis tetragonoloba powder) (6 g)
3.	Abrasive	Silicon carbide
4.	Abrasive mesh size	120, 220, 320
5.	Abrasive concentration (wt%)	30, 50, 70%
6.	Plasticizer	High flash point oil (20, 24, 28%)
7.	Workpiece	Gudgeon pin



Fig. 13.4 Workpiece images

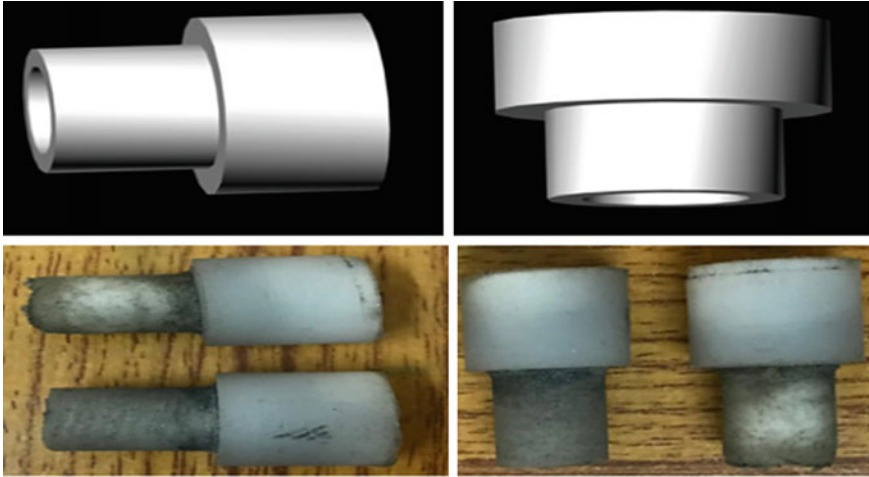


Fig. 13.5 Fixture image

Fixture for holding the workpiece is fabricated using lathe machine and designed ergonomically to reduce the time of workpiece mounting the design, as shown in Fig. 13.5. Fixture material used is nylon which is easy to machine and non-corrosive in nature.

Characterization of SDAFM

Fourier Transform Infrared Spectroscopy (FTIR)

The FTIR study shows the presence of amines, amides, alkanes, and aromatics that produce the elastic nature to the SDAFM. The peaks in Fig. 13.6 show various compounds present in the abrasive media and more present are alkanes in this sample. The more presence of alkanes is dominated, which produces the flexible nature of the carrier.

Field Emission Scanning Electron Microscopy (FESEM)

FESEM study for sample in Fig. 13.7 shows that the high-resolution image is captured by using a FESEM instrument with $500\times$ magnification and $5\ \mu\text{s}$ dwell with field-free lens mode. The image is showing how the abrasive media ingredient is mixed together and bonding between plasticizer and abrasive is observed.

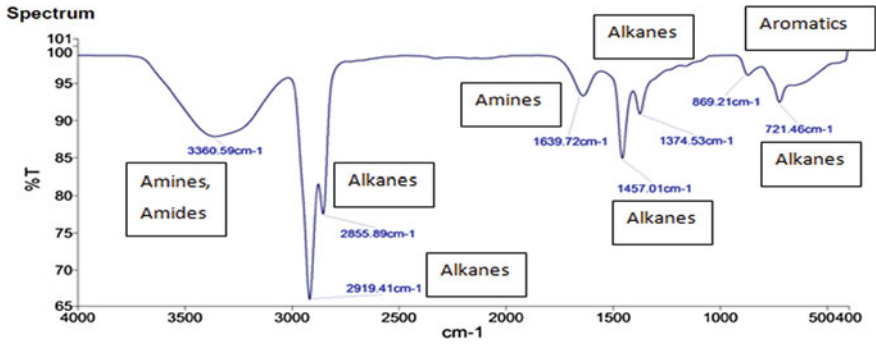


Fig. 13.6 FTIR analyses for media (mesh size 320, 30% abrasive concentration)

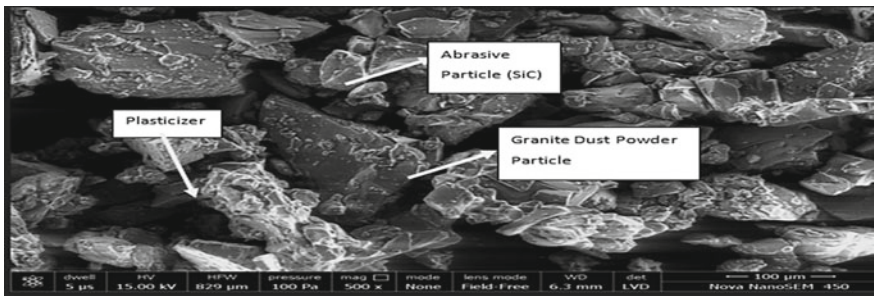


Fig. 13.7 SEM image of SDAFM with 220 mesh size and 70% abrasive concentration at 500× mag. with 5 μs Dwell

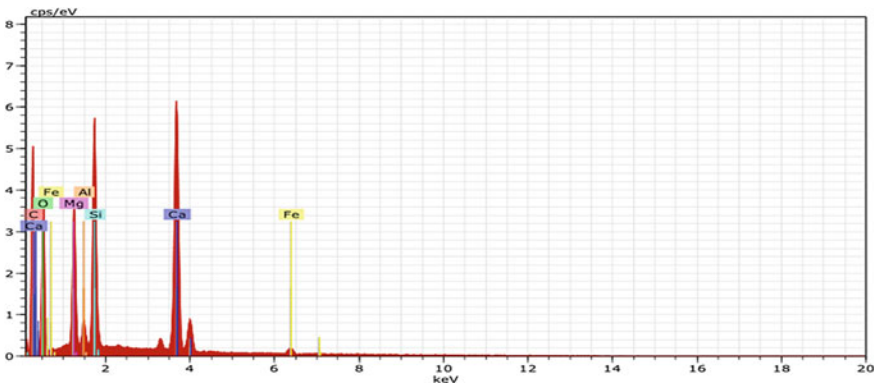


Fig. 13.8 Graph of elements for Sample 1 media

Figure 13.8 shows the graph generated by the data obtained from FESEM-EDS. In the graph, the x -axis represents kilo electron voltage (Kev) and the y -axis represents the count per second per electron voltage (cps/eV). From FESEM-EDS study the result shows the data on atomic number, atomic mass, and distribution of electrons in K, L, and M shells for the elements C, Ca, O, Si, Fe, Mg, Al.

Rheological Evaluation of the SDAFM

The rheological property of the media is a significant criterion for optimum surface finishing results in the AFM process. The viscosity of the media has considerable impacts on the AFM process performance. Hence, experimentations were performed to determine the impacts of mesh size, plasticizer %, percentage of the abrasive concentration, and temperature as mentioned in Table 13.2 on the media viscosity and the impacts of viscosity on surface roughness. Rheological studies were carried out for steady shear at various shear rates and the temperature is 20, 32, and 44 °C.

The abrasive (silicon carbide) is mixed with the base material and liquid synthesizer to gain a homogeneous mixture of different abrasive concentration. During the experimentations, the viscosity of abrasive media is additionally assessed by setting the temperature at 32 °C and shear rate at 100 s^{-1} so that the impact of abrasive mesh size, abrasive concentration, and liquid synthesizer on the abrasive media viscosity is determined. The study of the impacts of temperature on the viscosity of SDAFM samples is performed at various temperatures. After the study of the impacts of the media on its viscosity, samples of various grades of viscosity are used to study the viscosity effect on AFM performance. Table 13.3 presents the experimental outcomes for viscosity measurement for 27 set of different samples selected on the basis of design of experiments.

ANOVA Analysis

ANOVA and regression analysis was performed with the help of MINITAB 17 software. The study helps to know about the most significant parameter chosen as an input parameter. In Table 13.4, P -value indicates the significance of predictor term, which means if the P -value of any predictor term or factor is greater than 0.005 then the factor is insignificant and the effect of this factor on response parameter is less

Table 13.2 Process parameters and levels

Control factor	Level		
	I	II	III
A. Abrasive mesh size	120	220	320
B. % Abrasive concentration	30	50	70
C. % Liquid synthesizer	20	24	28
D. Temperature (°C)	20	32	44

Table 13.3 Viscosity measurement data for 27 set of different samples

S. No.	Abrasive mesh size	% Abrasive concentration	% Liquid synthesizer	Temperature (°C)	Viscosity (Pa s)
1	220	70	28	32	0.051500
2	220	30	20	32	0.037120
3	120	50	24	20	0.067543
4	220	50	28	20	0.107000
5	220	50	20	20	0.074300
6	320	30	24	32	0.121390
7	220	30	24	20	0.322400
8	120	70	24	32	0.231600
9	220	50	20	44	0.154800
10	220	30	24	44	0.041330
11	220	70	20	32	0.035239
12	120	50	20	32	0.070146
13	320	50	24	20	0.214200
14	120	50	28	32	0.087100
15	220	50	24	32	0.078725
16	120	50	24	44	0.388450
17	120	30	24	32	0.049600
18	320	50	24	44	0.125500
19	220	50	28	44	0.172000
20	220	70	24	44	0.430000
21	320	50	20	32	0.021673
22	220	50	24	32	0.094400
23	320	50	28	32	0.021326
24	220	30	28	32	0.050220
25	220	70	24	20	0.002370
26	220	50	24	32	0.102075
27	320	70	24	32	0.031790

than other parameters. Highest F -value with predictor term has the most remarkable input factor.

Table 13.5 shows that the designed model for viscosity fits about 98.74% of data points with an average distance of 0.0154100 from the fitted line and can be able to predict the response of new observations with accuracy of 96.51%.

Regression Analysis

Regression analysis is performed to estimate the relationship between independent and dependent variables. The main reason for creating a regression equation is to minimize the sum of squared error.

Table 13.4 Analysis of variance for viscosity

Source	DF	Adj SS	Adj MS	F-value	P-value
Regression	9	0.317293	0.035255	148.46	0.004
Mesh size	1	0.010714	0.010714	45.12	0.008
% Abrasive con.	1	0.002145	0.002145	9.03	0.009
% LS	1	0.000766	0.000766	3.23	0.005
Temp. (°C)	1	0.022905	0.022905	96.45	0.003
% LS * mesh size	1	0.024456	0.024456	102.98	0.007
Temp. (°C) * LS	1	0.052264	0.052264	220.09	0.006
Mesh size * %Abrasive con.	1	0.018442	0.018442	77.66	0.002
Mesh size * Temp. (°C)	1	0.041945	0.041945	176.63	0.008
%Abrasive con. * Temp. (°C)	1	0.125564	0.125564	528.76	0.006
Error	17	0.004037	0.000237		
Total	26	0.321330			

Table 13.5 Predicted summary for viscosity

S	R-sq	R-sq (adj)	R-sq (pred)
0.0154100	98.74%	98.08%	96.51%

The regression equation for viscosity is = $-1.403 + 0.004129$ Mesh Size— 0.03097% Abrasive concentration + 0.3749% LS— 0.05466 Temp. (°C)— 0.01545% LS * % LS + 0.000628 Temp. (°C) * Temp. (°C)— 0.000068 Mesh Size * % Abrasive concentration— 0.000085 Mesh Size * Temp. (°C) + 0.001476% Abrasive concentration * Temp.

Relationship of Viscosity with Different Input Factors

The viscosity of media during finishing process has a significant impact on the surface roughness. The effect of liquid synthesizer, temperature, abrasive concentration, and mesh size on viscosity is discussed in below section.

Effect of Mesh Sizes on Viscosity

Figure 13.9 shows the effect of the decrease in viscosity with abrasive mesh sizes. This is due to the increase in the quantity of extruded material that affect the abrasive media flow rate and pressure gradient and results in decrease in viscosity.

Effect of Percentage of Liquid Synthesizers on Viscosity

Figure 13.10 shows the effect of percentage of liquid synthesizer on viscosity. The viscosity will decrease due to the increase in percentage liquid in gel which results in flow ability and viscosity will decrease.

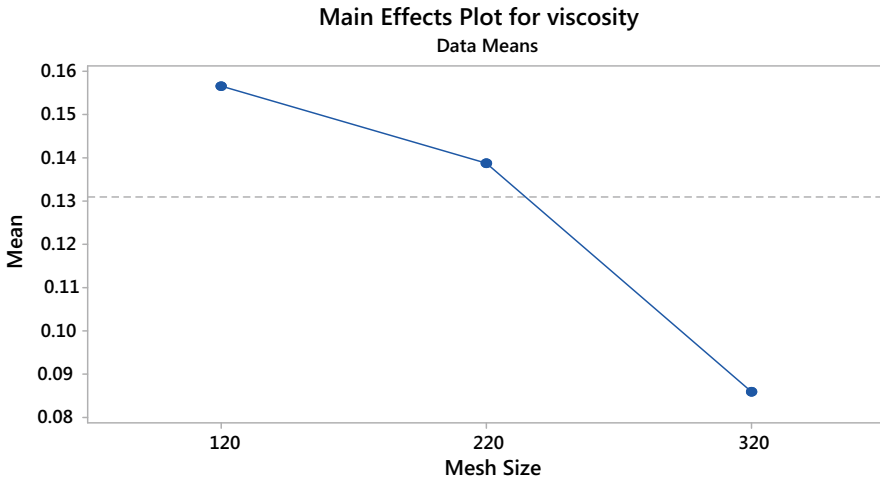


Fig. 13.9 Effect of abrasive mesh size on viscosity

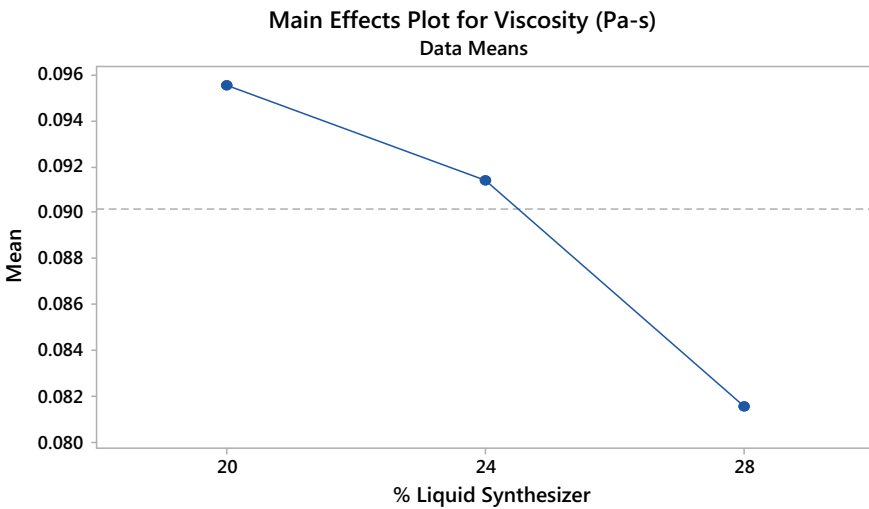


Fig. 13.10 Effect of percentage of liquid synthesizer on viscosity

Effect of Percentage Abrasive Concentration on Viscosity

Figure 13.11 shows the effect of abrasive concentration on viscosity. The viscosity will increase due to the decrease in the mobility of particles in the abrasive media. So with increase in abrasive concentration the viscosity decreases.

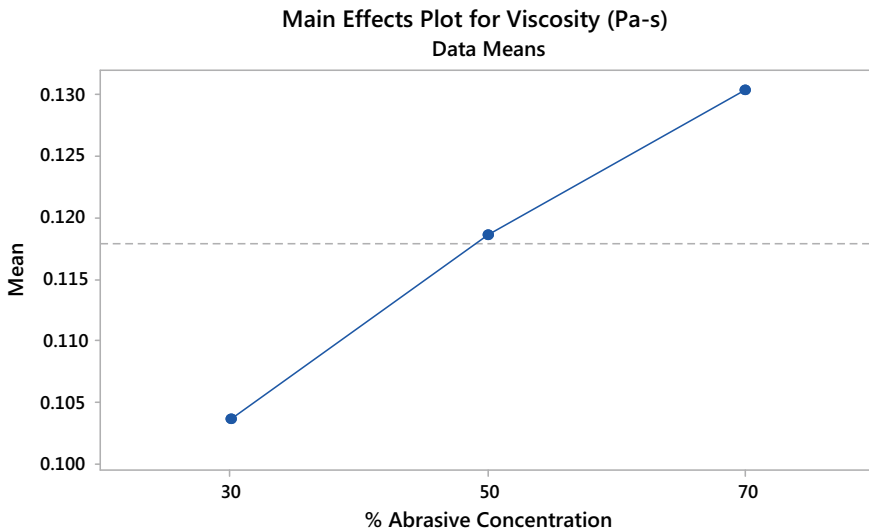


Fig. 13.11 Effect of percentage abrasive concentration on viscosity

Performance Study of SDAFM

Design of Experiment (DOE)

In this experiment, four process parameters, liquid synthesizer, finishing time, mesh size, and abrasive concentration, are considered as control factors. Each parameter has three-levels: low, medium, and high level. Four parameters with three levels are used in response surface design. L27 orthogonal array approach is used for the experiment. Table 13.6 shows the results of experiment performed as per the design of experiment.

Effect of Mesh Sizes on Average Surface Roughness (ΔR_a)

Figure 13.12 shows the decrease in surface roughness value with increase in the abrasive mesh sizes due to finer abrasive particles to create smaller indent on the finishing surface. This action provides a highly surface quality but unable to indent deeper.

Table 13.6 Results of experiment performed

S. No.	Abrasive mesh size	%Abrasive concentration	%Liquid synthesizer	Finishing time (minutes)	Improved surface roughness (μin)			
					ΔR_p	ΔR_a	ΔR_q	ΔR_z
1	220	75	45	9	240	55	68	8
2	220	60	30	9	208	68	145	101
3	220	90	60	9	216	21	67	397
4	220	90	30	9	32	50	13	80
5	120	75	30	9	28	3	5	44
6	220	75	30	11	25	32	14	64
7	220	60	45	11	59	33	28	103
8	220	90	45	11	261	104	141	590
9	320	60	45	9	12	13	5	18
10	320	75	45	7	107	43	51	158
11	120	75	45	11	6	11	2	9
12	120	60	45	9	119	32	24	140
13	220	75	30	7	28	16	22	95
14	120	75	45	7	37	17	29	261
15	220	75	45	9	150	21	40	212
16	220	75	45	9	270	73	96	466
17	220	75	60	11	22	4	6	61
18	320	75	45	11	166	36	76	431
19	220	75	60	7	53	14	22	77
20	220	60	60	9	47	10	14	85
21	120	75	60	9	632	130	303	59
22	220	60	45	7	4	54	2	10
23	320	90	45	9	204	21	53	301
24	320	75	30	9	517	74	187	919
25	320	75	60	9	248	25	83	423
26	220	90	45	7	28	9	3	44
27	120	90	45	9	250	58	80	542

Effect of Abrasive Concentration on Average Surface Roughness (ΔR_a)

Figure 13.13 shows increase in average surface roughness with increase in the abrasive concentration. This is due to more number of abrasive particles taking part in machining process and continues to remove fresh material from the work surface contributing to the increase in average surface roughness.

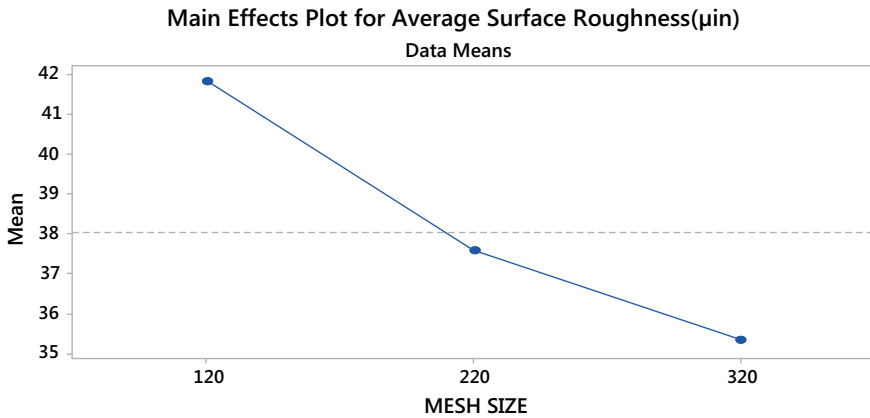


Fig. 13.12 Effect of mesh sizes on average surface roughness

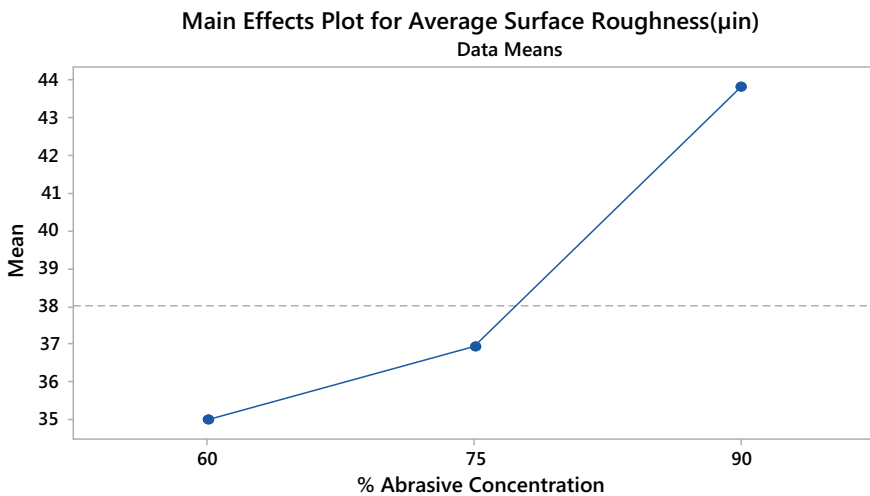


Fig. 13.13 Effect of abrasive concentration on average surface roughness

Effect of Liquid Synthesizer on Average Surface Roughness (ΔR_a)

Figure 13.14 shows decrease in surface roughness with increase in the liquid synthesizer due to weak bonding between the abrasive particles and polymer chains at low values of plasticizer and no effective transfer of radial force and axial force from polymers chains to abrasive particles.

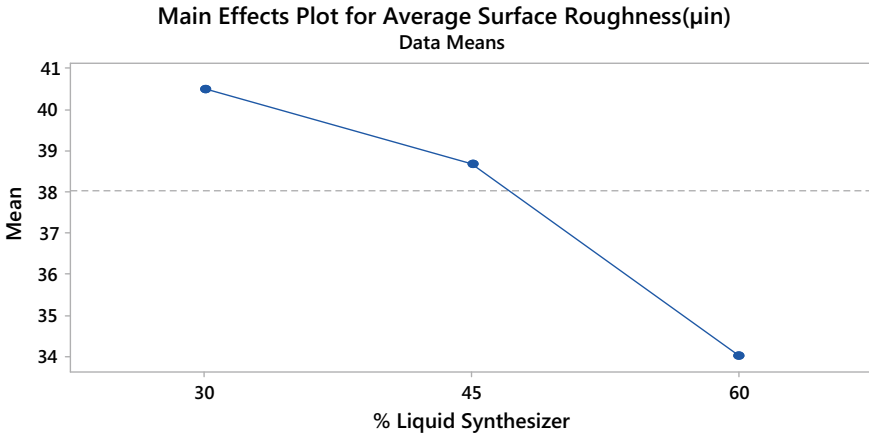


Fig. 13.14 Effect of liquid synthesizer on average surface roughness

Effect of Finishing Time on Average Surface Roughness (ΔR_a)

Figure 13.15 shows increase in average surface roughness with the finishing time. In the initial finishing time, the average surface roughness increases and then decrease in R_a value due to initial peak removed in initial cycles.

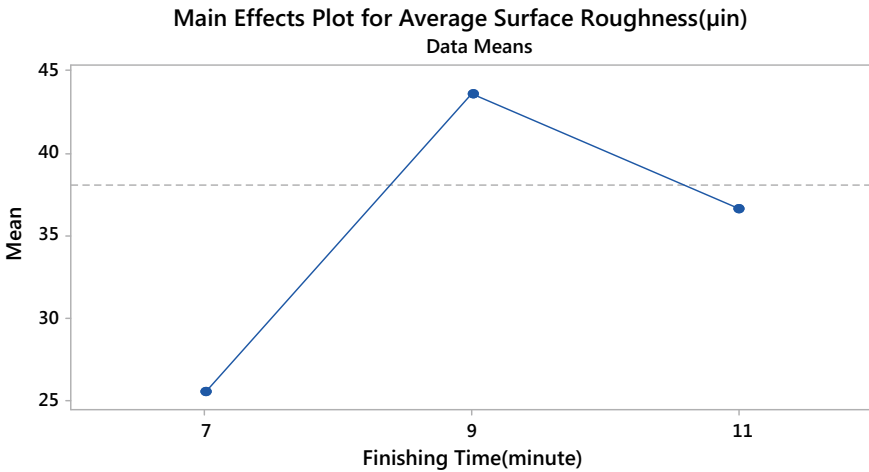


Fig. 13.15 Effect of finishing time on average surface roughness

Conclusion

In the current study the abrasive media (self-deformable abrasive flow media) is synthesized using industry waste, which is further used in abrasive flow machine for finishing application. Abrasive media have the property of no-adhesiveness, permeability, porosity, and thermal stable. During synthesization granite dust powder, gel, high flash point oil, and silicon carbide (abrasive mesh sizes 120, 220, 320) were used in SDAFM. Summary of conclusion is listed in the following:

1. Media developed is environmentally sustainable and less costly as compared with commercially available media.
2. Significant effect of abrasive concentration, abrasive mesh sizes, percentage of liquid synthesizer, temperature on viscosity of media was observed during experimentation.
3. There is significant effect of abrasive concentration, liquid synthesizer, and finishing time on average surface roughness.

Acknowledgements The author is thankful to TEQIP-III for providing the financial support for smooth conduction of experimental studies. Also, the author is thankful to “MNIT Jaipur” which gave the permission to perform experimental studies on abrasive media.

The author gratefully acknowledge the financial support of this study by CRS Project under TEQIPIII (project no. 15757174289) and Dr. Harlal Singh Mali (Co-PI) MNIT Jaipur as a Collaborative Institute (Material Research Centre and Advanced Mfg. & Mechatronic Lab) and Dr. Alok Khatri (Co-PI) for providing the experimental support to complete the research work smoothly.

References

1. Marras V, Careddu N, Internicola C, Siotto G (2010) Recovery and reuse of marble powder by-product. In: Global Stone Congress, pp 1–5
2. Almeida N, Branco F, Santos JR (2007) Recycling of stone slurry in industrial activities: application to concrete mixtures. *Build Environ* 42(2):810–819. <https://doi.org/10.1016/j.buildenv.2005.09.018>
3. Wang CY, Clausen R (2002) Marble cutting with single point cutting tool and diamond segments. *Int J Mach Tools Manuf* 42(9):1045–1054. [https://doi.org/10.1016/S0890-6955\(02\)00032-9](https://doi.org/10.1016/S0890-6955(02)00032-9)
4. Jain VK (2009) Investigations into abrasive flow finishing of complex work pieces using FEM. *Wear* 267(1):71–80. <https://doi.org/10.1016/j.wear.2008.11.005>
5. Kar KK (2009) Performance evaluation and rheological characterization of newly developed butyl rubber-based media for the abrasive flow machining process. *J Mater Process Technol* 209(4):2212–2221. <https://doi.org/10.1016/j.jmatprotec.2008.05.012>
6. Sankar MR, Jain V, Ramkumar J (2009) Experimental investigations into rotating workpiece abrasive flow finishing. *Wear* 267(1):43–51. <https://doi.org/10.1016/j.wear.2008.11.007>
7. Gorana V, Jain V, Lal G (2004) Experimental investigation into cutting forces and active grain density during abrasive flow machining. *Int J Mach Tools Manuf* 44(2):201–211. <https://doi.org/10.1016/j.ijmactools.2003.10.004>

8. Singh S, Shan HS, Kumar P (2008) Experimental studies on mechanism of material removal in abrasive flow machining process. *Mater Manuf Processes* 23(7):714–718. <https://doi.org/10.1080/10426910802317110>
9. Sambharia J, Mali HS (2017) Recent developments in abrasive flow finishing process: a review of current research and future prospects. *Proc IMechE Part B: J Eng Manuf* 223(2):1–12. <https://doi.org/10.1177/0954405417731466>
10. Davies P, Fletcher A (1995) The assessment of the rheological characteristics of various poly borosiloxane/grit mixtures as utilized in the abrasive flow machining process. *Proc Inst Mech Eng, Part C: J. Mech Eng Sci* 209(6):409–418. https://doi.org/10.1243/PIME_PROC_1995_209_171_02
11. Mali HS, Manna A (2010) Optimum selection of abrasive flow machining conditions during the fine finishing of Al/15 wt% SiC-MMC using the Taguchi method. *Int J Adv Manuf Technol* 50(9–12):1013–1024. <https://doi.org/10.1007/s00170-010-2565-y>
12. Cheema MS, Venkatesh G, Dvivedi A (2012) Developments in abrasive flow machining: a review on experimental investigations using abrasive flow machining variants and media. *Proc IMech, Part B: J Eng Manuf* 226(12):1951–1962. <https://doi.org/10.1177/0954405412462000>
13. Agrawal A, Jain VK, Muralidhar K (2005) Experimental determination of viscosity of abrasive flow machining media. *Int J Manuf Technol Manag* 7(2–4):142–156. <https://doi.org/10.1504/IJMTM.2005.006828>

Chapter 14

Enhancement of Electric Hybrid Vehicle



Dhyey R. Savaliya , Vaibhav M. Dholariya , Uttam B. Khunt ,
Abhishek Singh , Monik M. Dholariya , and Jenish H. Patel 

Introduction

An electric bicycle is a system of different components that improve the ride comfort with less effort, hence gives a smooth ride to the driver. Light electric vehicles are reducing urban vehicle overcrowding and local pollutant emissions [1]. Every electric vehicle has three goals: Increase the top speed of vehicle, increase the timespan of battery in a single charge and decrease the driver's effort. Solutions to the above problems are: Top speed is increased by the implementation of electric motor. The timespan of battery in a single charge is increased by using smart charging system in vehicle. By the use of electric motor, the pedaling time is decreased, so the driver's effort is also decreased. The bicycle has been an old-fashioned recreational product to a less polluting means of transportation and a compact, ultra-light personal mobility appliance [2].

For humans traveling has become essential. In order to stay with this fast-forward world, we need to travel from one place to another. It is very important that traveling time is very less with less efforts. Also it should be economical and easily available. With the fast-consuming resources of petrol and diesel, there is a need to find other different choice. Taking all this into account, a shift away from conventional-based fuels to using renewable sources of energy is necessary. Electric bike, which will

D. R. Savaliya (✉) · U. B. Khunt · J. H. Patel
Department of Automobile Engineering, Uka Tarsadia University, Surat 394350, India
e-mail: savaliyadhyye1997@gmail.com

V. M. Dholariya · A. Singh
Department of Mechanical Engineering, Uka Tarsadia University, Surat 394350, India

M. M. Dholariya
Department of Electrical Engineering, Uka Tarsadia University, Surat 394350, India

be driven by battery thus provides the required voltage to the motor by using some motor controller [3].

With the advancement in the bicycle industry, significant challenges are posed on the bicycle electric system. It involves a complex recharging system, which is used to replace the regenerative braking system, which results in improvement of fuel economy. The regeneration is better for single, three-switch method and stopping time is better for two switch and plugging [4]. E-bike helps in smooth and safe drive at a cost-effective price and it is a user-friendly vehicle [5]. E-bikes has less pollution, low maintenance cost, reduces noise as compared to conventional IC engine bikes. These bikes use chemical energy stored in the rechargeable battery packs [6].

Modern world demands high technology that gives solutions to the current and future problems. Fossil fuel shortage is the main problem nowadays. Considering the current ratio of usage of fossil fuels will let its life up to only next few decades. Undesirable climate changes are the red indication for not to use more fossil fuel any more. Best alternative for the automobile fuels to provide the mobility and transportation of peoples is by sustainable electrical bike. Future e-bike is the premier technical application as a visionary solution for the better world and the next generation. E-bike comprises the features like high mobility efficiency, compact in size, electrically powered, comfortable riding experience, lightweight vehicle [7]. An e-bike offers a cleaner travel, normally short to medium distance instead of fossil-fueled automotive. From conventional automobile for transportation, we experience problems like traffic congestion, parking difficulties, and pollution from fossil-fueled vehicles [8].

E-bike

An electric bicycle is also known as e-bike, e-motor bike. It is a bicycle with an electric motor and different arrangement used to run the bike. Power diagram of an e-bike is given in Fig. 14.1. Low-power e-bikes use small motor that is used to assist the rider's pedal-power. More powerful e-bikes are very closer to moped-style functionality: if the rider pedals during the ride then it is not an electric motorcycle.

E-bikes use rechargeable batteries, which provide electricity backup up to 25–35 km/h, depending on different laws, while more high-powered e-bike can run up to 45 km/h (28 mph).

E-bikes are the electric motor-powered version of motorcycle, which have been in use since the late nineteenth century.

E-bikes are the mechanical connection between the pedal and the wheel, as the power transmission is purely electric. This principle allows the cyclist to always pedal in optimal conditions and provides more freedom to the designer to effect the pedal feel and the cyclist's effort [1].

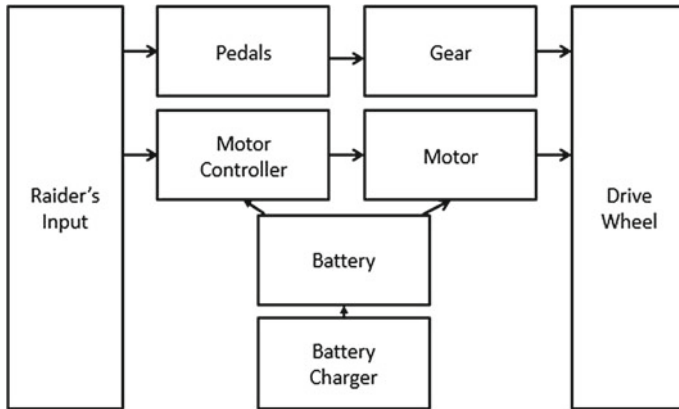


Fig. 14.1 Power diagram

Classes of E-bike

The classification of e-bikes is mainly decided on its power train. The motor of e-bike assists the rider using a pedal assist system or by a power on demand one. These can be defined as follows: In pedal assist system motor is regulated by pedaling. The pedal assist increases the effort of rider when he is pedaling. These e-bikes are known as pedelecs. These kinds of e-bikes have a sensor to detect the speed of pedalling, force of pedalling or both. If they sense the brake activation then they disable motor also.

In power on demand: Throttle is used to active the motor and this throttle is placed on the handlebar like in motorcycles or mopeds or scooters.

Thus, e-bikes can be classified as: Pedelecs or S-Pedelecs.

Pedelecs: It has pedal assist or motorassist. This type of bike has maximum speed of 25 km/h and mainly its motor power is less than or equal to 250 W, so it is legally placed in bicycles.

S-Pedelecs: It has only pedal assist system. This kind of bikes uses more than 250 W motor power, so its maximum speed is also higher than pedelecs. Its maximum speed is around 45 km/h. So it is legally classed as a moped because of its speed.

Motors and Drive Train

There are many types of motor used in e-bikes, like hub motor, brushed or brushless motor, geared motor and so on. There are many arrangements available in different complexities as per different cost. The electric power assists system used with chain drive or belt drive. The power of motor is transmitted through the chain and sprocket

arrangement. The power of motor is changed between 250 and 750 W to protect fast wear in drive train.

Battery

Normally e-bikes use rechargeable batteries. There are different types of battery available in the market. for example: lead-acid (SLA), nickel metal hydride (NiMH), nickel cadmium (NiCd) and lithium-ion (Li- ion). There are also different varieties of battery as per the voltage, weight, total charge capacity (Ah), ability to handle overcharging condition, number of cycles before losses in performance. The running cost of e-bike is very less but the battery replacement cost is high. The lifespan of battery depends on the type of use. Schematic charge/discharge cycles can help to increase the overall battery life. Transport vehicles are considered as one of the biggest contributors for global warming and air pollution. With the main focus on environment protection, many researches have been done to the development of electric vehicles (EVs). It has already been widely accepted that EV is a promising transportation alternative due to its high reduction in greenhouse gas emission and air pollution. Battery energy storage system is very important to energy storage and plays a major role in EVs. Among different kinds of batteries lithium-ion battery is the fastest developed and proved to be the most promising component for energy storage [9]. Battery is the most sensitive part in the powertrain of full e-bike or e-vehicle because of its cost and weight. The full electric vehicle range and price are mainly dependent on the battery performances [10]. Battery is the most sensitive element in hybrid powertrain, so a large recover current can cause damage to the battery and reduce its life. Nevertheless, the damage to be usually ignored in regenerative braking [11].

Battery Comparison

1. LEAD-ACID BATTERY (SEALED)

Normally these kinds of batteries are simple to manufacture and cheap in cost. This technology is well-known and reliable. This battery has lowest self-discharge rate in all rechargeable batteries. But we are not able to store these batteries in discharged condition. Lead acid battery has low energy density.

2. LITHIUM-ION BATTERY

This battery has the highest energy density to weight ratio and no memory effect. Li-ion-cobalt is the most developed Li-ion technology with flexible shape options. These batteries need periodic care for long life. However, these kinds of batteries can easily damage by discharge or over charge. All the lithium-ion technologies require a protection circuit to prohibit the overheating.

3. NICKEL CADMIUM BATTERY

Mostly these kinds of batteries have long shelf life in any state of charge and are available in wide range of sizes and performance options. These batteries have high discharge capacity. We are able to do fast and simple charging even after prolonged storage. On the other hand these kinds of batteries have relatively low energy density when compared with newer system and also high self-discharge rate. These batteries are environmentally unfriendly because of some toxic contained in NICD batteries.

System Parts with Specification

We used a simple bicycle with V type brakes having a tire size of 26 in. and frame size around 19.7 mm (Fig. 14.2). Another main part is a PMDC type motor attached to the bicycle, which runs on a 24-V power and gives power output of 250 W. The RPM after reduction is 300 on full load current of 13.4 A and no load current 2.2 A (Fig. 14.3). We can achieve 8 Nm constant torque and stall torque up to 40 Nm. In order to control the motion of the motor a PMDC motor controller is used which runs on 13.2 mA current and 24 V. It runs upon 250 W power. The throttle required for the acceleration of bicycle is a twist-type throttle with inner diameter 23 mm, weight 210 g and a wire length around 1.56 m. We need a DC–DC booster to charge our battery. The XL6009 boost module costs less and delivers superior performance. The best working voltage range is 5–32 V with the super-wide boost output voltage of 5–35 V. It also has circuit protection, overheating protection and short-circuiting protection. The motor is run by two batteries of 12 V with ampere rating 26 Ah. The battery comes with sealed maintenance free up to 24 months warranty and weighs

Fig. 14.2 Pedal system



Fig. 14.3 Motor system

up to 9 kg and occupies $167 \times 126 \times 175$ mm ($l \times b \times h$). For this work, we used lead acid battery just because of cost.

Methods of Producing Regenerative Energy

By Using Arduino and L293d

All Arduino circuits works on 5 V and our motor uses 9 or more than 9 V, so we cannot directly run the motor threwh Arduino; hence we need a device that can run on both voltage and operate our system. In addition, L293D is one of the best suitable IC which can easily operate motor and Arduino (Fig. 14.4). In L293D V_{ss} : continuous 5 V input on V_{ss} is necessary to operate the circuit. Enable 1/2: here enable 1 and enable 2 both are in opposite direction. To operate any one side of this circuit we need to supply 5 V high pulse on that side enable pin. Output 1/2/3/4: Output 1 and 2 both are on the same side and output 3 and 4 are on the opposite side. All these output pins are designed to connect with motor. Vs: this pin is connected to our external power supply like battery but battery has two terminals so we need two pins to connect battery with circuit. This Vs pin is used to connect to positive terminal of battery. GND: GND 1 and GND 2 are on the same side of the circuit and GND 3 and 4 are on the opposite side of the circuit. Here, full form of GND is GROUND. We can directly connect negative terminal of the battery on any of this one. In addition, Arduino ground pin is connected to any of this one. Input 1/2/3/4: these are connected with motor so that we can easily operate the motor. For example: when we give high

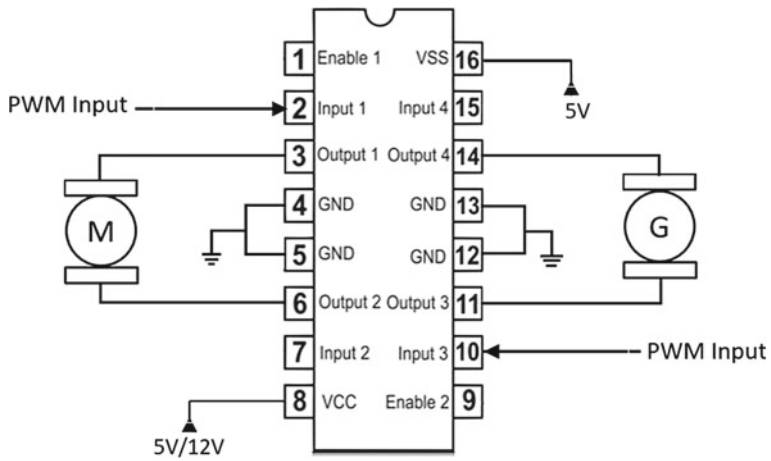


Fig. 14.4 L293D circuit diagram

pulse on input 1 and low pulse on input 2 at that time our left-hand side motor is run in forward direction and the same is applicable for vice versa (Fig. 14.5).

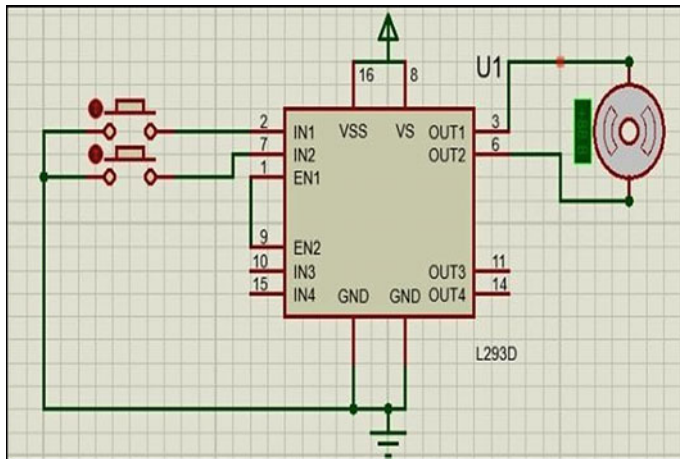


Fig. 14.5 Circuit diagram of L293d with switching

Arduino Coding

```

#define m1 2
#define m2 3
#define m3 4
#define m4 5
Void setup ()
{
pin Mode (m1, OUTPUT);
pin Mode (m2, OUTPUT);
pin Mode (m3, OUTPUT);
pin Mode (m4, OUTPUT);
}
Void loop ()
{
//forward
Digital write (m1, HIGH);
Digital write (m2, LOW);
//backward
Digital write (m3, LOW);
Digital write (m4, HIGH);
}

```

By Using Switching Method

Rider with the help of pedals runs conventional bicycles (Fig. 14.6) and the power-train of electric bicycle is simpler than the bicycle with energy regenerative system (Fig. 14.7). As shown in Fig. 14.8 energy regenerative system can be operating by some steps which are shown as below (Fig. 14.8) Start the e-Bike. When we press the accelerator pedal at that time current flows from battery to motor through controller, then wheel is rotated and bike is propelled. When we need to decelerate the vehicle without braking at that time press the switch so that current from the battery is cutoff and the motor works as a generator. At that same time our generator generates nearly about 3–15 V so that we are not able to charge 24 V battery system. We can use

Fig. 14.6 Power train of a Bicycle

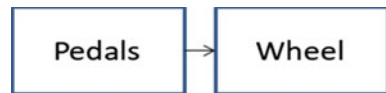


Fig. 14.7 Power train of e-bike

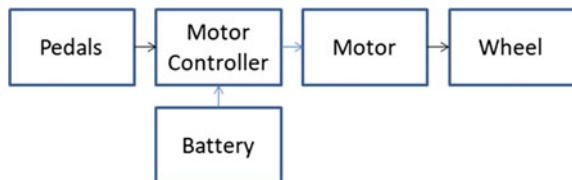
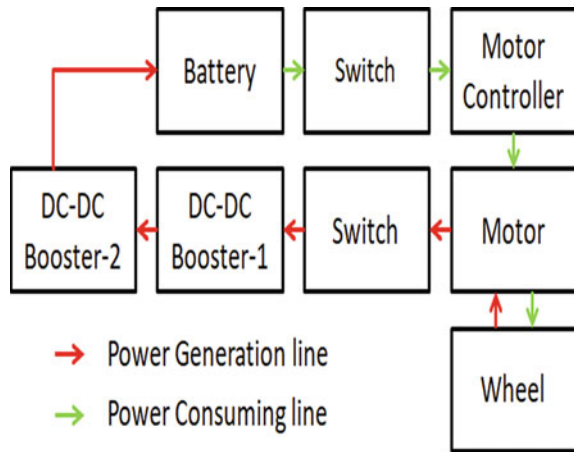


Fig. 14.8 Power train of e-bike with energy regenerative



DC–DC booster to boost the voltage so that we can charge the battery. When we use only one booster at that time, the booster is not able to boost the voltage and current levels to charge the battery sufficiently; hence we can use two booster circuits. To charge the battery with 6 A and 30 V, this current and voltage level is able to charge the battery rapidly. All the above conditions are applicable for braking application, but in braking, the charging of the system is very less. Therefore braking charging time is not much more efficient. When this energy regenerative system is on then at that time we are not able to accelerate the vehicle. Switch off the energy regenerative system to again accelerate or run the vehicle.

Calculation

Vehicle Speed Calculation

$$\begin{aligned}
 T2/T1 &= N1/N2 \\
 18/14 &= 300/N2 \\
 N2 &= 256.66 \text{ R.P.M.}
 \end{aligned}
 \tag{14.1}$$

where,

- T2 = Driven Gear Teeth
- T1 = Driving Gear Teeth
- N2 = Driven Gear Speed
- N1 = Driving Gear Speed

$$\begin{aligned}
 V1 &= r * \omega \\
 &= 0.33 * 2 \text{ N2}/60 \\
 &= 0.33 * 2200/60 \\
 &= 8.8652 \text{ m/s} \\
 &= 31.91496 \text{ km/h}
 \end{aligned}
 \tag{14.2}$$

where,

$V1 = \text{Minimum Speed (km/h)}$

Charging Time Calculation

Battery : 24 v 35 Ah Charger : 24 v 7 Ah

For Battery : Current(I) = 35 Ah

For Charger : Current(I) = 7 A

$$\begin{aligned}
 \text{Charging Time} &= \text{battery current rating} \div \text{charger current rating} \\
 &= 35/7 \\
 &= 5 : 00 \text{ h}
 \end{aligned}
 \tag{14.3}$$

Experimental Result

In the current time there are number of e-vehicles available in the market. They do not have regenerative system. So we developed this regenerative system. In the traditional electric cycles BLDC motors are used but in our system we used PMDC motor because it has no input power consumed for excitation, which improves the efficiency of DC motor. No field coil hence space for field coil is saved which reduces the overall size of the motor. Cheaper and economical for fractional kW rated applications as compared with BLDC motor. In our system, we have innovated two methods which are cheaper, simple in construction, less maintenance and easy to operate. In the operation, we have achieved the highest speed up to 35 km/h by changing the gear ratio of motor driving gear and wheel sprocket gear. We need this change because this only enables the motor to give max. speed of 15 km/h with the available traditional gear set. Under the condition that the motor and wheel gear ratio is 1:1. When we apply the 1:1.28 gear ratio (in other words motor has 14-teeth gear and wheel sprocket has 18-teeth gear set) (Eq. 14.1) we get nearly about 27 km/h speed with around 110 kg weight, which is better than the currently available gear set in the market (Eq. 14.2). The changes made are in our favor as our main goal is to regenerate the electricity when vehicle is in deceleration mode. When we attach the

motor at the wheel gear set in 1:1 ratio and if vehicle starts to decelerate, then at that time huge amount of load is transmitted to motor through wheel, so the problem of slipping of chain arises. Electricity regeneration can be done by many conventional methods, like by using different conventional ICs but we did the same thing in a different way for reduction in cost. Therefore, we need to fix clearance between both gears. We have used regenerative braking system using electrical switches and connected the electrical wires so that it is easy to operate and control. After the testing of recharging system, the charging voltage obtained is of the range 25–32 V and the current rating is 1.5–4.7 A, which is sufficient to charge the 24 V battery. Using this method, we can easily reduce the cost of the system largely and increase the efficiency because of a smaller number of components used in this system. If we use 24 V, 35 Ah battery and 24 V 7 A charger, then it take around 5 h to charge the full battery (Eq. 14.3).

Conclusion

From the above theoretical calculation and practical experimentation, we conclude that by changing the gear ratio the speed of vehicle is increased. By using the regenerative system we are able to generate the energy and with this energy we are able to charge the battery up to 30%.

If one vehicle can save about an average of 30% of energy, then an average of about 30–40% of charging electricity is conserved by using this type of vehicle. In addition, electric bill can also be reduced, as the battery can last long per charge.

The durability and convenience to consumer can be improved by using this type of vehicle. Charging of lead acid batteries can be done when vehicle is in motion and accelerator in rest condition. Thus, a number of different aspects with the use of e-bike in different situations emerge. These include lower energy cost per distance traveled for a single rider, savings in other costs such as insurance, license, registration, parking, and improvement of traffic flow, environmental friendliness, and the health benefits of the rider.

We can conclude that this e-bike is efficient and can reduce energy losses. It is economical for human being. E-bike has zero-pollution emission. Therefore, less pollution reduces the traffic visibility problem in city. E-bikes do not affect the environment and does not contribute to global warming effect. By using this kind of electric vehicle we can save our environment. In future, we can reduce the undesirable climate change by less use of conventional IC engines and more use of e-vehicles.

References

1. Guanetti J, Formentin S, Corno M, Savaresi SM (2017) Optimal energy management in series hybrid electric bicycles. *Automatica* 81:96–106
2. Salmeron-Manzano E, Manzano-Agugliaro F (2018) The electric bicycle: Worldwide research trends. *Energies* 11:1–16
3. Shinde Kung D (2017) Literature Review on Electric Bike. *IJRMET Int J Res Mech Eng Technol* 7:2249–5762
4. Joseph Godfrey A, Sankaranarayanan V (2018) A new electric braking system with energy regeneration for a BLDC motor driven electric vehicle. *Eng Sci Technol Int J* 21:704–713
5. Pothirasan N, Rajasekaran MP, Muneeswaran V (2018) Real time reactive power compensation for battery/photovoltaic hybrid power source for internet of hybrid electric vehicle system. *Cogn Syst Res* 52:473–488
6. Katoch S, Rahul Bindal R K (2019) Design and implementation of smart electric bike eco-friendly. *Int J Innov Technol Explor Eng* 8:965–967
7. Trivedi MM, Budhvani MK, Sapovadiya KM, Pansuriya DH, Chirag D (2017) Design & development of E-bike—a review. *Des Dev of E-Bike—A Rev* 1:36–43
8. Sharma Y, Banker P, Raikwar Y, Chauhan Y, Sharma M (2018) R&D on Electric Bike, 610–614
9. Liu D, Song Y, Li L, Liao H, Peng Y (2018) On-line life cycle health assessment for lithium-ion battery in electric vehicles. *J Clean Prod* 199:1050–1065
10. Redondo-Iglesias E, Venet P, Pelissier S (2018) Calendar and cycling ageing combination of batteries in electric vehicles. *Microelectron Reliab* 88–90:1212–1215
11. Wu J, Wang X, Li L, Qin C, Du Y (2018) Hierarchical control strategy with battery aging consideration for hybrid electric vehicle regenerative braking control. *Energy* 145:301–312

Chapter 15

Extraction of Phenolic Compounds from the Waste of *Borassus flabellifer*: A Step Toward Waste Valorization



Akshay Y. Bageshwar and Meghal A. Desai 

Introduction

Consumption of fruits and vegetables by humans has been observed from ancient times. Scientific studies have shown the positive effect of increased consumption of such fruits and vegetables toward preventing disease-causing conditions because of the presence of phytochemicals [1–3]. Polyphenols, vitamins, minerals, proteins, flavonoids and phenolic acids are the examples of phytochemicals that provide numerous immunity benefits due to antioxidant, antifungal, antibacterial activities and so on. Chemicals like polyphenols act as antioxidant and help in scavenging active oxygen species [4]. Reactive oxygen species (ROS) and various oxygen-centered free radicals keep on developing in human body which resulted in the death of cell and damage to the tissue. Cancer, cardiovascular problems and so on are implicated due to such oxygen species and radicals [5]. Oxidation is a process which is naturally occurring in the human body; hence, there is a need to balance the functioning of body by introducing antioxidants to maintain good health. Butylated hydroxyl anisole (BHA) and butylated hydroxy toluene (BHT) are the majorly used synthetic antioxidants which are effective but with some side effects [6]. Hence, there is a growing interest in searching antioxidants from natural resources. Further, promotion of the national health care programs by Government of India encourages the use of traditional herbal medicine since such drugs are easily available, show less or no side effects and have earned trust [7]. It has, therefore, become important to classify and estimate the required components in fruits and vegetables so as to obtain the benefits for health. One such natural source of phenolic contents is *Borassus flabellifer* Linn, commonly known as palmyra palm or doub palm. It is cultivated around the tropical

A. Y. Bageshwar · M. A. Desai (✉)
Chemical Engineering Department, Sardar Vallabhbhai National Institute of Technology, Surat
395007, Gujarat, India
e-mail: mad@ched.svnit.ac.in; desai_ma@yahoo.co.in

regions of India. Some countries like Thailand, Malaysia, Indonesia, Myanmar and Sri Lanka also cultivate palmyra palm on a large scale due to favorable climatic conditions [8].

B. flabellifer is known to be used for multiple purposes, viz., anti-laprotic, diuretic, analgesic, antipyretic, antiarthritic antiphlogistic and anti-inflammatory actions. The different parts of the tree have been used in curing various diseases, like fruit is useful in curing hyperdipsia, dyspepsia, skin diseases and fever [9–13]. The extract of the roots of this tree contained various phenolic compounds, that is, tannins, alkaloids, glycosides, terpenoids, flavonoids and saponins [14]. The phytochemical analysis of fruit of *B. flabellifer* has shown the presence of carbohydrates, amino acids, saponins, tannins, flavonoids and phenolic compounds in the extract [15]. All the parts of the tree like roots, leaves, fruits and seeds possess antioxidant activity due to the presence of phenolic compounds [14–18]. Various articles have reported on the useful activities and phytochemical analysis of various parts of *B. flabellifer* [10–18]. The fruit contains majorly two parts: a hard cover known as shell and gelatinous eatable endosperm, often called a tender fruit. However, there is no work reported on the shell of the fruit and it is the major waste generated after obtaining the fruits.

The objective of the present work was to extract the phenolic compounds from the shell of the fruits of *B. flabellifer*. The effect of various parameters like type of solvent (methanol, ethanol, acetone and water), solid loading (5–20 g), volume of solvent (50–200 mL), concentration of solvent (0–100%), temperature (25–65 °C) and extraction time (2–10 h) on extracting the phenolic compounds has been studied using solvent extraction technique. Based on parametric study, a combination of optimum conditions has been obtained. The process was then further improved by incorporating sonication in the system since ultrasound-assisted extraction has the ability to achieve a faster rate of extraction with comparable yield.

Experiments

Materials

The shells of the fruit of *B. flabellifer* were obtained from the local cultivator in Surat, India. The shells were dried under sunlight for about 4–5 days and then chopped into small pieces. Those pieces were ground in the laboratory grinder and screened to have size of the powdered material around 500 μm . The size reduction would help to improve the mass transfer rate during extraction. Methanol (Rankem Laboratory), ethanol (Advent Chembio Pvt. Ltd.), acetone (Loba Chemie Laboratory Reagents), sodium carbonate (Finar Chem), Folin-Ciocalteu phenol reagent (Sisco Research Laboratories), gallic acid (Finar Chem), tannic acid (S. D. Fine Chem Ltd.) were used for extraction as well as for analysis purposes along with distilled water.

Method

Extraction of Phenolic Compounds. The powdered material having an average size of 500 μm was subjected to extraction using conventional extraction technique. In this process, a fixed amount of powdered material was subjected to extraction along with the solvent. The mixture was kept in a round-bottom flask and a condenser was connected to it to prevent the loss of volatile solvents. The phenomenon of transfer of solute from solid material to solvent is termed as leaching. The leaching operation focuses on extracting valuable compounds, known as solute, from the solid feed using a suitable solvent. In case of natural product extraction, the solvent from the bulk volumes moves toward liquid film surrounding the solid material after which it diffuses through the film toward the solid surface. Once the solvent reaches the surface, it permeates through the cell wall toward the inner part of the cell, wherein the solute resides. The solvent upon reaching the cell dissolves the solute and when it becomes saturated moves outward through cell wall and then back diffusion. Finally, it reaches back to the bulk solution. The phenomenon continues till the whole solution becomes saturated and the driving force becomes zero.

Based on the solubility of the phenolic compounds in the solvent and its saturation, temperature, and extraction time, recovery of phenolic compounds changes. Therefore, the effect of various parameters, like type of solvent, solid loading, volume of solvent, concentration of solvent, temperature and extraction time on extracting the phenolic compounds has been studied while power was kept constant. Agitation was kept in the range of 350–400 rpm to ensure uniformity in temperature and mass transfer. The procedure along with the processing variables is presented in Fig. 15.1. Upon completion of the extraction, the solution was filtered to remove solid material and the filtrate was then stored for determining the total phenolic compounds (TPC). In the present work, TPC was measured in terms of gallic acid and tannic acid. Each experiment was conducted twice to ensure repeatability.

Ultrasound-Assisted Extraction. The sonicator bath from Aqua Scientific Instruments (Surat, India) was used for performing extraction in the presence of sonication. Since sonication has the ability to improve the process performance primarily by reducing the extraction time, the aim of this study was to estimate the time required for extracting the phenolic compounds using sonication process. All the parameters except time were kept constant and the extraction was carried out for time period in the range of 2–10 min.

Determination of Total Phenolic Compounds. The filtered extract was analyzed for TPC in terms of gallic acid (as mg of gallic acid equivalent weight (mg GAE)/g of feed material). The sample after dilution if required was assessed using UV-visible spectrophotometer (DR600, HACH). The method for determining TPC using UV-visible spectrophotometer was developed based on Folin-Ciocalteu method [19]. The standard solution of gallic acid was used to prepare the calibration curve (Fig. 15.2).

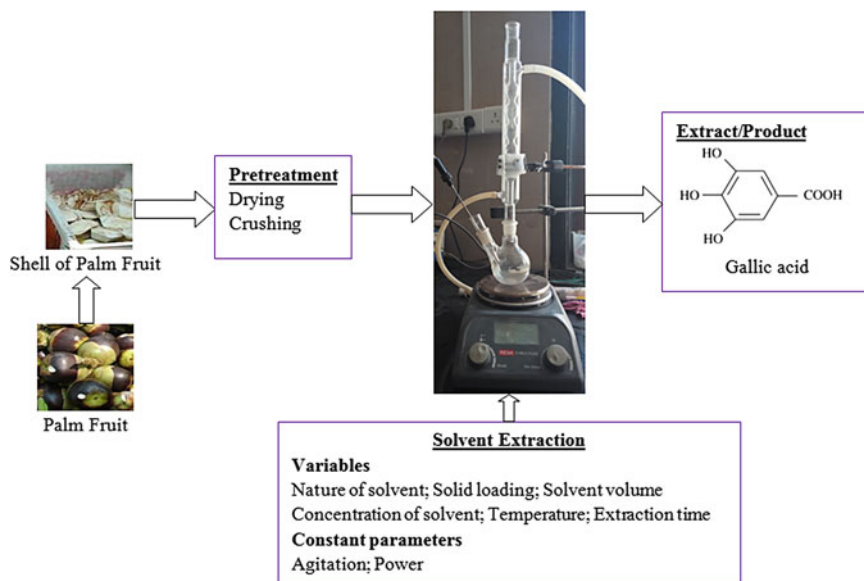


Fig. 15.1 Extraction of phenolic compounds using solvent extraction

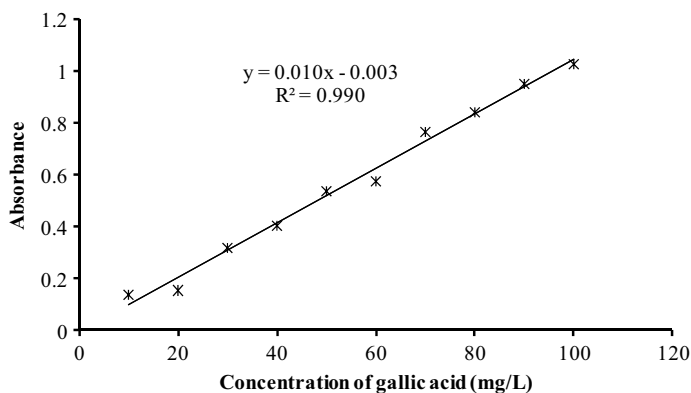


Fig. 15.2 Calibration curve for gallic acid using methanol as a solvent

In addition, TPC was determined in terms of tannic acid (mg of tannic acid equivalent weight (TAE)/g of feed material). The method used UV-visible spectrophotometer (DR600, HACH) for determining the concentration of TAE [20]. Using standard solution of tannic acid, the calibration curve was prepared having $R^2 = 0.992$.

Results and Discussion

Parametric Study

Effect of Nature of Solvent. It is always preferable to select a solvent which has a higher affinity toward the targeted compound, hence different solvents have been used to extract phenolic compounds from the shell and other parameters were kept constant at 5 g of solid loading, 50 mL pure solvent, 25 °C temperature and 6 h of extraction time (Fig. 15.3). As seen from the figure, methanol has provided the highest recovery of phenolic compounds (29.46 mg GAE/g) compared to other solvents while acetone has exhibited the lowest recovery. The solubility of phenolic compounds was more in methanol due to its polarity, and also the methanol was able to penetrate through the solid material easily compared to other solvents. Hence, a higher extraction of phenolic compounds was observed in case of methanol and was used for further studies. Similar results were obtained while extracting rosmarinic acid using methanol [21, 22].

Effect of Solid Loading. Solid loading assists in determining the capacity of the process and it is always desirable to operate the process at its maximum capacity. In order to observe the effect of solid loading, it was varied from 5 to 20 g while volume of the solvent, solvent concentration, temperature and extraction time were maintained at 100 mL, 100% methanol, 25 °C and 6 h, respectively. The influence was observed by determining the phenolic contents in terms of gallic acid and tannic acid (Fig. 15.4). A recovery of phenolic compounds has experienced a decreasing trend with a higher solid loading due to decrease in solvent to solid loading ratio. A higher amount of solid material in a fixed volume of solvent increases the solution viscosity which may impart resistance in mass transfer leading to reduced recovery of the solute [23]. TPC in terms of gallic acid equivalent was higher compared to TPC in terms of tannic acid equivalent. However, both have shown similar behavior upon

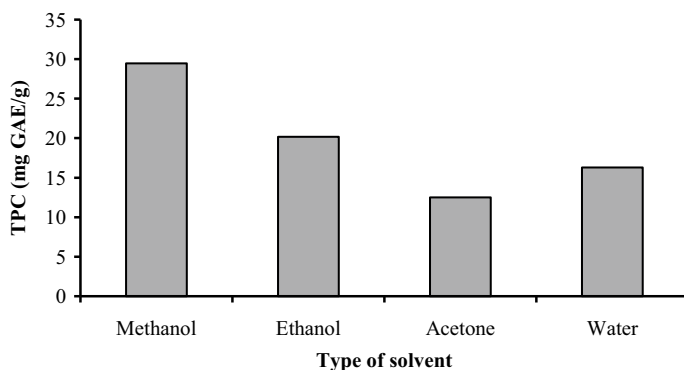


Fig. 15.3 Effect of nature of solvent on phenolic compounds

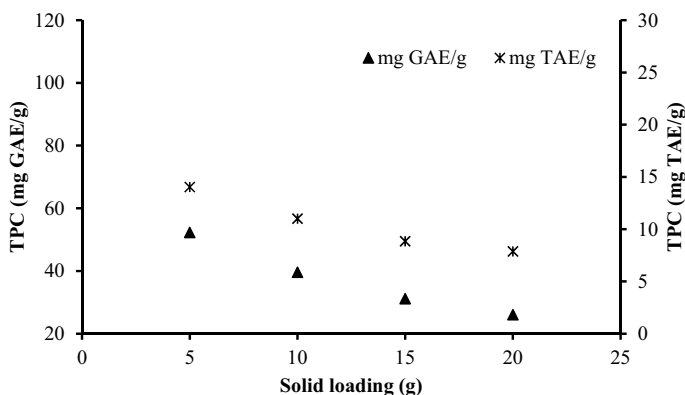


Fig. 15.4 Effect of solid loading on phenolic compounds

increasing the solid amount. The highest recovery was observed at 5 g (52.33 mg GAE/g and 14.04 mg TAE/g), and therefore, it was used for rest of the experiments. Similar observations have been made while isolating geraniol from the leaves of palmarosa [24].

Effect of Solvent Volume. In order to observe the influence of solvent volume on extraction of phenolic compounds, it was varied in the range of 50–200 mL while maintaining other parameters constant, that is, solid loading: 5 g, solvent concentration: 100% methanol, temperature: 25 °C and extraction time: 6 h. A higher solvent volume provides a higher solubilization capacity as well as improved driving force for mass transfer. It is based on the principle of mass transfer between solid and liquid medium, which provides increased concentration gradient [25]. As seen from Fig. 15.5, the highest extraction (67.29 mg GAE/g and 17.3 mg TAE/g) was observed for 200 mL.

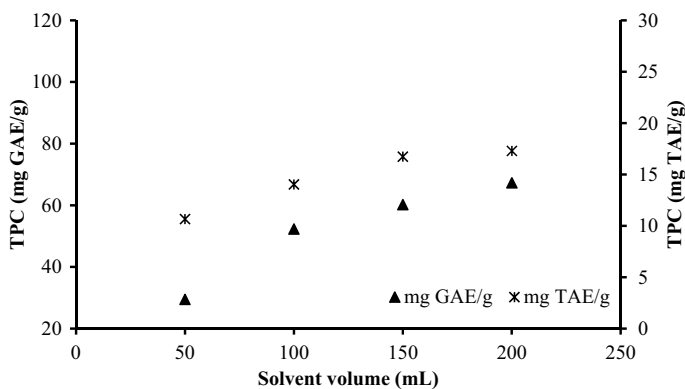


Fig. 15.5 Effect of solvent volume on phenolic compounds

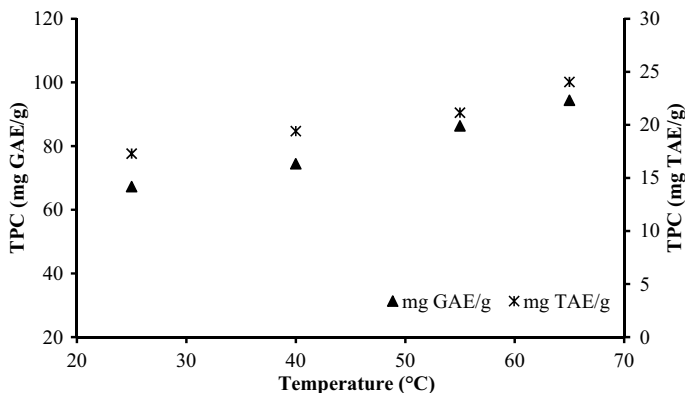


Fig. 15.6 Effect of temperature on phenolic compounds

Effect of Temperature. Diffusivity of solute toward solvent from solid and solubility of solute in solvent increase when temperature is increased [25, 26]. Hence, leaching is always preferred at an elevated temperature. Also, a higher temperature reduces the viscosity and surface tension of solvent which further enhances the rate of extraction [27]. However, one needs to ensure that there is no degradation of the solute in case of heat-sensitive compounds [25, 28]. In the present study, the temperature was varied from 25 to 65 °C and the other parameters were kept constant at 5 g of solid loading, 200 mL pure methanol and 6 h of extraction time (Fig. 15.6). At 65 °C, boiling of the solvent was observed; hence, the highest recovery might be expected. The phenolic compounds have exhibited a higher extraction upon increasing the temperature and the highest extraction was observed at 65 °C (94.42 mg GAE/g and 24.06 mg TAE/g).

Effect of Solvent Concentration. A change in the concentration of the solvent may lead to a change in the recovery of phenolic compounds due to the presence of two solvents (methanol and water) at the same time. The concentration of methanol was varied from 0 to 100% (v/v) while keeping other parameters constant, viz., solid loading: 5 g, solvent volume: 200 mL, temperature: 65 °C and extraction time: 6 h (Fig. 15.7). There was an increase in the TPC as the purity of solvent was changed from 0 (pure water) to 100 (pure methanol) % (v/v) which might be due to the higher affinity of the phenolic compounds toward methanol. However, at 75% (v/v) concentration the extraction efficiency was similar to that with the pure methanol, that is, 93.53 mg GAE/g and 23.67 mg TAE/g against 94.42 mg GAE/g and 24.06 mg TAE/g, respectively. Since the solubility of phenolic compounds was improved because of methanol, desorption of solute has become easier due to the presence of water [29], and such extraction efficiency could be expected. Hence, 75% (v/v) methanol was used for next experiments.

Effect of Extraction Time. A process should be provided with sufficient time so that the completion of the extraction can be achieved. A lesser time may lead to incomplete extraction, while a higher time may result in degradation of the solute

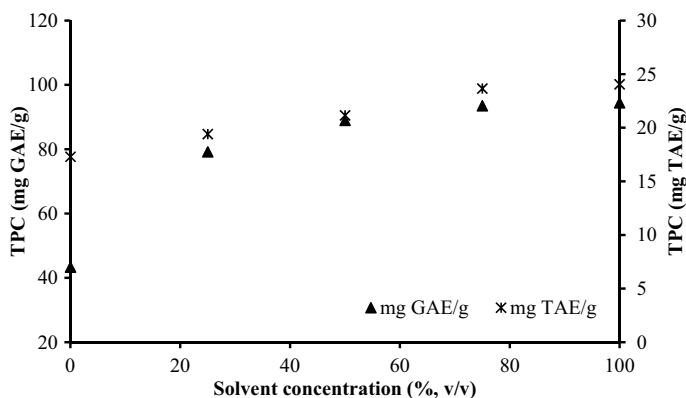


Fig. 15.7 Effect of solvent concentration on phenolic compounds

due to its exposure to the elevated temperature for a longer period. In the present work, the extraction time was varied in the range of 2–10 h, while keeping other parameters constant (5 g of solid loading, 200 mL methanol with 75% (v/v) concentration and 65 °C temperature). The highest recovery of phenolic compounds was achieved at 8 h that is, 110.3 mg GAE/g and 25.6 mg TAE/g, as shown in Fig. 15.8. As the time of extraction was further increased, a decrease in the extraction efficiency was observed. Since the compounds were exposed to elevated temperature for a longer time as well as they were prone to oxidation, a degradation of the compounds has been observed [30].

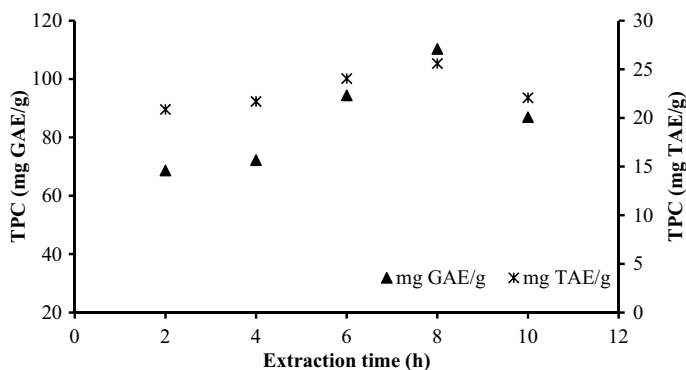


Fig. 15.8 Effect of extraction time on phenolic compounds

Ultrasound-Assisted Extraction

In conventional extraction (CE), solvent has to penetrate through the cell wall to solubilize the solute and then transfer back to the bulk solution. This step is regarded as the slowest step in the extraction process and leads to extended time of extraction [23, 24, 27]. Ultrasound-assisted extraction (UAE) has the ability improve the mass transfer by damaging the cells. In sonication, the propagation of sonic waves leads to the formation of bubbles, which in turn gets ruptured after attaining the maximum size. This rupture results in release of tremendous amount of energy at a molecular level. The energy has the sufficient intensity to damage the cell wall either by creating cracks, pores, or by breaking the cell walls. Also, a micro-jet phenomenon may assist in erosion of the cell wall or detexturation. These phenomena allow easy access of solute, better interaction between solute and solvent, and finally accelerate the dissolution of the solutes which are either residing in the cell or able to come out from the cell [27, 31]. Thus, the rate-limiting step observed in the convention extraction can be eliminated using sonication and the extraction time can be reduced which may further help in improving the production capacity [31].

In the present study, extraction of phenolic compounds was carried out in sonication bath at different time intervals (Fig. 15.9) with the combination of parameters which have provided a better extraction in conventional method except temperature, that is, solid loading: 5 g; solvent volume: 200 mL, concentration of solvent: 75% (v/v) methanol and temperature: 30 °C. As seen from the figure, the extraction time was greatly reduced from 8 h to 8 min when sonication was employed in the process and TPC was obtained as 92.08 mg GAE/g and 25.35 mg TAE/g.

Apart from the benefit of reduction in extraction time, other advantages are also obtained upon employing UAE like reduced power consumption, shrunken carbon footprint and almost negligible utility requirement in terms of cooling water. The comparison of both the techniques is shown in Fig. 15.10, where conventional method

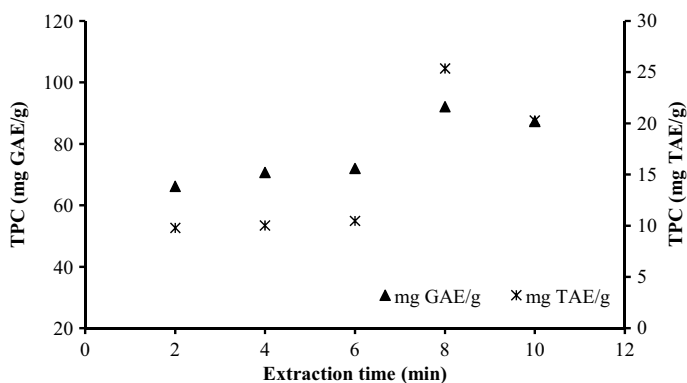


Fig. 15.9 Effect of extraction time on phenolic compounds in ultrasound-assisted extraction

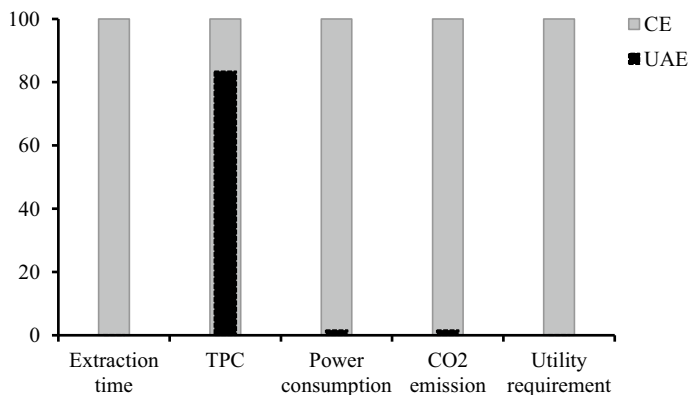


Fig. 15.10 Comparison of ultrasound-assisted extraction (UAE) with conventional extraction (CE)

has been considered as a reference (100%). Further improvement in the sonication process can be achieved by varying the sonication parameters, like frequency, amplitude and pulse ratio.

Conclusion

Borassus flabellifer is the natural source of phenolic compounds that can be used as an antioxidant for different medicinal purposes. The waste material, that is, shell left after using the fruit of this plant was evaluated for its possible utilization as the source of phenolic compounds. Among various solvents like methanol, ethanol, acetone and water, extraction of phenolic compounds was efficiently carried out using methanol. Various parameters like solid loading, volume of solvent, temperature, concentration of solvent and extraction time have been assessed to understand their impact on the recovery of phenolic compounds. The phenolic contents have been estimated in terms of gallic acid equivalent and tannic acid equivalent. From the one factor at a time study, a combination of optimum parameters was obtained as solid loading: 5 g, solvent volume: 200 mL, temperature: 65 °C, concentration of solvent: 75.5 (v/v) methanol and extraction time: 8 h. Under the set of optimized conditions, TPC was obtained as 110.3 mg GAE/g and 25.6 mg TAE/g. In order to overcome the limitation of the conventional technique, ultrasound-assisted extraction was employed which has reduced the extraction time from 8 h to 8 min, thereby providing sustainable alternative to the conventional technique. A detailed study on the process parameters of ultrasound-assisted extraction will further add value to the process.

References

1. Dragsted LO (2003) Antioxidant actions of polyphenols in humans. *Int J Vitam Nutr Res* 73(2):112–119
2. Hertog MGL, Fesrens EJM, Hollman PCH, Katan MB, Kromhout D (1993) Dietary antioxidant flavonoids and risk of coronary heart disease: the Zutphen Elderly study. *The Lancet* 342(8878):1007–1011
3. Yang CS, Landau JM, Huang MT, Newmark HL (2001) Inhibition of carcinogenesis by dietary polyphenolic compounds. *Annu Rev Nutr* 21:381–406
4. Sakihama Y, Cohen MF, Gace SC, Yamasaki H (2002) Plant phenolic antioxidant and prooxidant activities: phenolics induced oxidative damage mediated by metals in plants. *Toxicology* 177(1):67–80
5. Halliwell B, Gutteridge JMC (2015) *Free radicals in biology and medicine*. Oxford University Press, Oxford
6. Branen AL (1975) Toxicology and biochemistry of butylated hydroxyanisole and butylated hydroxytoluene. *J Am Oil Chem Soc* 52(2):59–63
7. www.ayush.gov.in (Access date: 08/05/2020)
8. Naknean P, Meenune M, Roudaut G (2010) Characterization of palm sap harvested in Songkhla province, Southern Thailand. *Int Food Res J* 17(4):977–986
9. Kapoor LD (2000) *Handbook of ayurvedic medicinal plants: herbal reference library*. CRC Press, Florida
10. Jamkhande PG, Suryawanshi VA, Kaylankar, TM, Patwekar SL (2016) Biological activities of leaves of ethnomedicinal plant, *Borassus flabellifer* Linn. (Palmyra palm): an antibacterial, antifungal and antioxidant evaluation. *Bull Fac Pharm, Cairo University* 54(1):59–66
11. Alamelumangai M, Dhanalakshmi J, Mathumitha M, Renganayaki RS, Muthukumaran P, Saraswathy N (2014) *In vitro* studies on phytochemical evaluation and antimicrobial activity of *Borassus flabellifer* Linn against some human pathogens. *Asian Pac J Trop Med* 7(Suppl 1):S182–S185
12. Paschapur MS, Patil MB, Kumar R, Patil SR (2009) Influence of ethanolic extract of *Borassus flabellifer* L. male flowers (inflorescences) on chemically induced acute inflammation and poly arthritis in rats. *Int J PharmTech Res* 1(3):551–556
13. Mosmann T (1983) Rapid colorimetric assay for cellular growth and survival: application to proliferation and cytotoxicity assays. *J Immunol Methods* 65(1–2):55–63
14. Saravanan C, Priya B, Asir BS, Uma S (2012) Preliminary phytochemical screening of antibacterial activity of Palmyra Palm (*Borassus flabellifer*) root extract. *Int J Pharm Sci Res* 3(11):4489–4491
15. Pramod HJ, Yadav AV, Raje VN, Mohite M, Wadkar GH (2013) Antioxidant activity of *Borassus flabellifer* (linn.) fruits. *Asian J Pharm Technol* 3(1):16–19
16. Sahni C, Shakil NA, Jha V, Gupta RK (2014) Screening of nutritional, phytochemical, antioxidant and antibacterial activity of the roots of *Borassus flabellifer* (Asian Palmyra Palm). *J Pharmacogn Phytochem* 3(4):58–68
17. Kommu S, Chiluka VL, Gowri Shankar NL, Matsyagiri L, Shankar M, Sandhya S (2011) Antioxidant activity of methanolic extracts of female *Borassus flabellifer* leaves and roots. *Der Pharmacia Sinica* 2(3):193–199
18. Arunachalam K, Saravanan S, Parimelazhagan T (2011) Nutritional analysis and antioxidant activity of Palmyrah (*Borassus flabellifer* L.) seed embryo for potential use as food source. *Food Sci Biotechnol* 20(1):143–149
19. Singleton VL, Rossi JA (1965) Colorimetry of total phenolics with phosphomolybdic-phosphotungstic acid reagents. *Am J Enol Vitic* 16(3):144–158
20. de Amorim ELC, de Castro VTNA, de Melo JG, Correa AJC, Sobrinho TJSP (2012) Standard operating procedures (SOP) for the spectrophotometric determination of phenolic compounds contained in plant samples. In: Akyar I (ed) *Latest research into quality control*. IntechOpen Limited, London, pp 47–66

21. Albu S, Joyce E, Paniwnyk L, Lorimer JP, Mason TJ (2004) Potential for the use of ultrasound in the extraction of antioxidants from *Rosmarinus officinalis* for the food and pharmaceutical industry. *Ultrason Sonochem* 11(3–4):261–265
22. Paniwnyk L, Cai H, Albu S, Mason TJ, Cole R (2009) The enhancement and scale up of the extraction of anti-oxidants from *Rosmarinus officinalis* using ultrasound. *Ultrason Sonochem* 16(2):287–292
23. Desai MA, Parikh JK (2012) Hydrotropic extraction of citral from *Cymbopogon flexuosus* (Steud.) Wats. *Ind Eng Chem Res* 51(9):3750–3757
24. Thakker MR, Parikh JK, Desai MA (2018) Ultrasound assisted hydrotropic extraction: a greener approach for the isolation of geraniol from the leaves of *Cymbopogon martini*. *ACS Sustain Chem Eng* 6(3):3215–3224
25. Pinelo M, Rubilar M, Jerez M, Sineiro J, Nunez MJ (2005) Effect of solvent, temperature, and solvent-to-solid ratio on the total phenolic content and antiradical activity of extracts from different components of grape pomace. *J Agric Food Chem* 53(6):2111–2117
26. Spigno G, de Faveri DM (2007) Antioxidants from grape stalks and marc: influence of extraction procedure on yield, purity and antioxidant power of the extracts. *J Food Eng* 78(3):793–801
27. Chemat F, Rombaut N, Sicaire A, Meullemiestre A, Fabiano-Tixier A, Abert-Vian M (2017) Ultrasound assisted extraction of food and natural products. mechanisms, techniques, combinations, protocols and applications. a review. *Ultrason Sonochem* 34:540–560
28. Spigno G, Tramelli L, de Faveri DM (2007) Effect of extraction time, temperature and solvent on concentration and antioxidant activity of grape marc phenolics. *J Food Eng* 81(1):200–208
29. Yilmaz Y, Toledo RT (2006) Oxygen radical absorbance capacities of grape/wine industry byproducts and effect of solvent type on extraction of grape seed polyphenols. *J Food Compos Anal* 19(1):41–48
30. Chew KK, Ng SY, Thoo YY, Khoo MZ, Wan Aida WM, Ho CW (2011) Effect of ethanol concentration, extraction time and extraction temperature on the recovery of phenolic compounds and antioxidant capacity of *Centella asiatica* extracts. *Int Food Res J* 18(4):571–578
31. Solanki KP, Desai MA, Parikh JK (2018) Sono hydrodistillation for isolation of citronella oil: a symbiotic effect of sonication and hydrodistillation towards energy efficiency and environment friendliness. *Ultrason Sonochem* 49:145–153

Chapter 16

Use of Sustainable Practices in Cement Production Industry: A Case Study



Vishal Naranje, T. V. S. Chidambaram, Rajeev Bhushan Garg,
and B. D. Bachchhav

Introduction

The well-being of our world continued social growth and human development depend on sustainable development. Cement is one of the most widely used building materials worldwide and is growing in production. Cement, more specifically in the developing world, is considered as a barometer of the economy's activities. Dust, carbon dioxide (CO₂), nitrogen oxides (NO_x), and sulfur dioxide (SO₂) are the most important emissions from cement plants and must be eliminated. Portland cement clinker produces approximately 800–900 kg of CO₂ per one ton. In addition to the issues of natural resources, the environmental problems associated with Green House Gases (GHGs) are to be a key factor in the future sustainable development of the cement industry. Therefore, it is necessary to assess the environmental impact of cement production process and to check the sustainability of that, for the improvement and contribution to the environment and ecosystem, especially in the twenty-first century.

The increase in market pressure makes sustainable manufacturing essential for industries. Many researchers presented a framework for measuring the sustainability of cement production unit [1–3]. Most of the researchers considered the three pillars to measure the sustainability namely, (i) Reducing other environmental impacts, (ii) Occupational health and safety (iii) Social responsibility.

V. Naranje (✉)
Amity University, Dubai, UAE
e-mail: vnaranje@amityuniversity.ae

T. V. S. Chidambaram · R. B. Garg
Star Cement Co. LLC, Dubai, UAE

B. D. Bachchhav
AISSMSCOE, Pune, India

Various cement manufacturing industries evaluate their sustainability by finding the importance of each of these parameters [4–6].

In this study, various environmental cost-effective novel methodologies are discussed that are used by the STAR Cement Co.LLC, RasAl Khaimah, UAE to improve the sustainability of cement manufacturing industry. The major objective is to elaborate the integrated, sustainable cement producing practices followed by the industry consider in this study. These initiatives can be useful to other similar cement manufacturing industry to improve the sustainability of the cement manufacturing plant. The next sections briefly described about the cement manufacturing process and sustainability practices and its benefits to the Cement industry.

Cement Manufacturing Process

The first step in the manufacture of cement is to blend various components of locally available raw material and fuel additives in such a manner that the resulting cement has the required chemical composition. The raw materials are ground into the powder form to make them more reactive and blended. The resultant raw mixture that is called as raw meal is then fed into a rotary cement furnace known as Kiln through a multistage preheating system called preheater. The raw meal having a temperature of 65–80 °C is heated up in multiple stages and finally in the kiln at 1300–1450 °C the clinker is formed. At a temperature range of between 800 and 900 °C, a process called calcination takes place, wherein the CO₂ from the raw meal is expelled forming reactive CaO from CaCO₃. It is then reacted with other components such as SiO₂, Al₂O₃ and Fe₂O₃ as a result of solid-state reactions and forms Alite (C₃S), Belite (C₂S), Calcium Aluminum (C₃A) and Calcium Aluminum Ferrite (C₄AF) compounds. The clinking process is completed when all the oxide components such as Silica, Alumina and Iron are combined with reactive CaO to form C₃S, C₂S, C₃A, and C₄AF crystals and eventually the amount of free lime (CaO) is reduced to a minimum level (less than 1.5%). The “clinker” is then ground into a powder form with a small amount of gypsum to produce “Ordinary Portland Cement,” the type of cement most widely used [7, 8]. Figure 16.1 shows the cement manufacturing process [9].

This research analyzes the sustainability practices implemented by the Star Cement on the basis of environmental impacts, occupational health and safety and social responsibility. The detail strategy is represented in Fig. 16.2. The Star Cement produces over 2.80 MTPA premium-grade clinker to satisfy customers with the ultra-modern Clinkerization unit is located in Ras-al-Khaimah and Fujairah, UAE. The temperature at the ambient air varies from 10 °C in winter to 50 °C in summer. Star Cement thrives on five group values namely “Integrity, Commitment, Passion, Seamlessness, and Speed” to produce and market high-quality clinker and cement that meets both BS EN and ASTM standards throughout the middle east region. Star Cement has received multiple MOCCA, EPDA, and WMA-RAK awards. In operation Star Cement, Ras Al Khaimah, has an Integrated Management System (IMS) with ISO 9001:2015, ISO 14001:2015, ISO 18001:2007 and ISO 50001:2011. Star

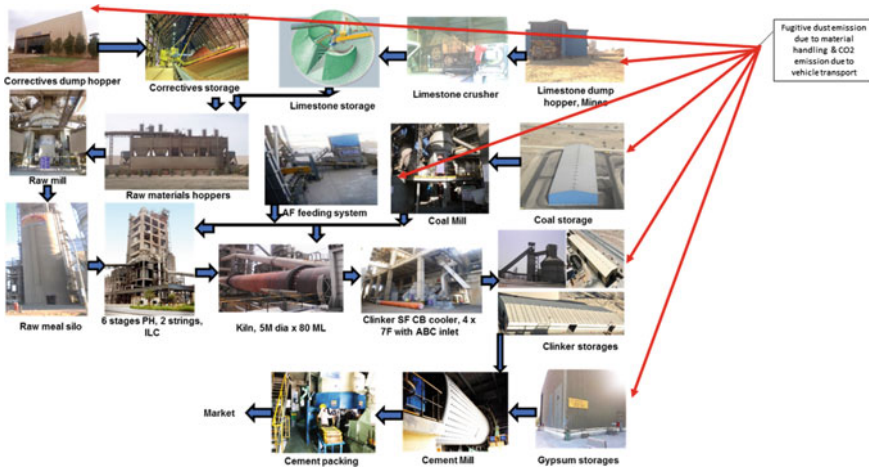


Fig. 16.1 Flow diagram of the cement manufacturing process

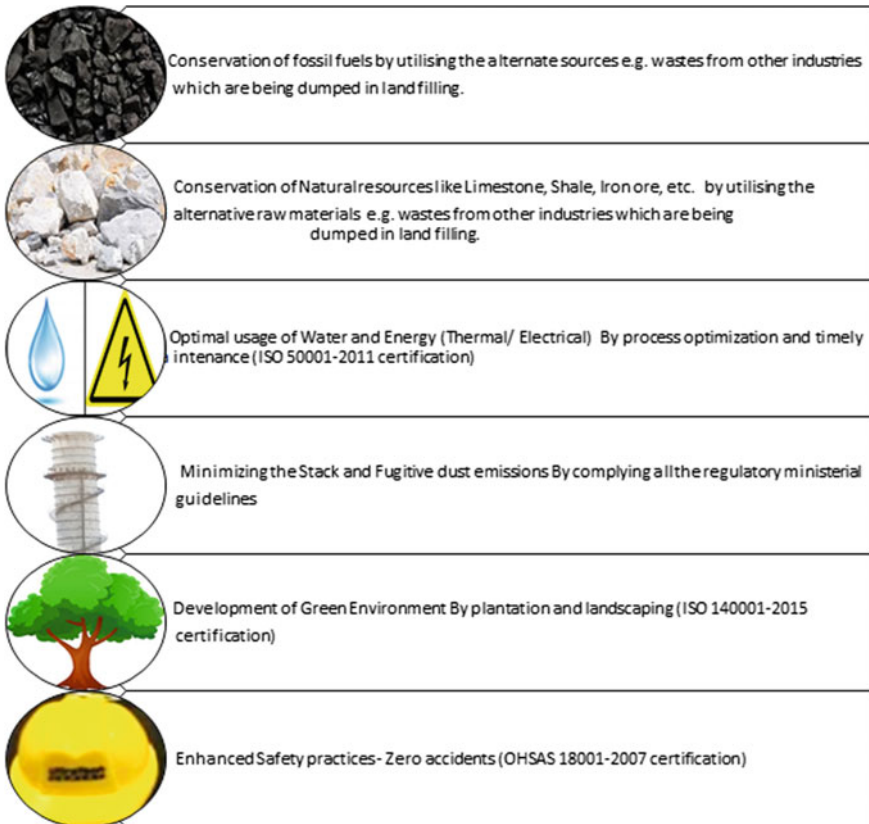


Fig. 16.2 Sustainable practices in cement industry

Cement is committed to value creation for its partners in environmental, health and safety and social terms, with its dream of becoming “The Champion” in Building Solutions.

Details of Sustainable Initiatives

Initiatives to Control the Environmental Impacts

Taking care of sustainable environment is the continual practice at Star Cement. Star Cement is supporting government bodies by using many wastes from different industries and burning these wastes as a fuel in its cement kiln, thereby aiding them in the safe and efficient disposal of non-biodegradable waste. Star Cement has taken many initiatives for the benefit of environment on sustained basis. Few of these initiatives are as listed below.

Completion of three numbers Environment Impact Assessment (EIA) studies approved by Environment Protection and Development Authority, Government of Ras Al Khaimah (EPDA-RAK) for the whole plant before the plant inception in 2005 and in the areas of using various Alternate Fuels(AF) and Alternate Raw Materials (ARM), respectively. Star Cement is using on regular basis different type of wastes like Paint waste from paint industries, oil waste from oil filtration plants, sludge from effluent treatment plants, waste ink from printing industries, waste and used tyres, waste wood from carpentry and construction business as alternative fuels for replacing the natural fossil fuel coal. The preferred wastes are having the high percentage of Lime (CaO), Silica (SiO₂), Alumina (Al₂O₃), Iron (Fe₂O₃), Alkalies (Na₂O & K₂O), Heat values (>3000 kcal/Kg) and less percentage of moisture H₂O, Less Chloride (Cl) and Sulfur (S or SO₃). The not preferred waste as an alternate fuel which are having bad odor, Oversized wastes, high chloride, high sulfur, heavy metals, high moisture and more logistics cost. Figure 16.3 shows the different types of preferred waste used as alternating fuel. Table 16.1 shows the year-wise distribution of usage of AF.

While using these wastes, it is mandatory to comply the rules and regulations set by local authority such as municipality, environment agency etc. A valid NOC from



Fig. 16.3 Various alternating fuel

Table 16.1 Year-wise usage of alternate fuel

FY	Alternate fuel consumption (MT)	Thermal substitution rate (TSR), %
2010–11	150.50	0.20
2011–12	15,477.30	4.60
2012–13	28,886.97	4.72
2013–14	26,728.24	4.34
2014–15	28,687.39	5.21
2015–16	16,160.29	2.68
2016–17	14,893.319	4.36
2017–18	24,965.468	7.67
2018–19	40,569.932	13.35

concerned Govt. authorities like Environment Protection Development Authority, Waste Management Agency, etc. is required before using these wastes.

Star Cement is the user of the highest alternate raw materials in the region. Star Cement is using the wastes, which are having silica, lime, alumina and iron contents like spent pot liner and pot skinning from aluminum industries, copper slag from ship companies, paint waste from paint industries. These alternate raw materials help in conservation of natural resources of limestone and other corrective materials like iron ore, shale, etc. as shown in Fig. 16.4.

Table 2 shows the Year-wise Usage of Alternate Raw Materials.

Star Cement initiatives of using AF to reduce the environmental impact. Company installed AF feeding system to maximize the use of AF in the country with a cost of AED 3.53 million in 2010–11 from Europe. This facility is capable to handle solid wastes 5–75 mm and use the walking floor concept for precise dosing quick action, safety flaps to avoid any backfire during the system stoppages. Figure 16.5 shows the solid AF feeding system.

Beside above measures to reduce the environmental impact of cement production, company initiated few more measures to control the air pollution, which are mentioned below.

1. Online continuous ambient air quality monitoring system for measurement of NO₂, SO₂, CO, TSP, PM10, PM2.5, O₃ and H₂S with its direct access to EPDA-RAK, on 24 × 7 basis.
2. An online continuous stack monitoring system for NO_x, SO_x, CO and SPM measurement with its direct access to EPDA-RAK, on 24 × 7 basis.
3. Well-designed, high-efficiency bag dust collectors at all the materials transfer points and handling the process's dust-laden gases to avoid fugitive dust emissions (Fig. 16.6).
4. Installation of radar type level indicators in all materials hoppers to prevent the materials spillages in case of hopper full conditions.
5. System for handling and usage of alternate fuels available in liquid form in controlled manner.

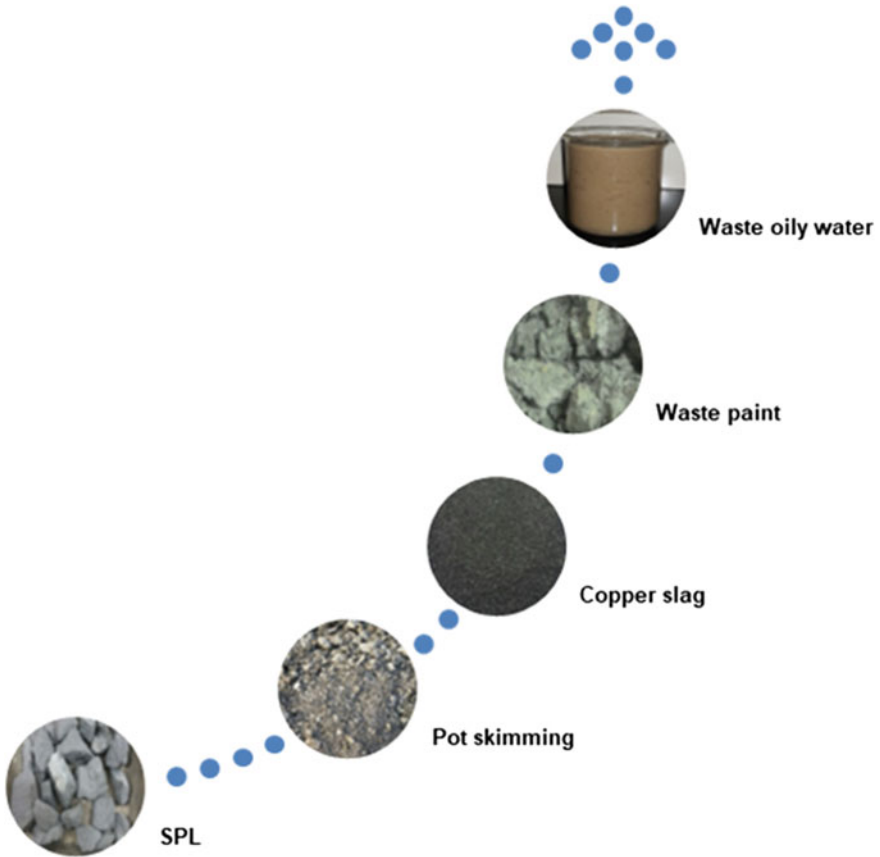


Fig. 16.4 Various alternating raw materials

Table 16.2 Year-wise usage of alternate raw materials

FY	ARM consumption	
	Tons	%
2013-14	2870.96	0.07
2014-15	11,350.03	0.297
2015-16	31,515.33	0.756
2016-17	35,758.241	0.850
2017-18	89,391.715	2.12
2018-19	65,632.018	1.4939



Fig. 16.5 Automatic solid wastes usage system

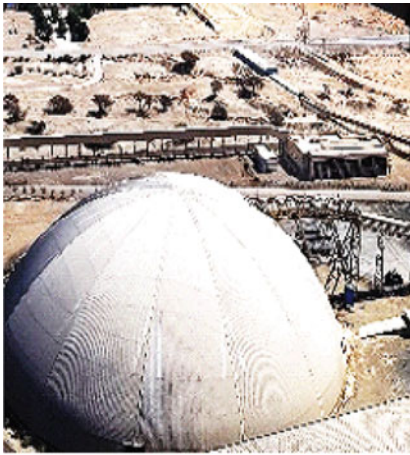
Fig. 16.6 Dust collector



6. A road sweeping machine is deployed on regular basis to clean the plant internal roads.
7. Well-concrete floor parking areas for 54 numbers (22 wheels) trailers are available inside the plant premises.

8. Fig. 16.7a–c shows the various types of closed storages for storing and handling all raw materials and fuels to prevent the fugitive dust emission.
9. Measurement and identification of metals and their compounds, total organic carbon, hydrogen chloride, hydrogen fluoride, ammonia, dioxins/furans, benzene, toluene, xylene, polyaromatic hydrocarbons, chlorobenzenes, PCBs, chloro-naphthalenes, etc. with their reporting to the Ministry of Climate Change and Water, UAE.

Star Cement is promoting the locally available raw materials specially limestone in more cost-effective and sustainable way to reaching global standards on emission



(a) Limestone storage



(b) Corrective materials storage



(c) Alternate fuel storage

Fig. 16.7 Various types of closed storages

through a balance of Portland Limestone Cement (PLC), Portland Slag Cement (PSC) and Portland Pozzolana Cement (PPC) production rather than importing slag/fly ash. This initiative helps to reduce the carbon footprint and promote region's economic growth. Star Cement has received and honored with many awards from the Government for its best environment sustainability practices.

Sustainability Measures for Employee Health and Safety

Health is considered as important in Star Cement for development and efficiency, maintaining a healthy life and fostering well-being for everybody, at all ages. Health and Safety at Star Cement is of the utmost importance for all those working for and on behalf of the Company with “Zero Damage, Zero Injuries and Zero Excuses.” Safety Goals drive the company to set a world-class safety culture. Safety is just not a necessity but a value for the company. To face emergency situations, if any, a well-prepared on-site Emergency Preparedness and Response Plan is in place. Fire extinguishers and fire hydrants are available with periodic inspection at all the respective locations as per the Civil Defence guidelines.

Few of the major health and safety practices in role are:

1. On a regular basis, Audiometric and silicosis tests of the employees working in sound porn areas of power plant.
2. Medical coverage to all employees and their family members.
3. Usage of all relevant PPEs in all the respective working areas of the plant premises.
4. Implementation of speed limit 15 km/h inside the plant premises as per the ministerial guidelines.
5. Installation of 73 no. CCTV cameras in and around the plant area for ensuring the safety practices.
6. Periodic First Aid training to the employees through a certified agency.
7. Periodic safety trainings to the employees from Civil Defence, Government of Ras Al Khaimah.
8. Emergency evacuation Mock drill program on regular basis to ensure the emergency safety practices.
9. Availability of Assembly Points at different locations of the plant for safeguarding the employees in case of emergency.
10. All safety policies and guidelines are in place with time to time trainings conducted by the specialists.

The details of safety and health key performance indicators are summarized in Table 16.3.

Table 16.3 Safety data of STAR Cement

Sr	Description	2015–16	2016–17	2017–18	2018–19	2019–20
1	Number of equipment/property damage incidents reported	11	9	6	6	9
2	Number of near miss cases reported	164	260	295	292	302
3	Number of first aid cases reported	8	6	5	4	1
4	Number of lost time work case reported	0	0	0	0	1
5	LTIFR number of LTI * 106/total yearly man-hours	0	0	0	0	1.36
6	Fatality rate (number of fatalities in a year/(number of directly employed) × 10,000	0	0	0	0	0

Social Initiatives

While part of the Aditya Birla Group (ABG), STAR Cement embraced the three key pillars of ABG Sustainable Business Framework (SBF)—responsible management, strategic stakeholder engagement and proofing of the future. The framework, in turn, is in line with international standards. Star Cement is well aligned with all Government Authorities such as MOCCA, EPDA, Waste Management, etc. for the Protection of the Environment by the proper use of waste generated and by avoiding it for landfill.

Around 2145 numbers, tree plantation along with a lot of landscaping is being developed in the factory premises. Star Cement is organizing Industry Connect Program and Tree Plantation events as a part of Environmental and Sustainability initiatives in Collaboration with local institutions like Amity University, Dubai, Manipal University, Dubai with an involvement of Government authorities MOCCA and EPDA. A total of 90 numbers, tree saplings have been planted during these events. We are working for equitable development in areas like safe drinking water, sanitation, healthcare, sustainable living and social change in line with global sustainability goals (SDGs). Star Cement has taken up several interventions to support local Government authorities by providing industrial trainings to many school children, community development, etc. and internship program and expert talk to various local university students.

As a social responsibility, Star Cement initiated the disposal of Waste oily water from Food industries in collaboration with Waste Management Authority, Ras Al Khaimah since 2018. Waste oil available after extraction <5% being used as alternate fuel and waste water after extraction being used for dust suppression in raw mill by in house installation with water pumps. An arrangement is developed to collect the waste water in a PVC water tank from dining hall, ware house's pantry and coal yard pantry which is approximately 3500 Lit per day and the same is being used with present sprinkler system for irrigation of lawn in front of dining hall and saplings

behind CCR car parking area. This initiative saves approximately 3500 L water per day. Star Cement is committed to incorporating sustainability into its business activities and seeks to adopt new ways to operate and innovative solutions that can offer a strategic stimulus to the business model for low carbon growth Ultratech has voluntarily joined the Cement Sustainability Initiative (CSI) in 2006 as part of the World Business Council for Sustainable Development, and Star Cement is an integral part of it. This helped to gain access to the best practices in the cement industry and benchmarks the company's own sustainability practices with global players.

Conclusion

The numerous sustainability initiatives the STAR Cement has adopted have been addressed at length. These initiatives have shown that in the last 10 years, consumption of alternative fuels has increased from 0.20 to 13.35% and, the percentage usage of ARM rises from 0.07 to 2.12%, reduction in Energy consumption (Electrical and Thermal). The specific power consumption (kWh/t Clinker) is reduced from 72.86 to 51.62 kWh/t Clinker and the specific heat consumption (Kcal/kg Clinker) is reduced 751–695 kcal/kg Clinker during the last 10 years. These initiatives help in significant savings of fuel and input raw materials cost. Beside this, the wastes from different industries are going to landfill and occupying area and polluting the environment. STAR Cement provides best incineration process to most of these wastes. This initiative helps to provide economic benefits to local communities, governments and to industry. The initiatives in the areas of employee health and safety reduced production loss time, equipment damage, etc. Therefore, similar kind of initiatives can be implemented in other cement manufacturing plant to reduce the cement production cost and improve the profitability of the company without compromising the final quality of cement.

References

1. Ekincioglu O, Gurguna AP, Engin Y, Tarhan M, Kumbaracibasi S (2013) Approaches for sustainable cement production—a case study from Turkey. *Energy Build* 66:136–142
2. Schneider M, Romer M, Tschudin M, Bolio H (2011) Sustainable cement production—present and future. *Cem Concr Res* 41:642–650
3. Kosmatka SH, Kerkhoff B, Panarese WC (2002) Design and control of concrete mixtures. Portland cement Association, Skokie
4. Gamble W (2005) Cement, mortar, and concrete. In: Baumeister; Avallone, McGraw Hill 177
5. Cement Industry (2004) Manufacturing process. Retrieved 22 April 2008, from http://www.energymanagertraining.com/cement/cement_01_process.htm
6. https://www.moccae.gov.ae/content/documents/QUARRY_GUIDELINES_English.pdf Regulatory Guidelines for Environmental Control in the Cement Industry, Ministerial decree number

7. Guidance on the Environmental Clearance (EC) Requirements for Development and Infrastructure Projects in the Emirate of Dubai. <https://portal.dm.gov.ae/SCWebUI/DOCS/%D8%A7%D8%B1%D8%B4%D8%A7%D8%AF%20%D9%81%D9%86%D9%8A.pdf>
8. Sangwan KS, Bhakar V, Digalwar AK (2019) A sustainability assessment framework for cement industry—a case study. *Benchmarking: An Int J* 26(2):470–497. <https://doi.org/10.1108/bij-01-2018-0021>
9. Ultratech Driving Growth through Sustainable development goals (SDGs), Sustainability Report, 2018–19

Chapter 17

Analysis, Modeling and Experimental Study of Stretching Stress in the Design of Pressure Sensor



Shrinkhla Ghildiyal, R. Balasubramaniam, and Joseph John

Introduction

Pressure is a critical parameter to be measured across the fields such as thermodynamic, aerodynamics, acoustic, fluid mechanics, soil mechanics and biophysics [1]. There are three types of pressure sensors, absolute, gauge and differential, to cover all these applications. A pressure-sensitive diaphragm is a critical part of a pressure sensor, and its proper design is important in order to have a pressure sensor, which is accurate as well as sensitive. Diaphragm is viewed as a spring element, which deflects by the application of pressure. A general definition of diaphragm is that it is a prestressed elastic element with firmly clamped edge, which responds to pressure in terms of deflection and stress [2–4]. The resistance to pressure loading is due to bending, tensile force and prestress in the diaphragm. The deflection of circular diaphragm is as follows [3, 5].

$$\frac{Pa^4}{Et^4} = \frac{16}{3(1-\nu^2)} \left(\frac{y}{t}\right) + \frac{7-\nu}{3(1-\nu^2)} \left(\frac{y}{t}\right)^3 \quad (17.1)$$

Here y is the deflection of the diaphragm at its center, ν is the Poisson's ratio, a is the diaphragm radius, P is the applied pressure, E is the Young's modulus and t the diaphragm thickness. If diaphragm deflection is small as compared with the diaphragm thickness, $\left(\frac{y}{t}\right)$ the first term on the right side of Eq. (17.1) is only the significant one and the second term can be neglected without much error. In this

S. Ghildiyal (✉) · R. Balasubramaniam
Homi Bhabha National Institute, Anushakti Nagar, Mumbai 40009, India
e-mail: shrinkhlaghildiyal@gmail.com

Bhabha Atomic Research Centre, Mumbai 400085, India

J. John
Indian Institute of Technology Bombay, Mumbai 400076, India

case, only bending moments are taken into account and tensile stress is neglected. Equation (17.1) is governed by bending and tensile forces on the diaphragm due to applied pressure only and is widely reported for the design of pressure sensors [2–4, 6–10]. However, prestress in the diaphragm is not taken into the consideration in Eq. (17.1) as well as in the above mentioned works. As explained in this paper, considering prestress of the diaphragm would improve the analytical model and give better agreement with experiments.

In the present study, we have mathematically analyzed the prestressed diaphragm, which provides the radial variation of stress due to the stretching stress at periphery (SSaP). This radial variation of stress is used further in COMSOL for obtaining the deflection characteristic of the pressure sensor. Finally, four gauges are tested and compared with the simulation results to predict the SSaP in them.

Mathematical Analysis of Prestretched Sensitive Element

A diaphragm of diameter $2a$ and thickness t is shown in (r, θ, z) plane (Fig. 17.1a), where t is much less than a . An infinitesimal size arc, of inner diameter r , thickness dr and angular size $2d\theta$ is considered for analysis (see Fig. 17.1b). σ is the stress on diaphragm and subscript indicate the direction of stress. dr , $2rd\theta$, $2(r + dr)d\theta$ are sides and t (along z axis) thickness of arc (Fig. 17.1c). Stress multiplied by area of a side gives the force in that plane. Stretching is radially symmetric along z axis, hence $\theta = 0^\circ$ is considered further for ease of analysis. Stretching stress at periphery is referred as SSaP in further study.

As SSaP is applied before clamping on the edge, there would not be any tensile or bending force due to pressure. Force (due to SSaP) balance on an infinitesimal element is as follows

$$2\sigma_\theta.dr.t.\sin d\theta + \sigma_r.2rd\theta.t = \sigma_{r+\Delta r}.2(r + dr)d\theta.t \quad (17.2.1)$$

As $d\theta$ is very small, $\sin d\theta = d\theta$, Eq. 17.2.1 modifies as follows

$$2\sigma_\theta.dr.d\theta.t + \sigma_r.2rd\theta.t = \sigma_{r+\Delta r}.2(r + dr)d\theta.t \quad (17.2.2)$$

Rearrangement of Eq. 17.2.2 gives

$$2\sigma_\theta dr + 2\sigma_r r = 2\left(\sigma_r + \frac{\partial\sigma_r}{\partial r}dr\right).(r + dr) \quad (17.2.3a)$$

$$\sigma_\theta dr + \sigma_r r = \sigma_r r + \sigma_r dr + \frac{\partial\sigma_r}{\partial r}rdr + \frac{\partial\sigma_r}{\partial r}(dr)^2 \quad (17.2.3b)$$

Ignoring the last term of right-hand side,

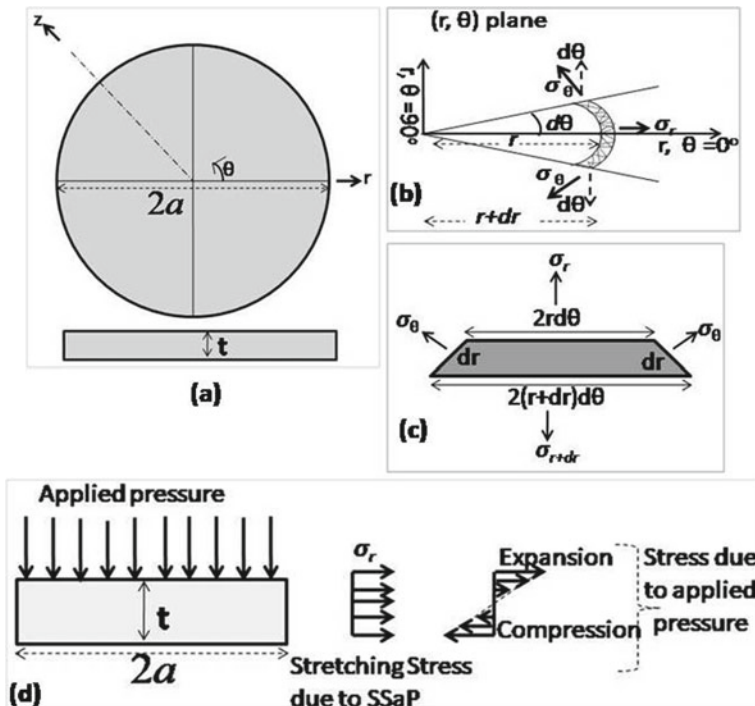


Fig. 17.1 **a** Diaphragm of diameter $2a$ and thickness t in (r, θ, z) coordinate system, **b** an infinitesimal element of dimension dr and $2d\theta$, **c** dimensions and forces acting infinitesimal element, **d** stresses on diaphragm due to SSaP and applied pressure

$$\begin{aligned} \sigma_\theta dr &= \sigma_r dr + \frac{\partial \sigma_r}{\partial r} r dr \\ \sigma_\theta dr &= \sigma_r dr + r d\sigma_r \\ \sigma_\theta dr &= d(r\sigma_r) \\ \sigma_\theta &= \frac{d(r\sigma_r)}{dr} \end{aligned} \tag{17.3}$$

We assume that stresses perpendicular to (r, θ) plane such as $\sigma_z = \sigma_{zx} = \sigma_{zy} = 0$. This assumption is valid here as there is no bending force on the diaphragm. The strain in diaphragm is as follows

$$\epsilon_r = \nabla r / r = \frac{1}{E} (\sigma_r - \sigma_\theta \nu) \tag{17.4.1}$$

$$\epsilon_z = \nabla t / t = -\frac{\nu}{E}(\sigma_r + \sigma_\theta) \quad (17.4.2)$$

The volume of diaphragm is given by

$$V = \pi r^2 t$$

The volumetric change in diaphragm is zero.

$$\frac{\nabla V}{V} = 2 \epsilon_r + \epsilon_z = 0 \quad (17.4.3)$$

From Eqs. 17.4.1–17.4.3

$$\sigma_\theta = \sigma_r \frac{2 - \nu}{3\nu} \quad (17.5)$$

From Eqs. (17.3) and (17.5)

$$\sigma_r \frac{2 - \nu}{3\nu} = \frac{d(r\sigma_r)}{dr} \quad (17.6.1)$$

Let $\frac{2-\nu}{3\nu} = k$

$$k\sigma_r = \frac{d(r\sigma_r)}{dr} \quad (17.6.2)$$

$$k\sigma_r = \sigma_r + r \frac{d(\sigma_r)}{dr} \quad (17.6.3)$$

Equation 17.6.3 can be as follows

$$(k - 1) \frac{dr}{r} = \frac{d(\sigma_r)}{\sigma_r} \quad (17.6.4)$$

Integrating both sides,

$$(k - 1) \ln r = \ln \sigma_r + c_1$$

Mathematical rearrangement

$$\sigma_r = c_0 r^{k-1}$$

Apply the boundary condition that SSaP is σ_o at the diaphragm periphery of diameter $2a$:

$$c_0 = \sigma_0 a^{1-k}$$

Hence the stress distribution in radial direction due to stretching is given by

$$\sigma_r = \sigma_0 \left(\frac{r}{a} \right)^{k-1} \quad (17.7)$$

Simulation of Sensor's Behavior

A prestressed diaphragm, clamped at periphery, is taken further for design simulation in COMSOL Multiphysics 4.3a. It is implemented in simulation using Eq. (17.7) as the initial condition. Following Eqs. (17.8.1–17.8.4) were used in FEM;

$$-\nabla \cdot \sigma = F_V \quad (17.8.1)$$

$$\sigma - \sigma_i = C(\varepsilon) \quad (17.8.2)$$

$$\varepsilon = \frac{1}{2} [(\nabla u)^T + \nabla u] \quad (17.8.3)$$

$$C = C(E, \nu) \quad (17.8.4)$$

F_V is the internal force per unit volume and it is negligible in the present case. σ is the stress on each node, σ_i is the initial stress. In the analysis, Eq. (17.7) is incorporated as initial stress σ_i in the body. ε is the strain due to the deformation of material, E is the elastic constant and ν the Poisson ratio of the material.

The range of SSaP and applied pressure considered in this study is 0–400 MPa and 0–100 mbar, respectively. Other than that, mechanical property of SS316L and diaphragm dimensions of 40.0 mm diameter and 0.20 mm thickness are used. Pressure is applied on the diaphragm along the z direction, while the stretching stress is along radial direction (see Fig. 17.1d). The deflection behavior of the diaphragm is studied here. The condition of SSaP = 0 MPa means diaphragm is clamped, but with no stretching. Deflection at the center of the diaphragm with varying SSaP and given applied pressure is shown in Fig. 17.2a. Three graphs, each corresponding to a given pressures of 10, 50 and 100 mbar, show that at a constant applied pressure maximum diaphragm deflection decreases with increasing SSaP.

The behavior of pressure-sensitive diaphragm, for range 0–100 mbar, at various SSaP is shown in Fig. 17.2b. The deflection at the center reduces with increasing SSaP, which consequently reduces sensitivity from 1.22 $\mu\text{m}/\text{mbar}$ (at no SSaP) to 0.18 $\mu\text{m}/\text{mbar}$ (at 400 MPa SSaP), respectively.

Another observation is that the behavior of sensor changes from nonlinear to linear as SSaP increases. It is due to the fact that diaphragm deflection y is a significant fraction of t at low SSaP, thus the $(y/t)^3$ term of Eq. (17.1) cannot be neglected,

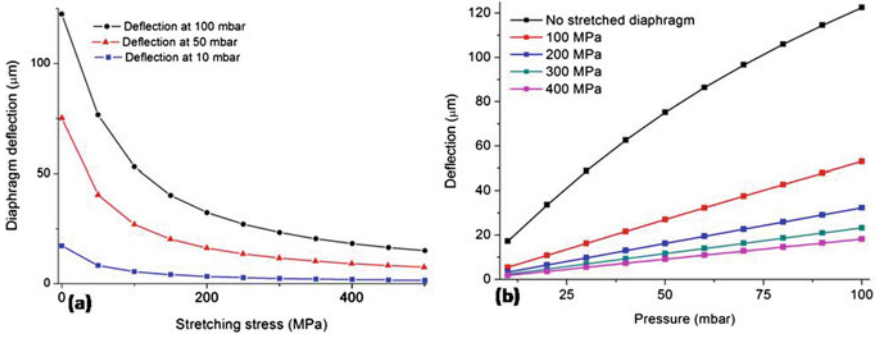


Fig. 17.2 Diaphragm deflection at center versus **a** Stretching stress at given applied pressure, **b** applied pressure at given SSaP

Table 17.1 Diaphragm deflection at two end points of SSaP and applied Pressure

SSaP (MPa)	Applied pressure (mbar)	Diaphragm deflection at center (μm)
0	10	17.20
	100	122.47
200	10	3.25
	100	32.31
400	10	1.82
	100	18.21

which introduces nonlinearity in behavior of the sensor. As SSaP increases, same term become quite small hence can be ignored without much error. In that case, sensor behaves linearly as per (y/t) term of Eq. (17.1). The diaphragm deflection at two extremes of the SSaP and applied pressure range is given in Table 17.1.

Experimental Study

To verify the above-discussed simulation, four pressure gauges of the same range, same material and same diaphragm dimensions are tested in same condition. The pressure-sensitive diaphragm in all the gauges is stretched by conventional mechanical method.

The test gauges are based on the principle of fiber optic Fabry Perot interferometer (FPI). FPI consists of two partially reflective plane surfaces, which are placed in proximity and parallel to each other. A normally incident optical beam undergoes multiple back and forth reflections between them. Because of partial transmission, there will also be multiple transmitted rays from each surface with a progressive and fixed phase difference, i.e., $\Phi, 2\Phi, 3\Phi, \dots, m\Phi$; therefore, it is a multibeam

interferometer. In an FPI, with separation L between its two surfaces, a transmitted beam (with m round trip travels) will travel length $2mL$, thus introducing phase $m\Phi = \frac{2\pi}{\lambda} 2mL$. When this interferometer is interrogated with broadband light, some wavelengths have maximum intensity due to constructive interference and some other wavelengths have minimum intensity due to destructive interference. Rest of the wavelengths have intensity in between them. Hence the reflective and transmissive signal of FPI have modulation, which is unique for an FPI gap L and spectral region of input light.

The test sensor has an FPI with sapphire as the first reflecting surface and stainless steel (SS) sheet (SS316L of diameter 40.0 mm and thickness 0.20 mm) as the second one. In order to achieve high reflectivity, an FPI surface of sapphire is coated with a broad band thin film reflective coating, while the SS316L sheet is surface finished with Chemo Mechanical Magneto Rheological finishing process.

The above-mentioned SS sheet, which is one of the two reflective surfaces of FPI, also works as the pressure-sensitive diaphragm of the gauge. It deflects with the applied pressure which changes the FPI gap and consequently corresponding reflective signal. An absolute FPI gap decreases with increasing applied pressure and each gap is calculated from the reflected spectrum by white light interferometric technique.

An optical setup based on white light interferometry scheme is employed to measure the above-discussed gap and subsequently to test the sensor (see Fig. 17.3). It consists of a Tungsten-Halogen lamp (THL) light source, a 3 dB fiber optic power splitter and optical spectrum analyzer. THL is a light source of visible and near infrared spectrum mostly. It launches optical signal into the FPI through the optical fiber splitter; the reflected signal from FPI goes into the analyzer by the same splitter. An optical signal from source to FPI is shown by dashed orange line and reflected signal from FPI to analyzer by blue dotted line. A diffraction grating and linear CCD array detector (3648 pixels) based optical spectrometer (Avantes make Model Avaspec3648ULS) is used as demodulation system of the sensor. It is used in the spectral range of 600–1000 nm with ≈ 0.20 nm resolution. The FPI gap ranges from 10 to 120 μm can be conveniently measured by this technique. The lower limit

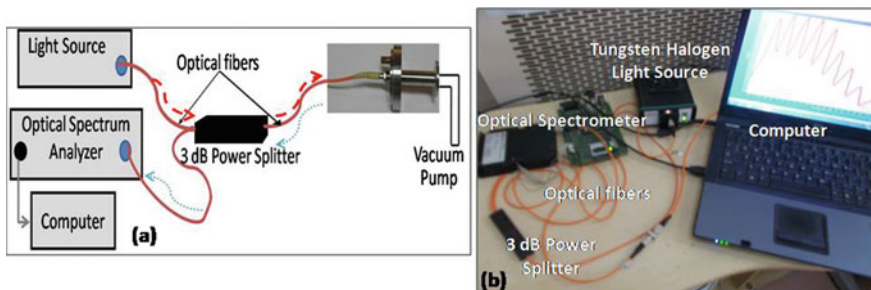


Fig. 17.3 Experimental setup **a)** Schematic, **b)** actual photograph of an optical setup

is governed by the range of spectrometer and the upper limit by the resolution of spectrometer.

The detailed description of design and manufacturing of these sensors and an algorithm to calculate the FPI gap from the reflected signal is given thoroughly in Ref. [11]. This algorithm is based on the fact that all wavelengths corresponding to intensity maxima or minima are in harmonic relation.

$$\lambda_m = 2l/m \tag{17.9}$$

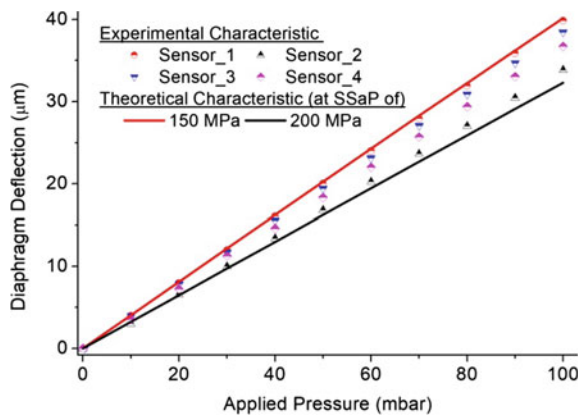
It indicates that m^{th} order of interference will be at λ_m wavelength, when FPI gap is l . Uncertainty in the measurement of gap depends on the uncertainty in λ_m measurement, which is the resolution of optical analyzer. Hence change in gap Δl which corresponds to the movement of m^{th} interference fringe within 0.20 nm (resolution of the spectrometer) cannot be measured. For example, FPI gap of 47.50 μm have an interference peak of index 130th at 730.769 nm (as per Eq. 17.9). The detectable change in FP gap will be when this peak moves by 0.20 nm; it corresponds to an FPI gap of 47.513 μm . Hence, theoretical uncertainty lies within 0.013 $\mu\text{m} = 13 \text{ nm}$.

Four sensors are tested in the range of 0–100 mbar in steps of 10 mbar. All of them have SS316L diaphragm of 40.0 mm diameter, 0.2 mm thickness and stretched by conventional mechanical method. The total deflection at the center of diaphragm for 100 mbar applied pressure is 39.85 μm , 38.47 μm , 36.73 μm and 33.85 μm for sensor 1, 2, 3 and 4, respectively. Test results of all the sensors are given in Fig. 17.4. Manufacturing, assembly and testing method of all four are also same.

Simulation results of the diaphragm deflection with applied pressure at various SSaP are compared with the above discussed experimental results. It is observed that the experimental characteristic of all four sensors lies within theoretical limits of 150–200 MPa range of SSaP (shown in Fig. 17.4).

As four pressure sensors were tested experimentally and all of them lies within fixed range of SSaP. Thus it is concluded that SSaP with the conventional method of stretching would be in the range of 150–200 MPa for the diaphragm of 40.0 mm

Fig. 17.4 Four sensors with diaphragm of same dimension show slightly different deflections at same applied pressure range and lies within 150–200 MPa range of SSaP



diameter and 0.2 mm thickness. The linear behavior for all the cases is also evident from the test results, which matches with simulation results also.

Conclusion

In this study, the radial variation of stretching stress due to given SSaP is mathematically analyzed. It is used further in COMSOL simulation to design the sensor and observe the effect the SSaP on the behavior of pressure-sensitive diaphragm. The simulation results showed that diaphragm deflection at 100 mbar applied pressure is 122.47 μm and 18.21 μm with 0 and 400 MPa SSaP, respectively. The sensor behavior is nonlinear in first case and becomes linear at higher SSaP. Hence it was observed that stretching on diaphragm improved linearity, but with reduced sensitivity. Four FPI-based pressure sensors of same type are tested in same pressure range. Their sensitivity decreases from 398.5 to 338.5 nm/mbar and linearity matches with simulation results. As four sensors lie in same range of SSaP, it is concluded that the conventional method of mechanical stretching on the diaphragm of 40 mm diameter and 0.2 mm thickness provides the SSaP in the range of 150–200 MPa.

References

1. Migeon A, Lenel AE (2010) Modern sensors handbook. In: Ripka P, Tipek A (eds) Modern sensors handbook, pp 1–46
2. Rangan CS, Sarma GR, Mani VSV (1983) “Pressure”, in instrumentation devices and systems. Tata McGraw Hill, New Delhi, pp 113–143
3. Zhu J, Wang M, Chen L, Ni X, Ni H (2017) An optical fiber Fabry-Perot pressure sensor using corrugated diaphragm and angle polished fiber. *Opt Fiber Technol* 34:42–46
4. Sposito A, Pechstedt RD (2016) Optical sensors for aerospace applications: brake temperature sensors and fuel pump pressure sensors for aircraft. In: 3rd IEEE international workshop on metrology for aerospace, MetroAeroSpace 2016—proceedings, pp 97–101
5. Mendez A, Morse TF, Keith AR, Mendez A, Morse TF, Ramsey KA (1993) Micromachined Fabry-Perot interferometer with corrugated silicon diaphragm for fiber optic sensing applications. *Integr Opt Microstruct* 1793:170–182
6. Patranbis D (1996) Pressure measurement. In: Principle of industrial instrumentation, 2nd edn. Tata McGraw-Hill, New Delhi, pp. 145–150
7. Ge Y, Cai K, Wang T, Zhang J (2018) MEMS pressure sensor based on optical Fabry-Perot interference. *Optik (Stuttg)* 165:35–40
8. Di Giovanni M (1982) Flat and corrugated diaphragm design handbook, 1st edn. Marcel Dekker, New York Basel
9. Zhang Y, Huang J, Lan X, Yuan L, Xiao H (2014) Simultaneous measurement of temperature and pressure with cascaded extrinsic Fabry-Perot interferometer and intrinsic Fabry-Perot interferometer sensors. *Opt Eng* 53(6):067101:1–5
10. Zhang Y, Yuan L, Lan X, Kaur A, Huang J, Xiao H (2013) High-temperature fiber-optic Fabry-Perot interferometric pressure sensor. *Opt Lett* 38(22):4609–4612
11. Ghildiyal S, Ranjan P, Mishra S, Balasubramaniam R, John J (2019) Fabry-Perot interferometer-based absolute pressure sensor with stainless steel diaphragm. *IEEE Sens J* 19(15):6093–6101

Chapter 18

On Numerical Modeling and Flow Analysis of Piston Bowl Geometry of a Compression Ignition Engine



Bridjesh Pappula , Geetha Narayanan Kannaiyan ,
and Seshaiiah Turaka 

Introduction

Advances in the field of computational fluid dynamics and in mathematical modeling along with high performance of computer systems have made it possible the comprehensive modeling of the in-cylinder flow. Modeling helps to gain insights and understand the swirl, radial velocity and turbulence intensities in the internal combustion engine cylinder. The longer the time it takes for fuel and air to mix, the performance of the engine worsens. In air–fuel mixing and combustion, swirl, squish and turbulence have major impact on a compression ignition engine. The design of good intake manifold greatly influences the swirl motion of the air to enhance the combustion [1]. Swirl motion also helps in higher soot oxidation [2]. The swirl motion also depends on the piston bowl geometry [3] and the cycle efficiency can be improved along with flexible injection timing [4]. On the other hand, the higher levels of swirl increase the angular velocity and angular momentum, which hinders the proper mixing of fuel and air and in-turn combustion [5]. Squish is the rapid acceleration of the air caused by compression to achieve the ignition temperature. The swirl and squish produces the turbulent flow at the end of compression [6] and the great intensity of turbulence which is needed during the compression stroke is generated with intense swirl during

B. Pappula (✉)

Department of Mechanical Engineering, MLR Institute of Technology, Hyderabad 500043, India
e-mail: meetbridjesh@gmail.com

G. N. Kannaiyan

Department of Science and Humanities, Sri Krishna College of Engineering and Technology,
Coimbatore 641008, India
e-mail: nkgeeth@gmail.com

S. Turaka

Department of Mechanical Engineering, QIS College of Engineering and Technology, Ongole
523272, India
e-mail: turakaseshaiah07@gmail.com

the suction stroke. The stability of these swirling movements allows to maintain large turbulence during the fuel injection phase results in increased dispersion of fuel and the micro mixing of fuel and air. This induces optimal condition for the initiation and the development of combustion process [7]. The turbulence can be enhanced with modifications on piston bowl geometries as they have significant impact on the combustion quality [8–10]. Above all, re-entrant combustion chamber geometries have more intense turbulence [11, 12]. Some earlier numerical studies [13–15] state that both NO_x and soot can be controlled by proper design of re-entrancy and fuel injection timing. The key for better fuel economy and to reduce exhaust gas emissions is the optimization of combustion chamber geometry [16–19].

The present study focuses on the chemical kinetics, combustion and emission characteristics of a compression ignition engine fuelled with waste plastic oil mixed with chemical composite additive (WPOCA) which is a mixture of 0.2 vol.% of soy lecithin and 2 vol.% of Di-tertiary butyl peroxide. The standard hemispherical piston bowl (HCC) was modified to toroidal spherical grooves piston bowl (TSG). The combustion process in engine in-cylinder was simulated using KIVA-4 code coupled with CHEMKIN. Validation of HCC at 80 and 100% loads was performed. Subsequently, numerical analysis was performed with TSG and compared.

Experimental Setup

The test rig for this study consists of a 5.2 kW compression ignition engine of model TV1, Kirloskar make. This engine is coupled with an eddy current dynamometer. Instruments needed to measure combustion performance and emanation characteristics such as AVL H12D pressure transducer, AVL 364 angle encoder, AVL Digas 444 gas analyzer, AVL make smoke meter are installed onto the test rig. AVL INDI MICRA-602-T10602A version V2.5 interfaces for online analysis. The detailed description of setup is presented in [20] and alongside, specifications of engine are appeared in Table 18.1. The physiochemical properties of test fuels are given in Table 18.2. Standard operating procedure has been followed in conducting the experiments.

Computational Tools

Reaction Mechanism of WPO and Sub Models

Simulation was carried using KIVA-4 code, which is coupled with CHEMKIN II for in-depth chemical calculation. Parameters such as species concentrations, initial pressure and temperature were given to CHEMKIN II from KIVA-4. Fuel chemistry of WPO was established by a multicomponent chemical reaction mechanism

Table 18.1 Engine specifications

Make and model	Kirloskar, TV1
Number of cylinders	1
Bore, mm	87.5
Stroke, mm	110
Piston bowl	Standard: Hemispherical Modified: Toroidal spherical groove
Compression ratio	17.5:1
Rated power, kW	5.2
Rated speed, rpm	1500
Fuel injection type	Direct injection
Number of nozzle holes	3
Fuel injection pressure, MPa	22
Fuel injection timing, °CA bTDC	23

Table 18.2 Properties of test fuels

Property	Diesel	WPO	WPOCA	ASTM method
Density @15°C (kg m ⁻³)	0.835	0.893	0.862	D4052
Calorific value (MJ kg ⁻¹)	45.4	34.2	41.8	D240
Kinematic viscosity (cSt)	2.15	3.12	2.78	D445
Flash point (°C)	49	58	56	D93
Boiling point (°C)	180–330	120–375	–	D7169-16
Self-ignition temperature (°C)	210	261	252	D1929-16
Cetane number	45	31	42	D4737
Oxygen content (wt%)	0.03	0.31	0.4	–

wherein, 69 species and 204 reactions are present [21]. The physical properties of vital components of WPO were added into KIVA-4 fuel library. The KIVA-4 code is based on finite volume scheme which solves the conservation equations of mass, momentum and energy. It enables to generate unrestricted grids more easily than structured grids for very complicated geometries. The unique feature of KIVA-4 is the multicomponent fuel evaporation algorithm and it also features combustion and emission formation mechanism along with fuel injection and ignition. In the present study, Kelvin-Helmholtz and Rayleigh-Taylor hybrid model has been used instead of Taylor Analog Breakup model for better simulation of fuel breakup process. RNG k- ϵ model was used to model turbulence.

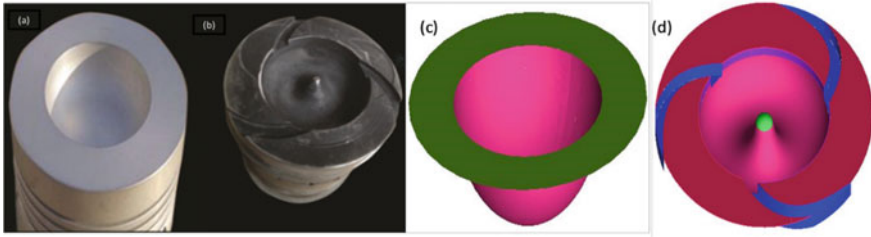


Fig. 18.1 Piston bowl **a** standard HCC, **b** modified TSG, **c** animated HCC, **d** animated TSG

Piston Bowl

The shape of combustion chamber is one of the decisive factors for creating air turbulence that determines the quantity and quality of combustion. To enhance the turbulence effect in combustion chamber, the HCC is modified to TSG. Piston bowl volume was kept consistent for both configurations with the goal that compression ratio should be same. It is understood that TSG geometry of piston bowl helps to allow more fuel and air with high velocity over the grooves. Some part of charge remains on piston land is forced into the bowl directly that helps to create whirl flow to get more atomization. The increase fuel air motion may affect to develop high turbulence. Conventional and animated HCC and TSG profiles are presented in Fig. 18.1a–d respectively.

Mesh Generation and CFD Methodology

Mesh independence was verified by generating cylinder pressure variations as a function of crank angle at 50% load and presented in Fig. 18.2. As can be seen from Fig. 18.2, there is no much deviation in cylinder pressure between fine mesh and medium mesh the computational study was executed considering the medium mesh.

The number of elements for HCC and TSG was 301,347 and 475,708, respectively. Likewise, the number of nodes for HCC and TSG was 53,355 and 84,851 respectively. Simulations are carried from 180 °CA (Crank Angle) to 390 °CA, i.e., start of the compression to 23 °CA after injection. This simplifies the cylinder geometry without intake and exhaust valve. Unstructured mesh consists of tetrahedral elements (volume or 3D) and triangular elements (surface or 2D) elements. Number of nodes increased with the complexity of the piston bowl shape. In order to reduce the time taken for CFD simulations, optimal element size (3D) is chosen for meshing to minimize the total number of nodes. Transient simulations are conducted from 180 °CA to 390 °CA, total duration of 210 °CA. “Dynamic mesh with in-cylinder option is chosen for the analysis to consider the piston motion. Dynamic mesh methods opted are smoothing and re-meshing. Spring base smoothing is opted with default settings

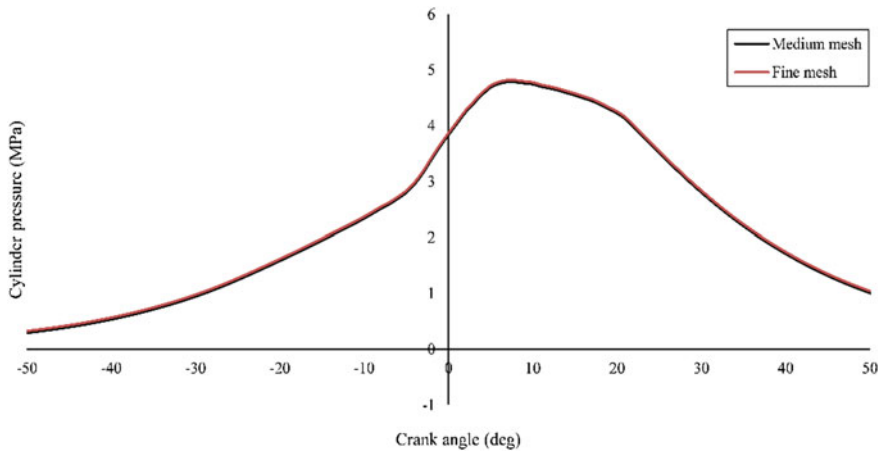


Fig. 18.2 Comparison of cylinder pressure for medium and fine mesh at 50% load

available. Re-meshing sizing function for local cells and local face with refinement interval of 5 is selected. Deforming dynamic mesh zone is created for cylinder walls. Rigid dynamic mesh zone is created for piston parts.”

Results and Discussion

Combustion

In design and optimization of combustion chamber, the basic phenomenon of spray formation, combustion, activation energy and vaporization rate is vital [22]. The spray of fuel impregnating onto the hot air typically undergoes boiling vaporization and attains combustion in no time. For the said fuel, WPOCA, the heat release rate and cylinder pressure curves for TSG and HCC piston profiles at 100% load are presented based on CFD and experimental values for comparison as Figs. 18.3 and 18.4, respectively.

The heat release rate values for piston profiles based on CFD, i.e., for CFD TSG, CFD HCC are 58.94 and 53.13 $\text{kJ/m}^3\text{deg}$, respectively. Likewise based on experimental results, the heat release rates for piston profiles, i.e., for Exp TSG and Exp HCC are 51.33 and 49.51 $\text{kJ/m}^3\text{deg}$, respectively. The cylinder pressure values for piston profiles based on CFD, i.e., for CFD TSG, CFD HCC are 5.86, 5.61 MPa and experimental results, the cylinder pressure values for piston profiles, i.e., for Exp TSG and Exp HCC are 5.47 and 4.78 MPa, respectively. The amount of oxygen in WPOCA being higher and the turbulence induced by toroidal profile contributes to the propagation of flame kernel and accelerate the combustion [23]. The theoretical

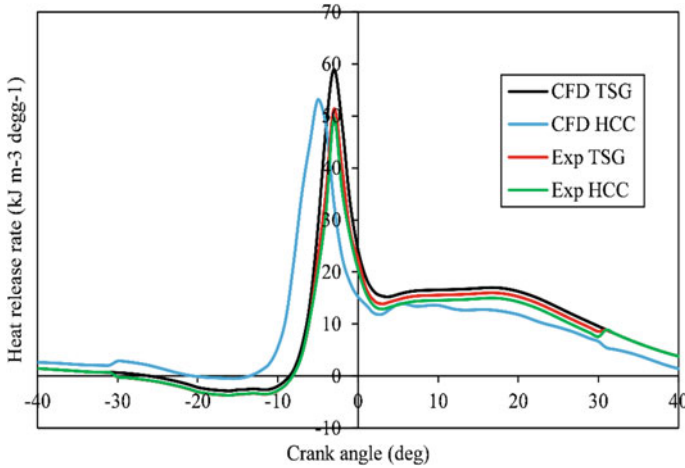


Fig. 18.3 Heat release plot for HCC and TSG profiles of pistons

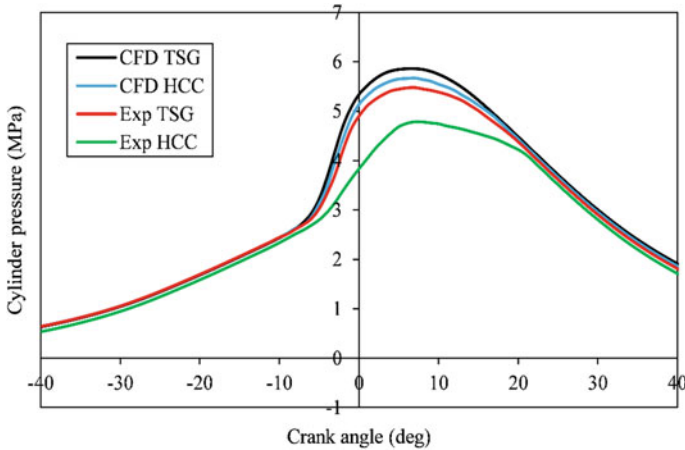


Fig. 18.4 Cylinder pressure plot for HCC and TSG profiles of pistons

computation of cylinder pressure provides the qualitative information on the combustion phenomenon. With increase in the surface temperature of air in the combustion chamber, the heat generation rate increases with decrease in rate of evaporation this results in decreased ignition delay period.

Turbulence Kinetic Energy (TKE) Distribution

Piston bowls produce swirl by forcing the air toward center of the cylinder and causes an increase in turbulence. The TKE distribution for TSG and HCC is presented in Fig. 18.5. TKE for TSG is higher than HCC, which is seen as spread across in greater area and is shifted toward the walls of the combustion chamber. TKE distribution is significant in TSG at a crank angle of 10° bTDC as compared at other crank angles and also with HCC. This may be due to the enhanced air entrainment in TSG profile resulting in better fuel air mixing. It is also understood that high TKE with high swirl results in high speed flame propagation.

Conclusion

The numerical investigation on the effect of piston bowl geometry on combustion characteristics of a compression ignition engine was performed. Two piston profiles namely HCC and TSG were considered for the study. The obtained numerical computation results were compared with the experimental results. The following conclusions were drawn:

- Turbulence effect is increased with TSG piston profile than the standard HCC piston profile.
- There was an increase in cylinder pressure by 3.24% in TSG as compared with HCC
- The heat release rate in TSG was higher than HCC by 9.85%.
- The ignition delay period is low in TSG resulting in increased heat release rate.
- To improve the combustion phenomenon, higher swirl with higher TKE is desired and a trade-off between swirl and TKE are as well desirable.

With decrease in bowl diameter in TSG, the TKE distribution increase as the piston travels toward top dead center position. To conclude, toroidal spherical grooves piston profile is preferred for the specified constant speed engine running at different loads. Further, emission characteristics should also be analyzed to optimize the combustion chamber geometry.

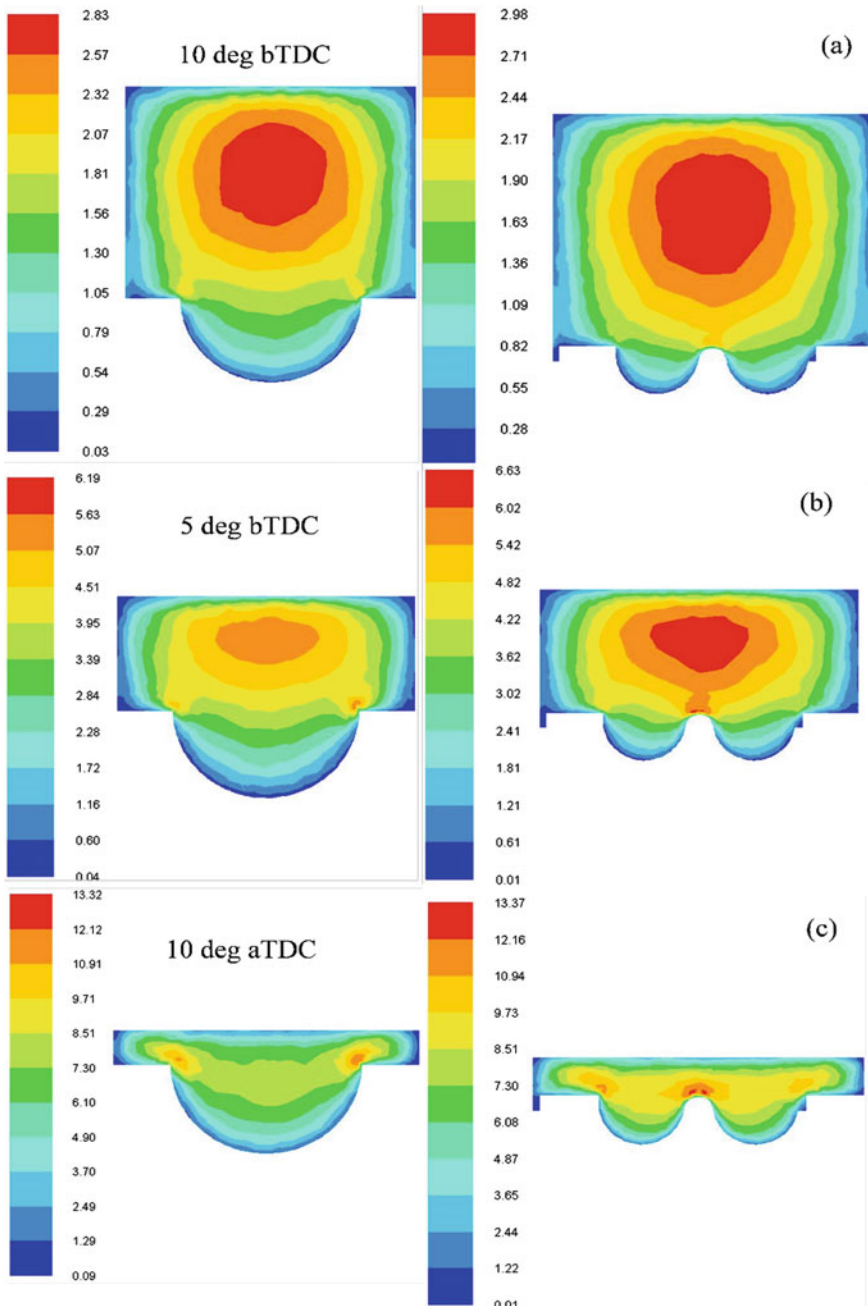


Fig. 18.5 Turbulence kinetic energy distribution plot for HCC and TSG profiles of pistons

References

1. Sanaev NK, Makhin AV, Sal'nitskii FA (2009) CAD systems in the production of diesel-engine pistons with a complex combustion chamber. *Russ Engin Res* 29:1089. <http://doi.org/10.3103/S1068798X09110057>
2. Fettes C, Schulze T, Leipertz A et al (2002) Combustion chamber wall influences on the vaporisation mixture formation and combustion in DI diesel engines with a small combustion chamber. *MTZ Worldw* 63:26–30. <https://doi.org/10.1007/BF03227569>
3. Yadav P, Saravanan CG, Edward J, Perumal R (2015) Experimental and numerical investigation of flow and combustion in a DI diesel engine with different piston geometries. SAE technical paper 2015-01-0378. <http://doi.org/10.4271/2015-01-0378>
4. Miles PC (2000) The influence of swirl on HSDI diesel combustion at moderate speed and load. SAE technical papers 2000-01-1829. <http://doi.org/10.4271/2000-01-1829>
5. Kook S, Bae C, Miles P, Choi D, Bergin M, Reitz R (2006) The effect of swirl ratio and fuel injection parameters on CO emission and fuel conversion efficiency for high dilution low temperature combustion in an automotive diesel engine. SAE Paper 2006-01-0197. <https://doi.org/10.4271/2006-01-0197>
6. Prasad BVVSU, Sharma CS, Anand TNC, Ravikrishna RV (2011) High swirl-inducing piston bowls in small diesel engines for emission reduction. *Appl Energy* 88:2355–2367. <https://doi.org/10.1016/j.apenergy.2010.12.068>
7. Heywood JB (1988) *Internal combustion engine fundamentals*. McGraw-Hill, New York
8. Prabhakaran P, Ramesh P, Saravanan CG, Loganathan M, James GE (2016) Experimental and numerical investigation of a swirl enhancing grooves on the flow and combustion characteristics of a DI diesel engine. *Energy* 115:1234–1245. <https://doi.org/10.1016/j.energy.2016.09.063>
9. Lv J, Bai M, Zhou L et al (2010) Effect of heat transfer space non-uniformity of combustion chamber components on in-cylinder heat transfer in diesel engine. *Front Energy Power Eng China* 4:392–401. <https://doi.org/10.1007/s11708-009-0066-1>
10. Taghavifar H, Khalilarya, Jafarmadar S (2014) Engine structure modifications effect on the flow behavior combustion and performance characteristics of DI diesel engine. *Energy Convers Manage* 85:20–32. <https://doi.org/10.1016/j.enconman.2014.05.076>
11. Choi GH, Lee JC, Kwon TY et al (2009) Combustion characteristics of a swirl chamber type diesel engine. *J Mech Sci Technol* 23:3385–3392. <https://doi.org/10.1007/s12206-009-1011-2>
12. Gureev VM, Khairullin AK, Varlamov FA et al (2017) Influence of combustion chamber geometry and compression ratio on the main parameters of a diesel aircraft engine. *Russ Aeronaut* 60:219–222. <https://doi.org/10.3103/S106879981702009X>
13. Binder KB (2010) Diesel Engine Combustion. In: Mollenhauer K, Tschöke H (eds) *Handbook of diesel engines*. Springer, Berlin, Heidelberg
14. Rakopoulos CD, Kosmadakis GM, Pariotis EG (2010) Investigation of piston bowl geometry and speed effects in a motored HIS engine using a CFD against a quasi-dimensional model. *Energy Convers Manage* 51:470–484. <https://doi.org/10.1016/j.enconman.2009.10.010>
15. Jaichander S, Annamalai K (2012) Influences of re-entrant combustion chamber geometry on the performance of pongamia biodiesel in a DI diesel engine. *Energy* 44:633–640. <https://doi.org/10.1016/j.energy.2012.05.029>
16. Sungwook P (2012) Optimization of combustion chamber geometry and engine operating conditions for compression ignition engines fueled with dimethyl ether. *Fuel* 97:61–71. <https://doi.org/10.1016/j.fuel.2012.03.004>
17. Sivakumar E, Silambarasan R (2020) Effect of 1,4-dioxane addition on operating characteristics of a neat biodiesels-fueled diesel engine. *Energy Sour Part A* 4:134–156. <https://doi.org/10.1080/15567036.2019.1704315>
18. Shahrokh H, Gerhard R, Anthony C, Michael E, Herbett M (2006) Application of CFD modeling in combustion bowl assessment of diesel engines using DoE methodology. SAE Technical Papers 2006-01-3330. <https://doi.org/10.4271/2006-01-3330>

19. Sivakumar E, Senthil R, Silambarasan R (2015) Study of performance and emission analysis of dual biodiesel fuelled on LHR diesel engine supported by EGR system. *Int J Mech Prod Eng Res Dev* 7:561–572. <https://doi.org/10.24247/ijmperddec201764>
20. Bridjesh P, Periyasamy P, Krishnachaitanya AV, Geetha NK (2018) MEA and DEE as additives on diesel engine using waste plastic oil diesel blends. *Sustain Environ Res* 28:142–147. <https://doi.org/10.1016/j.serj.2018.01.001>
21. Li J, Yang WM, An H, Maghbouli A, Chou SK (2014) Effects of piston bowl geometry on combustion and emission characteristics of biodiesel fueled diesel engines. *Fuel* 120:66–73. <https://doi.org/10.1016/j.fuel.2013.12.005>
22. Javed I, Baek SW, Waheed K (2013) Evaporation characteristics of heptane droplets with the addition of aluminum nanoparticles at elevated temperatures. *Combust Flame* 160:170–183. <https://doi.org/10.1016/j.combustflame.2012.09.005>
23. Li Xiaojie, Xiaobin H, Hong L (2018) A composite-fuel additive design method for n-decane low-temperature ignition enhancement. *Combust Flame* 188:262–272. <https://doi.org/10.1016/j.combustflame.2017.09.033>

Chapter 19

FEM-Based Thermal Modeling for Analyzing ECDM Process



Manoj Kumar , R. O. Vaishya , and N. M. Suri 

Introduction

Quartz glass is an important engineering material widely used in aerospace, defense, and electronic components. The quartz material offers superior characteristics over conventional material such as high strength to weight ratio, transparent, thermal, and chemical stability. Although there are other forms of glass-like borosilicate, soda-lime glass but quartz glass is preferred because of its high hardness and melting point. These properties make processing and machining difficult at the microlevel with precision when used in biomedical applications such as microfluidic devices [1, 2].

The conventional machining of quartz glass is nearly impossible under normal conditions due to its brittle nature. However, some sophisticated processes like CNC machining, diamond turning, and nontraditional machining can machine this material but have some limitations. The machining with advanced machining techniques like EDM and ECM is not possible due to the nonconducting nature of quartz material. The 3D structure can be fabricated using selective laser-induced etching, but the process is complex in comparison to selective laser melting in terms of post-treatment due to in-line capability [3]. Additive manufacturing has replaced manual glass production [4] but fine and deep microfeatures not possible. Lin and Chen [5] studied the effect of assisting machining techniques during machining of quartz glass depicts the cutting marks represents a brittle-ductile transition in biaxial ultrasonic-assisted machining. The glass polishing can be done with ultrasonic-assisted abrasive water jet machining through the plastic deformation material removal process [6].

M. Kumar (✉) · R. O. Vaishya · N. M. Suri
Department of Production & Industrial Engineering, Punjab Engineering College (Deemed to be University), Chandigarh 160012, India
e-mail: mnjbrd.02@gmail.com

ECDM is a hybrid process combining the features of the ECM and EDM process, which can machine almost any type of materials including fiber-reinforced polymer, metal matrix composite, ceramics, glass, and superalloys, etc. ECDM has the potential to machine nonconducting quartz glass material, which otherwise not possible with EDM and ECM process. ECDM is considered to be five times faster than its parent processes [7]. Kurafuji and Suda developed the ECDM process while machining glass and termed as electric discharge drilling [8]. Since then, a significant amount of development has been done to understand the process but still, the process has not been commercialized yet. Basak and Ghosh [9, 10] considered the process as an electric circuit and validated the model through experiments. Singh and Goud [11] claimed the developed 3D spark model has better results than earlier available 2D models. Wei et al. [12] simulated the model for a single spark through the finite element method for the discharge regime. Panda and Yadava [13] predicted the material removal through Gaussian heat flux input energy for traveling wire electrochemical discharge machining, for mild steel and glass workpiece material reported that with an increase in spark radius the material removal decreases. Paul and Korah [14] suggested that pulse DC has higher MRR compared with DC with a lower temperature range for borosilicate glass. Goud and Sharma [15] estimated the material removal rate using FEM, reported the enhancement in material removal rate for alumina and soda-lime glass by an increase in electrolyte concentration. The ECDM produces toxic fumes that raise health problems for the operator [16, 17]. The literature review on process FEM study is shown in Table 19.1.

The ECDM process is an evolving technique to machine difficult to process especially insulating materials. The process has tremendous potential to replace earlier existed expensive processes but very limited studies have been presented. The process parameters control and in-depth knowledge of the process are still to be explored. The literature shows that most of the work is experimental and very few theoretical models have been proposed. In this study, the 2D FEM model developed with Gaussian heat flow input to predict the thermal plots, and based on that, the material removal rate is calculated.

Methodology

Assumptions

The discharge energy produced due to electrochemical discharge phenomena is mainly responsible for material erosion, leaves craters at the machined surface. As the process is complex, therefore certain assumptions were made while developing and analyzing the model [15, 18, 19]

1. The shape, size, and nature of all sparks are the same.
2. The sample material is homogeneous and isotropic.
3. Each spark has a constant duty cycle.

Table 19.1 Summary of FEM study on the ECDM process

Sr. No.	Authors	Workpiece material	Inference
1	Rajput et al. 2020 [21]	Soda-lime glass	The CTAB surfactants added electrolyte at critical micelle concentration improves the material removal rate by 40%
2	Singh and Goud 2019 [11]	Soda-lime glass and quartz glass	The developed model was compared with already published data and found a maximum error of 1.95 mg/min for the material removal rate. The study shows 3D spark model has a closer agreement with published experimental data
3	Goud and Sharma 2017 [15]	Soda-lime glass and alumina	The 2D and 3D models have a similar trend for the material removal rate. The material removal rate increases from 10 to 45% electrolyte concentration
4	Paul and Korah 2016 [14]	Borosilicate glass	The comparison between DC and pulsed DC power source has been made using a curve fitting method. The MRR is increased by 1.675 times for pulse to normal DC power source
5	Panda and Yadava 2009 [13]	Mild steel and glass	For both the workpiece material, the MRR increases with an increase in the duty factor and ejection efficiency. The predicted material has a slightly higher value due to assumptions made
6	Wei et al. 2011 [12]	Soda-lime glass	The model was developed for a discharge regime for a single spark. The model found the drilling depth less than 0.3 mm and thermal power transfer 29.1%

(continued)

Table 19.1 (continued)

Sr. No.	Authors	Workpiece material	Inference
7	Bhondwe et al. 2006 [18]	Soda-lime glass and alumina	The easy material removal was observed for soda-lime glass compared with the alumina material. For soda-lime glass, the material removal rate holds a saturation value beyond 30% electrolyte concentration

4. The electrolyte level and tool wear are independent of the thermal spark.
5. The thermal melting of the workpiece is mainly responsible for the material.
6. The hemispherical is considered of thermal craters on the workpiece sample.
7. The Gaussian heat flux distribution is assumed for analysis.
8. The discharge efficiency during machining is taken as 100%.

Governing/Model Equation

For the above assumptions, the transient thermal diffusion equation governing the heat in the workpiece is given by Eq. (19.1).

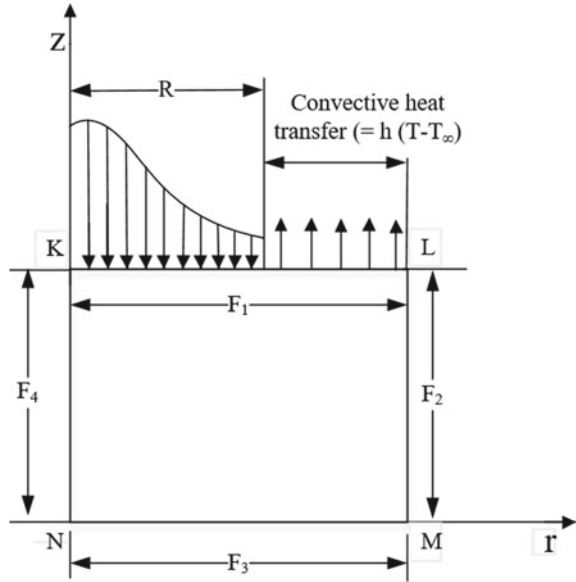
$$\frac{\partial T}{\partial t} = \alpha \left(\frac{\partial^2 T}{\partial x^2} + \frac{\partial^2 T}{\partial y^2} + \frac{\partial^2 T}{\partial z^2} \right) \tag{19.1}$$

where $\alpha \left(= \frac{k}{\rho c} \right)$. is the thermal diffusive coefficient. K , ρ , and c , are the thermal conductivity, density, and specific heat of the workpiece material, respectively. Further, x , y is the geometric coordinate points, while t and T are the time parameter and temperature during analysis. In the proposed study, Gaussian heat distribution is assumed during analysis is represented by Eq. (19.2) [18].

$$q(r) = \frac{4.45 R_w V_c I_c}{\pi r^2} \exp\left(-4.5 \frac{r^2}{R^2}\right) \tag{19.2}$$

where R_w is the energy partition of the workpiece, V_c and I_c are the critical voltage and current. Further, r and R are a radial distance from the KN plane along the y -axis and maximum spark radius, respectively, depicted in Fig. 19.1.

Fig. 19.1 Boundary condition of the study



Boundary Conditions

In the ECDM process, a spark occurs at one point over the large surface for a very small interval of time. The KLMN rectangular plot is shown in Fig. 19.1 that demonstrates the effect of a single spark. The effect of heat in the LM and MN plane is negligible and considered to be perfectly insulated. For the KN plane, when viewing in 3D, the heat generated would be symmetrical. However, along the KL plane, the heat dissipated in two modes. First, with the conduction mode, until the zone reaches the maximum value of radius R , beyond this point, the convective mode of heat transfer occurs [19]. The workpiece is assumed to be in infinite large comparing to that of spark. From the above discussion, the following representation can be made by Eqs. (19.3) and (19.4).

$$K \frac{\partial T}{\partial y} = \begin{cases} q(r), & \text{if } r \leq R \\ h(T - T_{\infty}), & \text{if } r > R. \end{cases} \tag{19.3}$$

$$\frac{\partial T}{\partial n} = 0 \tag{19.4}$$

Spark Radius and Fraction of Energy Partition

It is challenging to measure the spark radius for small pulse duration (mainly of order 10^{-4} s). In this study, spark radius is assumed to be constant, i.e., $150\ \mu\text{m}$, resulted from experimentation reported [20]. The current during machining is mainly governed by electrolyte concentration. A mathematical equation is derived for critical current as a function of electrolyte concentration using a curve fitting method represented by Eq. (19.5). For energy distribution, detailed and specific research was conducted by Kulkarni et al. [9, 10, 18, 20]. As per assumption, the only section of overall energy utilized to increase the temperature of quartz material, and the remaining energy used for a generation the electrolyte temperature surrounding the machining zone [9, 10, 12].

$$I = 0.71429 + 0.091378 \times C - 0.002.7056 \times C^2 + 3.2323 \times 10^{-5}C^3 \quad (19.5)$$

where I is the machining current, and C is the electrolyte concentration.

The material is removed from the workpiece once the temperature in the workpiece becomes higher than the melting point. The profile of material removal is shown in Fig. 19.2, assuming that curve follows the polynomial equation. Therefore, the volume of material removal and material removal rate is represented by Eqs. (19.7–19.8).

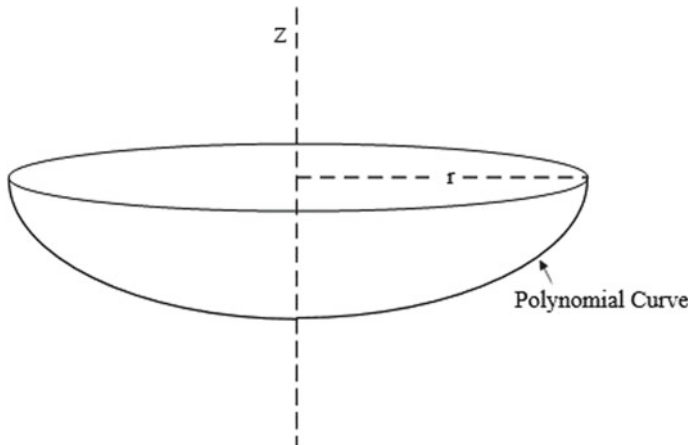


Fig. 19.2 Profile of material removal

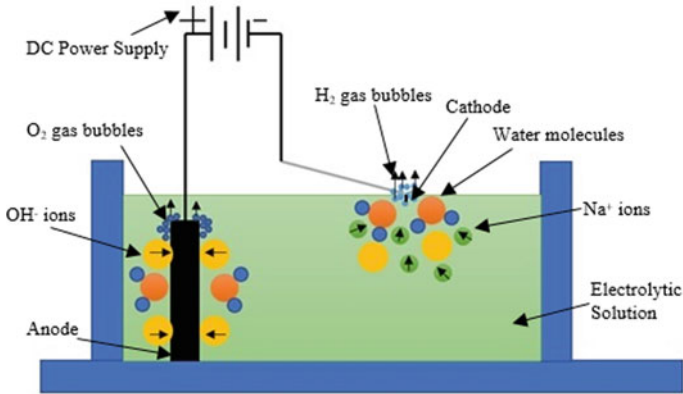


Fig. 19.3 Mechanism of the ECDM process

Mechanism and Calculation of the Material Removal Rate

From Fig. 19.3, two conductive electrodes namely cathode (mainly act as a tool) and anode (auxiliary electrode) is dipped in the conductive electrolyte such as KOH and NaOH. The ends of electrodes are connected with applied DC voltage power supply in which negative and positive end linked to tool and auxiliary electrode respectively. Under the action of the applied DC voltage source, the electrochemical reactions occur. The H₂ bubbles start forming across the tool and O₂ bubbles at the auxiliary electrode. With an increase in the applied voltage, the rate of the electrochemical reaction is increased, the H₂ gas bubbles grow in size, that shields the tool and forms a gas film, which leads to large electrical resistance through which thermal spark occurs. The intensity of spark varies with input energy available, assumed as Gaussian heat input by adjusting the quartz material in the close locality of electric discharge. The intensity of thermal spark is so high that it melts the workpiece, and ultimately material is removed through evaporation. The process is also called high-temperature chemical etching as the thermal spark is responsible for material removal in the form of a crater. The total material removal rate is calculated as material removal in one discharge and a total number of discharge per unit time [22].

Materials and Experimental Setup

The readily available quartz glass is used as the workpiece, procured from Hitech Ceramics, Chennai, India. The detailed working characteristics are listed in Table 19.2. The material having dimensions of 75 × 25 × 3 mm. The modeling and analysis of the workpiece are done using ANSYS 2016 software package.

Table 19.2 Properties of quartz glass

SiO ₂ content	Melting point	Electrical resistivity	Tensile strength	Moh's hardness	Density	Color
99.995%	1853 K	2×10^{19} (Ω cm) at 20 °C	70×10^3 KN/m ²	6	2200 kg/m ³	Transparent

The in-house built hybrid ECDCM process setup is utilized to conduct experiments. The NaOH electrolyte is used as an electrolyte due to its better specific conductance. The cylindrical shaped stainless steel and graphite are used as microtool and auxiliary electrode. The setup is fabricated by putting together the subparts like the machining tank, power supply, tool, anode, wiring system, and workpiece fixtures. The Pyrex glass having dimension $300 \times 300 \times 100$ mm is used as a machining chamber. The DC power supply is used as an input power supply having an output range of voltage and current 0–120 V and 0–10 Amp, respectively. The negative and positive terminal of DC power is connected to the tool and auxiliary electrode, respectively. The machining conditions affect the performance of any manufacturing process. The details of the experimental conditions are shown in Table 19.3. The material removal is estimated from the change in weight of quartz material before and after machining [23, 24].

$$\text{MRR} = \frac{m_i - m_f}{t} \quad (19.6)$$

The material is removed from the workpiece when the work material temperature (T) becomes greater than the melting point temperature (T_m), i.e., $T > T_m$. The isothermal planes of temperature distributions are processed to evaluate volume (V_1) of material removed. From Fig. 19.2, the material erosion from the quartz glass in the form of a hemisphere and expressed as

Table 19.3 Fixed and variable parameters of the ECDCM process

Fixed parameters		Variable parameters		Simulation study	Experimental study
Machine	In-house built ECDCM setup	Concentration (wt%)	15	0.0514	0.0606
Electrolyte	Sodium hydroxide		20	0.0809	0.0993
Sample material	Quartz glass		25	0.0954	0.1145
Anode	Graphite (L-80 mm)	Voltage (V)	45	0.0514	0.0606
Cathode	Stainless steel		50	0.1963	0.2393
Current	0–10 Amp		55	0.2789	0.3438

$$V_1 = \iiint r z \theta dr dz d\theta = \frac{2}{3} \pi r^2 z_p \quad (19.7)$$

$$V_2 = V_1 \times n \times \rho \quad (19.8)$$

where,

- MRR = material removal rate (mg/min)
- V_1 = Volume of material removed due to one spark
- V_2 = Final volume (mg/min)
- m_i = weight of the sample before the machining (mg)
- m_f = weight of the sample after machining (mg)
- t = time taken during machining (min)
- n = number of sparks per unit time
- ρ = density of workpiece (mg/mm³).

Results and Discussion

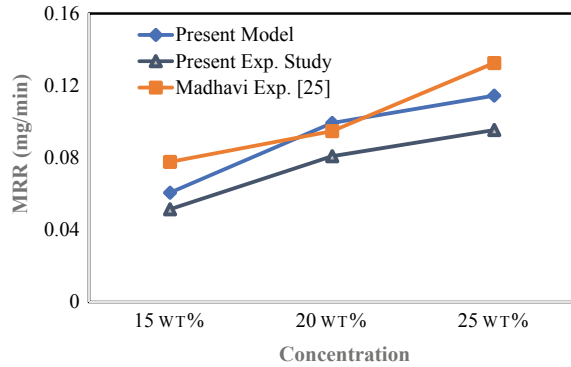
FEM Model

The FEM-based thermal model is established to estimate the material removal rate of quartz work material by acquiring the isothermal plots of temperature distributions. The development of the thermal model comprises applying the boundary conditions (Fig. 19.1) followed by meshing and ANSYS solver. The solver gives the temperature values at each of the element nodes. The model is meshed into small elements using a tetrahedron method with a patch algorithm. It enhances model solving accuracy. The profile preserving method is used for manual mapping and having volumetric transfer type. A total of 183,543 nodes are obtained during the model meshing with 100,793 elements. The heat input boundary is further refined for improving mesh accuracy.

Validations

The developed model is validated by comparing the simulated MRR of quartz with the previously reported experimental MRR [25] and the present experimental study. Figure 19.4 shows the comparison of simulated MRR with the experimental MRR [25] and the present study. It is found that the inclination of simulated MRR is similar when compared with the experimental study [25]. However, a difference in the MRR values is also seen due to the assumptions made in the present model. Moreover, experiments are also performed to assess the model validity and good agreement is observed between the two. Few differences are also observed which

Fig. 19.4 MRR comparison with previous and present study at different electrolyte concentrations



may be accounted for the assumptions made in the model, i.e., spark radius, energy transference, etc.

Parametric Study on MRR

Effect of Electrolyte Concentration on MRR

Figure 19.4 illustrates that the MRR of quartz improves successfully, the enhancement in electrolyte concentration from 15 to 30 wt%, an increase of 1.54 times in material removal rate is observed with the 100% increase in electrolyte concentration because it enhances the development rate of hydrogen bubbles inside the electrolyte. Subsequently, the quick formation of the gas film is seen at the tool vicinity. As a result, the high frequency of sparks observed over the work material that causes an increase in thermal energy input [26]. FEM simulation depicted that the quantity of thermal energy transmitted to the quartz glass increases with the increase in electrolyte concentration due to the increase in heat flux as seen in Fig. 19.5a. It increases the peak temperature of the work material as shown in Fig. 19.5b. The simulation results of the increase in work material are illustrated in Fig. 19.6. Thus, high MRR is observed at higher electrolyte concentration for quartz material.

Effect of Applied Voltage on MRR

Figure 19.7 shows the MRR variation of simulated and experimental MRR at different applied voltage. It is seen that MRR improves with the increment in applied voltage due to the increased thermal energy in the machining zone. An increase in applied voltage accelerates the electrolysis process that enables the quick formation of gas film and as a result, high spark intensity occurs over the work material. As a result, high MRR is obtained at high levels of the applied voltage.

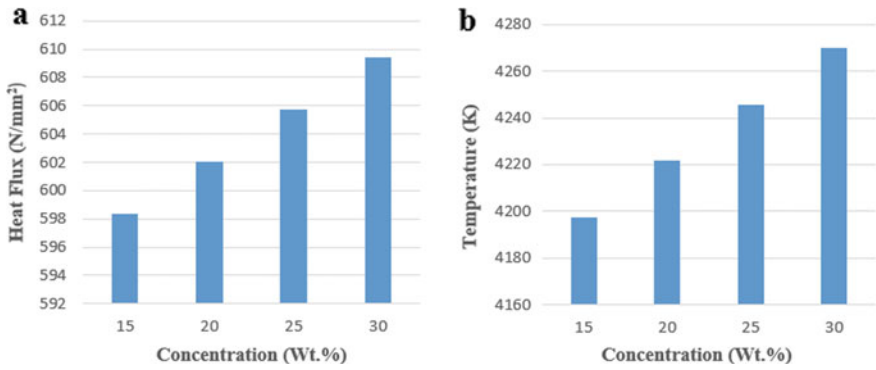


Fig. 19.5 Influence of electrolyte concentration on **a** heat flux (N/mm²), **b** temperature (K)

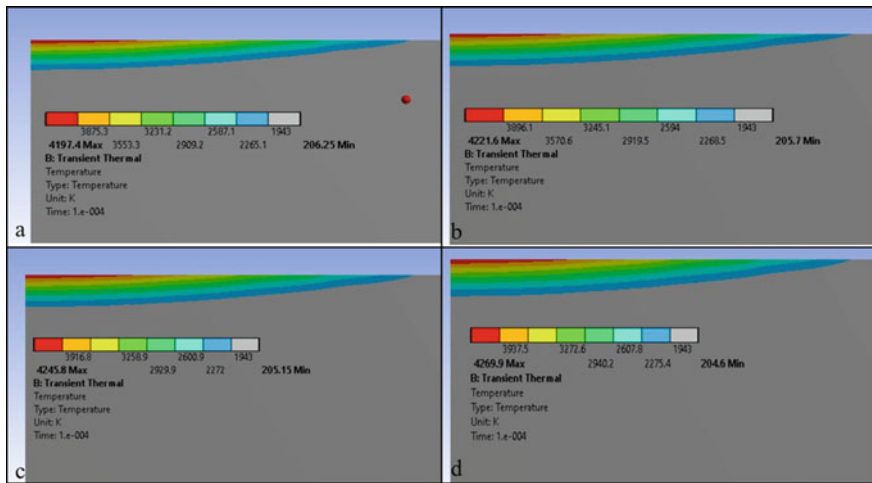
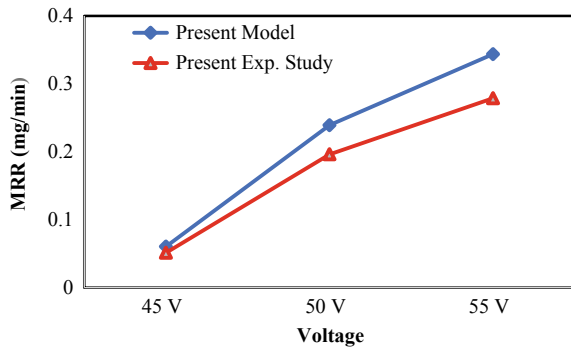


Fig. 19.6 Isothermal plots at electrolyte concentration **a** 15%, **b** 20%, **c** 25%, **d** 30%

Fig. 19.7 Influence of DC voltage on MRR



Conclusion

In the proposed study, the 2D Gaussian heat distribution model has been developed by a finite element analysis for quartz glass while machining using a micro electrochemical discharge machining process. The thermal plots were used to find the material removal from the workpiece. The effect of applied DC voltage and electrolyte concentration was studied on material removal and compared with the previously conducted study. The conclusion is summarized as follows.

The simulated model has a close agreement with the previous study and confirmation experimental study with a slight variation due to the assumption made while developing the model. The material removal rate is found to increase with an increase in the electrolyte concentration and applied voltage. The ECDM is a complex, random, and hybrid machining technique therefore, the model can be further developed to include the 3D spark region and other modes of material removal.

References

1. Singh J, Vaishya R, Kumar M (2019) Fabrication of micro features on quartz glass using developed WECDM setup. *ARPN J Eng Appl Sci* 14:725–731
2. Kumar M, Vaishya RO, Oza AD, Suri NM (2020) Experimental investigation of wire-electrochemical discharge machining (WECDM) performance characteristics for Quartz material. *Silicon* 12:2211–2220. <https://doi.org/10.1007/s12633-019-00309-z>
3. Gottmann J, Hermans M, Repiev N, Ortmann J (2017) Selective laser-induced etching of 3D precision quartz glass components for microfluidic applications-up-scaling of complexity and speed. *Micromachines* 8:110. <https://doi.org/10.3390/mi8040110>
4. Lin SY, Chen JZ (2017) Effect of various assisted machining technique applications on cutting performance of quartz glass milling. In: *Proceedings 2017 IEEE international conference on applied system innovation Mod Technol ICASI 2017*, pp 1583–1586. <https://doi.org/10.1109/ICASI.2017.7988232>
5. Witzendroff PV et al (2018) Additive manufacturing of glass: CO₂-Laser glass deposition printing. In: 10th CIRP conference on photonic technologies [LANE 2018] *Procedia CIRP* 74:272–275. <https://doi.org/10.1016/j.procir.2018.08.109>
6. Hou R, Wang T, Lv Z, Liu Y (2018) Experimental study of the ultrasonic vibration-assisted abrasive waterjet micromachining the Quartz glass. *Adv Mater Sci Eng*. <https://doi.org/10.1155/2018/8904234>
7. Crichton IM, McGeough JA (1985) Studies of the discharge mechanisms in electrochemical arc machining. *J Appl Electrochem* 15:113–119. <https://doi.org/10.1007/BF00617748>
8. Kurafuji H, Suda K (1968) Electrical discharge drilling of glass. *Ann CIRP* 16:415–418
9. Basak I, Ghosh A (1997) Mechanism of material removal in electrochemical discharge machining: a theoretical model and experimental verification. *J Mater Process Technol* 71:350–359. [https://doi.org/10.1016/S0924-0136\(97\)00097-6](https://doi.org/10.1016/S0924-0136(97)00097-6)
10. Basak I, Ghosh A (1996) Mechanism of spark generation during electrochemical discharge machining: a theoretical model and experimental verification. *J Mater Process Technol* 62:46–53. [https://doi.org/10.1016/0924-0136\(95\)02202-3](https://doi.org/10.1016/0924-0136(95)02202-3)
11. Singh D, Goud M (2018) A 3D spark model to evaluate MRR in ECDM. *J Adv Manuf Syst* 18:435–446. <https://doi.org/10.1142/S0219686719500239>

12. Wei C, Xu K, Ni J et al (2011) A finite element based model for electrochemical discharge machining in discharge regime. *Int J Adv Manuf Technol* 54:987–995. <https://doi.org/10.1007/s00170-010-3000-0>
13. Panda MC, Yadava V (2009) Finite element prediction of material removal rate due to traveling wire electrochemical spark machining. *Int J Adv Manuf Technol* 45:506–520. <https://doi.org/10.1007/s00170-009-1992-0>
14. Paul L, Korah LV (2016) Effect of power source in ECDM process with FEM Modeling. *Procedia Technol* 25:1175–1181. <https://doi.org/10.1016/j.protcy.2016.08.236>
15. Goud M, Sharma AK (2017) A three-dimensional finite element simulation approach to analyze material removal in electrochemical discharge machining. *Proc Inst Mech Eng Part C J Mech Eng Sci* 231:2417–2428. <https://doi.org/10.1177/0954406216636167>
16. Dhiman P, Vaishya R, Kumar M (2019) A review on machining by electrochemical discharge phenomena. *Int J Tech Innov Mod Eng Sci* 5:71–74
17. Singh M, Singh S (2020) Sustainable electrochemical discharge machining process: characterization of emission products and occupational risks to operator. *Mach Sci Technol*. <https://doi.org/10.1080/10910344.2020.1752238>
18. Bhondwe KL, Yadava V, Kathiresan G (2006) Finite element prediction of material removal rate due to electro-chemical spark machining. *Int J Mach Tools Manuf* 46:1699–1706. <https://doi.org/10.1016/j.ijmactools.2005.12.005>
19. Wang YK, Xie BC, Wang ZL, Peng ZL (2011) Micro EDM deposition in air by single discharge thermo simulation. *Trans Nonferrous Met Soc China* 21:450–455. [https://doi.org/10.1016/S1003-6326\(11\)61623-3](https://doi.org/10.1016/S1003-6326(11)61623-3)
20. Kulkarni A, Sharan R, Lal GK (2003) Measurement of temperature transients in the electrochemical discharge machining process. *AIP Conf Proc* 684:1069–1074. <https://doi.org/10.1063/1.1627271>
21. Rajput V, Goud M, Suri NM (2020) Performance analysis of ECDM process using surfactant mixed electrolyte. In: Sharma V, Dixit U, Sørby K, Bhardwaj A, Trehan R (eds) *Manufacturing engineering*, Springer, Singapore, pp 285–300. https://doi.org/10.1007/978-981-15-4619-8_22
22. Rajput V, Goud MM, Suri NM (2019) Experimental investigation to improve the removal rate of material in ECDM process by utilizing different tool electrode shapes. *Int J Techn Innov Modern Eng Sci (IJTIMES)* 5:333–341
23. Kumar M, Vaishya RO, Suri NM (2020) Machinability study of Zirconia material by micro-ECDM. In: Sharma V, Dixit U, Sørby K, Bhardwaj A, Trehan R (eds) *Manufacturing engineering*, Springer, Singapore, Pp 195–209. https://doi.org/10.1007/978-981-15-4619-8_15
24. Oza AD, Kumar A, Badheka V, Arora A (2019) Traveling wire electrochemical discharge machining (TW-ECDM) of Quartz using zinc coated brass wire: investigations on material removal rate and Kerf width characteristics. *Silicon* 11:2873–2884. <https://doi.org/10.1007/s12633-019-0070-y>
25. Bindu MJ, Hiremath SS (2019) Machining and characterization of channels and textures on Quartz glass using μ -ECDM process. *Silicon* 11:2919–2931. <https://doi.org/10.1007/s12633-019-0083-6>
26. Oza AD, Kumar A, Badheka V (2020) Improving quartz micro-machining performance by magnetohydrodynamic and zinc-coated assisted traveling wire-electrochemical discharge machining process. *Mater Today Proc* 28:970–976. <https://doi.org/10.1016/j.matpr.2019.12.334>

Chapter 20

Designing and Analyzing the Different Parameters of Pulp Removal Machine



Chiraya Hans Wilson and Bobby K. George

Introduction

Gelatin has got inevitable usages in the pharmaceutical and food industries. Many of the gelatin manufacturing industries use ossein as the raw material for production of gelatin. Ossein is bone material of animals generally chipped to size of about 0.5 cm. The raw material ossein contains large amount of impurities. Therefore, it is necessary to filter out the impurities during the production of gelatin as in [1]. For filtration process, paper pulp cake placed over the filtration plate acts as the permissible membrane. By filtering the ossein using paper pulp, we could attain microfiltration of ossein. During filtration process, the impurities present in ossein such as insoluble mineral salts would get filtered at the paper pulp membrane. So it is required to replace the impure paper pulp membrane with new membrane as well as clean the filtration plate after each filtration process. In Gelatin industries, the removing of contaminated paper pulp and cleaning of filtration plate is done manually. This process of cleaning of filtration plate has got many industrial issues. First, the cleaning of filtration plate is done using high pressure water jet nozzle and it is also done in an open space. While doing this, the paper pulp splashes to nearby machine parts and surroundings and even it can cause accidents to the workers in filtration area. Second, the workers take large amount of time in cleaning the filtration plate, this is because the paper pulp gets more sticky with time, therefore it sticks to filtration plate and with mere spraying of water the pulp does not go off from the filtration plate. So for cleaning, the filtration plate it would take an average time period of 1 h. Third, large amount of water is utilized for cleaning of a filtration

C. Hans Wilson (✉) · B. K. George
Department of Production Engineering GEC, Thrissur, India
e-mail: hanswilson007@gmail.com

B. K. George
e-mail: bobykgeorge@gmail.com

plate. Finally, the pulp making area seems to be very untidy and unsafe working environment. In this thesis, we resolve these issues by developing an automated pulp removal machine for cleaning up the filtration plate.

Related Works

Abdalbasit Mariod [2] discusses the different sources, extraction methods and industrial applications of gelatin. It is done by conducting a study in gelatin manufacturing industries. Rohit Singh Solanki [3] a hand-operated axial-flow neem depulper was designed, developed and evaluated to meet the demand of neem seeds and its products. Using standard mechanical design procedures, an axial-flow hand-operated neem depulper was developed.

Pratima Bajpai [4] has done a research in the field cleanliness requirement for pulp is high. Large and hard particles in the pulp suspension can damage or cause erosion in the machinery. Presses and some parts of a paper machine can be particularly sensitive. Centrifugal cleaning is usually used for the bleached pulp, except for cleaning for sand removal, which is also used in unbleached screening systems.

Methodology and Objectives

In this thesis, quantitative research methodology is chosen for designing the pulp removal machines. In this approach, we take the data, values according to the real scenario and study related to those data are done. So it can be said that the result obtained from the study is much related to the current or practical events happening in industry. To conduct study regarding gelatin, a gelatin manufacturing is selected and live data are taken quantitatively from it. Designing a machine component, there is no rigid rule. The problem may be attempted in several ways. Following this methodology, the main objectives of this paper are framed:

1. Identification of problems at paper pulp making plant.
2. Development and designing the pulp removal machines 3D models in Solid-works.
3. Analyzing the different parameters such as cost of the machine, energy consumes and space utilized.

Problem Definition

In Gelatin plant, the removing of contaminated paper pulp and cleaning of filtration plate is done manually. This process of cleaning of filtration plate has got many industrial issues. First, the cleaning of filtration plate is done using high pressure

water jet nozzle and it is also done in an open space. While doing this, the paper pulp splashes to nearby machine parts and surroundings and even it can cause accidents to the workers in filtration area. Second, the workers take large amount of time in cleaning the filtration plate, this is because the paper pulp gets more sticky with time, therefore it sticks to filtration plate and with mere spraying of water the pulp does not go off from the filtration plate. So for cleaning, the filtration plate it would take an average time period of 1 h. Third, large amount of water is utilized for cleaning of a filtration plate. Finally, the pulp making area seems to be very untidy and unsafe working environment.

In this thesis, we resolve these issues by developing an automated pulp removal machine for cleaning up the filtration plate.

Paper Pulp Filtration Plate

The pulp is placed in form of cake over this filtration plate. Design of automated pulp removal machine is developed for cleaning the contaminated pulp over this filtration plate. The filtration plate is made of stainless steel. It has got a circular cross-section. The pulp is placed over the filtration plate. With the thickness of 60 + 5 mm

Inner diameter of filtration plate = 120 mm

Outer diameter of filtration plate = 600 mm.

Thickness of paper pulp = 60 + 5 mm (see Fig. 20.1).

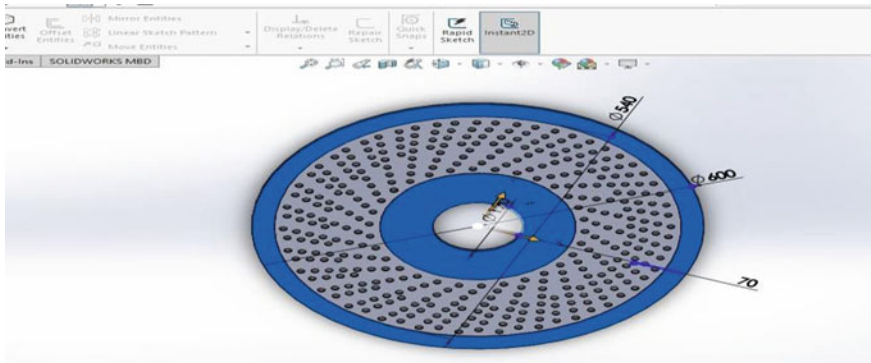


Fig. 20.1 Circular mesh

Average Time—Screen Immersed in Hot Water Tank

The following are the duration in which screen is immersed in hot water tank.

Average number of plate employed in screen washing tank in single tank is about 28 screens. Average time, the screen is been immersed in hot water is about 64 min (1 h 04 min).

Average Time—for Washing the Screen

The following is the time taken for washing the screen manually.

Average time for washing the filtration screen using pump = 2.32 min. Average total time for washing (per screen) = Average time immersed + Average time for washing screen using pump = 64 + 2.3 min = 66.32 min + queuing time + carrying time.

Results

The software used for designing is SOLIDWORKS 2016.

Pulp Removal Machine I

The main components of pulp removal machine I are belt conveyor, pulp removal vibrator, pulp removal blade case, high speed nozzle, pulp removal brush, air blower holder, pulp filtering mesh, motors, water collecting tank, machine cover guard and pulp removal machine holding frame.

Working of pulp removal machine I:

The circular screen is loaded on the pulp removal vibrator, due to the reciprocating motion—the pulp gets separated from plate and falls underneath. Then it moves over the conveyor belt as in [5]. Conveyer belt carries the screen to the pulp removal blade, it clear off any further remaining of the pulp over screen. Thereafter conveyor carries to the brushing and nozzle area, the brushing is done by the sliding motion performed by motor, here water splashing and cleaning using water are done simultaneously. Then air blower comes to the action, it pumps air over circular screen, which removes after droplets and pulp drops present over the mesh and makes the circular mesh dry. Then the mesh moves to circular mesh end collector. The splashed water or water used for cleaning is guided to the filtering mesh/screen for reusing, the filtering mesh prevents pulp in going to the water collection tank (see Fig. 20.2). Water pumped back using motor to water collection tank to the nozzle head.

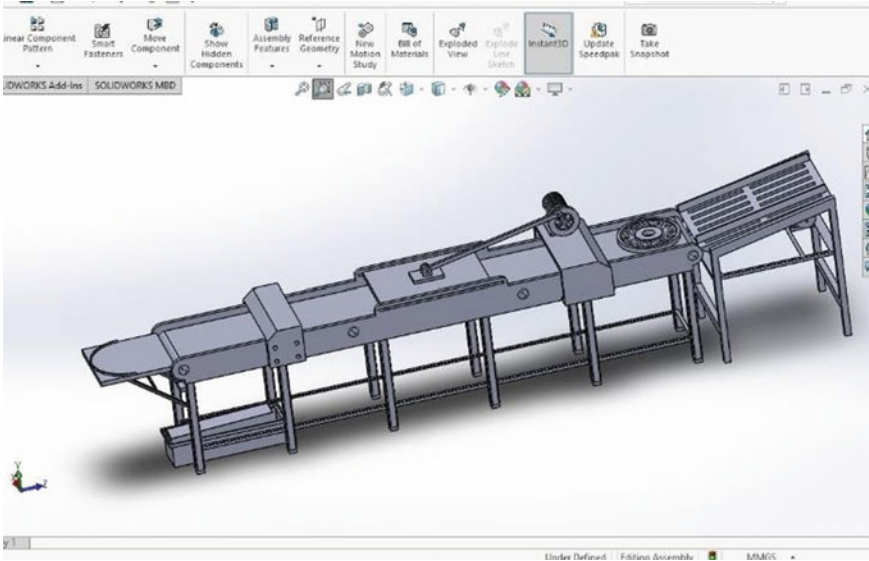


Fig. 20.2 Pulp removal machine I

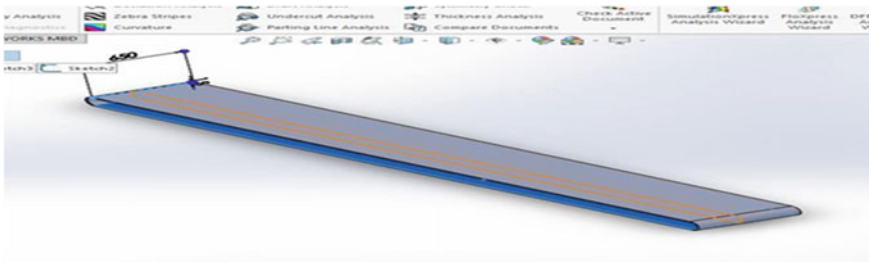


Fig. 20.3 Belt conveyor

Belt Conveyor

Belt width:

The diameter of the circular screen = 600 mm

The standard belt width available = 650 mm [6] Belt width is selected as 650 mm (see Fig. 20.3).

Pulp Removal Vibrator

Length of the vibrator = 1200 mm, breadth = 900 mm

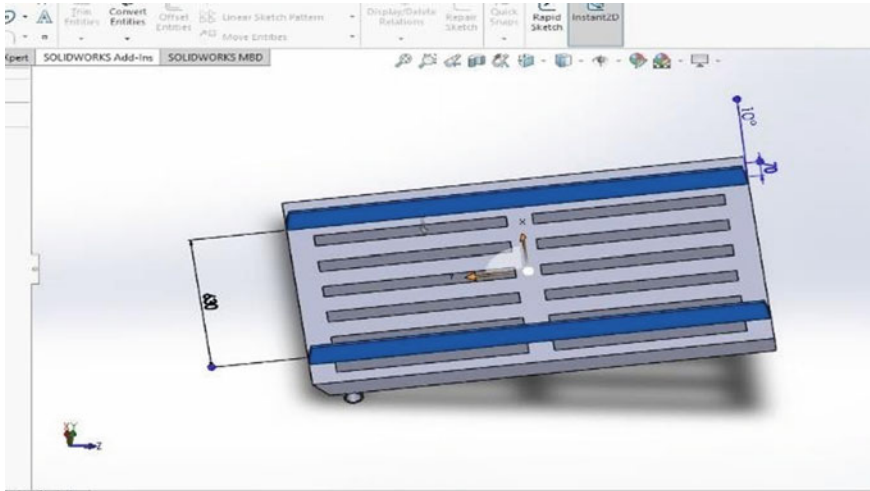


Fig. 20.4 Pulp removal vibrator

A guider path is given to keep the circular screen in position during vibration.
 Guider path width is given as 630 mm (5% tolerance to circular screen width)
 Guider path height = 70 mm (see Fig. 20.4).

Pulp Removal Blade Case

Breadth of the blade case = 900 mm.

It has got housing to hold pulp removal blade.

Blade is placed with a height just above the circular screen thickness.

Blade peel off the pulp remains present on the circular mesh, which comes about from vibrator.

Stainless steel blades could be selected due to its long-lasting life, resist corrosion and easy to maintain.

Pulp Removal Brush and Nozzle

Width of the pulp removal brush and nozzle holder = 900 mm Length of the pulp removal brush and nozzle holder = 1200 mm.

Length is taken as twice the diameter of circular screen, this to facilitate more brush and nozzle time over the screen.

Nozzle is placed along the brushes, which facilitates both washing and brushing simultaneously.

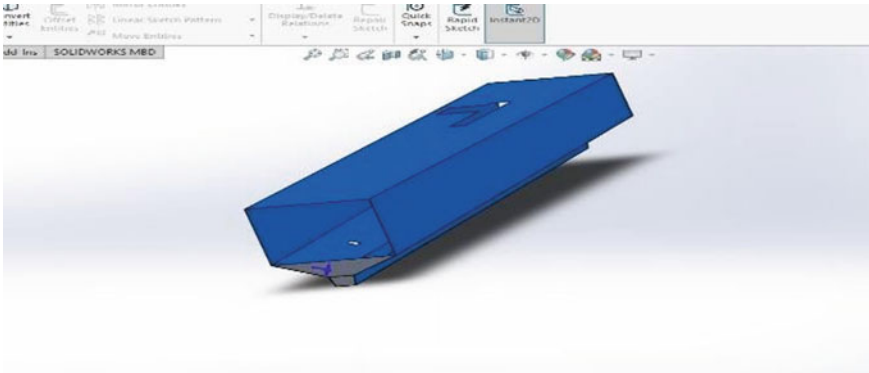


Fig. 20.5 Machine cover guard

Water Collecting Tank

Length of the water collecting tank = 1000 mm, breadth of the water collecting tank = 200 mm, height of the water collecting tank = 230 mm.

The water is collected and is pumped back to the nozzle head, this ensures efficient use of water. Pump carries water back to the nozzle.

Machine Cover Guard

It is a covering given to the machine parts. It focuses on human safety, prevents splashing of water and pulp during cleaning. Machine cover guard directs water and pulp to filtering mesh and after collecting tank.

Length of machine cover guard = 5250 mm, breadth of the machine cover guard = 945 mm (see Fig. 20.5).

Air Blower Holder

Air blower holder is housing for air blower. After washing with water, the circular mesh contains water droplets on its surface. The air blower pumps air at high velocity, which splashes out the water droplets and makes the circular screen dry.

Length of the air blower holder = 350 mm, breadth of the air blower holder = 900 mm.

Pulp Removal Machine Holding Frame

Length of the frame = 5100 mm, breadth of the frame = 900 mm (see Fig. 20.6).

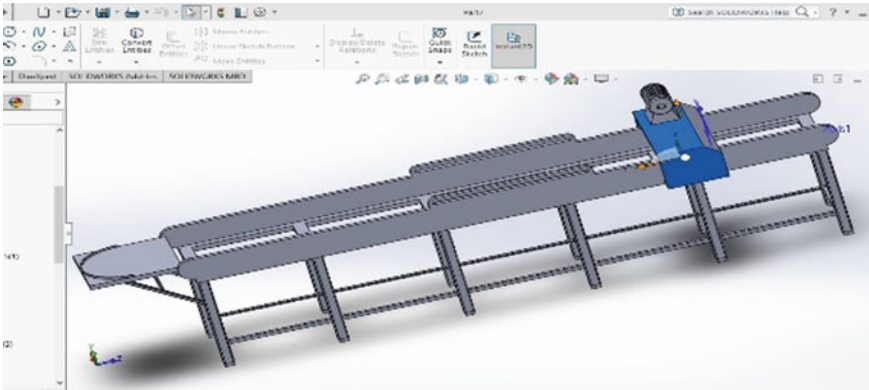


Fig. 20.6 Pulp removal machine holding frame

Pulp Removal Machine II

The main components of pulp removal machine II are lead screw, machine outer cover, nozzle and brushes, machine stand, filtering mesh, water collecting tank, sensors and other accessories and motor

Working of Pulp removal machine II:

The circular screen/mesh for pulp removal is placed on the screen holder on the lead screw as in ref. [7]. The lead screw translates the turning motion to linear motion. When the lead screw turns in clock-wise direction, the circular screen travels down. During the motion, water from nozzle at high velocity splashes the pulp remains on the circular screen. The brush gets rubbed over the circular screen, which removes the pulp residuals. When the circular mesh reaches the bottom end of the pulp removal machine, the sensor senses it, gives a command to reverse the direction of rotation. This result in anticlock-wise rotation of lead screw, which makes circular screen to travel back through lead screw. During its return journey, screen again rubbed with brushes and also washed with high speed nozzle (see Fig. 20.7).

Lead Screw

Length of the lead screw = 1200 mm, diameter of the lead screw = 50 mm, pitch = 50 mm (clockwise), number of revolution = 25.

Lead = number of start \times pitch = 50 mm \times 2 = 100 mm, total length of the lead screw shaft = 1350 mm (see Fig. 20.8).

Fig. 20.7 Pulp removal machine II

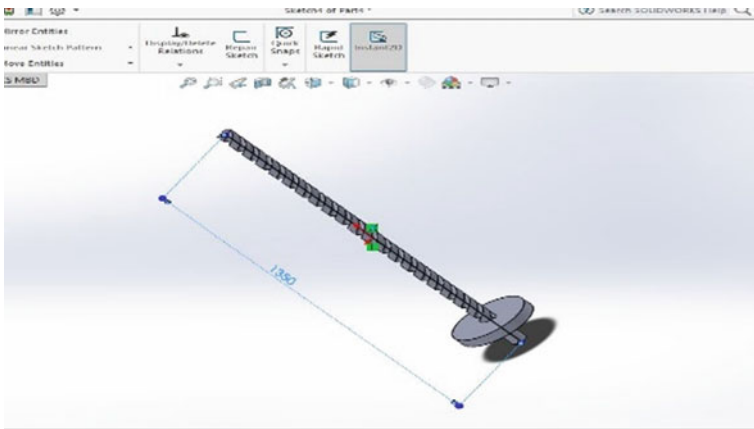
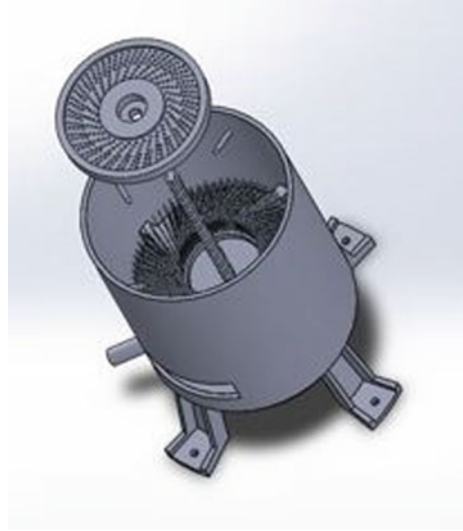


Fig. 20.8 Lead screw

Nozzles and Brushes

Brushes and nozzles are used for cleaning pulp from circular mesh. These are installed on the circular frame of the machine. Nozzle splashes water at high velocity (for this standard nozzle with proper pressured need to be selected). Brushes rubs over the circular screen and cleans up the pulp (see the Fig. 20.9).

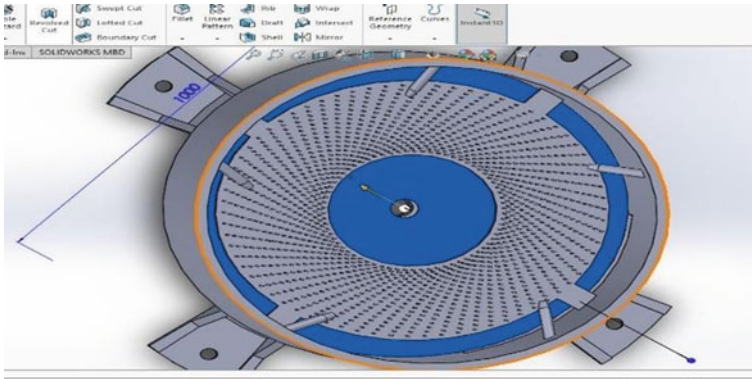


Fig. 20.9 Nozzles and brushes

Machine Outer Cover

Diameter of the outer cover = 800 mm (designed 25% more than the circular screen diameter)

Length of the outer cover = 1200 mm

It is housings of brushes, nozzle, lead screw, filtration mesh and water collecting tank.

Cost Estimation of Automated Pulp Removal Machine

In this section, we estimate the approximate cost of the two automated pulp removal machine. The cost includes the raw material cost, cost of the motor, nozzle and other accessories. Then comparison of both products with regards to approximate estimated cost is also done.

Estimated Cost of Automated Pulp Removal Machine I

1. Raw material cost

This includes raw material cost of all parts of the automated pulp removal machine I such as pulp removal vibrator, belt conveyor, pulp removal blade case, pulp removal brush and nozzle, pulp filtering mesh, water collecting tank and pulp removal machine frame as in [8].

Aluminium alloy is chosen as the building material for the machine. The material aluminium is chosen to make the automated pulp removal machine light in weight and also materials hold properties such as excellent corrosion resistance and are easy to work with heavy machinery due to its thermal and electrical conductivity as in [9]. Because of its lightweight and general availability, aluminium is fairly

Fig. 20.10 Approximate weight of component parts of pulp removal machine I

SL NO	MACHINE PARTS	WEIGHT(KG)
1	Pulp Removal Vibrator with Stand	148.58
2	Pulp Removal Blade Case	21.5
3	MachineCover Guard	61.31
4	Water Collecting Tank	29.93
5	Pulp Removal Nozzle & Brush Holder	62.47
6	Air Blower Holer	21.5
7	Filtering Mesh	1.26
8	Machine Holding Frame	171.28
	TOTAL WEIGHT OF THE MACHINE	517.83

inexpensive compared to other metals. The density of the aluminium alloy is 0.002 g/mm³.

Proposed raw material weight of the Pulp removal machine I = 517.83 kg (see Fig. 20.10). Cost of the aluminium alloy = 140/kg

Therefore, raw material cost of the pulp removal machine I = Cost per kilogram × Total weight = 140 × 517.83 = 72,496.2 rupees

2. Accessories Cost

Here the cost of other accessories such as nozzle, motor, cutting blade and air blower.

The total accessories cost of automated pulp removal machine I = 19,280 rupees.

3. Total Cost

Total cost = raw material cost + other accessories cost = 72,496.2 + 19,280 = 91,776.2 rupees (excluding labour charges + government tax)

Estimated Cost of Automated Pulp Removal Machine II

1. Raw Material Cost

This includes raw material cost of all parts of the automated pulp removal machine II such as lead screw, machine outer case and frame, bottom cover and water collecting tank.

Proposed raw material weight of the pulp removal machine II = 211.66 kg (see Fig. 20.11). Cost of the aluminium alloy = 140/kg.

Therefore, raw material cost of the pulp removal machine I = Cost per kilogram × Total weight = 140 × 211.66 = 29,632.4 rupees.

2. Accessories Cost

Here the cost of other accessories includes nozzle and motors. The total accessories cost of automated pulp removal machine II = 8480 rupees.

3. Total Cost

Total cost = raw material cost + other accessories cost = 29,632.4 + 8480 = 38,112.4 rupees (excluding labour charges + government tax).

SL NO	MACHINE PARTS	WEIGHT(KG)
1	MachineCover Guard and holding grame	178.36
2	Water collecting tank	12.92
3	Lead screw	11.3
4	Bottom cover	9.08
	TOTAL WEIGHT OF THE MACHINE	211.66

Fig. 20.11 Approximate weight of component parts of pulp removal machine II

Space Consumed by Automated Pulp Removal Machines

Space utilization is a strategically important space management measure. For the efficient operation of each production process, individual machines and equipment must be used in the maximal possible measure.

Space Consumed by Automated Pulp Removal Machine I

Length of the machine = 7256 mm = 7.256 m

Width of the machine = 1246 mm = 1.245 m Height of the machine = 1560 mm = 1.560 m

Therefore, total floor space consumed = length of machine \times with of machine = $7.256 \times 1.245 = 9.0337 \text{ m}^2$

Total volume space consumed = Total floor space \times height of the machine = $9.0337 \times 1.560 = 14.092 \text{ m}^3$.

Space Consumed by Automated Pulp Removal Machine II

This machine is a vertical type machine, which consumes vertical space more compare with horizontal.

The following calculation shows the space utilized by the machine. Length of the machine = 1139 mm.

Width of the machine = 1139 mm, Height of the machine = 2131mm.

Therefore total floor space consumed = length of machine \times width of machine = $1.139 \times 1.139 = 1.2973 \text{ m}^2$.

Total volume space consumed = total floor space \times height of the machine = $1.2973 \times 2.131 = 2.7645 \text{ m}^3$.

Energy Consumed by Automated Pulp Removal Machines

Energy efficiency has become key driver of sustainable development of a firm. Higher energy consumed equipment bring down the profit margin of the organization. Therefore, energy efficient machines play great role with profit of firm. Here we are calculating the energy consumed by the machines. For this, we consider a duration period of one hour. Following shows the energy consumption rate of individual machines.

Energy Consumed by Automated Pulp Removal Machine I

The following are the motor usage and its energy consumption for duration of an hour.

- (1) The power consumed by the motor (used in conveyor system) = 1.49 KW
- (2) The power consumed by the motor (used in pulp removal vibrator) = 1.49 KW
- (3) The power consumed by the motor (used in high pressure nozzle) = 0.372 KW
- (4) The power consumed by the motor (used in brushing an cleaning system) = 0.746 KW.

Therefore, the total power consumed by the automated pulp removal machine I for 1 h = total of power consumed by individual motor = 4.096 KW.

Energy Consumed by Automated Pulp Removal Machine II

The following are the motor usage and its energy consumption for duration of an hour.

- (1) The power consumed by the motor (used in lead screw mechanism) = 1.49 KW
- (2) The power consumed by the motor (used in high pressure nozzle) = 0.372 KW.

Therefore, the total power consumed by the automated pulp removal machine.

II for 1 h = total of power consumed by individual motor = 1.862 KW.

Conclusions

The studies show that industrial and environmental issues caused by manual filtration plate cleaning process could be resolved by using the automated pulp cleaning machine. Both the pulp removal machine that is designed could solve the issues caused by manual cleaning. On further study of each individual machine, it shows that the pulp removal machine II has got more advantage than the pulp removal machine I.

In account of cost incurred, energy consumed, space utilized the pulp removal machine II stood at higher end than pulp removal machine I. On the other hand,

when coming to the setting time, the pulp removal machine I seems to have upper hand than pulp removal machine II, it is because the pulp removal machine I works with a conveyor system. Although the time taken for the cleaning is almost same, but looking towards future aspect, pulp removal machine I has more advantage than machine II. It is because machine I has higher throughput with less setting time and also its can easily bridge with pre- and post-filtration.

References

1. Choi YS, Hong SR, Lee YM, Song KW, Park MH, Nam YS (1999) Study on gelatin-containing artificial skin: I. Preparation and characteristics of novel gelatin-alginate sponge. *Biomaterials* 20:409–417
2. Abdalbasit Adam Mariod HFA (2014) Review: gelatin, source, extraction and industrial applications 2(2):135–147
3. Rohit Singh S (2017) Design, development and evaluation of neem Depulper, vol 48(4)
4. Bajpai P (2018) Biermann's Handbook of Pulp and Paper Pulp Cleaning, Screening, and Fractionation, 3rd edn, Elsevier India
5. Jagtap AA, Vaidya S, Samrutwar AR, Kamadi RG, Bhende NV (2015) Design of material handling equipment: belt conveyor system for crushed biomass wood using V merge conveying system 7(7). ISSN: 2278-7798
6. Fleiter T, Fehrenbach D, Worrell E, Eichhammer W (2012) Energy efficiency in the German pulp and paper industry—a model-based assessment of saving potentials. *Energy* 40:84–99
7. Patel J, Rana M (2017) A review work the on lead screw 5(6):302–304. ID: IJSRDV5I60202
8. Huang XX, Newnes LB, Parry GC (2011) The adaption of product cost estimation techniques to estimate the cost of service, pp 417–431. <https://doi.org/10.1080/0951192X.2011.596281>
9. Prasad DS, Shoba C, Ramanaiah N (2014) Investigations on mechanical properties of aluminum hybrid composites 3(1):79–85

Chapter 21

Fabrication and Analysis of Apparatus for Measuring Stored Renewable Hydrogen Energy in Metal Hydrides



Rohan Kalamkar , Vivek Yakkundi, and Aneesh Gangal

Introduction

Hydrogen is considered as futuristic fuel for next-generation vehicles based on Polymer Electrolyte Membrane Fuel Cell (PEMFC) [1]. PEMFC translates the chemical energy of hydrogen directly into electrical energy [2, 3]. Hydrogen has a high average heating value, i.e., 120 MJ/kg of H₂ [4]. It is necessary to have a hydrogen storage mode and mechanism to deliver this energy in a usable form. For sourcing electrical power to the applications, a fuel cell is used as a battery [5]. The average gravimetric energy density of hydrogen is 120 MJ/Kg, compared with the energy density of petrol, which is 44 MJ/Kg. The volumetric density of hydrogen is sparse with 0.01 MJ/L [6] compared with 32 MJ/L of petrol. The energy required to ignite a hydrogen–air mixture is very low only 0.02 MJ, which is about one-fourteenth of the energy needed to ignite natural gas [7]. For establishing realistic hydrogen storage technologies, a 9 wt% gravimetric storage objective has been proposed for hydrogen-powered vehicles by the US Department of Energy for attaining a 500 km driving range [8]. However, the materials tested so far did not even reach close to the DOE set targets. Figure 21.1 shows a block diagram of the working of PEMFC.

R. Kalamkar (✉)

Mechanical Engineering Department, Gharda Institute of Technology, Lavel, India
e-mail: rohanhirve@gmail.com

V. Yakkundi

Mechanical Engineering Department, Lokmanya Tilak College of Engineering, Navi Mumbai, India
e-mail: vivek.yakkundi@gmail.com

A. Gangal

Mechanical Engineering Department, SSPM's College of Engineering, Kankavali, India
e-mail: aneeshgangel@gmail.com

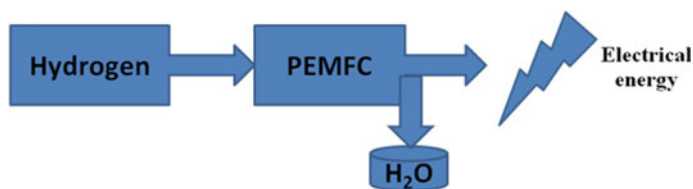


Fig. 21.1 Block diagram of working of PEMFC

The storage of hydrogen is possible as compressed gas, liquid at cryogenic temperature, or solid-state hydride phase. Pressure vessels commercially available are either of 5000 and 10,000 psi compressed hydrogen [9]. The energy density of hydrogen can be doubled as compared to the 10,000 psi compressed hydrogen to 70 g/L by liquefaction to the temperature of 20 K [10]. Thus the high pressure compressed hydrogen storage has issues concerning the strength of the material, the safety of the tank, and finally, the tank weight, while the issues with liquid hydrogen storage are the boil-off loss and the energy requirements for liquefaction. However, both these issues are addressed in solid-state hydrogen storage where hydrogen combines either physically or chemically with some of the materials to give hydrides and hydrogen can be obtained whenever required by either thermal stimulation or some other technique like hydrolysis [11].

This work consists of the fabrication of experimental setup to measure stored renewable hydrogen energy in solid metal hydrides. This experimental setup evaluates the absorption/desorption kinetics of sample materials based on a volumetric approach. The working range of this fabricated of the experimental setup is 0.05–50 bar pressure and 300–723 K temperature. It comprises of a reactor for the interactivity of hydrogen gas with the solid sample material and measuring cell to examine the weight% capacity of hydrogen storage [12]. The fabricated system has a volume of 150 cm³ having 100 bar internal pressure capacity. The setup is made up of stainless steel material with a high-resolution pressure transducer. The wt% capacity of stored hydrogen is determined using van der Waals equation for a real gas. The effect of ball-milled sample materials on the magnification of hydrogen wt% reported in this work. This research study also describes the outcome of additive Zeolite on enhancement in hydrogen capacity with a reduction in reaction temperature. Characterization is done using Fourier-transform infrared spectroscopy (FTIR) and Transmission electron microscopy (TEM) spectroscopy methods for validation.

Experimental

Sievert's type apparatus fabricated to measure hydrogen stored in solid-state powder materials. The instrument uses a volumetric method to determine wt% of stored hydrogen. The device works within a range of 0.05–50 bar pressure and 300–723 K temperature. The pressure sensor takes an input of 9–30 V DC and provides an

outcome of 4–20 mA. The K type thermocouples are used with two-wire legs welded together at for temperature measurement at a junction. This experimental setup comprises a vacuum system of 10^{-5} mbar range to remove gas molecules from a system. The pressure change in the system corresponds to the hydrogen concentration of the sample material [13]. The temperature of a gas, system volume and pressure change in the system used as data for the van der Waals equation for finding out wt% H_2 stored [14, 15]. For the estimation of concealed volumes in the system, the gas expansion method was used. Figure 21.2 represents (a) conceptual apparatus schematic diagram and (b) shows the photograph of the fabricated experimental setup.

The outcome of this measurement is pressure composition (PC) isotherms graphs, which designate the characteristics of the sample material. The graph consists of α —region corresponds to the starting of hydride formation, β —region specifies an increase in the concentration of hydrogen, and the third region is the saturation phase. The constant pressure, i.e., plateau region in the graph, represents the equilibrium pressure of hydrogen [16]. Figure 21.3 illustrates an ideal PC isotherm.

The tubing and the reactor volume estimated using the calibration of the experimental setup before performing the experiments. In an indirect method of gas expansion, the standard cell of size 350 cc was used. Equation 21.1 represents van der Waals equation for a real gas.

$$\left(P + \frac{n^2 a}{V^2} \right) (V - nb) = nRT \tag{21.1}$$

The a is the correction for intermolecular forces, which is $0.0248 \text{ J m}^3/\text{mol}^2$, b is the correction for finite molecular size, which is $2.66 \times 10^{-5} \text{ m}^3/\text{mol}^2$ [5]. For $P_1 = 7.9 \text{ bar}$, volume = 350 cc (0.00035 m^3) and temperature $T = 298 \text{ K}$ number of

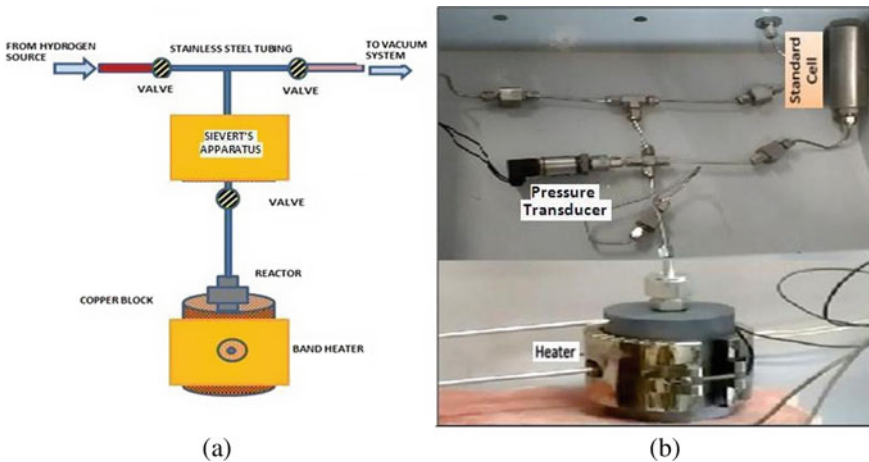


Fig. 21.2 a Apparatus schematic diagram. b Photograph of fabricated experimental setup

Fig. 21.3 Ideal pressure composition (PC) isotherm

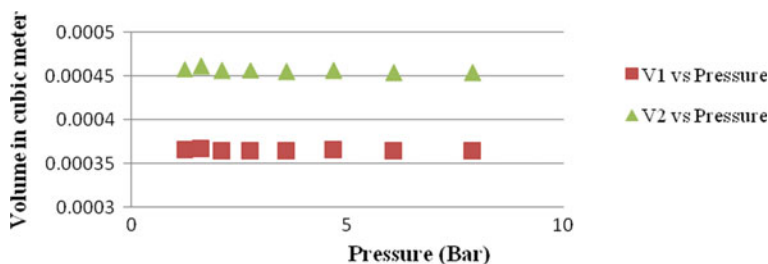
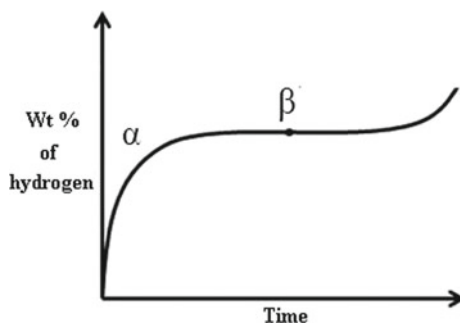


Fig. 21.4 Calibration curve

moles are calculated as $N = 0.11066$ from Eq. 21.1. For $P_2 = 7.6$ bar, $P_3 = 6.08$ bar and keeping all other parameters the same, tubing volume as 14 cc and the reactor volume as 90 cc calculated. Figure 21.4 specifies the calibration curve.

Result and Discussions

In a closed material hydrogen system, the sequences of changes are observed in hydrogen pressure at the isothermal condition. Wt% of hydrogen estimated using system pressure and sample temperature. The total number of moles evaluated using van der Waals equation for a real gas. Magnesium and Aluminum crystalline powder (Sigma-Aldrich) is ball milled for 12 h. The transmission electron microscopy (TEM) technique is used for the characterization. The electron diffraction patterns of Mg and Al nanoparticles are shown in Fig. 21.5. Particle size calculated from images was approximately 60–80 nm. The images stipulate ringed pattern and differently oriented lattice fringes.

Magnesium powder is a nontoxic grey crystalline solid used for the hydrogenation test. Magnesium hydride (MgH_2) has 9 MJ/kg of energy density [17]. With low-cost available magnesium, MgH_2 has about 7.7 wt% hydrogen storage capacity [18]. Mg crystalline powder and ball-milled Mg particles were allowed to react separately

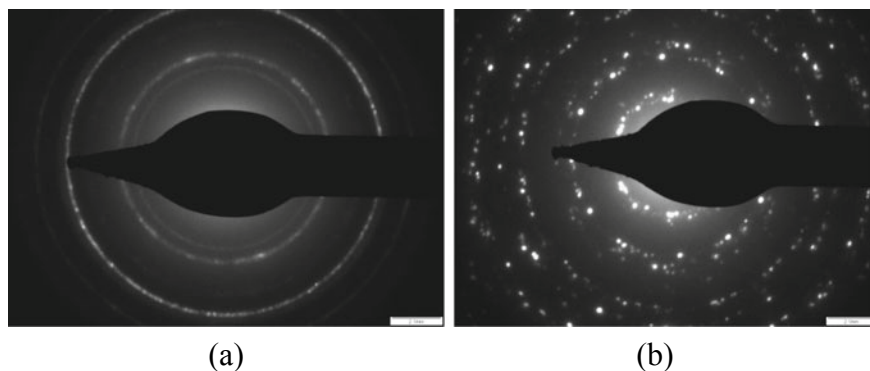


Fig. 21.5 **a** Electron diffraction pattern of Mg. **b** Electron diffraction pattern of Al

with the hydrogen gas, filled in the 350 cc cylinder at 14.5 bar pressure with constant temperature 573 K. The results plotted in the graph were average of three tests. Results show hydrogen storage of 4.38 wt% in the case of Mg crystalline powder and 5.10 wt% in the case of ball-milled Mg. Aluminum is a silvery white, soft, nonmagnetic, and ductile metal. Aluminum hydride (AlH_3) contains 10.1 wt% of hydrogen [19]. Al crystalline powder and ball-milled Al nanoparticle were allowed to react separately with the hydrogen, keeping pressure and temperature the same as in the case of Mg. Results specify hydrogen storage of 2.8 wt% in the case of Al crystalline powder and 3.7–4.0 wt% in the case of ball-milled Al nanoparticles. The outcome of the experiment stipulates that optimum time for the milling process boosts the sample's hydrogen storage capability. The peak hydrogen absorption temperature decreases slowly with decreasing the average particle size of the sample material. Figure 21.6 indicates the effect of particle size on hydrogen storage.

Zeolites are also the microporous solids widely used for adsorbents and catalysts. Zeolite is used as hydrogen storage materials, but the amount of hydrogen taken up by both these materials was not sufficient from the application point of view [20].

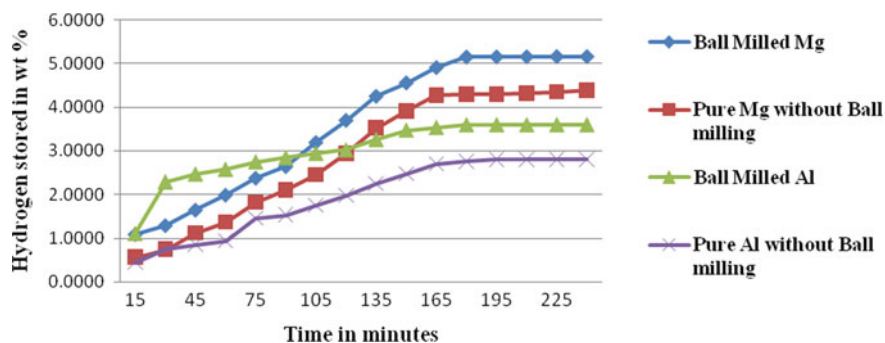


Fig. 21.6 Effect of particle size on hydrogen storage

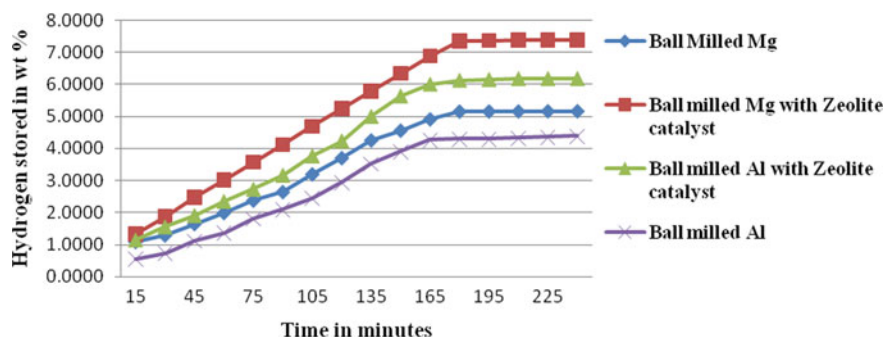


Fig. 21.7 Hydrogenation test results of Magnesium and Aluminum

This observation led to the thought that if both materials physisorbed hydrogen, it may assist hydrogenation by accelerating the reaction rate. Therefore the use of Zeolite as catalysts for hydrogenation experiments was proposed. The Zeolite ($\text{Ag}_{84}\text{Na}_2[(\text{AlO}_2)_{86}(\text{SiO}_2)_{106}] \times \text{H}_2\text{O}-\text{N.H.}$ Chemicals) nanoparticles are mixed with Mg and Al nanoparticle in 1:10 mass ratio. Both the materials were milled for 1 h to obtain a homogenous mixture. The consequences of the addition of the catalysts were observed. The coverage and surface temperature are influencing the reactivity of Zeolite [21]. The mean test results' footprint revealed optimum hydrogen storage of 7.38 wt% at the temperature of 453 K and 14.5 bar pressure using Zeolite as a catalyst in the test. Further, the hydrogenation tests of Al nanoparticles with the hydrogen gas in the presence of Zeolite catalyst were conducted. Mean outcome indicates hydrogen storage of 6.18 wt% in Aluminum using Zeolite as a catalyst keeping all other conditions the same as in case of Mg-Zeolite hydrogenation test. Each sample test repeated thrice, and average results are represented graphically in Fig. 21.7.

Validation by Spectroscopy

Infrared radiations traveled through the samples in Fourier transform infrared spectroscopy. The characterization represents the molecular absorption/transmission, and this spectrum was unique for the molecular structure of the respective sample [22]. In this work, the FTIR transmittance spectrum [23] recorded using a Jasco FT/IR-6100A system [SAIF, IITB]. In Transmission Electron Microscopy, an electron beam focused on the samples using the condenser lens system. Magnified image and the X-ray produced through interaction were analyzed for evaluating the elemental composition [24]. Philips CM200 TEM used with voltage range 20–200 kV and the resolution of 2.8 Å [SAIF, IITB] for this work. FTIR and TEM tests conducted at IIT Bombay, SAIF laboratory facility. Figures 21.8, 21.9, 21.10 and 21.11 represent the

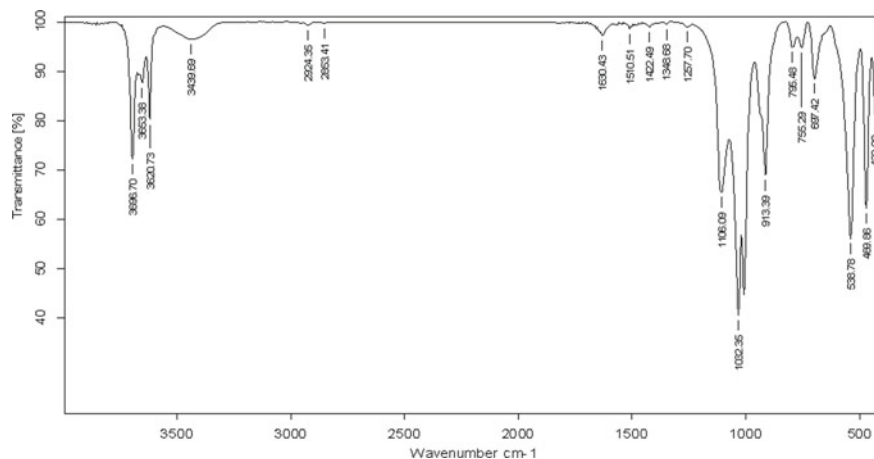


Fig. 21.8 FTIR of Mg crystalline powder

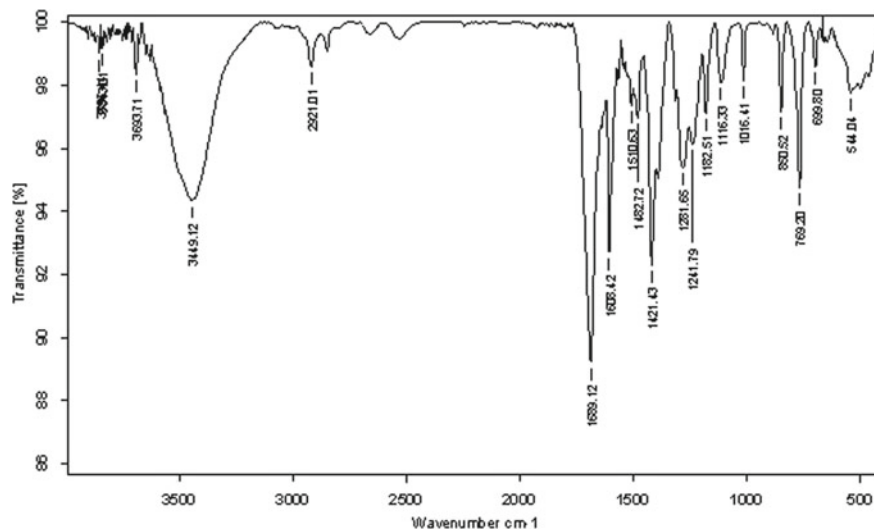


Fig. 21.9 FTIR of ball-milled Mg with Zeolite catalyst

FTIR transmittance spectra of Mg crystalline powder, ball-milled Mg with Zeolite catalyst, Al crystalline powder, ball-milled Al with Zeolite catalyst respectively.

Transmittance spectra of Mg of solid residue after hydrogenation tests with additive Zeolite depicted that the frequencies are greatly affected, i.e., stretching and wagging was observed, 1639 cm^{-1} , 1421 cm^{-1} in Mg-Zeolite and 1605 cm^{-1} , 659 cm^{-1} in Al-Zeolite solid residue. Storage of hydrogen reflects in terms of broadening of the transmittance peaks, 3449 cm^{-1} , 2921 cm^{-1} in Mg-Zeolite and

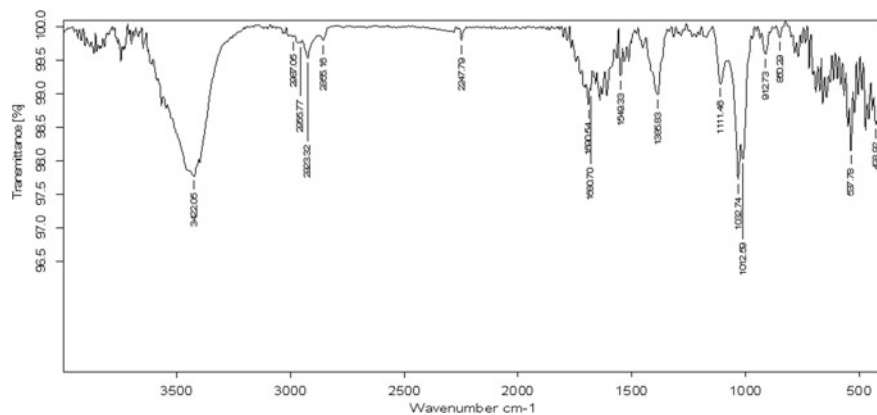


Fig. 21.10 FTIR of Al crystalline powder

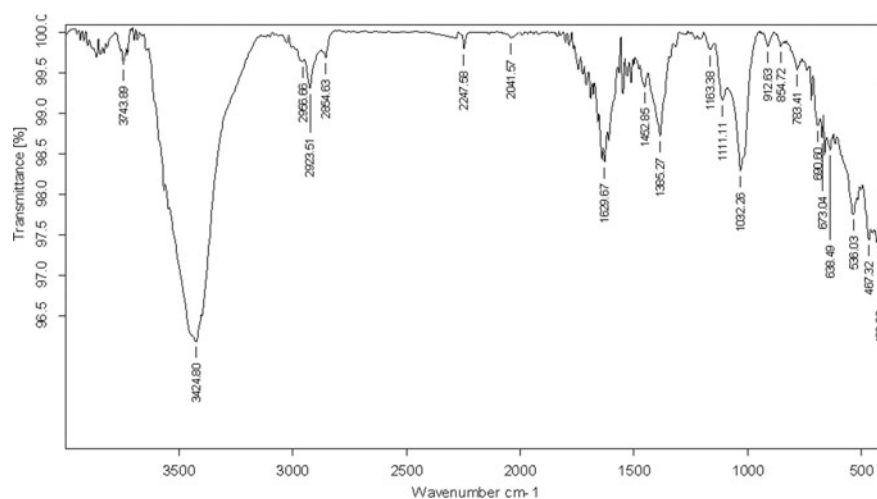


Fig. 21.11 FTIR of ball-milled Al with Zeolite catalyst

3443 cm^{-1} , 2923 cm^{-1} in Al-Zeolite solid residue when compared with the spectrum of crystalline powder. The increase in sharpness of the spectrum peak implies hydrogen absorption kinetics [25]. FTIR spectra of solid residue after tests do not show any bands corresponding to Zeolite-H which designate Zeolite additive do not take part in reactions. Figure 21.12 shows TEM images of Mg and Al sample materials. TEM images before and after hydrogenation indicate the reduction in the pores with enhancement in the intensity of dark spots/ patches. It signifies hydride formation in Mg compared with BCC-structured catalyst imbedded in the MgH_2 matrix images [26]. HRTEM images of Mg and Al with additives reflecting hydride formation [27, 28].

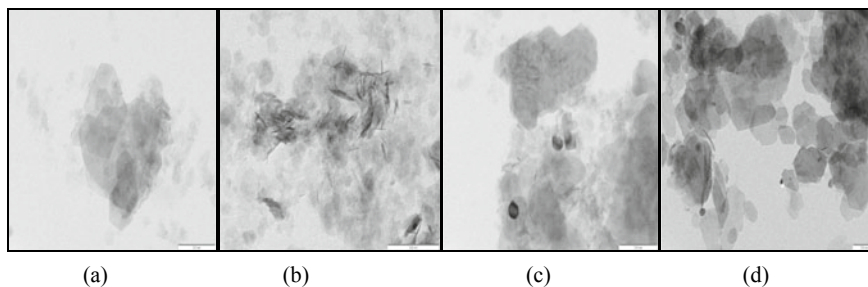


Fig. 21.12 **a** TEM image of Mg crystalline powder. **b** TEM image of milled Mg with Zeolite. **c** TEM image of Al crystalline powder. **d** TEM image of milled Al with Zeolite

Conclusion

The analysis of the fabricated apparatus noticed experimental errors within 10% in correlation with accuracy. The lightweight metals Mg and Al suggested encouraging materials for H₂ storage, but having an issue of the slow kinetics. The hydrogenation of Mg and Al with and without Zeolite additives was made to refine the behavior. The additives enhance the net H₂ storage around 2.23 wt% in Mg and 2.10 wt% in Al using Zeolite as a catalyst during isothermal reactions. The passiveness during hydrogenation in the surface of additives increases sorption, which reflects in edges in the transmittance spectra. Additives accelerate the rate of reaction as well as decreasing the reaction temperature by 120 K in Mg and 150 K in Al. No foaming was observed with additives. Hence, the catalyst improves the reaction kinetics behavior of Magnesium. Validations of the experimental outcomes using FTIR and TEM characterization found to be similar when correlated with the previously published research articles to authenticate the experimental system.

Acknowledgements Authors are grateful to the Gharda Institute of Technology, Lavel, for the support received concerning the work presented in the paper.

References

1. Gangal AC, Kale P, Edla R (2012) Study of kinetics and thermal decomposition of ammonia borane in presence of silicon nanoparticles. *Int J Hydrogen Energy* 37(8):123–134
2. Kalamkar R, Yakkundi V, Gangal A (2020) Hydrogen storage characteristics of mixture of lithium amide and lithium hydride using severt's type apparatus. In: Pawar P, Ronge B, Balasubramaniam R, Vibhute A, Apte S (eds) *Techno-societal 2018*. Springer, Cham, pp 1037–1044
3. Gangal AC, Sharma P (2013) Kinetic analysis and modeling of thermal decomposition of Amonia borane. *Int J Chem Kinet* 45(7):452–461
4. Dehghani AR, Tharumalingam E (2019) Study of energy storage system and environmental challenges of batteries. *Renew Sustain Energ Rev* 104:192–208

5. Gangal A (2013) Ammonia borane as hydrogen storage material. Thesis. Department of Energy Science & Engineering IIT Bombay
6. Zuttel A (2004) Hydrogen storage methods. *Naturwissenschaften* 91(4):157–172
7. Zuttel A (2003) Materials for hydrogen storage. *Mater Today* 6(9):24–33
8. Khan SA, Bahadar Khan S, Ullah Khan L (2018) Fourier transform infrared spectroscopy: fundamentals and application in functional groups and nanomaterials characterization. In: Sharma S (ed) *Handbook of materials characterization*. Springer Nature, pp 317–344
9. Vishwanathan B, Scibioh MA (2006) *Fuel cells*. Hyderabad University Press.
10. Zhou C, Fang ZZ (2019) Capturing low-pressure hydrogen using V-Ti-Cr catalyzed magnesium hydride. *J Power Sourc* 413:139–147
11. Williams D, Carter C (2009) *Transmission electron microscopy. A textbook for material science/I basics*. The University of Alabama in Huntsville. USA. Springer
12. Ramaprabhu S, Rajalakshmi N (1998) Design and development of hydrogen absorption/desorption high pressure apparatus based on the pressure reduction method. *Int J Hydrogen Energy* 23(9):797–801
13. Liang H, Chen D (2019) Efficient hydrogen storage with the combination of metal Mg and porous nanostructured material. *Int J Hydrogen Energy* 44(31):16824–16832
14. Abe JO, Popoola API (2019) Hydrogen energy, economy and storage: review and recommendation. *Int J Hydrogen Energy* 44(29):15072–15086
15. Zheng J, Liu X, Ping Xu (2012) Development of high pressure gaseous hydrogen storage technologies. *Int J Hydrogen Energy* 37(1):1048–1057
16. Kalamkar R, Gangal A, Yakkundi V (2017) Development of experimental setup for measurement of stored hydrogen in solids by volumetric method. In: Pawar P, Ronge B, Balasubramanian R, Seshabhatar S (eds) *Techno-societal 2016*. ICATSA 2016. Springer, Cham, pp 569–577
17. Kral L, Cermak J (2019) Improvement of hydrogen storage properties of Mg by catalytic effect of Al-containing phases in Mg-Al-Ti-Zr-C powders. *Int J Hydrogen Energy* 44(26):13561–13568
18. Staffell L, Scamman D (2019) The roll of hydrogen and fuel cells in the global energy system. *Energy Environ Sci* 12:463–491
19. Graetz J, Reilly JJ (2011) Aluminum hydride as a hydrogen and energy storage material: past, present and future. *J Alloy Compd* 509(2):5517–5528
20. Li M, Bai Y, Zhang C (2019) Review on the research of hydrogen storage system fast refueling in fuel cell vehicle. *Int J Hydrogen Energy* 44(21):10677–10693
21. Khalim Khafidz N, Yaakob Z, Timmiati SN (2019) Hydrogen sorption of magnesium oxide carbon nanofibre composite. *Malaysian J Analyt Sci* 23(1):60–70
22. Kale P, Gangal A, Edla R (2012) Investigation of hydrogen storage behavior of silicon nanoparticles. *Int J Hydrogen Energy* 37(4):3741–3747
23. Edla R, Gangal A, Manna J (2014) Kinetics and the thermal decomposition of sodium Alanate in the presence of $MmNi_4.5Al_{0.5}$ nanoparticles. *Mater Res Express* 1(1)
24. Source: https://www1.eere.energy.gov/hydrogenandfuelcells/pdfs/freedomcar_targets_explanations.pdf
25. Gao S, Wang X, He T, Yan M (2019) Effects of nano-composites (FeB, FeB/CNTs) on hydrogen storage properties of MgH_2 . *J Power Sourc* 438:227006
26. Manoharan Y, Hosseini SE, Butler B (2019) Review: hydrogen fuel cell vehicles. current status and future prospect. *Appl Sci* 9(11):2296
27. Jalil Z, Rahwanto A, Ismail I (2018) The use of nano-silicon carbide and nickel as catalyst in magnesium hydrides (MgH_2) for hydrogen storage material application. *Mater Res Express* 5(6)
28. Beattie SD, Humphries T, Weaver L, Sean McGrady G (2008) Temporal and spatial imaging of hydrogen storage materials: watching solvent and hydrogen desorption from aluminium hydride by transmission electron microscopy. *Chem Commun* 37:4448–4450

Chapter 22

Investigation of Wind Loads on Utility-Scale Seasonal Tilt Solar PV Power Plants



Syed Abdul Mateen and Kiran S. Bhole

Introduction

As all, we know now a day's climate change is a real issue, which is mainly because of environmental pollution. One of the measures to address this issue is the use of renewable energy [1]. The use of a thermoelectric module is one of the renewable sources [2, 3]. The solar system is most adaptable in all other forms of renewable energy systems. The solar industry is growing rapidly in the last 3 years in India. India's solar installed capacity reached 37.62 GW as of 31 May 2020; also India is at fifth position for generating solar energy in the world. Solar energy has various advantages, as it has zero raw fuel costs. It will give you unlimited supply and there are no environmental issues [4]. The substitute to use the fossil fuel is the power generated from the photovoltaic system. Photovoltaic panels are usually mounted on the rooftops of residential or commercial buildings but these systems are generally smaller than ground-mounted PV systems.

Mainly there are three different types of solar module mount structures (MMS). (1) Fixed tilt module mount structure. (2) Single or double axis solar tracker. (3) Seasonal tilt module mounts structure. One of the commonly used is a fixed tilt module mount structure. In fixed tilt MMS, the tilt angle is always fixed. But it produces less energy than other solar module mount structure [5]. Another type is a single or double axis solar tracker. This system is continuously tracking the position of the sun in order to get the maximum energy. These systems have maximum energy output compared with the other solar MMS, but it is very costly system because of the motor driven

S. Abdul Mateen · K. S. Bhole (✉)
Department of Mechanical Engineering, Sardar Patel College of Engineering, Andheri, Mumbai
400058, India
e-mail: kiran_bhole@spce.ac.in

S. Abdul Mateen
e-mail: abdulmateensyed7@gmail.com

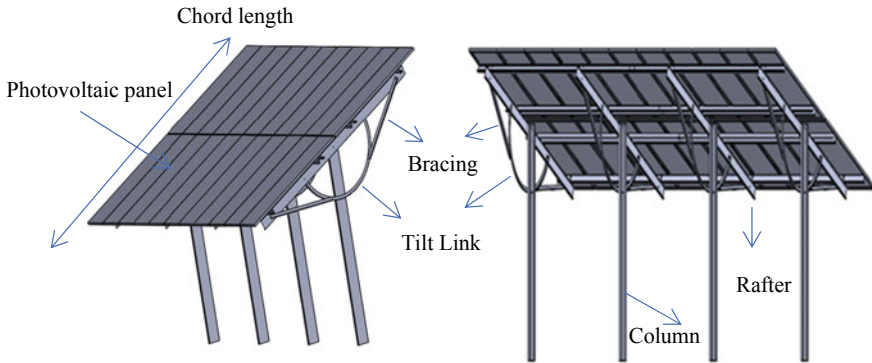


Fig. 22.1 Seasonal tilt module mount structure

tracker unit [6]. Now we will discuss seasonal tilt module mount structure. It provides flexibility in changing the tilt angle of MMS. Depend upon the different seasons and weather conditions, we can change the tilt angle in order to get the maximum energy. Overall PV output can be increased by 5–6% by adjusting the tilt angle twice or thrice a year [7]. The tilt angle ranging from 5 to 40 degrees, and we can simply change the angle using screw jack. Seasonal tilt MMS has many advantages as it is economical, simpler, and durable. It has lower maintenance requirements than a tracking system and stable under extreme weather conditions. That is why we have chosen the seasonal tilt MMS for our analysis.

Seasonal Tilt Module Mount Structure

Solar panels are also called a module, although module is electrical term. Seasonal tilt MMS have series of purlin, tilt link and columns. Modules are rested on the series of purlin and purlin is fixed on rafter as you can see in Fig. 22.1. Tilting links are provided to support rafter and column and used to change the angle of tilt, allowing the rotation of elevation of the PV grid at as 5°, 10°, 15°, 20°, 25°. The Purlins are supported over the rafter. Seasonal tilt MMS is supporting 22 modules. The size of each panel is $1 \times 2 \text{ m}^2$. Modules are placed in portrait position over the Purlin (C-type). Rafters are cold-formed light gauged steel sections and supporting Purlin. Rafters are hinged to the column and braced by bracing member.

CFD Analysis

As we are performing analysis on a utility scale above is our layout for flow simulation. We have leftover one structure in the middle row just to check the effects of

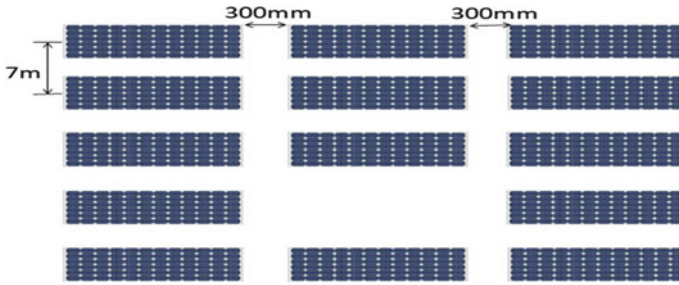


Fig. 22.2 Layout for flow simulation

loads on the surrounding structure. The overall size of the layout is $11 \times 32 \text{ m}^2$. The horizontal distance between the two structures is 300 mm and the vertical center to center distance is 7 m. For our analysis purpose, we have chosen five different tilt angles as 5° , 10° , 15° , 20° , 25° . For CFD analysis, we are using Solidworks flow simulation software (Fig. 22.2).

Flow Simulation from Front Side

We are using six different free stream velocities as 33, 39, 44, 47, 50, 55 m/s, these are the Indian standards IS: 875 wind speed, which is used in different regions [8]. In flow simulation for each tilt angle, we have used all six different wind speeds and for each tilt angle at a specific speed, we have calculated normal force acting on the panel. First of all, we have flowed air from the front side and obtain the value of normal forces.

As you can see in Fig. 22.3, a 3D wind tunnel is created in simulation software. The distance between the inlet wall and the first row of the panel is 60 m, and from side walls and back wall it has given a distance of 10 m, also the distance between the

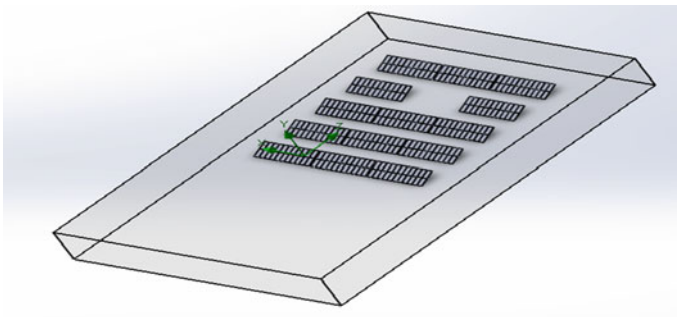


Fig. 22.3 Wind Tunnel under axial load from front side

top and bottom wall is 10 ms. We have fixed all the rows of panels in a fixed plane. We have used global mesh, and the mesh element size is 100 mm. Arrow indicates the air direction.

Results of Flow Simulation

When air flow from the front side, it is found that the maximum normal force is acting on the first row of solar panels as you can see in Fig. 22.4. In Fig. 22.4a, we can see the flow trajectory is of red color on the very first row which means only the first row of panels are experiencing a very large amount of wind loads compared with the remaining rows of panels. Figure 22.4b shows the pressure distribution across the whole panel's layout.

From the graph, we have found that as the tilt angle increase with the increasing wind speed normal force acting on a panel is also going to increase. When air flow from the front side, it is found that the maximum normal force is 1760 N at 25° tilt angle and wind speed of 55 m/s. and minimum normal force is 110 N at 5° tilt angle and wind speed of 33 m/s. It is concluded that wind uplift increases when there is an increase in tilt angle for solar panel.

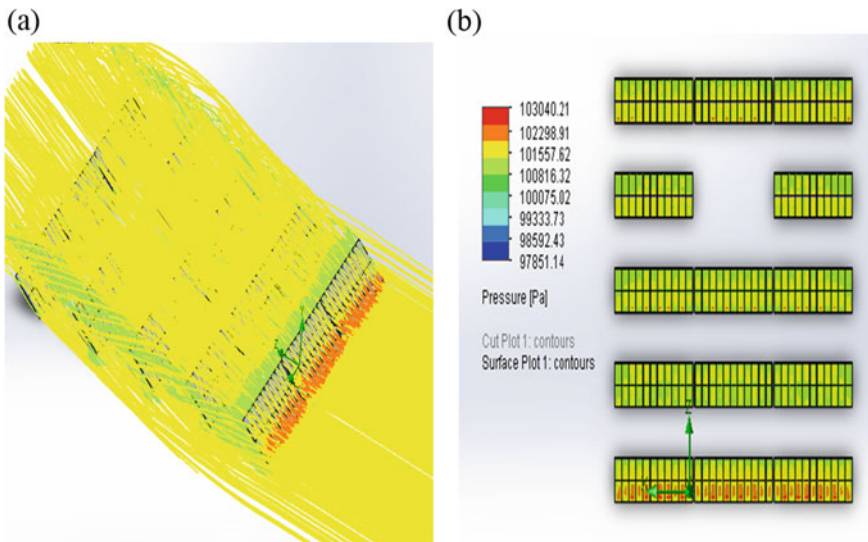


Fig. 22.4 a Flow trajectory over panels; b Pressure distribution on panel

Flow Simulation from Back Side

When air flow from the backside for each five different tilt angles at six different wind speeds. From this simulation, we have obtained the value of maximum normal force acting on the panels from the backside.

The 3D wind tunnel is created in simulation software as you can see in Fig. 22.5. Arrow indicates the air direction. In the above-created wind tunnel, we have considered clearance of 50 m from both front side and backside and 10 m clearance from the left and right side. The distance between the top and bottom wall is 10 m. We have used global mesh, and the mesh element size is 100 mm (Fig. 22.6).

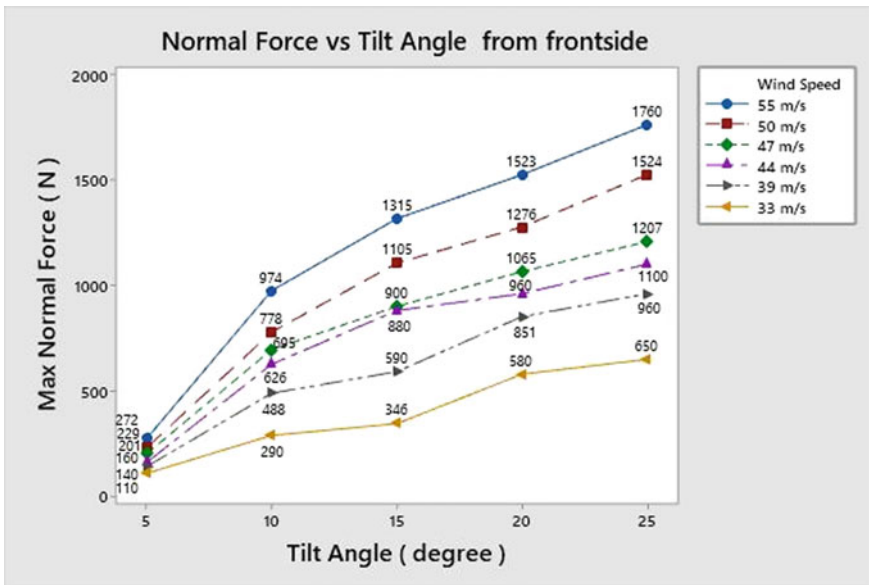


Fig. 22.5 Normal force against tilt angle

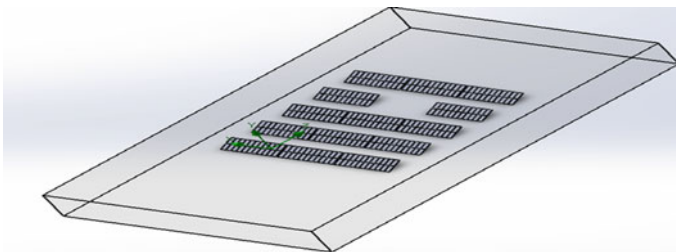


Fig. 22.6 Wind tunnel model under axial wind load

Results of Flow Simulation

When air flow from the back side, it is found that the maximum normal force is acting on the backside of the first row of solar panels as you can see in Fig. 22.7. Figure 22.7a represents the flow trajectory over the panels. Only the first row of panels from the backside is experiencing a very large amount of wind loads compared with the remaining rows of panels. In Fig. 22.7b, red color indicates the maximum pressure acting on the very first row of panels from the backside.

From the graph, we have found that as the tilt angle goes on increasing with the increasing wind speed normal force acting on a panel is also going to increase. When air flow from the backside, it is found that the maximum normal force is 2115 N at 25° tilt angle and wind speed of 55 m/s. and minimum normal force is 103 N at 5° tilt angle and wind speed of 33 m/s.

Flow Simulation at 45° Angle of Attack

When air flow at a 45-degree angle of attack for each five different tilt angles at six different wind speeds. We have chosen a 45-degree angle of attack because panels will face maximum wind load at 45° compared with any other angle of attack ranging from 10° to 80° [9]. From this simulation, we will obtain the value of maximum normal force acting on the panels (Fig. 22.8).

Similarly in this case also 3D wind tunnel is created in simulation software as you can see in Fig. 22.9 and the arrow indicates the air direction. The distance between the top and bottom wall is 10 m. We have used global mesh, and mesh element size is 100 mm.

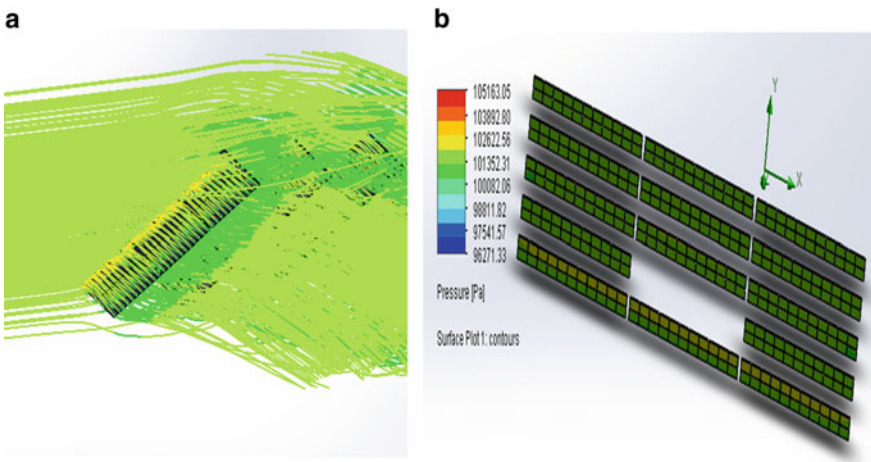


Fig. 22.7 a Flow trajectory over panel; b Pressure distribution on panel

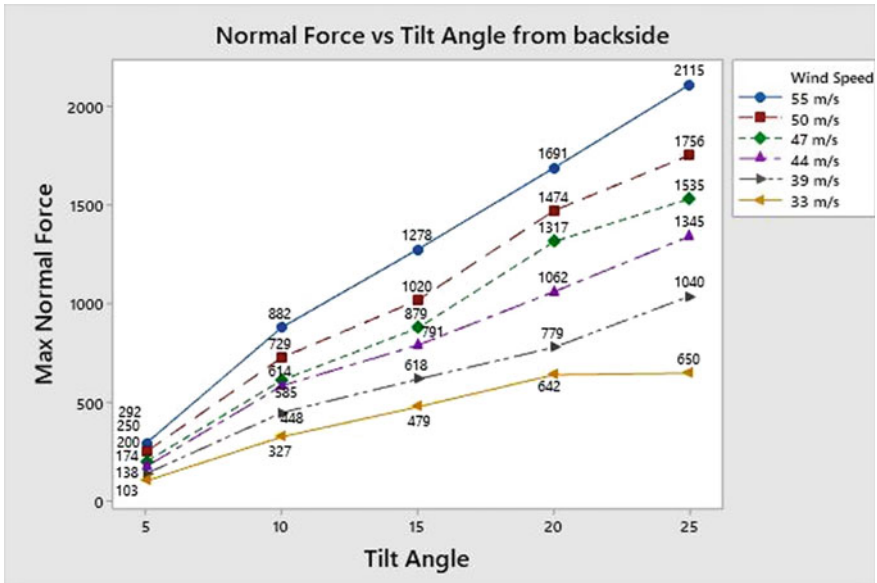


Fig. 22.8 Normal force against tilt angle

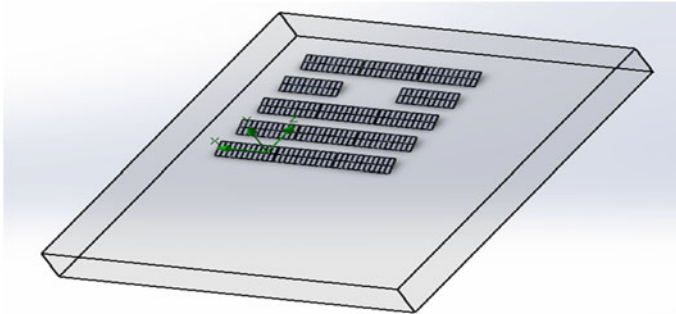


Fig. 22.9 Wind tunnel model for analysis

Result of Flow Simulation

When air flow at 45-degree angle of attack, it is found that maximum wind loads are acting on the first row of panels as well as some side panels of the other rows also which you can see clearly in Fig. 22.10. In Fig. 22.10a, flow trajectory showing the red color are the panels that are experiencing maximum wind loads. Figure 22.10b representing the pressure distribution over the panels. In this case, some panels of each row are experiencing the maximum amount of wind loads (Fig. 22.11).

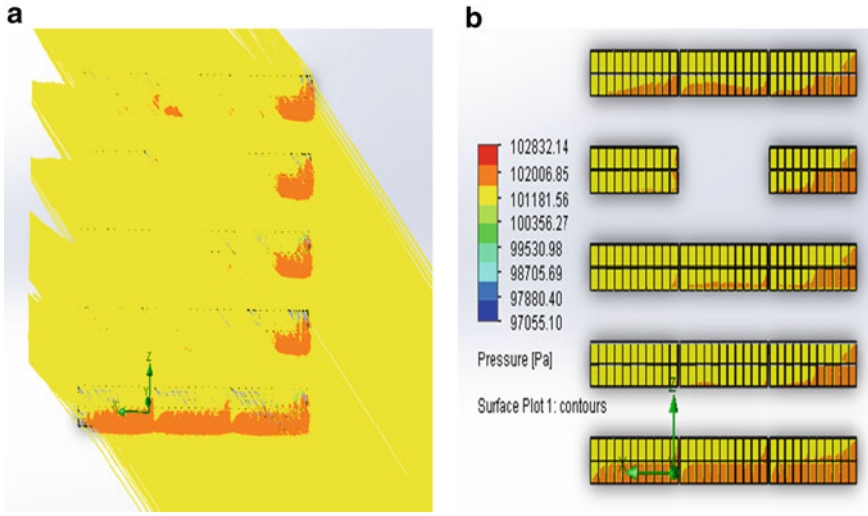


Fig. 22.10 a Flow trajectory; b Pressure distribution on panel

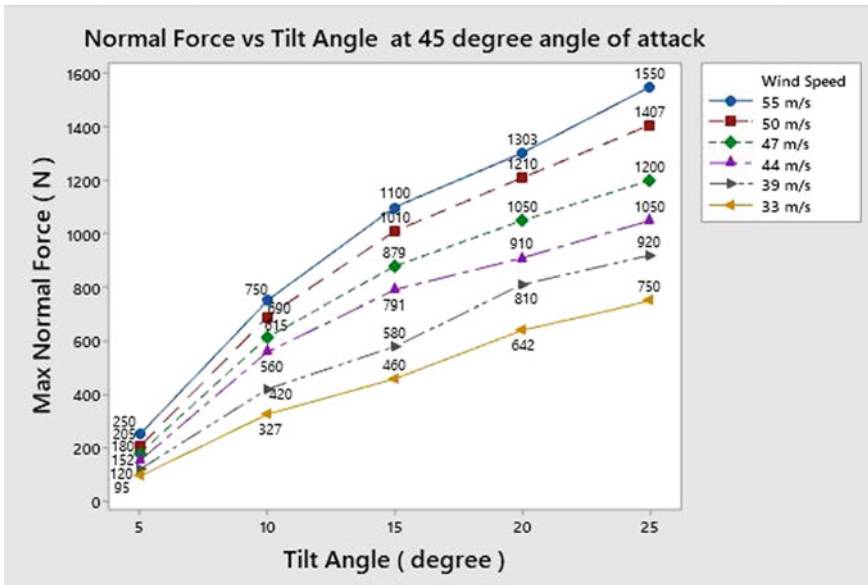


Fig. 22.11 Normal force against tilt angle

From the above graph, we have found that as the tilt angle goes on increasing with the increasing wind speed normal force acting on a panel is also going to increase. When air flow at 45-degree angle of attack, it is found that maximum normal force obtained is 1550 N at 25° tilt angle and wind speed of 55 m/s, and minimum normal force is 95 N at 5° tilt angle and wind speed of 33 m/s.

Static Analysis

This work specifically addresses the Seasonal tilt Module Mounting Structure (MMS) subjected to wind load. The analysis aims to provide the verification of structural stability considering wind for the solar MMS by means of the structural FE analysis. This FE analysis we have done in software called ANSYS. Structural members are considered as homogenous and assumed that they do not contain defects. Rafter to Purlin and Purlin to Module connections are assumed Bonded and Other connections are assumed no-separation. Panel density is 1850 kg m^{-3} and stiffness is $2.1e + 07 \text{ N/m}^2$ [10]. Density and stiffness such that the panel can be considered as a rigid body with mass behavior. Dynamic and static forces exerted on the panel will be directly transferred to purlin without deforming it [11]. Analysis approach using finite element methods has been necessary because of the need to carefully investigate the magnitude of stresses arising from maximum wind loads obtain from flow simulation.

Boundary Conditions and Loads

The analysis aims to provide the verification of structural stability considering wind loads for the solar MMS by means of the structural FE analysis. We have chosen material as a structural steel for analysis. From flow simulation, we obtain a maximum downward force of 1760 N, and the size of each panel is $1 \times 2 \text{ m}^2$. Column's bottom end is constrained in all three directions. Pressure on the panel due to wind loading is applied on the Panel face as normal pressure of 880 Pa. We have considered mesh element size of 25 mm (Fig. 22.12).

Results

We have calculated the von-Mises equivalent stress and total deformation. The static analysis of any module mount structure is done for only supporting structure [12, 13].

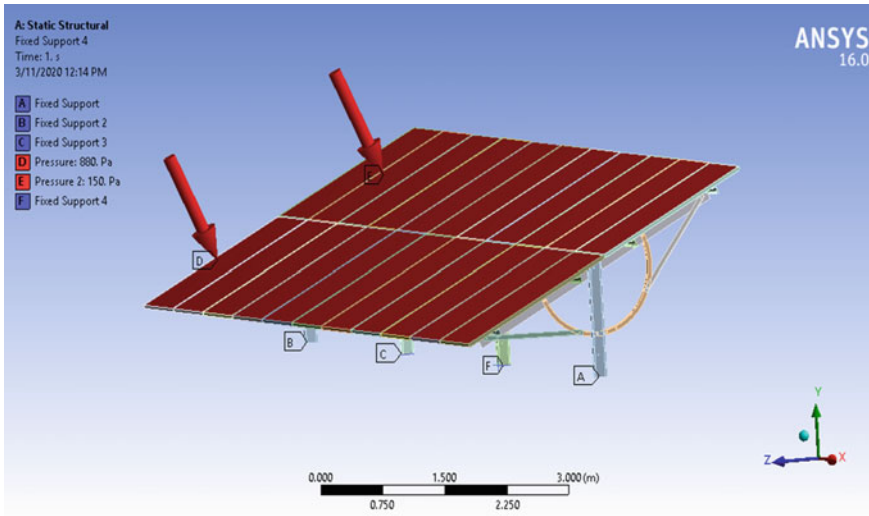


Fig. 22.12 Boundary conditions and loads

Equivalent Stresses Plot

Analysis approach using finite element methods has been necessary because of the need to carefully investigate the magnitude of stresses arising from various wind loads. After applying the maximum downward normal force, we have got the values of equivalent stress. It is seen that when we apply normal force, it will try to downward the structure. From Fig. 22.13, it is found that maximum stress is acting at the joint between purlin and rafter.

- Maximum stress = 202 Mpa
- Minimum stress = 10559 pa.

Deformation Plot

When we apply maximum normal force obtain from simulation, it is found that maximum deformation is coming at the edge of rafter and minimum deformation is at the bottom of purlin as you can see clearly in the Fig. 22.14.

- Maximum deformation = 3 mm.

Conclusion

We have obtained all the values of maximum normal forces at the entire five different tilt angles for six different Indian standard wind speeds. This work carried out to

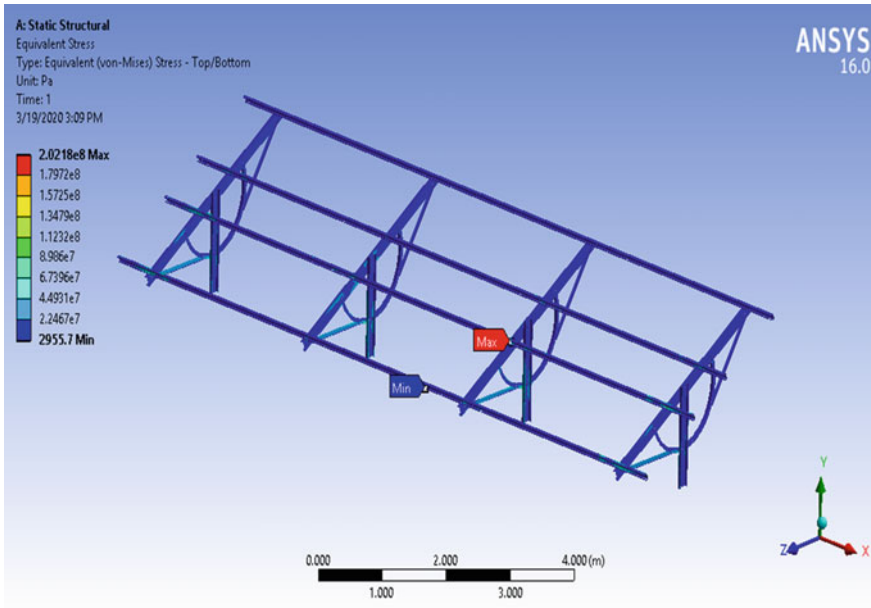


Fig. 22.13 Equivalent stresses plots

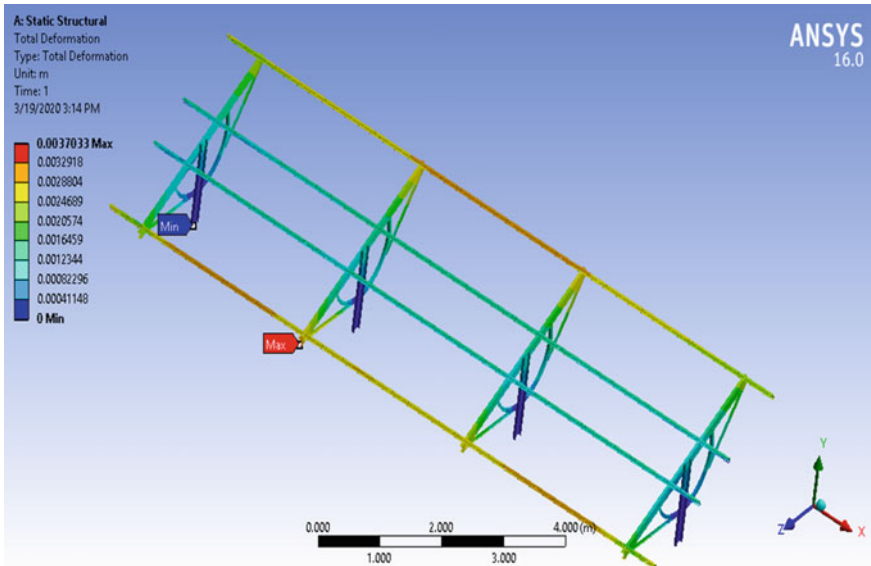


Fig. 22.14 Deformation plot

substantiate assembly of the seasonal tilt PV module mounting structure, which is influenced by wind load obtained from the flow simulation. The work demonstrates that stresses arising in the specified areas are within allowable limits and that the PV module mounting structure is therefore satisfactory for the intended service. Furthermore, we can do an investigation of the dynamic effect on the same seasonal tilt solar PV power plants.

References

1. Cain JH, Banks D (2015) Wind loads on utility scale solar PV power plants. Paper presented at international conference on wind engineering SEAOC convention proceedings
2. Kolambekar RB, Bhole K (2015) Development of prototype for waste heat recovery from thermoelectric system at Godrej vikhroli plant. Paper presented at international conference on nascent technologies in the engineering field (ICNTE)
3. Khadke R, Bhole K (2017) Characterization of radial curved fin heat sink under natural and forced convection. Paper presented at international conference on advances in materials and manufacturing applications (IConAMMA-2017) 17–19, Bengaluru, India
4. Uematsu Y (2007) Wind force coefficients for designing free-standing canopy roofs. *J Wind Eng Ind Aerodyn* 95:1486–1510
5. Chou C-C (2019) Wind loads on a solar panel at high tilt angles. *Appl Sci* 9(8):1594
6. Kao-Chun S (2018) Numerical simulation of wind loads on solar panels. *Mod Phys Lett B* 32(12):1840009
7. Strobel K, Banks D (2014) Effects of vortex shedding in arrays of long inclined flat plate and ramifications for ground-mounted photovoltaic arrays. *J Wind Eng Ind Aerodyn* 133:146–149
8. IS:875 (Part 3–1987), (1989) India standard code of practice for design of loads (other than earthquakes) for buildings and structures, part 3 (wind loads). Bureau of Indian Standards, New Delhi
9. Genc Celik1 G, Celik O (2019) A case study of structural failure of mounting systems for solar panels from south-eastern Turkey: an investigation of design parameters under extreme weather events. *Int J Eng Sci Invent* 8(1):16–23
10. Chung C (2019) Wind loads on a PV. Array *Appl Sci* 9(12):2466
11. Camellia A, Milchis T (2019) Wind loading on solar panels. *Műszaki Tudományos Közlemények* 10:73–78
12. Reina GP, De Stefano G (2017) Computational evaluation of wind loads on sun-tracking ground-mounted photovoltaic panel arrays. *J Wind Eng Ind Aerodyn* 170:283–293
13. Abiola-Ogedengbe A, Hangan H, Siddiqui K (2015) Experimental investigation of wind effects on a standalone photovoltaic (PV) module. *Renew Energ* 657–665

Chapter 23

Application of Neural Network to Predict Printability of Polycaprolactone Using FDM



Rahul Narkhede , Ravi Teja Karumuri , Ashish R. Prajapati ,
and Harshit K. Dave 

Introduction

Additive manufacturing (AM) has been emerging in recent years, enabling the fabrication of complex 3D structures from a variety of materials. AM allows fabrication of 3D structures in a layer-wise fashion, allowing control on the internal and external geometry, using three-dimensional computer-aided design (CAD) models. Fused Deposition Modelling (FDM), also referred by Fused Filament Fabrication (FFF), is a widely used AM process because of its low cost and ease in operation. In FDM, a polymer filament is passed through a heated nozzle, which causes the filament to be extruded in a semiliquid state and deposited on a heated bed to manufacture a 3D object in a layer-wise fashion according to CAD data [1]. A wide range of materials such as Polylactic acid (PLA), Polyester, Polyamide, Polyethylene, Polypropylene, Acrylonitrile-Butadiene Styrene (ABS) and Polycaprolactone (PCL) are feasible for use in FDM process. However, FDM is a complex process, which is affected by many parameters. Various process parameters such as extrusion temperature, heated bed temperature, raster orientation, layer thickness, infill pattern, raster width, infill density, and printing speed play a role in making it possible to print a part successfully [2]. Changes in these parameters can influence the part quality and even lead to the failure of the process in manufacturing the part. Many studies have been carried out to investigate the influence of different process parameters on the part quality and its mechanical properties using professional FDM 3D printers [3, 4] as well as low-cost opensource FDM 3D printers [5, 6]. Moreover, many experimental methods have been implemented to optimise the process parameters of FDM, such as Taguchi method [7, 8], factorial designs [9], ANOVA [10, 11], and fuzzy logic [12]. While

R. Narkhede (✉) · R. T. Karumuri · A. R. Prajapati · H. K. Dave
Department of Mechanical Engineering, S. V. National Institute of Technology, Surat 395007,
India
e-mail: narkhede.rahul2013@gmail.com

performing studies involving optimisation of FDM process parameters, especially with materials other than the commonly used ABS and PLA, different process failures like nozzle clogging, filament breakage, warping of part and detachment of part from print bed occur, which fail to manufacture the part. Many times, the FDM parts can have typical defects such as overfilling, cracking and voids. An empirical or theoretical relationship between the FDM process parameters and their effect on the 3D printed part can be useful to mitigate such failures. This relationship between the process parameters and their effect on the fabricated part is often highly non-linear because of the high amount of input variables playing their roles. Unfortunately, such a relationship becomes complicated as the number of parameters taken into account is increased. Neural Network (NN) models can deal with a high amount of input variables and can be applied in studying the effect of process parameters on manufactured part for different AM processes [13–15]. NNs are data-driven models that automatically develop the relationship linking the input parameters and output categories based on the data provided. Most studies applying NN models to determine the relationship of FDM process parameters on the fabricated object have used ABS [11, 16–18]. ABS and PLA have been commonly used in such studies to determine the effect of FDM process parameters on the part quality. PCL is a material that meets the criteria for medical applications and especially as an implantable material. Although, many studies have focussed on fabrication of scaffolds using PCL, very few have focussed on the effect of FDM process parameters over the print quality and mechanical properties [19–21]. Moreover, many process parameters are involved in the successful part fabrication. NNs can handle more variables and provide an output that can assist in predicting the effect of the FDM process parameters in obtaining a successfully fabricated part.

Thus, a neural network has been applied in this study to predict the effect of FDM process parameters on the fabrication of PCL part. In this work, a neural network is developed to predict the probability of a given set of process parameters to result in the successful fabrication of PCL part using the FDM process. A feed-forward neural network is developed by training it with the data recorded in tuning the process parameters to fabricate a PCL part by an FDM 3D printer. This work can assist designers in the biomedical field in predicting the printability of a PCL part by FDM process.

Experimental Section

Materials and Methods

PCL filament having a diameter of 1.75 mm has been used to fabricate the parts using a 3D Jet FDM 3D Printer as shown in Fig. 23.1. In the attempts to determine the parameters to fabricate the PCL part successfully, eight parameters, viz. nozzle diameter, nozzle temperature, heated bed temperature, printing speed, raster

Fig. 23.1 3D Jet FDM 3D printer



width, layer height, infill density and ambient temperature range, were considered. Table 23.1 mentions the values of process parameters used in the study. All the 45 data samples of the parameter values categorised into ‘success’ or ‘failure’ are mentioned in Table 23.2. The combinations were categorised in the ‘success’ category if they resulted in a PCL part with desirable quality as checked by visual inspection. The combinations which led to a PCL part that lacked the desirable quality were categorised in the ‘failure’ category. The combinations numbered as 6, 27, 29, 33, 39, 41, 43, 44 and 45 are repetitions of one of the other 36 unique combinations.

Table 23.1 FDM process parameters used in the study

S. No.	Process parameter	Range
1	Nozzle diameter (mm)	0.4 and 0.8
2	Nozzle temperature (°C)	75–200
3	Bed temperature (°C)	0–60
4	Printing speed (mm/s)	10–55
5	Raster width (mm)	0.9–1.5
6	Layer height (mm)	0.1–0.4
7	Infill density (%)	60, 80 and 100
8	Ambient temperature*	0 and 1

*Binary notation was used in data for ambient temperatures. 0 and 1 represent the ambient temperature range of 35–40 °C and 25–28 °C, respectively

Table 23.2 Combinations of process parameter categorised as 'success' or 'failure'

S. No.	Nozzle diameter (mm)	Nozzle temperature (°C)	Bed temperature (°C)	Printing speed (mm/s)	Raster width (mm)	Layer height (mm)	Infill density (%)	Ambient Temp. ^a	Success or failure ^b
1	0.4	200	50	55	1.5	0.1	100	0	0
2	0.4	200	40	55	1.5	0.1	100	0	0
3	0.8	180	60	55	1.5	0.1	100	0	0
4	0.8	175	50	55	1.5	0.1	100	0	0
5	0.8	125	35	55	1.5	0.1	100	0	0
6	0.8	125	35	55	1.5	0.1	100	0	0
7	0.8	125	45	55	1.5	0.1	100	0	0
8	0.4	175	50	55	1.5	0.1	100	0	0
9	0.4	125	50	30	1.5	0.2	100	0	0
10	0.4	100	60	15	1	0.2	100	1	0
11	0.8	100	50	10	1.5	0.1	100	0	0
12	0.8	75	45	10	1.5	0.1	100	0	0
13	0.8	100	45	20	0.9	0.3	100	1	0
14	0.8	100	50	30	1.5	0.2	80	1	0
15	0.4	90	45	30	0.9	0.3	80	1	0
16	0.4	85	40	20	0.9	0.1	100	1	0
17	0.4	90	50	15	1	0.2	60	1	0
18	0.8	80	45	10	1.5	0.1	100	0	0
19	0.8	85	45	10	1.5	0.1	100	0	0
20	0.8	90	50	10	1.5	0.1	100	1	1

(continued)

Table 23.2 (continued)

S. No.	Nozzle diameter (mm)	Nozzle temperature (°C)	Bed temperature (°C)	Printing speed (mm/s)	Raster width (mm)	Layer height (mm)	Infill density (%)	Ambient Temp. ^a	Success or failure ^b
21	0.8	90	50	10	1	0.1	100	1	0
22	0.8	90	40	10	1	0.1	100	1	0
23	0.8	90	40	10	0.9	0.1	100	1	1
24	0.8	90	50	10	0.9	0.1	100	1	1
25	0.8	90	0	10	0.9	0.1	30	0	0
26	0.8	90	50	10	0.9	0.3	30	0	0
27	0.8	90	50	10	0.9	0.3	30	0	0
28	0.8	90	50	10	0.9	0.3	100	1	1
29	0.8	90	50	10	0.9	0.3	100	1	1
30	0.8	90	50	10	0.9	0.3	60	1	0
31	0.8	90	45	10	0.9	0.3	100	1	1
32	0.8	90	45	10	0.9	0.2	100	1	1
33	0.8	90	45	10	0.9	0.2	100	1	1
34	0.8	90	45	10	0.9	0.2	60	1	1
35	0.8	90	45	10	0.9	0.4	80	1	1
36	0.8	90	45	10	0.9	0.2	60	1	0
37	0.8	90	50	10	0.9	0.2	60	1	1
38	0.8	90	45	10	0.9	0.2	80	1	1
39	0.8	90	45	10	0.9	0.2	100	1	1
40	0.8	90	45	10	0.9	0.3	60	1	1

(continued)

Table 23.2 (continued)

S. No.	Nozzle diameter (mm)	Nozzle temperature (°C)	Bed temperature (°C)	Printing speed (mm/s)	Raster width (mm)	Layer height (mm)	Infill density (%)	Ambient Temp. ^a	Success or failure ^b
41	0.8	90	45	10	0.9	0.3	100	1	1
42	0.8	90	45	10	0.9	0.4	60	1	1
43	0.8	90	45	10	0.9	0.4	80	1	1
44	0.8	90	45	10	0.9	0.4	80	1	1
45	0.8	90	45	10	0.9	0.3	100	1	1

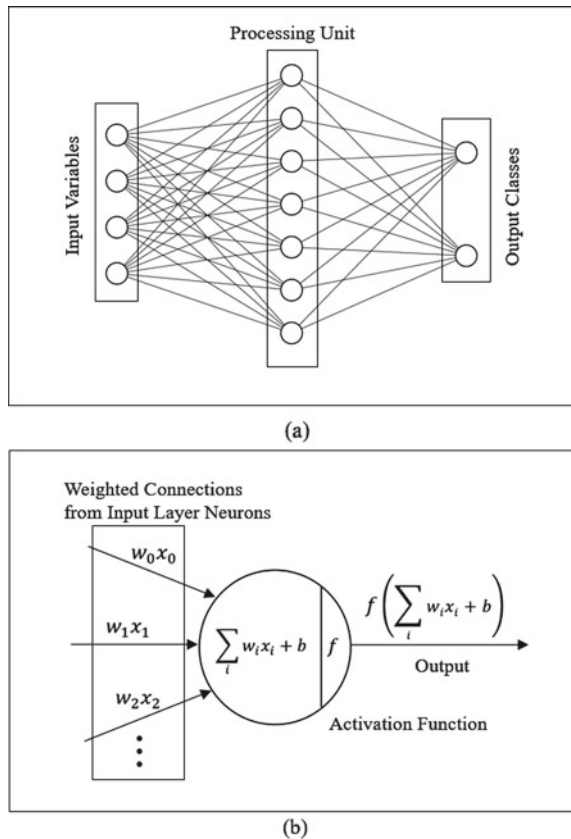
^aBinary notation was used in data for ambient temperatures. 0 and 1 represent the ambient temperature range of 35–40 °C and 25–28 °C, respectively

^bBinary notation 1 and 0 was used to mention 'success' and 'failure', respectively

Development of Neural Network Model

A neural network (NN) is a densely interconnected network of simple processing elements called neurons. Any NN consists of three types of layers, the input layer, hidden layer and the output layer [22]. An architecture of NN is shown in Fig. 23.2a. The neurons in the input layer carry the input variables. Similarly, the neurons in the output layer represent the output categories for classification. The hidden layer acts as the processing unit of the NN. Figure 23.2b shows the representation of a hidden layer neuron. Every connection between the neurons has a weight (w), making it a weighted connection, the magnitude of which is equal to the product of the weight and the input value ($w_i x_i$). The weights of these connections are allotted by training the NN in several iterations. These iterations are conducted to reduce the deviation between the true output and the output predicted by using the NN. This deviation is measured in terms of a loss function. The threshold value that offsets the hidden and the output layer is represented by (b). The activation function (f) introduces the non-linear nature of the relationship generated by the NN. All this is brought together

Fig. 23.2 **a** Architecture of a neural network with four input layer neurons, seven hidden neurons and two output layer neurons; **b** Representation of a hidden layer neuron



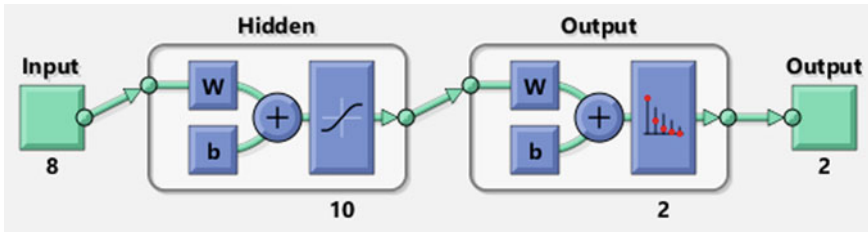


Fig. 23.3 The architecture of the neural network generated in work

by the output from each hidden layer neuron (y) and is given by,

$$y = f\left(\sum_i w_i x_i + b\right) \tag{23.1}$$

where w_i is the weight of the link, x_i is the i th input variable, b is the threshold value of the neuron, and f is the activation function [23].

In this iterative process, the back-propagation algorithm is the most widely used method to repeatedly alter the weights of the connections in the network to minimise the loss function. The back-propagation algorithm uses a chain rule to train the network [24]. Once the NN has been trained, it can be used to obtain the outputs for new unseen inputs.

A MATLAB code was generated for creating the NN model. The NN has a two-layer feed-forward type network with a hidden layer having a sigmoid activation function and an output layer having a softmax activation function as illustrated in Fig. 23.3.

The sigmoid activation function that introduces non-linearity to the relationship generated using NN is given as,

$$f(x) = \frac{1}{1 + e^{-x}} \tag{23.2}$$

The softmax activation function, which provides a probability distribution of its inputs proportional to their exponentials, is given by,

$$f(x_i) = \frac{e^{x_i}}{\sum_j^k e^{x_j}} \tag{23.3}$$

where k is the number of classes into which the sample set has to be classified. As the output of the softmax function is a probability distribution of the input variable proportional to its exponential, $0 \leq f(x_i) \leq 1$ and $\sum_{j=1}^k f(x_j) = 1$.

The deviation between the value predicted by the network and the true value fed to the network is determined in terms of the cross-entropy loss function. The loss function is given as,

$$\text{loss} = - \sum_{i=1}^n \sum_{j=1}^k p_{ij} \ln q_{ij} \quad (23.4)$$

where n represents the number of samples, k represents the number of classes, p_{ij} indicates the true probability of sample i to belong to the class j , and q_{ij} is the output probability by the network for sample i to belong to class j , which in this NN, is the value provided by the softmax function.

A scaled conjugate gradient back-propagation algorithm is applied for training the neural network used in this work. The data are fed in the form of input data to the network and target data for defining the desired network output. The input data are divided into three different types, viz. training set, validation set and testing set. The samples in the training set are used to train the network so that the network weights are altered repeatedly by the back-propagation algorithm. The validation samples do not take part in the adjustment of the weights. They are used for evaluating the network accuracy to avoid overfitting while training the network. Testing samples do not affect the network but provide a final measure of the network accuracy after training. If the network does not perform satisfactorily, it can be retrained to get more accurate results [25]. In this work, 70% of the data were used for training, 15% for testing and the rest 15% for validation purpose. The NN model was trained nine times with three iterations each for 10, 20 and 30 number of hidden neurons. In order to check for the successful working of the NN, the confusion matrix of each iteration was evaluated, as shown in Fig. 23.3. The diagonal cells of the confusion matrix indicate the number of correctly classified cases and the off-diagonal cells indicate the incorrectly classified cases. The bottom right cell shown in dark grey indicates the total per cent of correctly and incorrectly classified cases in green and red colour, respectively [25]. The confusion matrices of all the iterations are shown in Fig. 23.4.

Results and Discussion

The 0.8 mm nozzle diameter was the most suitable for proper extrusion. While using a 0.4 mm nozzle diameter, filament buckling caused the print failure. Buckling of the filament was seen frequently, causing the filament to stack between the feed rollers and the entry of the heating element. The buckling of the filament might be due to the higher backpressure on the filament from the heating element side of the feed roller [26]. The nozzle temperature is one of the primary effective processing parameters in FDM. It was noticed that a nozzle temperature of 90 °C resulted in successful fabrication of the PCL part. Temperatures above 90 °C allowed proper extrusion of the material but were too high to allow sufficient solidification of the deposited layer within the printing time. The insufficient solidification of the deposited layer led to deformation of the part as the deposited layers could not retain their shape during the printing of subsequent layers. Nozzle temperatures below 90 °C caused the buckling of the filament due to the insufficient liquefaction. Heated bed temperatures above

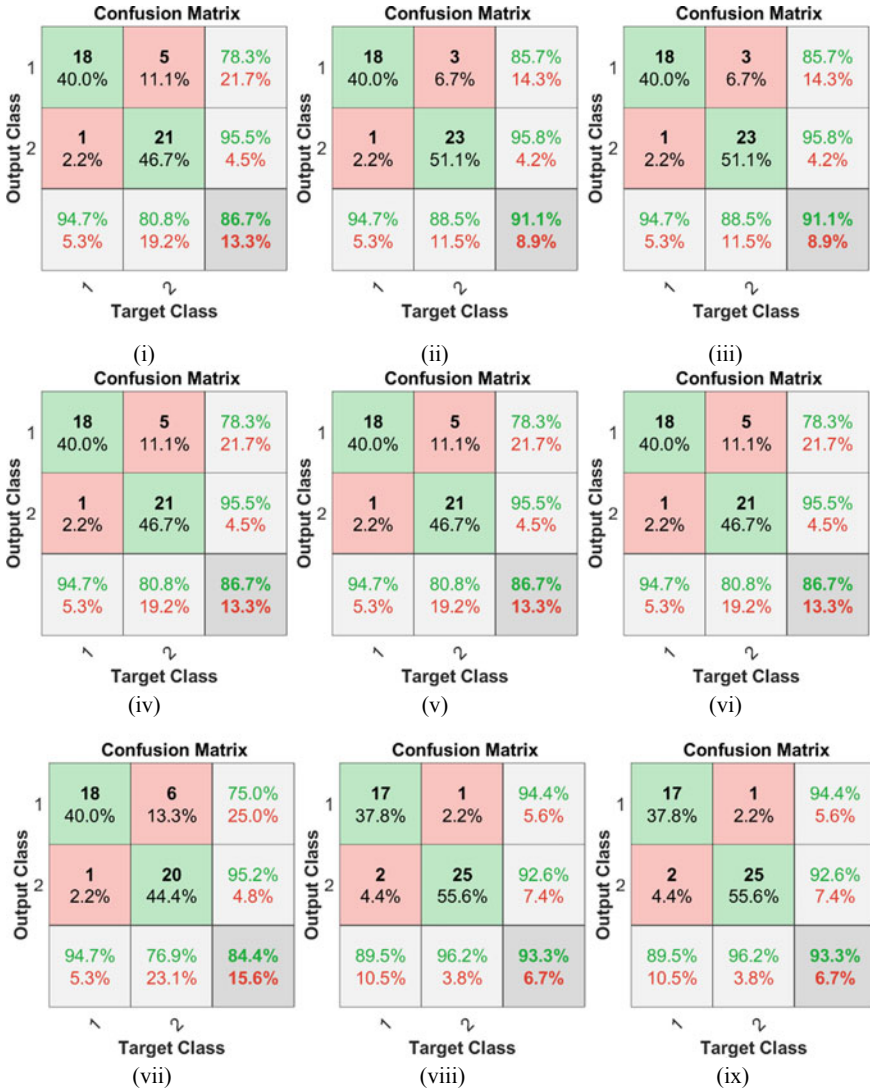


Fig. 23.4 Confusion matrices of iterations by training the NN (i) hidden neurons: 10, iteration: 1 (ii) hidden neurons: 10, iteration: 2 (iii) hidden neurons: 10, iteration: 3 (iv) hidden neurons: 20, iteration: 1 (v) hidden neurons: 20, iteration: 2 (vi) hidden neurons: 20, iteration: 3 (vii) hidden neurons: 30, iteration: 1 (viii) hidden neurons: 30, iteration: 2 (ix) hidden neurons: 30, iteration: 3

50 °C hindered the proper solidification of the deposited layers, thus causing the printed part to deform after subsequent layers were printed. Heated bed temperature below 45 °C caused eventual warping of the printed part, and the part lost its adhesion to the bed, thus getting dragged along with the nozzle.

A low printing speed of 10 mm/s was most suitable for fabricating a PCL part. While using higher printing speeds, the buckling of the filament was observed frequently. This buckling might be due to the increase in the extrusion rate at higher printing speeds, leading to an increment in the backpressure on the filament. A raster width of 0.9 mm was found to be most suitable for successful printing of the PCL part. A higher value of the raster width set in the slicing process resulted in unfused rasters. In contrast, a raster width lower than 0.9 mm caused the unsolidified deposited material to ooze outside the perimeters. It was found that with the proper selection of other parameters, the PCL part could be fabricated successfully with all the three-layer heights considered. A lower layer height of 0.2 mm increased the printing time, which led to higher chances of warping of the part. It was noticed that while using a lower layer height, the insufficiently solidified material of the previous layer got dragged along with the nozzle leading to deformations in part. Higher layer heights of 0.3 and 0.4 mm did not cause any issues while fabrication of the PCL printed part. Although, a higher layer height reduced the printing time. The infill densities of 60, 80 and 100% resulted in successful fabrication of part when the other parameters considered were set in the range feasible for printing. However, higher infill density led to deformations in a few cases. It was observed that the PCL part could not be fabricated with the ambient temperature in the range of 35–40 °C because it led to insufficient solidification of the layers deposited during the FDM process. Ambient temperature in the range of 25–28 °C was suitable for the proper fabrication of the PCL part as it allowed sufficient solidification of the deposited layers.

Every parameter has influenced the FDM process in the printability of the PCL part. Thus, the NN can help in determining the printability of PCL based on a particular set of process parameters. Out of all the iterations with three different values of hidden neurons, the NN with 30 hidden neurons showed better accuracy than other cases as seen in Fig. 23.5. The best accuracy obtained by using 30 hidden neurons was 93.3%.

Thus, the NN with 30 hidden neurons was considered for the proposed application. Finally, a particular set of parameters was fed to the NN model, as shown in Table 23.3. The output provided by the NN was a pair of two values, depicting the probability of the given set of parameters to belong to ‘success’ category and the ‘failure’ category. The probability of the ‘success’ category was 0.9998 and that of the ‘failure’ category was 1.6877×10^{-4} . The output predicted by this NN can be interpreted as—the parameters mentioned in Table 23.3 result in a successful print of PCL part. Figure 23.6 shows that the PCL part was fabricated successfully using the parameters shown in Table 23.3.

Conclusion

In this work, various set of process parameter values were used to fabricate a PCL part by the FDM process. The final values of the process parameters that resulted in the successful fabrication of the part were determined. A data of 45 such combinations

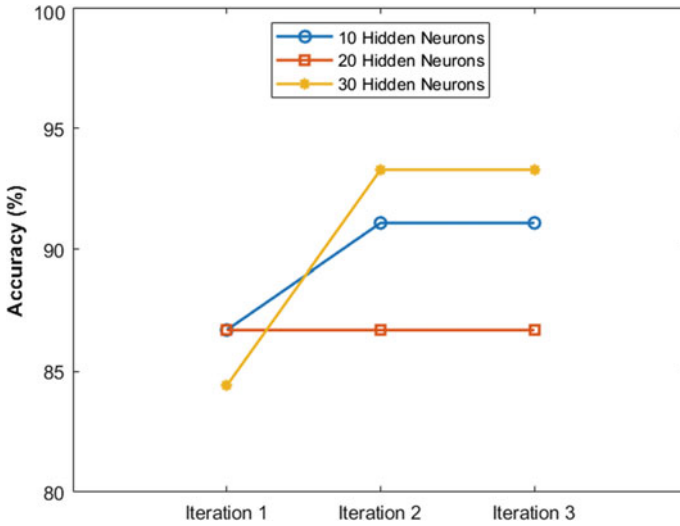


Fig. 23.5 Accuracy of each of the three iterations with 10, 20 and 30 hidden neurons

Table 23.3 Parameters fed to the final NN model

Process parameter	Value
Nozzle diameter	0.8 mm
Nozzle temperature	90 °C
Heated bed temperature	45 °C
Printing speed	10 mm/s
Raster width	0.9 mm
Layer height	0.3 mm
Infill density	80%
Ambient temperature	25–28 °C

Fig. 23.6 PCL part fabricated using the parameters mentioned in Table 23.3



with the classification as successful print or print failure were used to develop a neural network model using a MATLAB code. The neural network was trained for three times each, using three different values of hidden neurons (10, 20, and 30). The model, which resulted in the highest accuracy, was considered for final use. A particular set of process parameter values was fed to the network. The neural network provided the probability of the given set of process parameters to result in the successful fabrication of a PCL part by the FDM process. The result predicted by the NN was validated by printing a PCL part with the same set of process parameter values. From this work, the conclusions that can be drawn are as follows:

- The set of process parameters that resulted in a successful fabrication of a PCL part in this work are nozzle diameter of 0.8 mm, nozzle temperature of 90 °C, bed temperature in the range of 45–50 °C, printing speed of 10 mm/s, raster width of 0.9 mm, layer height of 0.3–0.4 mm, infill density of 60–100% and under ambient temperature in the range of 25–28 °C.
- The most common reasons for the failure of the process were filament buckling between the feed rollers and heating element, and deformation of the part because of insufficient solidification.
- The NN with 30 hidden neurons performed better than other cases with the highest accuracy of 93.3%. It was also noticed that the NN with 10 hidden neurons showed better accuracy than that with 20 hidden neurons. This indicates that a higher number of hidden neurons do not always result in higher accuracy, and it is necessary to train networks with different levels of hidden neurons until a desirable accuracy is obtained.

This neural network model is a useful tool to predict the result of a particular set of FDM process parameters on the printability of PCL.

References

1. Gibson I, Rosen D, Stucker B (2010) Additive manufacturing technologies. Springer, Boston, MA
2. Popescu D, Zapciu A, Amza C, Baciuf, Marinescu R (2018) FDM process parameters influence over the mechanical properties of polymer specimens: a review. *Polym Testing* 69:157–166
3. Chacón JM, Caminero MA, García-Plaza E, Núñez PJ (2017) Additive manufacturing of PLA structures using fused deposition modelling: effect of process parameters on mechanical properties and their optimal selection. *Mater Des* 124:143–157
4. Sun Q, Rizvi GM, Bellehumeur CT, Gu P (2008) Effect of processing conditions on the bonding quality of FDM polymer filaments. *Rapid Prototyping J* 14:72–80
5. Deng X, Zeng Z, Peng B, Yan S, Ke W (2018) Mechanical properties optimisation of poly-ether-ether-ketone via fused deposition modeling. *Materials* 11:216
6. Fernandez-Vicente M, Calle W, Ferrandiz S, Conejero A (2016) Effect of infill parameters on tensile mechanical behavior in desktop 3D printing. *3D printing and additive manufacturing* 3:183–192
7. Lee BH, Abdullah J, Khan ZA (2005) Optimisation of rapid prototyping parameters for production of flexible ABS object. *J Mater Process Technol* 169:54–61

8. Che CW, Ta-Wei L, Shr-Shiung H (2007) Optimising the rapid prototyping process by integrating the Taguchi method with the Gray relational analysis. *Rapid Prototyping J* 13:304–315
9. Mohamed OA, Masood SH, Bhowmik JL, Nikzad M, Azadmanjiri J (2016) Effect of process parameters on dynamic mechanical performance of FDM PC/ABS printed parts through design of experiment. *J Mater Eng Perform* 25:2922–2935
10. Srivastava M, Rathee S (2018) Optimisation of FDM process parameters by Taguchi method for imparting customised properties to components. *Virtual Phys Prototyping* 13:203–210
11. Sood AK, Ohdar RK, Mahapatra SS (2009) Parametric appraisal of fused deposition modelling process using the grey Taguchi method. *Proc Inst Mech Eng Part B: J Eng Manuf* 224:135–145
12. Sahu RK, Mahapatra SS, Sood AK (2013) A study on dimensional accuracy of fused deposition modeling (FDM) processed parts using fuzzy logic. *J Manuf Sci Prod* 13:183–197
13. Sood AK, Ohdar RK, Mahapatra SS (2012) Experimental investigation and empirical modelling of FDM process for compressive strength improvement. *J Adv Res* 3:81–90
14. Shen X, Yao J, Wang Y, Yang J (2004) Density prediction of selective laser sintering parts based on artificial neural network. In: Yin FL, Wang J, Guo C (eds) *Advances in neural networks—ISNN 2004*. ISNN 2004. Lecture Notes in Computer Science, vol 3174. Springer, Berlin, Heidelberg, pp 832–840
15. Rong-Ji W, Xin-hua L, Qing-ding W, Lingling W (2009) Optimising process parameters for selective laser sintering based on neural network and genetic algorithm. *Int J Adv Manuf Technol* 42:1035–1042
16. Vosniakos G-C, Maroulis T, Pantelis D (2007) A method for optimizing process parameters in layer-based rapid prototyping. *Proc Inst Mech Eng Part B: J Eng Manuf* 221(8):1329–1340
17. Sood AK, Eqbal A, Toppo V, Ohdar RK, Mahapatra SS (2012) An investigation on sliding wear of FDM built parts. *CIRP J Manufact Sci Technol* 5:48–54
18. Panda BN, Bahubalendruni MVAR, Biswal BB (2015) A general regression neural network approach for the evaluation of compressive strength of FDM prototypes. *Neural Comput Appl* 26:1129–1136
19. Zein I, Hutmacher DW, Tan KC, Teoh SH (2002) Fused deposition modeling of novel scaffold architectures for tissue engineering applications. *Biomaterials* 23:1169–1185
20. Ceretti E, Ginestra P, Neto PI, Fiorentino A, Da JVL (2017) Multi-layered scaffolds production via fused deposition modeling (FDM) using an open source 3D printer : process parameters optimisation for dimensional accuracy and design reproducibility. In: Shih A, Cao J (eds) *3rd CIRP conferences on biomanufacturing 2017*, vol 65. Chicago, U.S., Procedia CIRP, pp 13–18
21. Yen H-J, Tseng C-S, Hsu S, Tsai C-L (2009) Evaluation of chondrocyte growth in the highly porous scaffolds made by fused deposition manufacturing (FDM) filled with type II collagen. *Biomed Microdevices* 11:615–624
22. Goldberg Y (2017) Neural network methods for natural language processing. *Synthesis Lect Human Language Technol* 10:1–309
23. Vijayaraghavan V, Garg A, Lam JSL, Panda B, Mahapatra SS (2015) Process characterisation of 3D-printed FDM components using improved evolutionary computational approach. *Int J Adv Manuf Technol* 78:781–793
24. Rumelhart DE, Hinton GE, Williams RJ (1986) Learning representations by back-propagating errors. *Nature* 323:533–536
25. Beale MH, Hagan MT, Demuth HB (2013) *Neural network toolbox TM 7 user' s guide*, Mathworks Inc
26. Yang Z, Jin L, Yan Y, Mei Y (2018) Filament breakage monitoring in fused deposition modeling using acoustic emission technique. *Sensors* 18:749

Chapter 24

ANFIS-Based Prediction Model for Tool Wear Criteria During Orbital Electrical Discharge Machining of Ti6Al4V



Naisarg H. Sagathiya , Ashish R. Prajapati , Keyur P. Desai, and Harshit K. Dave 

Introduction

Since World War II, to address the growing list of industrial requirements, researchers have developed number of nontraditional machining processes. Electrical discharge machining (EDM) is a versatile nontraditional material removal process in which it is possible to machine any shaped cavity using a tool having the same shape that of the desired cavity. In EDM, both the work material and the tool are needed to be conductors of electricity, and both of them are submerged in a dielectric medium. Initiation of discharges is created by applying high voltage difference between the workpiece and tool, overcoming the breakdown strength of the dielectric fluid at the small gap between the two materials. A small channel of plasma is formed in the gap and expands further with discharge duration [1]. This plasma channel creates an extremely high temperature, which eventually melts and evaporates material from both the tool and workpiece.

In EDM, the size of the hole machined will always be greater than that of the tool, which is called as overcut. Overcut in EDM cannot be eliminated. It can be minimized by selecting the optimum input parameters. Minimization of overcut also endures the problem of flushing and removal of solidified partials from hole cavity. This problem can be rectified by using orbital movement of the tool. It increases clearance gap between the electrode and the hole, which helps in flushing the dielectric fluid to the bottom of the hole, which ultimately improves flushing. Also, the shape of the electrical discharge machined cavity dramatically depends on the shape and size of the tool electrode [2]. It is not possible for a single size tool to machine cavity of different sizes. So, to machine different sizes of hole using a single size tool, orbital

N. H. Sagathiya · A. R. Prajapati (✉) · K. P. Desai · H. K. Dave
Department of Mechanical Engineering, S. V. National Institute of Technology, Surat 395007,
India
e-mail: [iamarp5155@gmail.com](mailto:iamp5155@gmail.com)

EDM is used. Orbital tool movement in EDM process is used to detach the size of the electrode from the size of the hole to be machined. Hence, the standard the size electrode from the market can be utilized to machine a hole of size bigger than the electrode.

Tsai and Wang [3] did a comparative analysis of six neural networks and ANFIS models to predict the material removal rate (MRR). They concluded that ANFIS model gave the best results with a 16.33% error. Mandal et al. [4] have used ANN to model the electrical discharge machining process. They predicted the values of MRR and TWR utilizing those models. Pradhan et al. [5] have studied two artificial intelligent models, namely radial basis function neural network (RBFN) and back propagation neural network (BPN) to predict the surface roughness of electrical discharge machined parts of AISI D2 steel. They observed that both the methods gave satisfactory results and the difference between the predicted and experimental values by both the methods found lower. Markopoulos et al. [6] have predicted the surface roughness of EDMed parts of different steel grades using ANN. Gao et al. [7] have studied the four different algorithms of ANN to predict the MRR and TWR. They observed that the Levenberg Marquardt algorithm (LM) gave minimum error while predicting the values selected response parameters. Caydas et al. [8] have used ANFIS to anticipate the thickness of white layer (WLT) and surface roughness values of wire-ED machined surface. They made a model with reasonable difference between experimental and predicted values. Rao et al. [9] carried out experiments on M-250, HE15, Ti6Al4V and 15CDV6 materials machined with EDM process. They developed models for surface roughness using ANN along with or without the genetic algorithm (GA). They found that the model designed using ANN with GA gave lower error compared to other model. Maji et al. [10] have developed the models of ANFIS using linear and nonlinear membership functions (MFs) to predict the MRR and surface roughness values. They concluded that using nonlinear membership functions, models gave slightly better results.

Dave et al. [11] have studied the EDM of nickel-based alloy under orbital tool movement using Taguchi L25 orthogonal array. They found out the most significant variables affecting MRR and surface roughness are pulse on time and current. Prabhu et al. [12] studied the modeling of carbon nanotube (CNT)-based EDM of tool steel D2 using ANFIS mathematical approach. They predicted the surface roughness of parts machined with and without CNT mixed dielectric with acceptable errors. Al-Ghamdi et al. [13] made the relationship between EDM parameters and MRR using five ANFIS models with 51, 6, 9, 19 and 21 rules and found that model with 21 and 9 runs gave better results. Mathai et al. [14] have studied the effects of EDM parameters on end wear of the tool. They carried out experiments on Ti6Al4V alloy using copper electrode of square cross-section. They found out that pulse ON time affects the most on tool wear characteristics. Hourmand et al. [15] worked on nanopowder mixed EDM of a metal matrix composite Al-Mg₂Si material. They used ANFIS model to predict the MRR. From ANFIS model, they observed that the interaction of voltage–current and pulse on time–current has the highest effects on MRR. Dave [16] has applied PSO (particle swarm optimization) and TLBO (teaching learning-based optimization) techniques on orbital path EDM process to get the optimized

(maximum) values of MRR of the Nickel alloy and ANSI 304 steel materials. He found that TLBO technique generated higher value of MRR compared with PSO even by using less number of iterations.

Several authors have developed models creating relation between input–output parameters of die-sinking EDM and wire EDM using ANFIS and other modeling techniques. However, no work has been reported on the modeling of orbital EDM process on Ti6Al4V alloy using copper tool utilizing ANFIS technique. In the present study, ANFIS models have been developed to establish relationship between orbital EDM parameters, which are orbital radius, orbital speed, current, pulse on time and duty factor with response parameters, namely tool wear rate and tool end wear.

Adaptive Neuro-Fuzzy Interface System (ANFIS)

Fuzzy modeling, initially developed by Takagi and Suguno has found number of applications in the prediction, interface and control. ANFIS is one of the most frequently used fuzzy interface systems, especially in practical applications. ANFIS was originally proposed by Jang in 1993 after which it has been modified according to modern needs. ANFIS generates a relationship between input and output by combining fuzzy logic tool and ANN. Fuzzy logic does not have any predefined technique for conversion, and it takes longer time to cope up with the membership functions (MFs). However, ANN has better learning capacity to accommodate with environment. Thus, ANN is combined with fuzzy logic to cop up with fuzzy logic MFs.

A fuzzy interface system has three essential components, which are based on the “If-Then” rule, technique interface and fuzzy set membership. A detailed view of FIS is given in Fig. 24.1. FIS changes the given value into fuzzy value with the help of membership functions, which has values between 0 and 1. Basic components of knowledge base are database and rule base for generating the results [17].

The adaptive network is a multilayer feed-forward neural network. The basic diagram of adaptive network is composed of number of interconnected nodes. Every node performs a particular function on incoming function coming to the node. By selecting the proper learning method, the error of the output can be reduced. ANFIS

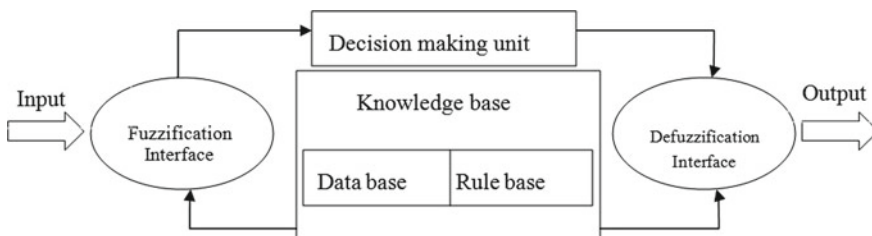


Fig. 24.1 Fuzzy interface system (FIS)

provides two optimization methods, namely, back propagation and hybrid. Basic back propagation algorithm has some limitation of slow convergence, which always tends to stay local. Because of this limitation of back propagation algorithm, a hybrid learning algorithm has been used in this study.

ANFIS Architecture

ANFIS architecture is made of five network layers and the hybrid algorithm has been used to train system based on the input–output data. Takagi and Sugeno’s diagram of ANFIS, which has two input parameters (x and y) and one output function (z) with two membership functions (MFs) are shown in Fig. 24.2. Two fuzzy rules (If-Then) of first-order Sugeno modes are given below:

$$\text{Rule 1 : If } x \text{ is } A_1 \text{ and } y \text{ is } B_1 \text{ Then } f_1 = p_1 x + q_1 y + r_1 \quad (24.1)$$

$$\text{Rule 2 : If } x \text{ is } A_2 \text{ and } y \text{ is } B_2 \text{ Then } f_2 = p_2 x + q_2 y + r_2 \quad (24.2)$$

where, A_1, A_2, B_1 and B_2 are input functional parameters, and p_1, q_1, r_1, p_2, q_2 and r_2 are output functional parameters.

All the layers of ANFIS model, which are shown in Fig. 24.2, are described below:

Layer 1: In this fuzzification layer, each input is the adaptive node that transformed into linguistic with the help of MFs. Every node (i) in this layer is the square node with a node function as:

$$O_i^1 = \mu_{A_i}(x), \quad (24.3)$$

where, $i = 1, 2$ and μ_{A_i} is a degree of membership functions for input x

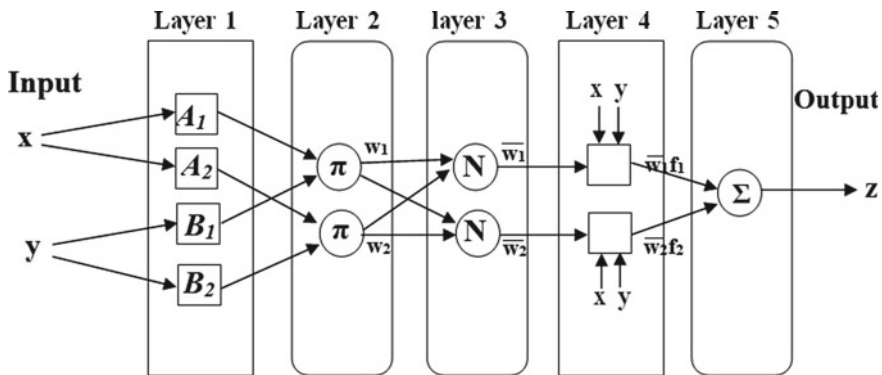


Fig. 24.2 ANFIS architecture

Layer 2: Each node in this layer is a circular node, which multiplies the incoming signal and sends data out. In this layer, each node is a nonadaptive type. It can be given as below:

$$\omega_i = \mu_{A_i}(x)\mu_{B_i}(y), i = 1, 2 \quad (24.4)$$

Layer 3: Each node in this layer in circular shape is labeled with N , and all of them are fixed. It represents the firing strength from layer 2. Firing strength can be calculated as below:

$$\bar{\omega}_i = \frac{\omega_i}{\omega_1 + \omega_2}, i = 1, 2 \quad (24.5)$$

Layer 4: This is a defuzzification layer, which is adaptive. Each node (i) in this layer is a square node with function:

$$\bar{\omega}_i f_i = (p_i x + q_i y + r_i) \quad (24.6)$$

where, ω_i is the output from layer 3, and $(p_i x + q_i y + r_i)$ is called as consequent parameter.

Layer 5: This single node layer is the output layer, which is modeled by ANFIS. It is shown in a circular shape and labeled as Σ , that is overall output by summation of all incoming output:

$$\sum_i \bar{\omega}_i f_i = \frac{\sum_i \omega_i f_i}{\sum_i \omega_i}, \quad (24.7)$$

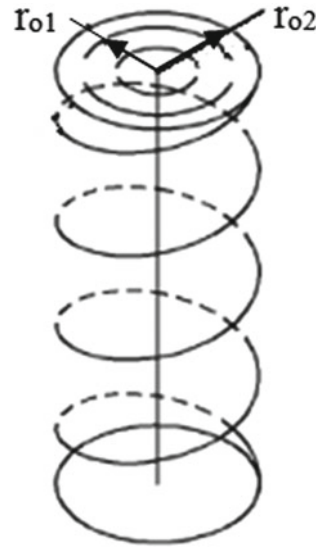
From the above ANFIS model, a relationship between input and output values can be successfully established using different combinations of MFs, rule bases and other parameters from the loaded database.

Experimental Plan and Procedure

Machine Setup

In the present study, Titanium superalloy Ti6Al4V as a workpiece is selected for the experimentation. Ti6Al4V material has an excellent combination of toughness, strength, corrosion-resistance and high strength to weight ratio. Copper with positive polarity is taken as a tool electrode material of 9 mm diameter. The size of the workpiece is 15 mm × 15 mm × 10 mm, in which a hole of depth 4 mm of different diameter was generated. Single diameter tool is used to drill the holes of five different

Fig. 24.3 Helical tool movement path



diameters. Standard EDM oil has been chosen as a dielectric fluid in the present experiments.

Joemars JM322 EDM machine is used in the study. It is equipped with orbital cutting attachment, which can be utilized for boring operation. With the orbital motion of tool, it can be possible to disassociate the size of the cavity with that of the tool. In these experiments, helical movement of the tool is selected, in which tool moves simultaneously in all three axes x , y and z in helical path, which is illustrated in Fig. 24.3. As shown in Fig. 24.4a, workpiece is fixed in workpiece fixture and electrode tool held in tool holder. Side flushing has been used, in which dielectric fluid jet of 1 bar pressure was directed towards the sparking area through a nozzle. Condition of tool and workpiece after machining can be observed in Fig. 24.4b. After the completion of machining, both the tool and workpiece were thoroughly cleaned using acetone and placed on ultrasonic vibrator to remove the carbon soot from the tool and workpiece surfaces and then dried using tissue paper to remove the remaining oil stain.

Experimental Design

Total five input parameters, namely orbital speed (S_o^-), orbital radius (r_o), duty factor (DF), pulse ON time (t_{ON}) and current (I) are selected with five levels for each parameter. Values of all the selected parameters are chosen as the difference between two values remains nearly same. The values of each level for all selected parameters are given in Table 24.1. The following experiment is designed with Taguchi's L25 orthogonal array as there are total five input parameters and five levels for each

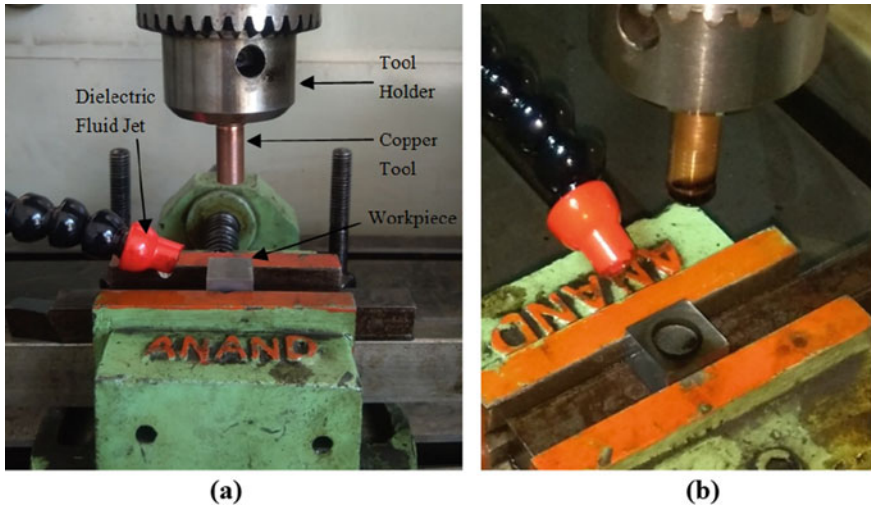


Fig. 24.4 a Machining setup, b Tool and W/P condition after machining

Table 24.1 selected parameters along with their levels

Parameter	P1	P2	P3	P4	Unit
Orbital radius (r_o)	0.4	0.8	1.2	1.6	mm
Orbital speed (S_o)	0.05	0.07	0.09	0.11	mm/s
Current (I)	9	13	17	21	A
Pulse ON time (t_{ON})	93	165	240	315	μ s
Duty factor (DF)	0.4	0.5	0.6	0.7	–

parameter. In this design, there are total 25 rows. All the experiments have been done twice for precise evaluation of results. So, total 50 workpieces and tools have been prepared for experimentation.

Two response characteristics, TWR and tool end wear were selected for ANFIS modeling. To calculate the TWR, weights of the tool before and after machining were measured using Citizen made precision electronic weighing machine having resolution of 0.001 gm. Then, the weights are converted into volume by using density of the tool material. Machining time is counted using precision watch having resolution of 1 s. TWR (mm^3/min) has been calculated by utilizing the following equation:

$$\text{TWR} = \frac{(T_{wi} - T_{wf})}{\rho_T \times t} \tag{24.8}$$

where

T_{wi} Initial weight of the tool (gm)

T_{wf} Final weight of tool (gm)
 ρ_T density of tool material (gm/mm³)
 t machining time (min)

Tool end wear (mm) is a change in the length of the tool before and after machining. It was measured in the EDM machine itself with 0.001 mm precision. The following equation can calculate the tool end wear:

$$\text{End wear } \Delta l_T = l_{T_i} - l_{T_f} \quad (24.9)$$

where, l_{T_i} is the length of the tool before machining and l_{T_f} is the maximum length of the tool after machining.

Result and Discussion

As discussed in the earlier section, Taguchi's L25 orthogonal array design is selected for experimentation, and all the experiments were done twice. The average of these two result data is used in the modeling process. Result data of both the chosen response parameters with Taguchi's L25 design are given in Table 24.2. From the result table, it can be seen that the highest values of tool wear criteria are found during experiment number 9.

ANFIS Model for TWR and Tool End Wear

ANFIS model was developed in MATLAB Mathwork software. The neuro-fuzzy tool available in this software was used to structure ANFIS. In the present study, 80% of the experimental data (20 experiments) were selected randomly for the training process and 20% of data (five experiments) for testing purpose. It means that five results for both the selected responses were predicted using ANFIS model and then compared with experimental results. Sugeno type fuzzy interface system with hybrid learning algorithm is utilized for the modeling of both the response parameters.

In the ANFIS structure generated by the software have five input parameters with one output parameter. In third layer, a total of 20 rules were used for the prediction of the output values. In layer 1, fuzzification of input parameters takes place to 20 membership function in layer 2. To make a model, first, it is needed to call the training data in the ANFIS work system. These data help in searching the constant of the membership function. In the present study, subtractive clustering fuzzy interface system has been selected. Parameters of the subtractive clustering technique used in this study are given in Table 24.3. These ANFIS variables have been optimized after a number of tests.

Table 24.2 Experimental design and results of TWR and tool end wear

Exp.	Orbital radius (mm)	Orbital speed (mm/s)	Current (A)	Pulse ON time (μs)	DF	TWR (mm ³ /min)	Tool end wear (mm)
1	0.4	0.05	9	93	0.4	0.036	0.271
2	0.4	0.07	13	165	0.5	0.057	0.199
3	0.4	0.09	17	240	0.6	0.0985	0.271
4	0.4	0.11	21	315	0.7	0.102	0.183
5	0.4	0.13	28	385	0.8	0.171	0.307
6	0.8	0.05	13	240	0.7	0.0428	0.135
7	0.8	0.07	17	315	0.8	0.0542	0.149
8	0.8	0.09	21	385	0.4	0.0836	0.259
9	0.8	0.11	28	93	0.5	0.8146	1.108
10	0.8	0.13	9	165	0.6	0.0299	0.195
11	1.2	0.05	17	385	0.5	0.0656	0.249
12	1.2	0.07	21	93	0.6	0.2529	0.811
13	1.2	0.09	28	165	0.7	0.2448	0.584
14	1.2	0.11	9	240	0.8	0.0138	0.057
15	1.2	0.13	13	315	0.4	0.0309	0.225
16	1.6	0.05	21	165	0.8	0.1235	0.452
17	1.6	0.07	28	240	0.4	0.2352	0.646
18	1.6	0.09	9	315	0.5	0.0155	0.154
19	1.6	0.11	13	385	0.6	0.0416	0.223
20	1.6	0.13	17	93	0.7	0.1251	0.558
21	2	0.05	28	315	0.6	0.2307	0.613
22	2	0.07	9	385	0.7	0.0182	0.13
23	2	0.09	13	93	0.8	0.0657	0.531
24	2	0.11	17	165	0.4	0.095	0.596
25	2	0.13	21	240	0.5	0.1365	0.587

The data are trained using hybrid optimization method with 50 epochs. ANFIS then calculated the error between input values and the predicted values generated from the model.

Model Performance for the Prediction of Tool Wear Rate and Tool End Wear

As in the present research, Taguchi’s L25 experimental design is used; there are total 25 output readings. Out of which 20 data were selected randomly for training

Table 24.3 ANFIS criteria used in creating the model

Criteria	Descriptor/values
FIS structure	Sugeno subtractive clustering
Number of training and testing data	20 and 5
Reject ratio	0.15
Squash factor	1.25
Accept ratio	0.1
Range of influence	0.5
Number of outputs	1
Number of inputs	5
Optimization method	Hybrid
Numbers of input membership functions	20 20 20 20 20
Number of training epochs	50

the model. The remaining five data were used for the prediction of both the output parameters. The error between experimental values and predicted value has been evaluated by statistical equations. ANFIS model performance is evaluated by using statistical functions, namely root mean square error (RMSE) and mean absolute error (MAE). Equations for these functions are given below:

$$MAE = \frac{1}{n} \sum_{t=1}^n |P_t - E_t| \tag{24.10}$$

$$RSME = \sqrt{\frac{\sum_{t=1}^n (P_t - E_t)^2}{n}} \tag{24.11}$$

where, P_t is predicted result from ANFIS, E_t is experimental result, and n is the total number of data selected for the calculation of error.

The lower value of RSME indicates the better predictability of the model. As it can be observed from Table 24.4 that model for tool wear rate gave smaller error than the model for the tool end wear. While measuring the tool end wear, the taper on the tool was not considered, this is nullified in the calculation of TWR. The predicted and experimental values of both TWR and tool end wear in graphical form are shown in Fig. 24.5a, b, respectively.

Table 24.4 Errors of predicted result

Response characteristic	MAE	RSME
Tool wear rate	0.01164	0.01415
Tool end wear	0.0396	0.04583

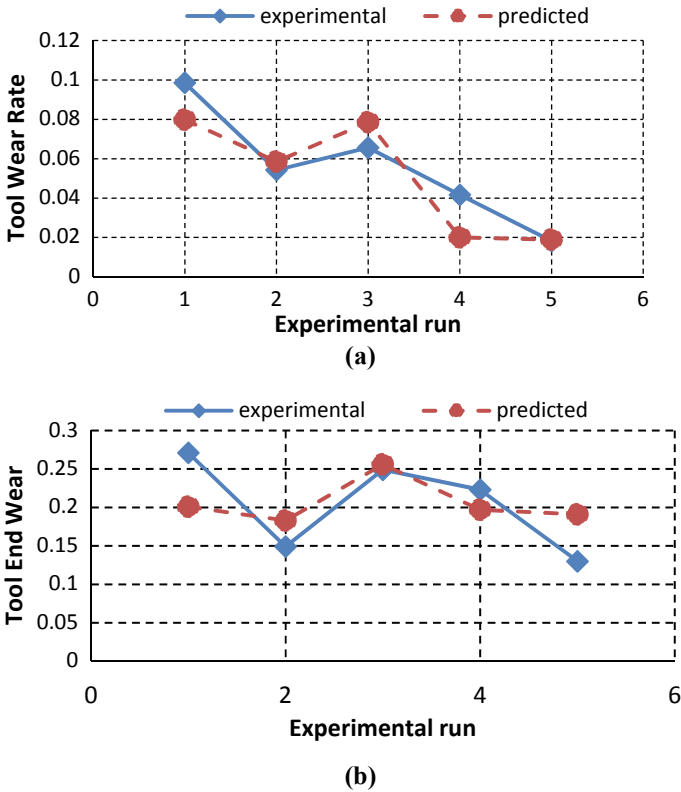
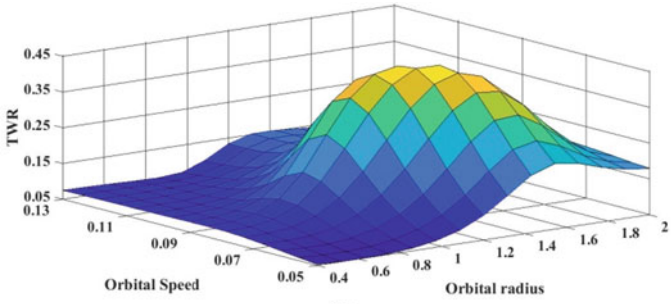


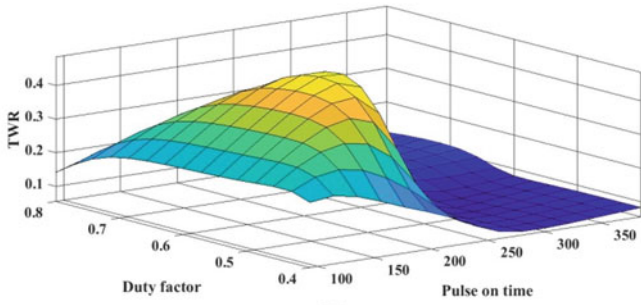
Fig. 24.5 Comparative diagram of experimental and predicted values through ANFIS for **a** TWR and **b** Tool end wear

From Fig. 24.5a, it can be seen that two predicted values (experimental runs 1 and 4) have a relatively larger error for tool wear rate than other experimental runs. Error for two predicted values (experimental runs 2 and 5) has minimum error compared with others. In the case of the tool end wear also errors found higher for two values (experimental runs 1 and 5), which can be observed in Fig. 24.5b. While the experimental run 3 has the lowest error. Thus, ANFIS model can be used for generating a model with minimum values of error.

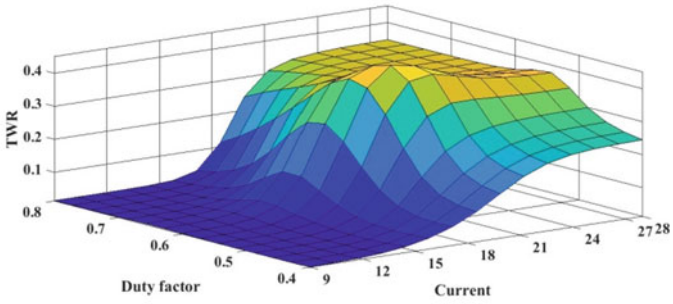
Moreover, ANFIS has generated nonlinear surface plots of response variable against two input variables. Some of the selected surface graphs of two input parameters with TWR and tool end wear are shown in Figs. 24.6 and 24.7, respectively. TWR and tool end wear found larger at the high orbital radius values (Figs. 24.6a and 7a). From Fig. 24.6b, it can be observed that tool wear rate decreases with an increase in t_{ON} . Also, from Fig. 24.6c, TWR is found increasing with an increase in current values. Figure 24.6b indicates that, at lower pulse on time values, tool end wear is more significant compared with higher values. By observing Fig. 24.7b, it can be said that the tool end has worn significantly when the lower machining time



(a)



(b)



(c)

Fig. 24.6 Change in tool wear rate with respect to **a** orbital speed (S_o) and orbital radius (r_o), **b** Duty factor and Pulse on time and **c** Duty factor and current

was used. Referring to Fig. 24.7c, tool end wear is found to be increasing with an increase in current and duty factor values.

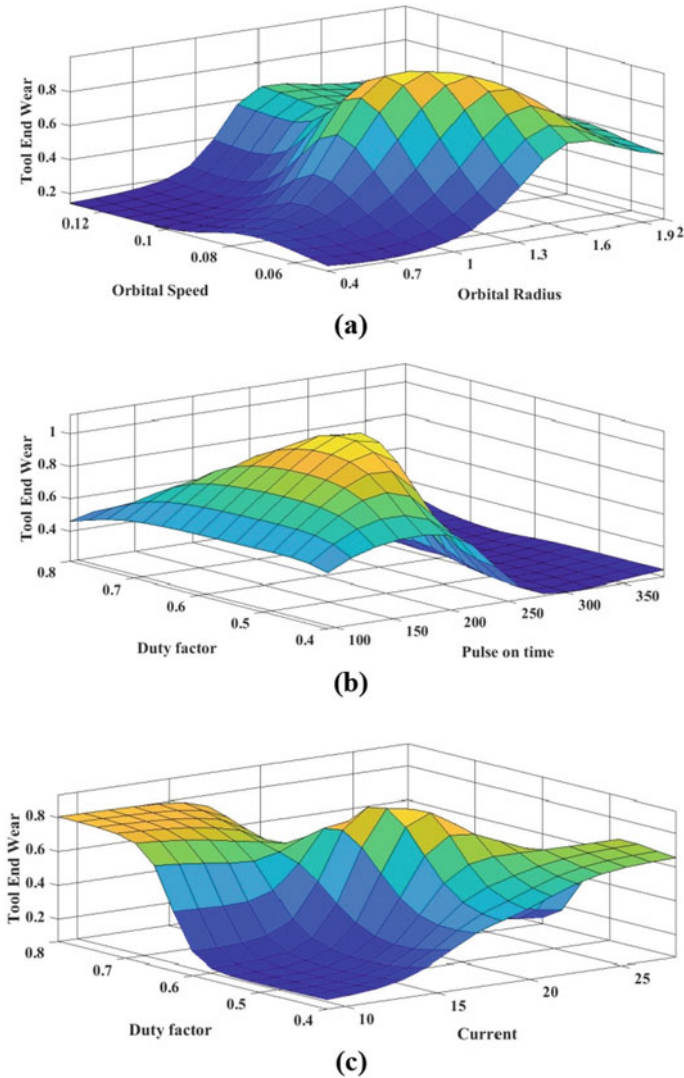


Fig. 24.7 Change in tool end rate with respect to **a** orbital speed (S_o) and orbital radius (r_o), **b** Duty factor and Pulse on time and **c** Duty factor and current

Conclusion

Orbital tool movement in EDM helps in drilling the hole of different diameters with a single diameter tool. In the present research work, models for tool wear rate and tool end wear were successfully developed using ANFIS. The developed model helped in predicting the values of responses with reasonable errors. Error predicted for tool

end wear was found higher than the error anticipated for tool wear rate. Results show an increasing trend on tool wear characteristics with an increase in the current values. Also, tool wear characteristics were found lower at higher pulse on time and lower orbital radius. It can be concluded that with the help of the surface graphs, prediction of the behavior of responses because of a change in the independent parameters can be easily generated through ANFIS. Thus, ANFIS modeling can be utilized for process planning to predict the tool wear prior to the machining initiation.

References

1. Kunieda M, Lauwers B, Rajurkar KP, Schumacher BM (2005) Advancing EDM through fundamental insight into the process. *CIRP Ann* 54(2):64–87
2. Benedict GF (1987) *Nontraditional manufacturing processes*. CRC Press, vol 19
3. Tsai KM, Wang PJ (2001) Predictions on surface finish in electrical discharge machining based upon neural network models. *Int J Mach Tools Manuf* 41(10):1385–1403. <https://doi.org/10.18178/ijmmm.2017.5.3.309>
4. Mandal D, Pal SK, Saha P (2007) Modeling of electrical discharge machining process using back propagation neural network and multi-objective optimization using non-dominating sorting genetic algorithm-II. *J Mater Process Technol* 186(1–3):154–162. <https://doi.org/10.1016/j.jmatprotec.2006.12.030>
5. Pradhan MK, Das R, Biswas CK (2009) Comparisons of neural network models on surface roughness in electrical discharge machining. *Proc Inst Mech Eng J Eng Manuf* 223(7):801–808
6. Markopoulos AP, Manolakos DE, Vaxevanidis NM (2008) Artificial neural network models for the prediction of surface roughness in electrical discharge machining. *J Intell Manuf* 19(3):283–292. <https://doi.org/10.1007/s10845-008-0081-9>
7. Gao Q, Zhang QH, Su SP, Zhang JH, Ge RY (2008) Prediction models and generalization performance study in electrical discharge machining. *Appl Mech Mater* 12:677–681. <https://doi.org/10.4028/www.scientific.net/AMM.10-12.677>
8. Çaydaş U, Haşçalık A, Ekici S (2009) An adaptive neuro-fuzzy inference system (ANFIS) model for wire-EDM. *Expert Syst Appl* 36(3):6135–6139. <https://doi.org/10.1016/j.eswa.2008.07.019>
9. Rao KRM, Rangajanardhaa G, Hanumantha Rao D, Sreenivasa Rao M (2009) Development of hybrid model and optimization of surface roughness in electric discharge machining using artificial neural networks and genetic algorithm. *J Mater Process Technol* 209(3):1512–1520
10. Maji K, Pratihari DK (2010) Forward and reverse mappings of electrical discharge machining process using adaptive network-based fuzzy inference system. *Expert Syst Appl* 37(12):8566–8574. <https://doi.org/10.1016/j.eswa.2010.05.019>
11. Dave H, Desai K, Raval H (2012) Experimental investigations on orbital electro discharge machining of Inconel 718 using Taguchi technique. *Int J Mod Manuf Technol* 4(1):53–58
12. Prabhu S, Uma M, Vinayagam BK (2013) Adaptive neuro-fuzzy interference system modelling of carbon nanotube-based electrical discharge machining process. *J Brazilian Soc Mech Sci Eng* 35(4):505–516. <https://doi.org/10.1007/s40430-013-0047-5>
13. Al-Ghamdi K, Taylan O (2015) A comparative study on modelling material removal rate by ANFIS and polynomial methods in electrical discharge machining process. *Comput Ind Eng* 79:27–41
14. Mathai VJ, Dave HK, Desai KP (2017) Study on effect of process parameters on end wear of tool electrode during planetary EDM of Ti-6Al-4V. *Int J Mater Mech Manuf* 5(3):159–163
15. Hourmand M, Sarhan AA, Farahany S, Sayuti M (2019) Microstructure characterization and maximization of the material removal rate in nano-powder mixed EDM of Al-Mg₂Si metal

- matrix composite-ANFIS and RSM approaches. *Int J Adv Manuf Technol* 101(9–12):2723–2737. <https://doi.org/10.1007/s00170-018-3130-3>
16. Dave HK (2019) Optimization of orbital electro discharge machining parameters using TLBO and PSO algorithms. *Int J Mod Manuf Technol* 11(2):2067–3604
 17. Jang JS (1993) ANFIS: adaptive-network-based fuzzy inference system. *IEEE Trans Syst Man Cyber* 23(3):665–685

Chapter 25

Evaluation of Metal Foam of Al6061 + MgO Using PM Route



Rahul Rathod, Bhupesh Goyal, Prashantsingh Tomar, and Akash Pandey

Introduction

Metal Foams are new type of material that has porous structure, which makes them different from other metals. They are manufactured by various techniques and many are still under development. Nowadays, there is an environment of manufacturing a new class of material that occupies less mass and weight, with high strength, good thermal conductivity and good acoustic damping capacity as compared with other materials, which result in the generation of metal foam that fulfils the required properties [1]. In current scenario, the techniques that are used to manufacture porous materials are not able to control the different parameters like porosity, density etc. Metal foam also finds its applications in the defence [2]. Al foams can convert much of the impact energy into plastic energy and absorb much more energy than bulk metals at relatively low stresses [3].

Generally, porous materials classified in two types:

- Closed cell
- Open cell.

The closed-cell metal foam possesses porosity in the range of 30–40% while open-cell metal foam contains 60–90% porosity in them [4–6]. Open-cell foam is used in the field of thermal applications [1, 7] while closed-cell foam finds its uses in the field of structural applications, sound absorbing and vibration damping [4, 8].

Different methods are introduced to manufacture the metal foam such as Alporas process, powder metallurgy, space holder, gas eutectic decomposition, entrapped gas

R. Rathod (✉) · B. Goyal · P. Tomar
Department of Mechanical Engineering, Parul University, Vadodara 391760, India
e-mail: rahulrathod819@gmail.com

A. Pandey
The Maharaja Sayajirao University, Vadodara 390002, India

expansion, etc. using different blowing agents such as TiH_2 [9, 10], CaCO_3 [11, 12], MgO [13]. Material like Tin can also be used as foaming agent by maintaining the decomposition temperature [7].

At present, the processes used to manufacture metal foams are not completely controlled, i.e., the pores of the metal foam obtained are not in proper shape and size and are not aligned properly. The preheat temperature plays a vital role in increasing the porosity of the metal foam [13]. But the control of processing metal foam is improving rapidly. Metal foams have some promising properties, which make them more attractive and efficient as compared with other metallic structures. Metal foams can offer significant performance gains in light, stiff structures, for the efficient absorption of energy, for thermal management and perhaps for acoustic control and other, more specialized applications [1]. They can also be recycled and are non-toxic.

There are two types of metal foam, closed-cell metal foam and open-cell metal foam. The closed-cell metal foam possesses 30–40% porosity while open-cell metal foam contains 60–90% porosity in them. Different methods are introduced to manufacture the metal foam such as Alporas process, powder metallurgy, NaCl used as a space holder, gas eutectic decomposition, entrapped gas expansion, etc., using different blowing agents such as TiH_2 , MgCO_3 , ZrH_2 , CaCO_3 , MgO . The Al6061 powder mixed with blowing agent MgO in desired quantity is mixed with Silica gel, which is used to bind the mixture and compacted at a pressure of 100–150 Psi and a precursor is obtained, which consists of a coin-shaped structure. The obtained precursor is then heated in muffle furnace at temperature ranging from 890 to 880 °C. As a result, gases start to generate inside the precursor in the form of bubbles and after solidification the metal foam is obtained, which possesses a porous structure. The solidification rate of the metal foam increases due to low porosity of the metal foam obtained [14]. The silica gel used as binding agent oxidizes and does not have any reaction on the aluminium and MgO , so good metal foam is obtained using PM route.

In matter or energy transportation applications, open-cell metal foams are been used frequently [15]. For sound absorbing as well as thermal applications, open-cell structures are used as they exhibit higher thermal conductivity [16]. The hot stage microscopy is used for determining the foaming kinetics of obtained metal foam [17].

Experimental

Powder Metallurgy Method

Alloy powders are mixed with the blowing agent to form metal foam. Powder metallurgy also known as the powder compact foaming technique has improved its status in current industrial trend. This technique involves mixing of metal alloy powders with an appropriate foaming agent and compressing the mixture with a dense product

called precursor material [18]. According to previous research, it can also be produced without using any foaming agent [13]. The heating of foamable precursor is carried out above the melting point of the alloy [4]. The major difficulty observed with this process is the inequality between the decomposition temperature of the foaming agent and melting temperature of Aluminium [1].

This process starts by blending of metal into powder form and cold compacting with the die compression or axial compaction. 5 g of Al6061 powder is mixed with the 2% of MgO, used as a blowing agent and 1–2% of silica gel is used as binding agent so that it binds the material during removal from the die after compaction under a pressure of 100–150 Psi then the compacted powder is further heated to its melting temperature of about 880–890 °C and holding it for about 3–4 min so that maximum amount of gas can be generated. As a result, the blowing agent starts to release the gas in the form of bubbles, which create voids and the metal foam is obtained after the solidification is done under room temperature. The density of pores obtained will depend on the solidification time and the percentage of blowing agent added to the metal powder [13, 19]. Highest foaming efficiency can be obtained at 700 MPa compaction pressure and 800 °C temperatures [11].

Porosity Calculation

To calculate the porosity of the metal foam, first a beaker is filled with 100 ml of water. A sample of compacted metal piece that does not have porosity is put into the beaker, containing 100 ml of water. Note down the change in volume of the water displaced by the metal piece. Now fill another beaker with same amount of water (i.e., 100 ml) and then put the porous sample into the beaker. Now note down the change in volume of the water displaced by the porous metal piece. So the porosity of the metal foam can be calculated by P .

$$P = \frac{(V_s - V_e)}{100} \%$$

where V_s is the change in volume of the water displaced by the sample metal piece and V_p is the change in volume of the water displaced by the porous metal piece. This method is only applicable to find surface porous material while the method to find internal porosity is still under development.

Results and Discussion

Scanning electron microscope test has been carried out on the metal foam, which shows the microscopic structure of the metal foam obtained at a pressure between 120 and 150 Psi and 880–890 °C temperatures. In Fig. 25.1, the metal foam is compacted

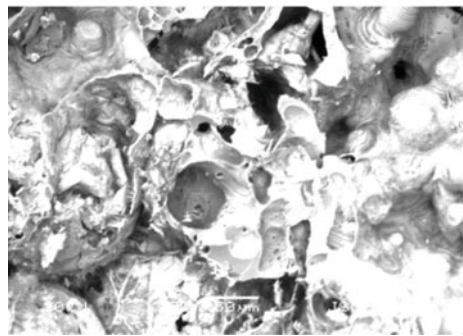
Fig. 25.1 **a** Aluminium metal foam at 100 Psi and 890 °C, **b** Cross-section and **c** SEM (Scanning Electron Microscope) of Al metal foam



(a)



(b)



(c)

at 100 Psi pressure, which shows that the proper melting of the aluminium starts at that point of temperature, which can be seen in the SEM result, while Fig. 25.2 shows the metal foam compacted at 120 Psi pressure and 880°C gives the analysis of metal foam having maximum porosity as compared with other metal foam sample obtained. Figure 25.3 shows the porous structure of the metal foam obtained under

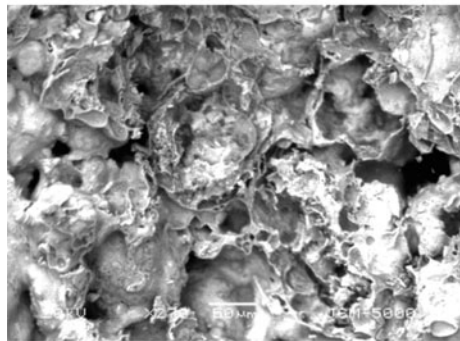
Fig. 25.2 **a** Aluminium metal foam at 120 Psi and 880 °C, **b** Cross-section and **c** SEM (Scanning Electron Microscope) of Al metal foam



(a)



(b)



(c)

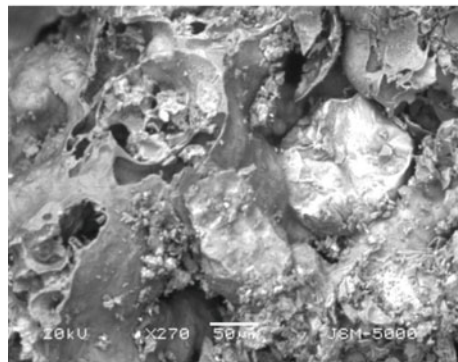
Fig. 25.3 **a** Aluminium metal foam at 150 Psi and 880 °C, **b** Cross-section and **c** SEM (Scanning Electron Microscope) of Al metal foam



(a)



(b)



(c)

Table 25.1 Design of experiments

S. No	Al (g)	MgO (%)	Pressure (Psi)	Temperature (°C)
1	5	2	100	850
2	5	2	100	860
3	5	2	100	870
4	5	2	100	880
5	5	2	100	890
6	5	2	120	880
7	5	2	150	880
8	5	2	170	880
9	5	2	200	880
10	5	2	250	880
11	5	2	250	800

120 Psi pressure and 880 °C. Due to the heating the precursor above melting point, the blowing agent mixed with the aluminium powder starts to generate gas in the form of bubbles and when air cooling is done the bubbles generated inside the precursor gets entrapped inside the precursor and metal foam is obtained, which have porous structure.

While calculating porosity, it was seen that the water was fully absorbed by the metal foam and the deflection of water is displaced by the metal foam is clearly seen when it was placed inside the 100 ml beaker containing water. The SEM result shows that the pores obtained in the metal foam with uneven shape and sizes were obtained. Best result can be analyzed by calculating porosity of the metal foam obtained at different pressure and temperature. It was seen that the best results were shown by the metal foam, which was compacted at 120 Psi pressure and 880 °C temperature by calculating porosity of the metal foam, i.e., 66.6% was observed (Table 25.1).

In Fig. 25.4, as we increase the pressure and temperature for manufacturing of metal foam from 100 to 250 Psi and 800–890 °C, the porosity of the metal foam varies with varying pressure and temperature. The best results can be obtained by SEM analysis, which shows the porous structure inside the fifth, sixth and seventh sample of metal foam, which are compacted at 100–150 Psi and heated at 880–890°C, respectively.

The fifth sample has porosity of about 33.3% while sample sixth shows 66.6% porosity and sample seventh has 53.3% porosity inside it. Figures 25.2 and 25.3 have been compacted at a pressure of 120 and 150 Psi and temperature at 880 °C, respectively. As the SEM results show that the aluminium metal foam of sample 5, 6 and 7 has a porous structure inside it which can be seen at 50 µm.

As we increase the pressure from 150 to 250 Psi and temperature 880 °C, there will be not much change in the surface area and height of the metal foam obtained this is because of the pressure applied for cold compacting is higher, which increases the density of the precursor and when the precursor is been heated at 880 °C temperature,

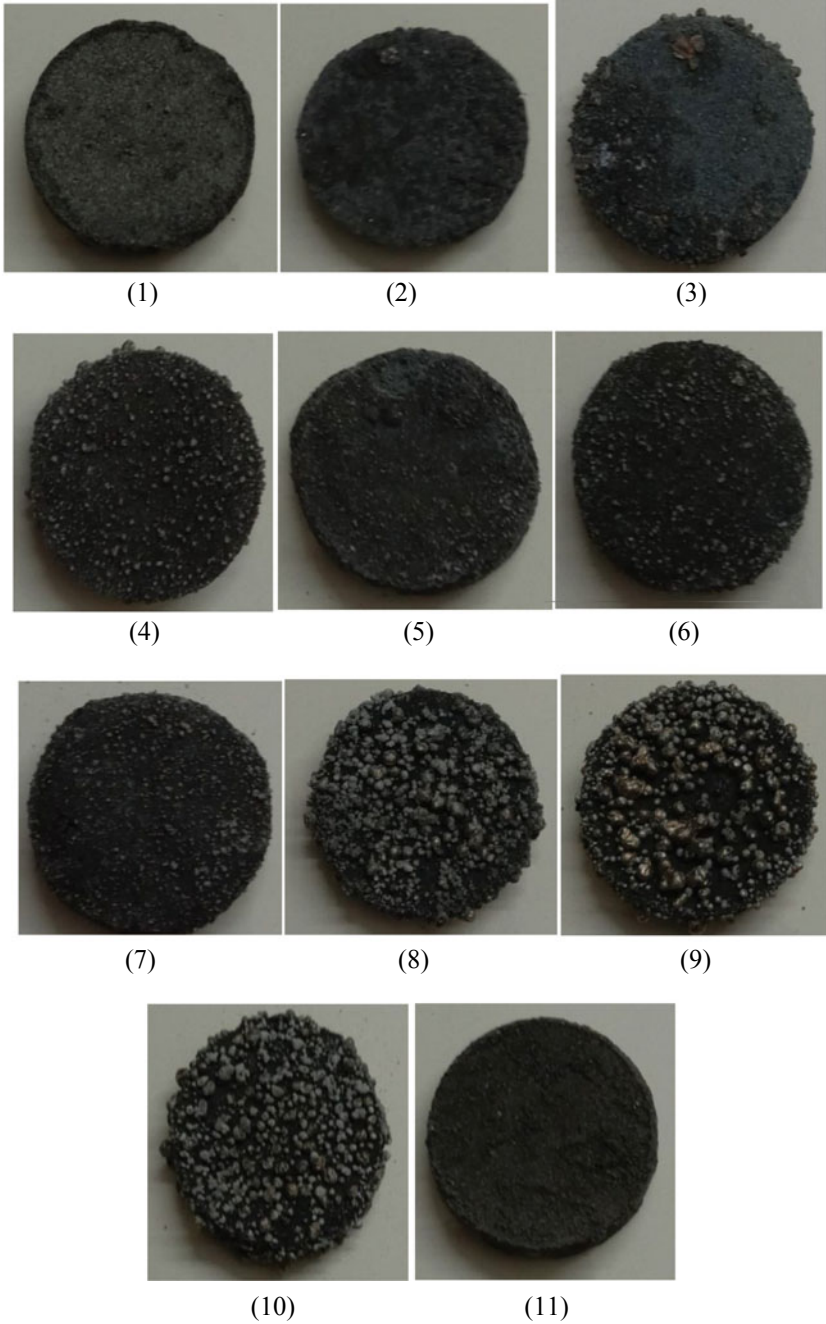


Fig. 25.4 Aluminium metal foam obtained from 100 to 250 Psi pressure and at 800–890 °C temperature

the magnesium oxide mixed with the aluminium powder is unable to make gases in the form of bubbles, which result into less increase in the surface area and low porosity can be observed.

Conclusion

- SEM test shows the microstructure inside the metal foam, which consists of porous structure.
- Due to melting of aluminium metal above 800 °C, the magnesium oxide mixed with the aluminium starts to generate gas in the form of bubbles and the bubbles are been entrapped because of the solidification done at room temperature. The porosity of the metal foam depends on the varying percentage of the magnesium oxide, which acts as blowing agent.
- The magnesium oxide is a good blowing agent that can generate bubbles even at low temperatures, which reduces the time of manufacturing of metal foam.
- Good metal foams that have 30–70% porosity can be obtained at 100–150 Psi pressure and 880–890 °C temperature through PM route.

Acknowledgements I express my gratitude to Dr Akash Pandey, MS University, Vadodara and Mr Bhupesh Goyal, Parul Institute of Technology, Vadodara for providing facility at Institute. I am also thankful to Students Open Innovation Council, Government of Gujarat, India for funding this project.

References

1. Matijasevic-Lux B, Banhart J, Fiechter S, Görke O, Wanderka N (2006) Modification of titanium hydride for improved aluminium foam manufacture. *Acta Mater.* 54, 1887–1900
2. Gokhale AA, Ravi Kumar NV, Sudhakar B, Sahu SN, Basumatary H, Dhara S (2011) cellular metals and ceramics for defence applications. *Defence Sci J* 61(6)
3. Guden M, Yuksel S (2006) SiC particulate aluminium composite foams produced from powder compacts: foaming and compression behavior. *J Mater Sci* 41
4. Banhart J (2001) Manufacture, characterization and application of cellular metal and metal foams. *Prog Mater Sci* 48
5. Ashby MF, Evans AG, Fleck NA, Gibson LJ, Hutchinson JW, Wadley HNG (2000) *Metal foams: a design guide*. Butterworth Heinemann
6. Banhart J (2005) Aluminium foams for lighter vehicles, *Int J Veh Des* 37(2/3)
7. Bai Q, Guo Z, Li H, Yang X, Jin L, Yan J (2017) Experimental investigation on the solidification behaviour of phase change material in open-cell metal foams. *Energ Proced* 142
8. Mahajan SM, Jadhav GA (2015) Aluminium foaming for lighter structure. *Int J Comput Eng Res (IJCER)* 5
9. Koikea R, Matsumotoa T, Kakinumaa Y, Aoyamaa T, Odab Y, Kuriyab T, Kondob M (2018) *Procedia manufacturing* 18
10. Yang D, Chen J, Chen W, Wang L, Wang H, Jiang J, Ma A Fabrication of cellular Zn–Mg alloy foam by gas release reaction via powder metallurgical approach S1005–0302(17)30092-0

11. Lu G, Hao H, Wang F, Zhang X (2013) Preparation of closed-cell Mg foams using SiO₂-coated CaCO₃ as blowing agent in atmosphere, *Trans Nonferrous Met Soc China* 23
12. Neu TR, Mukherjee M, Garcia-Moreno F, Banhart J (2012) Magnesium and magnesium alloy foams. In: 7th international conference on porous metals and metallic foams
13. Aguirre-Perale LY, Jung I-H, Drew RAL (2012) Foaming behavior of powder metallurgical Al-Sn foams. *Acta Mater* 60
14. Baez-Pimiento S, Hernandez-Rojas ME, Palomar-Pardave ME (2015) Processing and characterization of open-cell aluminium foams obtained through infiltration processes. *Proced Mater Sci* 9
15. Mahaidina AA, Abdullaha N, Mohammada M, Omara MA, Suleimana MJ, Zainona NM, Hadia MAN, Abd Jalila MN, Omara AZ, Mohd Hijazi MB (2016) Effect of sintering cycle on physical and mechanical properties of open pore cell copper foam. *Proced Chem* 19
16. Duartea I, Ferreirab JMF (2014) Evolution of metallic foams using hot-stage microscopy. *Proced Mater Sci* 4
17. Uzun A (2019) Production of aluminium foams reinforced with silicon carbide and carbon nanotubes prepared by powder metallurgy method. *Compos Part B* 172
18. Weise J, Stanzick H, Banhart J (2003) Semi solid processing of complex shaped foamable material. *Cell Met Met Foam Technol*. © MIT-Verlag
19. Omar MY, Xiang C, Gupta N, Strbik OM, Cho K (2015) Data characterizing flexural properties of Al/Al₂O₃ syntactic foam core metal matrix sandwich. *Data in Brief* 5
20. Kassim Hassan Z (2019) Production of metal foams by using powder metallurgy method. *AIP Conf Proceed* 2123:020004

Chapter 26

Mechanical and Wear Characterization of Epoxy Resin-Based Functionally Graded Material for Sustainable Utilization of Stone Industry Waste



Aakash Sharma and Vikash Gautam

Introduction

The potential to acknowledge and use materials is essential over time. Due to environmental reasons, many scientists and engineers recognize the importance of using innovative materials. There is always an unceasing growth in the field of materials. Furthermore, the human pursuance to find a new material is never complete by utilizing environmental waste that may work under certain conditions. Significant progress has been made in the development of materials from metals to alloys and functionally graded materials (FGM) based on specific activity. The term “FGM” was coined by the Japanese in 1984 to develop high temperature materials. The idea is to produce a material from a different composition that is resistant to high temperatures on the one hand and good thermal conductivity on the other.

Naebe [1] presented in their article, a review of the latest advances in the investigation of functionally graded materials. The main objective of the research has always been the manufacturing of FGM/C and, therefore, various processing techniques for the preparation of FGM/C are discussed, e.g., CVD, thermal spray, centrifugal casting, electrophoretic deposition, spark plasma sintering, etc. In their articles, Shinohara [2] discussed the challenges of fabricating functionally graded materials and classified its future applications and current issues in various scientific and technological fields, including aerospace, (bio) mechanics, energy engineering, sensor

A. Sharma (✉) · V. Gautam

Department of Mechanical Engineering, Swami Keshvanand Institute of Technology, Jaipur 302025, India

e-mail: aakasharma1507@gmail.com

technology and tribology. Researchers also fabricated graded composites using thermoset resins like Ni/Epoxy resin FGM by magnetic field driving method [3], functionally graded porous polymer structure by Thermal bonding lamination technique [4].

FGMs are innovative materials with varying composition. However, there is not much research work done to develop functionally graded materials for Microelectromechanical systems (MEMS) applications. Hasssanin and Jiang [5] discussed a process for fabricating ceramic micro components using the combined properties of Alumina and Zirconia by soft lithography technique. Rezapoor et al. fabricated Fe-TiC functionally graded coating and evaluated its mechanical properties [6]. Salcedo [7] simulated a 3D functionally graded material using material. Gupta and Talha [8] in their review focussed on the recent developments in modeling and simulation techniques of FGM/S. Polajnar and Kalin [9] investigated friction and wear performance of functionally graded ductile iron (FGDI). Fabrication of W-Cu functionally graded materials using spark plasma sintering [10] and its mechanical characterization [11, 12] is also common among researchers.

Techniques of exploiting filler and reinforcement material for the fabrication of functional composites are more common among researchers such as aerosol and coremat filled epoxy composites [13], glass fiber reinforced composite [14], granite epoxy composite with cast iron filler [15], graphite micro filled epoxy composites [16], granite dust filled Polycarbonate (PC) hardened epoxy composite [17], functionally graded aluminium composites using centrifugal casting [18], graded natural fiber/epoxy composite by centrifugal casting using banana trunk as natural fiber [19], granite powder filled epoxy composites [20], marble dust filled epoxy composites [21], granite powder—epoxy composites for chemical resistance testing [22], epoxy resin with flyash particulates as filler [23], polybutylene terephthalate (PBT) toughened epoxy composite [24], granite powder reinforced in toughened epoxy with unsaturated polyester [25], composite filled with glass fiber [26], granite filled composites for wind turbine applications [27, 28], epoxy resin-based ceramic filled composite [29], bamboo/jute—glass fiber-reinforced polymer (GFRP) composite [30], hybrid composites filled with glass fiber and milled carbon [31] etc.

Depending on their behavior, the functional grading of material serves two purposes. The current literature shows that the use of a large number of fillers and fibers in functional grading of polymers are advantageous in enhancing the mechanical as well as wear properties. Waste products from the stone industry, such as granite powder, are widely and prominently exploited in the fabrication of composites. Depending on the background, existing applications focus on the composition of uniform and graduate compounds. Polymer-based granite powder reinforcement homogeneous and FGM samples were examined to determine their mechanical and wear properties.

Materials and Methodology

The standardized composite material is manufactured using a stone industry waste, i.e., granite powder combined with araldite epoxy resin (LY-556) as matrix reinforcing adhesive material. The hardener (HY-917) is used for curing the resin with the composition ratio of 1:10 wt% with epoxy. Granite and epoxy were weighed using an electronic weighing machine and then mixed evenly by hand for about 10 min to remove air bubbles. A mixture of granite and epoxy is carefully found in the glass test tubes 15 mm in diameter and 125 mm long as shown in Fig. 26.1. The composition of granite dust and epoxy is shown in Table 26.1.

Graded samples are produced by vertical centrifugal casting method (Fig. 26.2). First, the glass tubes are coated internally with a wax-releasing agent. The raw material is poured into cylindrical glass tubes with the prescribed weight ratio and rotated for 45 min at 1500 rpm. Prepared samples were left unattended for 48 h at room temperature and then for further testing, extricated from the glass tubes.

Fig. 26.1 Epoxy-granite mixture in glass tube after VCC process



Table 26.1 Material composition

Specimen	Granite dust (%)	Epoxy (%)
A	0	100
B	5	95
C	10	90
D	15	85

Fig. 26.2 Experimental setup for vertical centrifugal casting



Mechanical Characterization

The hardness of the samples was measured using the C-Scale Rockwell Hardness Tester. It was tested by taking initial load of 10 kgf and main load of 150 kgf for dwell time sufficient enough for indentation. Since it is one of the indentation techniques for determining hardness, we used a 120° diamond spheroconical indenter. Figure 26.3 shows indentation marks on the specimens after determining hardness.

A standard sample size of 55 mm × 10 mm is designed for the Charpy impact test rig shown in Fig. 26.4 in accordance with the ASTM E23 standard. Due to the cylindrical shape of the specimens, the anvil had a designed tooling to hold the samples tight enough to withstand the impact of the high potential hammer/pendulum. The energy absorbed by the specimen before fracture can be noted from the energy readout which when divided by cross-section area of the specimen gives us the impact strength.

Sliding Wear Analysis

The wear was tested under dry conditions on the Pin-On-Disc Tribometer (DUCOM) shown in Fig. 26.5a. The experiments were performed according to the factors and levels given in Table 26.2. The test specimens as in Fig. 26.5b required to perform sliding wear analysis were made to a standard size by machining. The sample with diameter 10 mm and length 35 mm were developed as per the requirements of the

Fig. 26.3 Test specimens for rockwell hardness testing

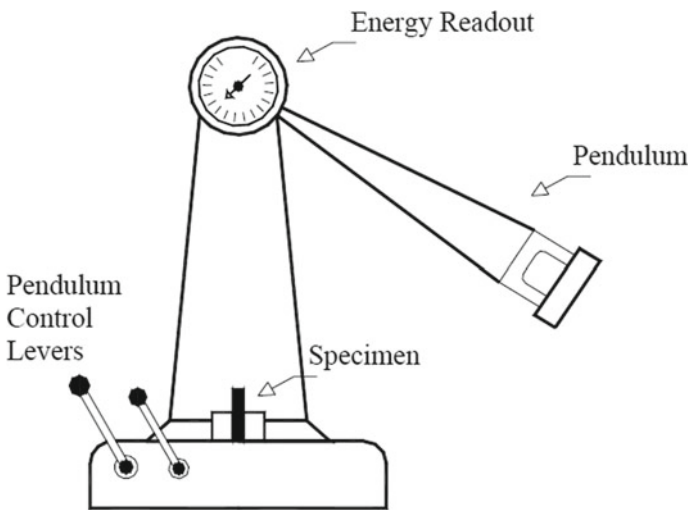
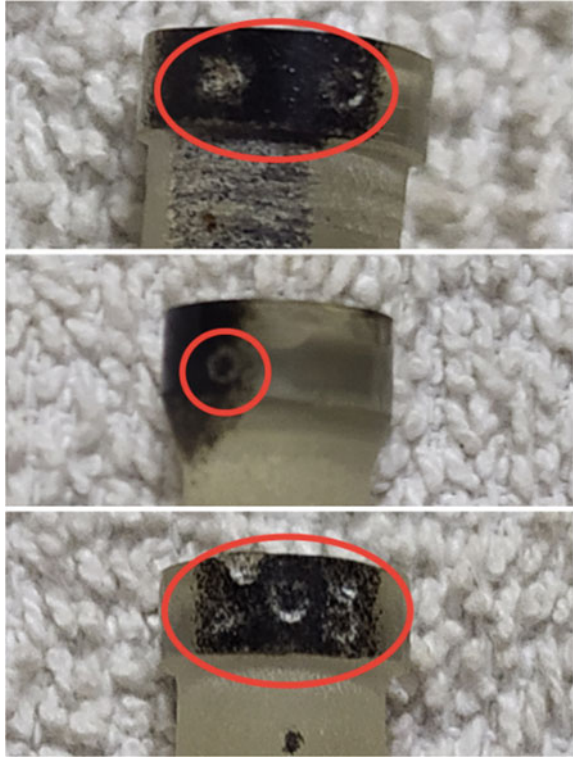
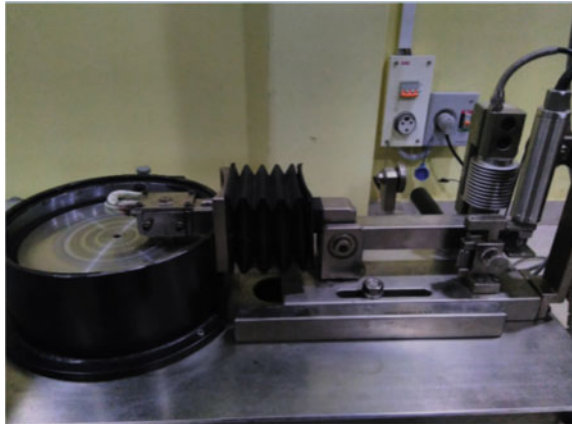


Fig. 26.4 Experimental diagram of charpy impact test

Fig. 26.5 **a** Experimental setup of Pin-On-Disc tribometer and **b** Test specimens for sliding wear analysis



(A)



(B)

Table 26.2 The factors and levels of the experiments

Control factor	Levels				Units
	I	II	III	IV	
Speed	375	750	1125	1500	RPM
Load	7.5	15	22.5	30	Newton
Fiber content	0	5	10	15	%
Distance	150	300	450	600	Meters

Tribometer. The test surface was ground with 400 and 800 high quality SiC abrasive paper to make sure that specimens make proper contact with the steel disc. The sample surfaces were cleaned with soft cotton soaked in acetone after each tribometer run to remove debris caused by wear.

The tests were carried out at different loads, sliding velocities and sliding distances to determine the effect of these variables on the wear rate of compounds produced at a variable proportion of the granite content. The Weighing Electronic Accuracy Machine (WENSAR) is used to measure the mass loss due to wear.

The specific wear rate was analyzed using following equation [21]

$$W_S = \frac{\Delta m}{\rho \times t \times V_S \times F_N}$$

where, W_S is specific wear rate, Δm is mass loss due to wear, ρ is mass per unit volume of the composite, t is the time duration, V_S is the sliding velocity and F_N is average normal load.

Micrographic Observation

Morphological imaging was observed using an LV JEOL JSM-6480 scanning electron microscope. The clean sample was mounted with silver paste on the hole and gold coated under the vacuum in the spray unit for better conductivity before observation. Figures below show the electronic micrograph of granite dust at different magnifications. Granite powder SEM micrographs show that granite powder was fatally present in the group because of the fact that the fabrication method selected was vertical centrifugal casting due to which the powder particles were shown as agglomerates as in Fig. 26.6 and it was also shown that the particles under observation are forked or V-shaped in nature (Fig. 26.7).

Design of Experiment

Taguchi Technology is an optimization tool used to reduce the time required for experiments and determine the impact of effective production parameters. L16 orthogonal imaging was considered in this study to evaluate the performance of material sliding wear and not the mechanical parameters because of the presence of variable factors and levels that is being used in the assessment of specific wear rate of the graded samples [20]. Table 26.3 shows the L₁₆ orthogonal array of factors and their DOE notations.

Fig. 26.6 Micrographs showing agglomeration of granite particles

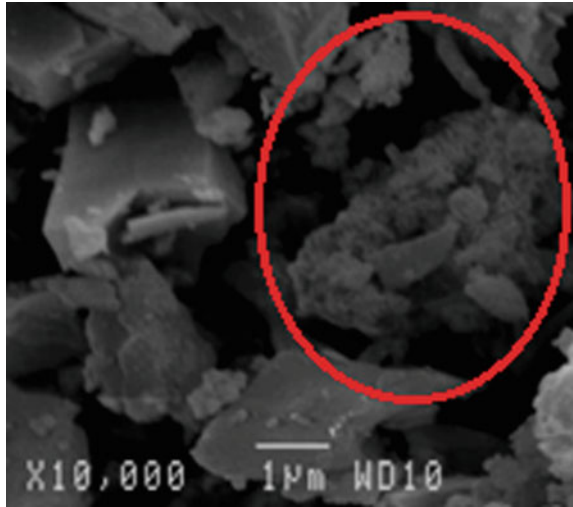
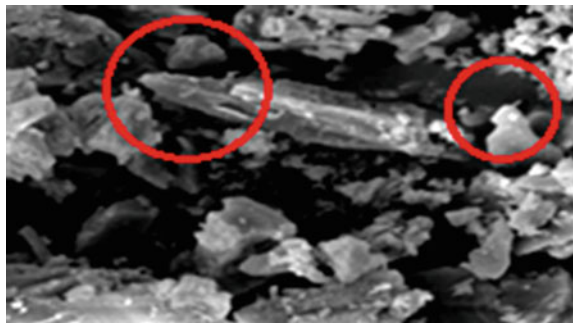


Fig. 26.7 Micrographs showing pointed nature of granite dust



Result and Discussion

Influence of Filler Loading on Hardness and Impact Strength of Polymer Composite

The hardness of FGM composites increases significantly as the weight percentage of granite powder increases, as shown in Fig. 26.8. The hardness of the FGM samples taken from five different sites was in the strict range $(40.8 \pm 0.6 - 53.75 \pm 0.9)$ HV for (0–15)% of granite powder by weight. Maximum hardness was observed at 15% wt. of granite dust for FGM composites.

The evaluation of total absorbed energy during the fracture of the resulted epoxy composite is carried out by standard Charpy impact test. The outcome of Charpy test is shown in Fig. 26.9. It is worth noting that the impact strength of the fabricated material exhibits an increasing approach.

Table 26.3 L₁₆ orthogonal design of experiment

S. No.	Speed (RPM)	Load (N)	Filler (%)	Distance (m)	DOE notations
1.	375	7.5	0	150	A11
2.	375	15	5	300	A12
3.	375	22.5	10	450	A13
4.	375	30	15	600	A14
5.	750	7.5	5	450	B11
6.	750	15	0	600	B12
7.	750	22.5	15	150	B13
8.	750	30	10	300	B14
9.	1125	7.5	10	600	C11
10.	1125	15	15	450	C12
11.	1125	22.5	0	300	C13
12.	1125	30	5	150	C14
13.	1500	7.5	15	300	D11
14.	1500	15	10	150	D12
15.	1500	22.5	5	600	D13
16.	1500	30	0	450	D14

Fig. 26.8 Variation of hardness with granite content

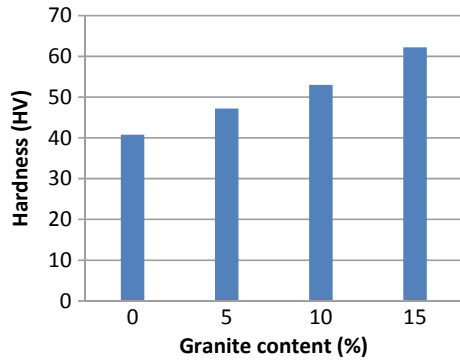
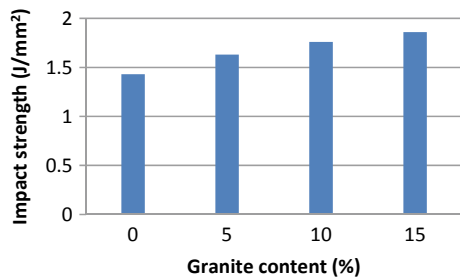


Fig. 26.9 Variation of Impact strength with Granite content



Adding filler material from 0 to 15 wt% increases the toughness potential of the material. However, the results were acquired successfully in the range $(1.43 \pm 0.006 - 1.86 \pm 0.003) \text{ J/mm}^2$ for granite dust content.

Wear Analysis

The aggregate signal-to-noise ratio (SN ratio) of the wear rate of the FGM composite was found to be 43.898 dB. The wear result of fabricated composite materials is converted into signal to noise ratio. For smaller specific wear rate, the function “less is better” is used as presented in equation below.

$$\frac{S}{N} = -10 \log \left[\frac{1}{n} \left(\sum y^2 \right) \right]$$

where n is the number of observations and y is the data observed.

The wear analysis results are evaluated using the formation of Analysis Programming Minitab 18. Examination of the output revealed that A4, B3, C4 and D2 factor combination gives least wear rate (Fig. 26.10). Table 26.4 indicates the specific wear ratios of FGM (W). It can be seen that FGM alloys with granite dust content exhibit the highest wear resistance. If the appropriate testing technique is followed, the test produces enhanced wear rates.

Effect of Applied Load

The effect of various normal loads on the wear rate of reinforced specimens at fixed parameters, such as a sliding velocity of 143.25 rpm (0.75 m/s) and a sliding distance of 750 m is shown in Fig. 26.11. The wear rate of all samples increases with an increase in normal load. This is due to the fact that increased friction at a higher load leads to an increase in deboning and cracking of the specimens. It is also observed that under all test conditions, the rate of specific wear decreases with the addition of granite powder to 15 wt%.

The specific wear is directly proportional to the normal load, this is clearly visible when we infer from Fig. 26.11, and the reason for this behavior is relative as the normal load increases, there is a significant increase in the frictional thrust which in turn increases the area of friction. This leads to more weight loss and ultimately increases in wear.

Effect of Sliding Velocity

Figure 26.12 shows the influence of sliding velocity on the wear behavior of the epoxy matrix sample and reinforced by different weight fractions of granite (5, 10, 15%) at constant specification like applied load of 55 N and a sliding distance of 750 m. It can be seen that the wear rate of the composite decreases with increasing slip velocity, in contrast to the increase in load, and the weakest wear resistance is observed for the unreinforced epoxy matrix sample. It is also clear that wear rate

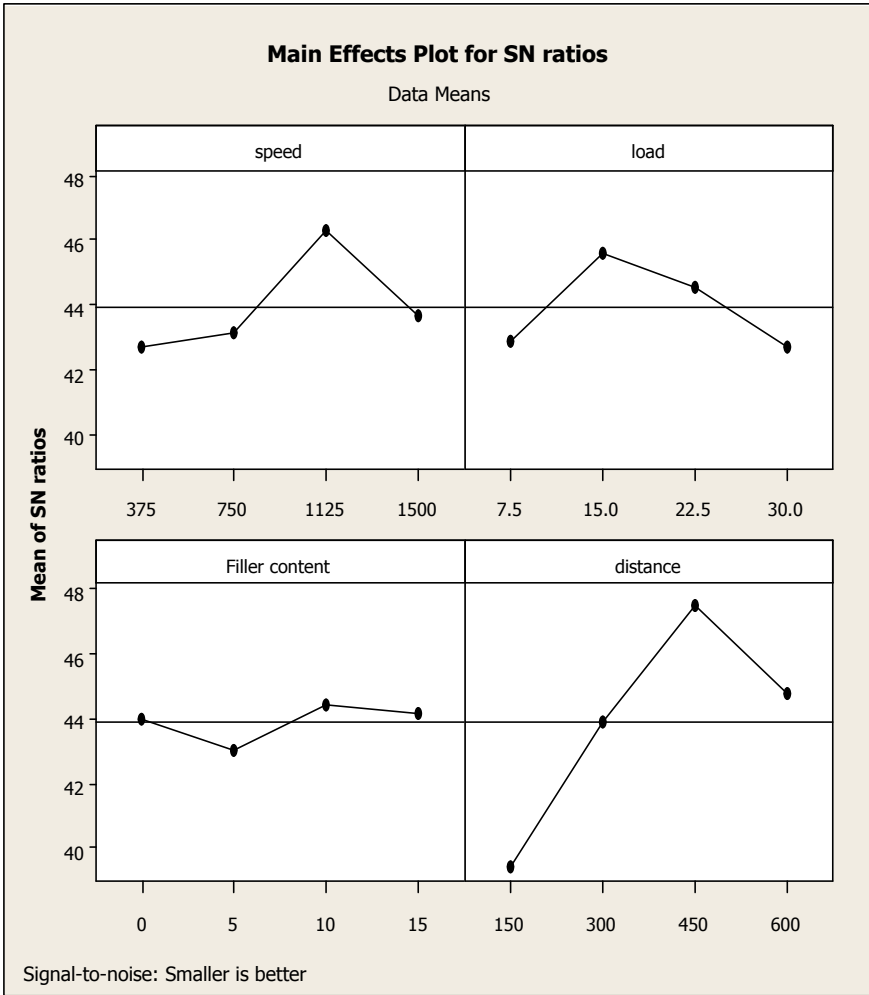


Fig. 26.10 Effect of control factors on wear rate of FGM composite

shows a declining trend under all test conditions with an increase in granite content, and the highest wear resistance is observed at 15% by weight of granite powder. Compared with the matrix, the abrasion resistance of the reinforced composites is higher due to the fact that granite particles impart additional strength to the epoxy composites and as a result shows excellent wear resistance.

Effect of Sliding Distance

Figure 26.13 shows the estimated wear rate for different sliding distances under test conditions. The graph illustrates the change in wear rate with sliding distance under a normal load of 55 N and sliding velocity of 143.25 RPM (0.75 m/s).

Table 26.4 Experimental design using L₁₆ orthogonal array

S. No.	DOE notations	Sliding wear (W)	S/N ratio
1.	A11	1.57E-02	36.07095
2.	A12	6.76E-03	43.40107
3.	A13	4.98E-03	46.05541
4.	A14	5.62E-03	45.00527
5.	B11	4.38E-03	47.17052
6.	B12	6.06E-03	44.35055
7.	B13	1.06E-02	39.46933
8.	B14	8.64E-03	41.26973
9.	C11	4.68E-03	46.59508
10.	C12	2.96E-03	50.57417
11.	C13	3.41E-03	49.34491
12.	C14	1.20E-02	38.43086
13.	D11	8.32E-03	41.59753
14.	D12	6.43E-03	43.83578
15.	D13	6.94E-03	43.17281
16.	D14	4.96E-03	46.09037

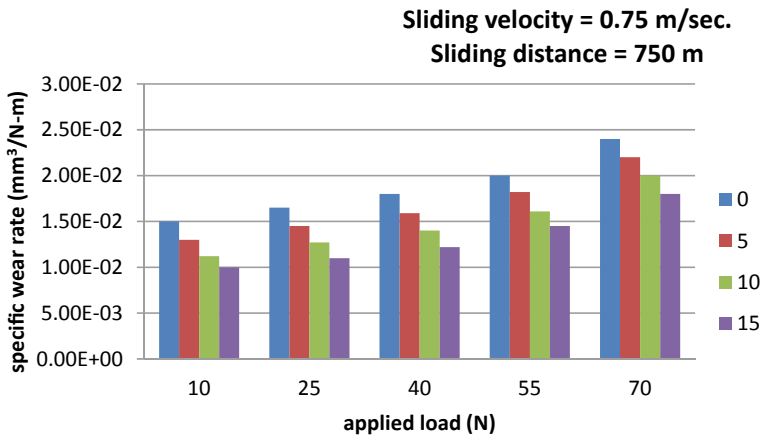


Fig. 26.11 Impact of load on wear rate with Granite content

All reinforced epoxy composites show improved wear resistance compared with matrix materials. It was observed that the wear rate increased with sliding distance for all samples. This may be due to the distinction of irregularities from the sample surface as shown in Fig. 26.14. It was also observed that the composites reinforced with 15 wt% granite powder showed minimal wear rates under all test conditions.

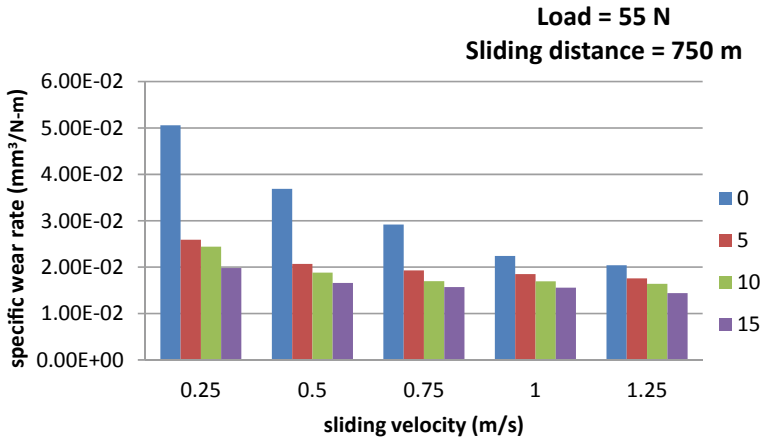


Fig. 26.12 Impact of sliding velocity on wear rate with Granite

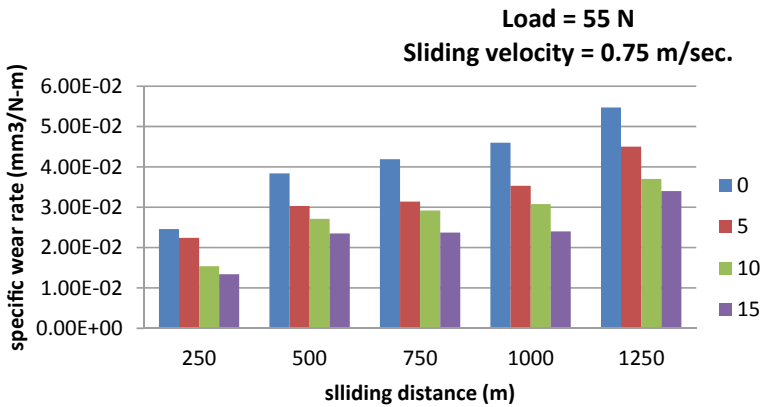


Fig. 26.13 Impact of sliding distance on wear rate with Granite

Fig. 26.14 Worn out surface irregularity of specimen



This again shows that the addition of fillers can improve the wear resistance of composites.

Conclusion

In the present investigation, graded granite dust reinforced epoxy composites are prepared by sustainable utilization of stone industry waste and their effect on the mechanical and wear performance is examined.

1. The hardness is increased with increment of granite filler into base matrix. The maximum hardness is 62.5 HV for 15 wt% granite reinforced FGM and minimum hardness is 40.3 HV for virgin FGM.
2. The impact strength is increased with increment of granite filler into base matrix. The maximum Impact strength is 1.86 J/mm^2 for 15 wt% granite reinforced FGM and minimum impact strength is 1.43 J/mm^2 for virgin FGM.
3. Granite powder electron microscope scanning was analyzed under different amplitude conditions.
4. The aggregate for signal-to-noise ratio (SN ratio) of wear rate for FGM composite is established to be 43.898 db.
5. The optimum levels of control factors are 1500 rpm, 22.5 N, 15 wt% and 300 m.
6. These results are mainly with correspondence to the above given reinforcements, it can be further inferred from the references that high granite dust content (i.e., 30–50%) will lead to excellent enhancement in wear characteristics of the fabricated composites.

References

1. Naebe M, Shirvanimoghaddam K (2016) Functionally graded materials: a review of fabrication and properties. *Appl Mater Today* 5:223–245
2. Shinohara Y (2013) Functionally graded materials. In: Somiya S (ed) *Handbook of advanced ceramics*. Academic Press, Oxford, pp 1179–1187
3. Li J, Peng X, Yang Y, Xu J, Wang P, Hong B, Jin D, Jin H, Wang X, Ge H (2018) A novel magnetic-field-driving method for fabricating Ni/epoxy resin functionally graded materials. *Mater Lett* 222:70–73
4. Zhang Y, Wang J (2017) Fabrication of functionally graded porous polymer structures using thermal bonding lamination techniques. *Proc Manufact* 10:866–875
5. Hassanin H, Jiang K (2018) Microfabrication of components based on functionally graded materials. *Adv Ceram Matrix Compos* 697–709
6. Rezapoor M, Razavi M, Zakeri M, Rahimipour MR, Nikzad L (2018) Fabrication of functionally graded Fe-TiC wear resistant coating on CK45 steel substrate by plasma spray and evaluation of mechanical properties. *Ceram Int* 44:22378–22386
7. Salcedo E, Baek D, Berndt A, Ryu JE (2018) Simulation and validation of three dimension functionally graded materials by material jetting. *Addit Manufact* 22:351–359



8. Gupta A, Talha M (2015) Recent development in modeling and analysis of functionally graded materials and structures. *Prog Aerosp Sci* 79:1–14
9. Polajnar M, Kalin M, Thorbjornsson I, Thorgrimsson JT, Botor-Probierz A (2017) Friction and wear performance of functionally graded ductile iron for brake pads. *Wear* 382–383:85–94
10. Chaubey AK, Gupta R, Kumar R, Verma B, Kanpara S, Bathula S, Khirwadkar SS, Dhar A (2018) Fabrication and characterization of W-Cu functionally graded material by spark plasma sintering process. *Fusion Eng Des* 135:24–30
11. Yusefi A, Parvin N, Mohammadi H (2018) W–Cu functionally graded material: low temperature fabrication and mechanical characterization. *J Phys Chem Solids* 115:26–35
12. Shen WP, Li Q, Chang K, Zhou ZJ, Ge CC (2007) Manufacturing and testing W/Cu functionally graded material mock-ups for plasma facing components. *J Nucl Mater* 367–370:1449–1452
13. Anigol NB, Pol AS (2015) Study of Effect of various fillers on mechanical properties of carbon-epoxy composites. *Int Res J Eng Technol (IRJET)* 02:798–802
14. Kumar BN, Ramesh BT (2015) Development and characterization of epoxy resin based granite powder and glass fibre reinforced composite. *Int J Mod Trends Eng Res (IJMTER)* 02:49–60
15. Balakrishna SS, Girish H, Kumar GCM, Narendranath S (2016) Analysis on mechanical and dynamic behavior of granite epoxy composites with cast iron particulates as filler. *Ind J Adv Chem Sci* 122–126
16. Kulkarni HB, Mahamuni SS, Gaikwad PM, Pula MA, Mahamuni S, Bansode SH, Kulkarni AA, Shete YB, Nehatrao SA (2017) Enhanced mechanical properties of epoxy/graphite composites. *Int J Adv Eng Res Stud* 6:01–05
17. Kareem AA (2013) Mechanical properties of granite powder as filler for polycarbonate toughened epoxy resin. *Int J Pharma Sci* 3:254–257
18. Radhika N, Raghu R (2016) Development of functionally graded aluminium composites using centrifugal casting and influence of reinforcements on mechanical and wear properties. *Trans Nonferrous Met Soc China* 26:905–916
19. Jamian S, Ayob SN, Abidin MRZ, Nor NHM (2016) Fabrication of functionally graded natural fibre/epoxy cylinder using centrifugal casting method. *ARPN J Eng Appl Sci* 11:2327–2331
20. Piratelli-Filho A, Shimabukuro F (2008) Characterization of compression strength of granite epoxy composites using design of experiments. *Mater Res* 11:399–404
21. Gangil B, Kukshal V, Sharma A, Patnaik A, Kumar S (2019) Development of hybrid fiber reinforced functionally graded polymer composites for mechanical and wear analysis. *AIP Conf Proc* 2057:1–8
22. Ramakrishna HV, Padma Priya S, Rai SK, Rajulu AV (2005) Tensile, impact, and chemical resistance properties of granite powder-epoxy composites. *J Reinf Plast Compos* 24:451–455
23. Srivastava VK, Shembekar PS (1990) Tensile and fracture properties of epoxy resin filled with flyash particles. *J Mater Sci* 25:3513–3516
24. Ramakrishna HV, Rai SK (2006) Utilization of granite powder as a filler for polybutylene terephthalate toughened epoxy resin. *J Miner Mater Charact Eng* 5:1–19
25. Ramakrishna HV, Rai SK (2006) Effect on the mechanical properties and water absorption of granite powder composites on toughening epoxy with unsaturated polyester and unsaturated polyester with epoxy resin. *J Reinf Plast Compos* 25:17–32
26. Ray S, Rout AK, Sahoo AK (2017) A study on tribological behavior of glass-epoxy composite filled with granite dust. *IOP Conf Ser Mater Sci Eng* 225:1–8
27. Pawar MJ, Patnaik A, Nagar R (2015) Experimental investigation and numerical simulation of granite powder filled polymer composites for wind turbine blade: a comparative analysis. *Polym Compos* 1–8
28. Pawar MJ, Patnaik A, Nagar R (2016) Mechanical and thermo-mechanical analysis based numerical simulation of granite powder filled polymer composites for wind turbine blade. *Fib Polym* 17:1078–1089
29. Abdalrazaq I, Soud WA, Abdullah OS (2013) Effects of different types of ceramic fillers on wear characteristics of glass fibers-epoxy composite. *J Eng Dev* 17

30. Gangil B, Kumar S (2017) comparative evaluation on mechanical properties of jute/bamboo-glass hybrid reinforced polyester composites. *Asian J Sci Technol* 08:5190–5194
31. Soni S, Rana RS, Singh B, Rana S (2018) Synthesis and characterization of epoxy based hybrid composite reinforced with glass fiber and milled carbon. *Mater Today: Proc* 5:4050–4058

Chapter 27

Acoustic Emission System for Monitoring Mechanical Behavior During Ultrasonic Metal Welding



Vijay Dodiya, Sarthak Bhavsar, Naman Kansara, Nikhil Murarka, Keyur P. Desai, Harshit K. Dave , and Himanshu V. Patel 

Introduction

Ultrasonic metal welding (USMW) gained notable attention as a solid-state joining process. USMW is extensively used in the electrical, electronics and automobile sector due to its advantage over other conventional joining methods. Another advantage of the process has capability to join dissimilar, multiple, and thin layers of metals at low temperatures [1, 2]. USMW is solid-state welding process therefore no consumable materials are required and maximum process temperature is only 40% of the absolute melting temperature of the substrate materials. The quality issues are rising such as porosity, heat-affected zone or burn-through during the conventional fusion welding processes while USMW has no as such issues during the welding [3, 4]. Literature reports that using USMW technique, soft metals such as aluminum (Al), nickel (Ni), copper (Cu), gold (Au) and silver (Ag) can also be welded. USMW is not suitable for hard ferrous alloy and thickness greater than 3 mm is also constraint for this process [5, 6]. Interlayer technique in ultrasonic welding can be useful to weld Molybdenum material [7].

Zhao et al. [2] proposed a new technology that could monitor in situ transient temperature. They found that weld temperature increased with amplitude.

Liu et al. [8] investigated microstructure and mechanical properties of Al/Cu ultrasonically welded joints. They found weld time is an important parameter for weld strength. The recrystallization was observed at the weld interface for maximum weld temperature, i.e., 360°.

Balle et al. [9] performed experimental study to identify process parameters to weld metal to composite material. The weld temperature for metal/carbon fiber textile

V. Dodiya · S. Bhavsar · N. Kansara · N. Murarka · K. P. Desai · H. K. Dave · H. V. Patel (✉)
Department of Mechanical Engineering, S.V. National Institute of Technology, Surat 395007,
India
e-mail: hpsvnit07@gmail.com

joints was found within the range of 350–400 °C and from the SEM micrograph, it was found intensive bonding connection at the interface.

Cao et al. [10] developed FEM model to study resistance heat produce during the ultrasonic welding. They measured temperature using thermocouples. They performed experimental validation in terms of interface temperature, horn displacement and cross-section pattern. They found good agreement between experimentation and FEM model.

Lionetto et al. [11] performed experimental investigation on ultrasonic welding of carbon fiber-reinforced composite to aluminum metal. They observed high weld temperature and plastic deformation due to high force and high frequency shear oscillations during welding. They found force is significant for the higher lap shear strength.

Watanabe et al. [12] performed experiments with combinations of dissimilar metals are aluminum–copper and aluminum–austenitic stainless steel (SUS304) to identify the effect of the material hardness, thermal properties, and surface roughness on ultrasonically welded joint. From their study, they concluded that process parameters like weld time, clamping pressure affect the weld strength of Aluminum–Copper joint.

Haddadi and Tsivoulas [13] welded Al 6111-T4 material using USMW. They studied mechanical performance and thermal behavior of the weld joint. They reported that temperature increase with weld time and the highest value was 440 °C at maximum weld time.

Elangovan et al. [14] have used response surface methodology (RSM) with genetic algorithm (GA) to obtain optimum process parameter for maximum weld strength. They observed that as pressure increases weld strength decreases because relative motion between weld surfaces reduces. On the other hand, increasing amplitude causes more area for rubbing leading to higher weld strength.

Thus, from the literature review, it is observed that weld pressure, amplitude and weld time are the governing parameters for weld strength and quality of the weld. In this study, USMW of pure copper specimen has been done to investigate the lap shear and T-Peel test with different combinations of input parameters. During the process, in situ temperature measurement has been performed during the process. Also, in situ quality measurement has been performed using piezoceramic acoustic emission sensor.

Experimental Study

Experimental Setup

Ultrasonic welding was carried out using Ultrasonic M-4000 Metal Welding press (3000 W, 20 kHz), which is shown in Fig. 27.2 with microprocessor system MPS-4 and generator. The sonotrode used along with M-4000 is made of hardened steel.

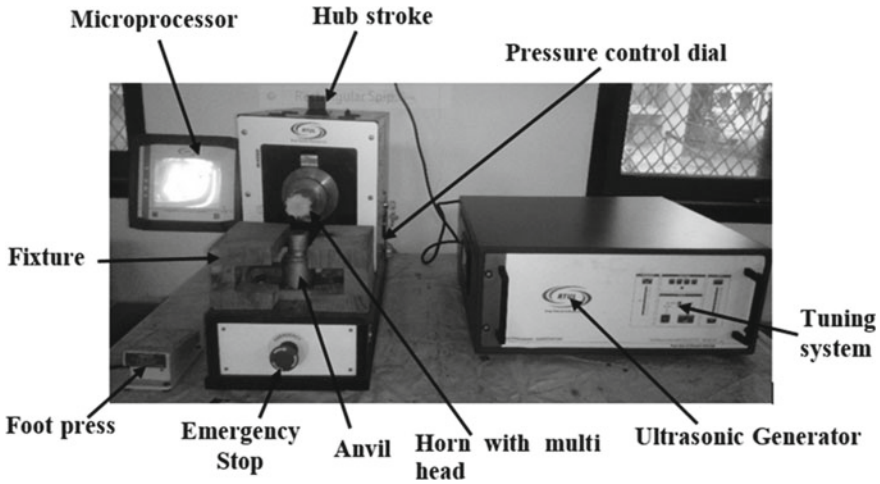


Fig. 27.1 Ultrasonic Metal welding setup

Anvil block has knurling impressions to provide grip to the specimen placed on it and it is made up of steel. The parameters that can be varied on this machine tool setup are amplitude and weld time. Figure 27.1 shows the ultrasonic welding setup. The placement of the sensor on machine tool is a crucial aspect to collect accurate data. For the temperature measurement, k-type thermocouple was used that was placed closest to the weld zone to get capture weld zone temperature during the process. Kistler makes Piezoceramic Acoustic Emission Sensor was used to monitor in situ weld quality. The sensor was clamped through magnetic clamp on the weld specimen. The sensor and thermocouple were connected through National Instrument to make data acquisition system.

Material

In the present study, the first stage was the preparations of work specimen. All the specimens were cut from the copper sheets. The ASTM D1002-01 [15] and ASTM D1876-08 [16] standards were referred during the specimen preparation. The overlap distance during the welding was kept 25 mm. Before welding, workpieces were cleaned with acetone to remove the surface impurities as it may also affect the bond strength. Figure 27.2 shows the dimensions of the specimen prepared as per the standards.

In the present work, amplitude and weld time are considered as the controlled factors and varied at three levels as shown in Table 27.1. The pressure was kept constant 1.5 bar. In the present work, amplitude range is selected from 10 to 20 μm

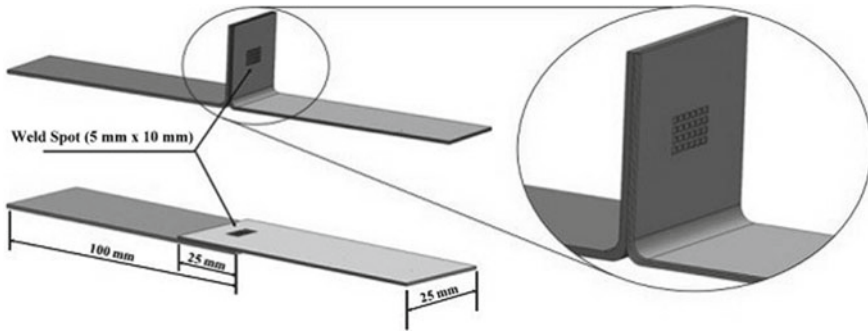


Fig. 27.2 Specimen for T-peel test and lap shear test

Table 27.1 Parameters and levels for the experiments

Parameter	Unit	Level 1	Level 2	Level 3
Weld time	S	1	1.5	2
Amplitude	μm	10	15	20

to utilize maximum capacity of machine tool. The experimental plan was designed as per L9 orthogonal array, which considers two parameters each at three levels.

Results and Discussion

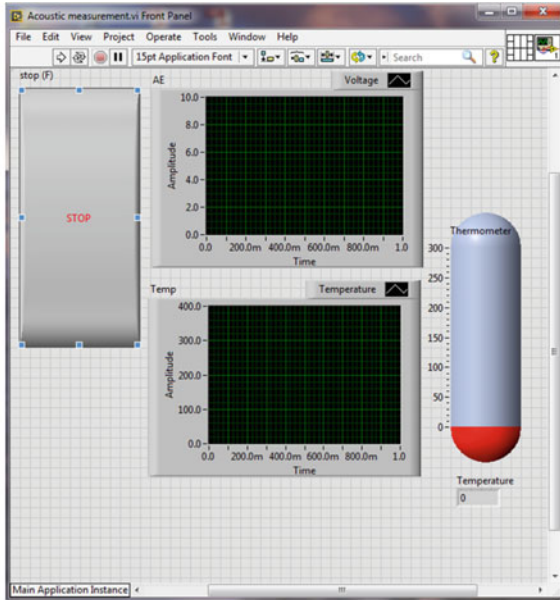
The ultrasonic welding was performed on Cu–Cu strips. During welding, weld temperature and the deformation were sensed by Acoustic Emission (AE) sensor. Figure 27.3 shows the interface of data collection using a LabVIEW software. Table 27.2 represents the data collected during the welding and postwelding.

Thermal Behavior

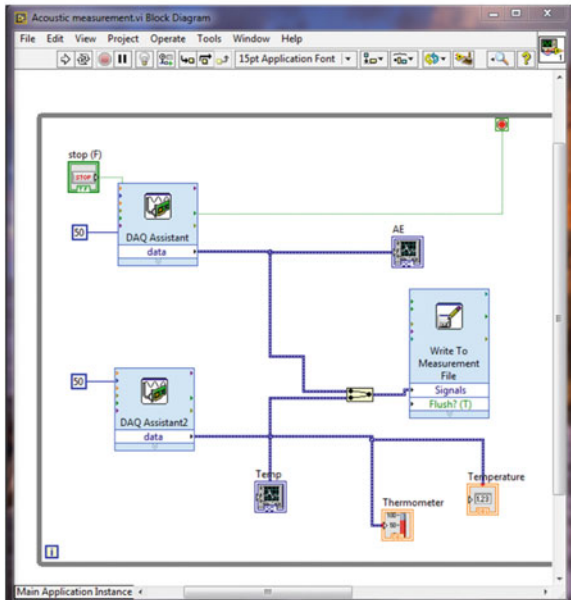
During the ultrasonic metal, welding maximum temperature was recorded with help of K-type thermocouple. The effect of weld time was studied at different weld time. Figure 27.4 shows the effect of weld time on weld interface temperature during the sample fabrication for Lap shear test and T-peel test.

From Fig. 27.4, it can be observed that the maximum weld temperature, i.e., 357.80 °C was recorded during welding of Lap shear specimen. The maximum temperature was achieved for the combination amplitude 20 μm and 1.5 s weld time. Due to the higher amplitude, rubbing action covers higher area and it produces more

Fig. 27.3 LabVIEW interface



(a) Measurement Panel



(b) Block diagram for the measurement

Table 27.2 Results obtained during USMW

S. No.	Weld time (s)	Amplitude, A (μm)	Lap shear test		T-Peel test	
			Max temperature (°C)	Load (N)	Max temperature (°C)	Load (N)
1	1	10	240.35	31.51	298.26	4.84
2	1	15	209.27	30.20	206.37	0.37
3	1	20	208.19	15.61	280.72	1.55
4	1.5	10	183.15	28.38	251.75	5.93
5	1.5	15	235.43	28.52	405.88	3.02
6	1.5	20	357.80	32.28	397.48	3.06
7	2	10	256.77	28.66	376.20	1.88
8	2	15	285.74	27.77	441.16	1.86
9	2	20	353.56	30.67	463.68	1.78

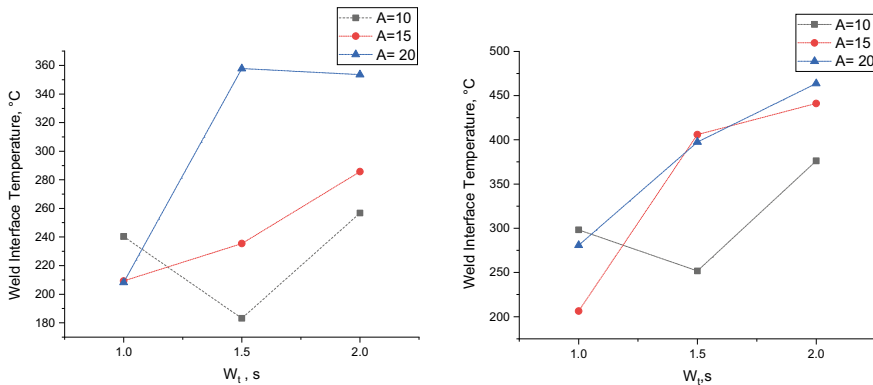


Fig. 27.4 Effect of weld time on weld interface temperature

frictional heat between the interfaces that are under modest pressure. Similarly, the highest temperature was recorded 463.68 °C for maximum amplitude and weld time.

Mechanical Behavior

The ultrasonically welded specimens were tested for Lap shear test and T-Peel test. Figure 27.5 shows the effect of weld time on Lap shear strength and T-Peel strength. Both mechanical strengths were measured using Kudale make tensometer.

It can be seen that maximum lap shear strength was obtained for higher amplitude and moderated weld time. It is also observed that as the weld time increases weld

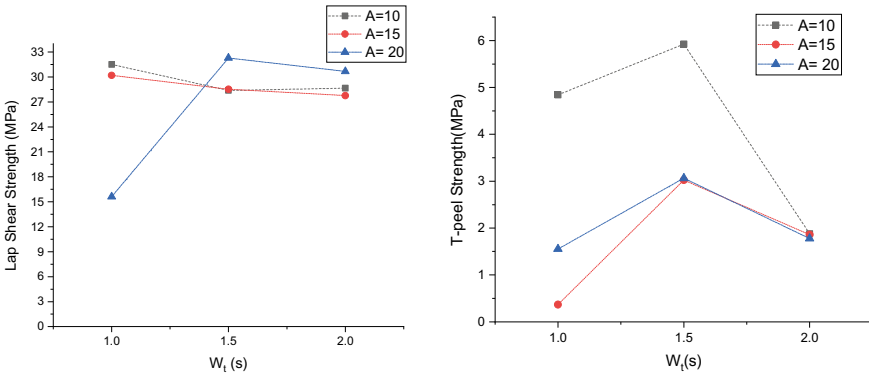


Fig. 27.5 Effect of weld time on lap shear and T-Peel strength

strength also increases up to moderated weld time. As the more weld time given to weld interface, more plastic deformation occurs and it produces strong bond at interface under the constant modest pressure. The continuous increase in weld time produces adverse effects on weld strength. It produces the over weld of specimen and it damages the bond due to excess vibrational energy. The over welded specimen consists of weak bonding mechanism that leads to lower lap shear strength as well as T-Peel strength. It was also observed that amplitude stepping affects the weld strength of the ultrasonically welded joints.

Weld Quality Monitoring

Piezoceramic acoustic emission sensor was used to monitor in situ weld quality during the ultrasonic welding process. Acoustic emission (AE) involves a sensor that converts process sounds into electrical output to a measurable variable. Air-borne emission has the human audible ranges between 20 and 20 kHz. The typical sensor for this emission is a microphone placed nearby the weld zone. Figure 27.6 shows the AE signal waveform during the welding. The AE data are converted into mV it ranges -10 V to 10 V. Figure 27.6a shows AE data collected for the maximum lap shear testing at weld time 1.5 and amplitude 20 μm . It can be observed that maximum amplitude can produce higher friction heat between the weld interfaces that lead to maximum lap shear strength, i.e., 32.28 MPa. It is also observed that for this combination of parameters, maximum weld interface temperature, i.e., 357.80 $^{\circ}\text{C}$ was achieved among all combinations. Figure 27.6b shows the AE data collected during T-peel testing. The maximum interface temperature was observed for 2 s weld time and 20 μm amplitude. Figure 27.6 shows the Maximum deformation was observed at same time when maximum weld time was observed during the process.

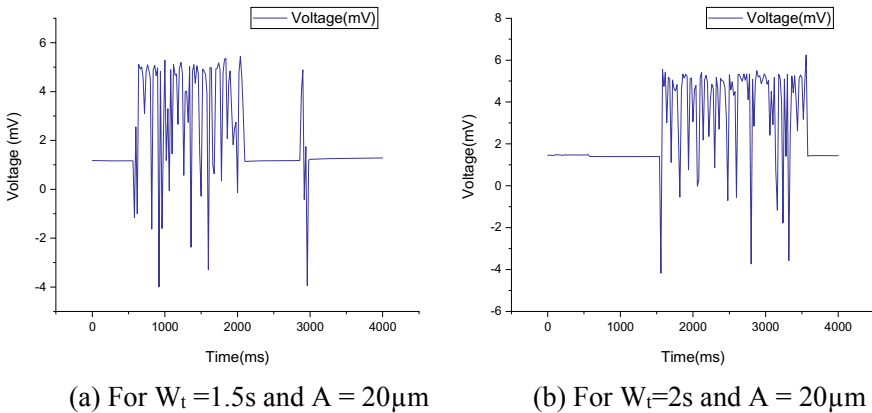


Fig. 27.6 AE signal waveform during welding

Conclusions

In the present work, Cu–Cu specimens were ultrasonically welded to study the effect of weld time and amplitude on Lap shear strength and T-Peel strength. During the ultrasonic welding process, in situ temperature and quality were measured using thermocouple and AE sensor, respectively. From the above study, following conclusions can be drawn:

1. In situ temperature and quality measurement were successfully carried out using K-type thermocouple and piezoceramic acoustic emission sensor.
2. Longer weld time results into higher weld strength because a higher welding time facilitates in providing prolonged application of vibrational energy, thereby resulting into better weldment.
3. The amplitude stepping shows better weld strength for lap shear and T-Peel testing.
4. As the amplitude and weld time increase the weld interface temperature also rises for both cases.
5. AE results and weld interface temperature show the good agreement during the welding process.

References

1. Balandin GF, Kuznetsov VA, Silin LL (1967) Fretting action between members in ultrasonic welding of metals. *Weld Prod* 110:77–80
2. Zhao J, Li H, Choi H, Cai W, Abell JA, Li X (2013) Insertable thin film thermocouples for in situ transient temperature monitoring in ultrasonic metal welding of battery tabs. *J Manuf Proc* 15:136–140 <https://doi.org/10.1016/j.jmapro.2012.10.002> (Elsevier)

3. Ventrella VA, Berretta JR, de Rossi W (2010) Pulsed Nd: YAG laser seam welding of AISI 316L stainless steel thin foils. *J Mater Process Technol* 210:1838–1843. <https://doi.org/10.1016/j.jmatprotec.2010.06.015> (Elsevier)
4. Hirata Y (2003). Pulsed arc welding. *Weld Int* 17:98–115. <https://doi.org/10.1533/wint.2003.3075> (Taylor & Francis)
5. Annoni M, Carboni M (2011) Ultrasonic metal welding of AA 6022-T4 lap joints: part I—technological characterisation and static mechanical behaviour. *Sci Technol Weld Join* 16:107–115. <https://doi.org/10.1179/1362171810y.0000000014> (Taylor & Francis)
6. Patel HV, Dave HK (2016) Effect of parameters on weld strength during ultrasonic welding of Al–Al strip. *J Manuf Eng* 11:121–125 (SME)
7. Patel SK, Dave HK, Patel HV (2020) Ultrasonic welding of molybdenum using aluminium interlayer. In: *Advances in additive manufacturing and joining* Springer, Singapore, pp 669–677. https://doi.org/10.1007/978-981-32-9433-2_59
8. Liu G, Hu X, Fu Y, Li Y (2017) Microstructure and mechanical properties of ultrasonic welded joint of 1060 aluminum alloy and T2 pure copper. *Metals* vol 7. MDPI, pp 361. <http://dx.doi.org/10.21533/pen.v4i1.46>
9. Balle F, Wagner G, Eifler D (2009) Ultrasonic metal welding of aluminium sheets to carbon fibre reinforced thermoplastic composites. *Adv Eng Mater* 11:35–39. <https://doi.org/10.1002/adem.200800271> (Wiley)
10. Li H, Cao B, Yang JW, Liu J (2018) Modeling of resistance heat assisted ultrasonic welding of Cu–Al joint. *J Mater Proc Technol* 256:121–130 (Elsevier). <https://doi.org/10.1016/j.jmatprotec.2018.02.008>
11. Lionetto F, Mele C, Leo P, D’Ostuni S, Balle F, Maffezzoli A (2018) Ultrasonic spot welding of carbon fiber reinforced epoxy composites to aluminum: mechanical and electrochemical characterization. *Compos Part B: Eng* 144:134–142. <https://doi.org/10.1016/j.compositesb.2018.02.026> (Elsevier)
12. Watanabe T, Yanagisawa A, Konuma S, Yoneda A, Ohashi O (1999) Ultrasonic welding of Al–Cu and Al–SUS304. Study of ultrasonic welding of dissimilar metals (1st Report). *Weld Int* 13:875–886. <https://doi.org/10.1080/09507119909452065> (Taylor & Francis)
13. Haddadi F, Tsivoulas D (2016) Grain structure texture and mechanical property evolution of automotive aluminium sheet during high power ultrasonic welding. *Mater Charact* 118:340–351. <https://doi.org/10.1016/j.matchar.2016.06.004> (Elsevier)
14. Elangovan S, Prakasan K, Jaiganesh V (2010) Optimization of ultrasonic welding parameters for copper to copper joints using design of experiments. *Int J Adv nced Manufact Technol* 51:163–171. <https://doi.org/10.1007/s00170-010-2627-1> (Springer)
15. ASTM D1002-2001. Standard test method for apparent shear strength of single-lap-joint adhesively bonded metal specimens by tension loading (metal-to-metal). *Am Soc Test Mater*. <https://doi.org/10.1520/d1002-10r19>
16. ASTM D1876-08. Standard test method for peel resistance of adhesives (T-peel test). West Conshohocken: American Soc Test Mater. <https://doi.org/10.1520/d1876-08r15e01>

Chapter 28

Analysis of Enablers of Humanitarian Supply Chain Management



Sachin Agarwal and Ravi Kant

Introduction

Humanitarian supply chain management (HSCM) becomes the imperative field of research for policymakers, academicians and researchers since last decades mainly after 2004 when the Tsunami occurred in the Indian Ocean. Disaster affects the normal functioning of the society, which results in economic and social losses. Thomas and Kopczak [1] define HSCM as “the process of planning, implementing and controlling the efficient, cost-effective flow and storage of goods and materials, as well as related information, from the point of origin to the point of consumption, for the purpose of alleviating the suffering of vulnerable people.” Van Wassenhove [2] stated that “disaster relief operations consist of 80% logistics cost, and in recent years contributions in the field of humanitarian logistics (HL) and humanitarian supply chain (HSC) rises dramatically.” Enablers are the success factor that helps in the successful implementation of HSCM. This study identified 12 enablers from an extensive literature review for efficient and effective HSCM implementation.

Literature Review

The enablers of HSC are different from those of commercial supply chains [3]. Enablers in HSC are crucial for proper execution of strategic and financial planning, which is planned in the predisaster phase. Pettit and Beresford [4] explained

S. Agarwal (✉) · R. Kant
Department of Mechanical Engineering, S.V. National Institute of Technology, Surat, India
e-mail: engineer.sachinagarwal@gmail.com

R. Kant
e-mail: ravikant.med@gmail.com

Table 28.1 HSCMEs and literature support

Code	Enablers	Literature support
HSCME1	Medical facility	[3, 8, 9]
HSCME2	Donor support	[4]
HSCME3	Relief items assessment	[3, 10, 11]
HSCME4	Information system	[4]
HSCME5	Food and water delivery	[3]
HSCME6	Cooperation	[4]
HSCME7	Strategic planning	[7, 12]
HSCME8	Emergency shelter	[13]
HSCME9	Financial planning	[4, 12]
HSCME10	Early warning	[13]
HSCME11	Skills	[8]
HSCME12	Capacity planning	[7, 12]

the enablers of the commercial business supply chain in the field of HL and SCM. Strategic planning, capacity planning, collaboration, and continuous improvement inventory management, human resource management, information technology are important success factors in the humanitarian logistics field based on commercial context [4]. Oloruntoba [3] emphasized that “relief and response to cyclone Larry which hit Australia in 2006 is considered as more effective and successful because some best practices have been implemented by communities as well as government organizations.” Zhou et al. [5] discussed the identification of CSFs in emergency management. Li et al. [6] discussed “five important factors namely Reasonable organisational structure and clear awareness of responsibilities, Clear procedure of reporting and submitting information, Government unity of leadership to plan and coordinate as a whole, Application of modern logistics technology and Regular organisation of simulated disaster exercise as the enablers in emergency management.” Yadav and Barve [7] identified 12 enablers of HSC and analyzed the relationship among the identified enablers using Interpretive Structural Modeling (ISM) methodology. Several studies identify the enablers for successful HSCM implementation [8–11]. Singh et al. [11] discussed the interaction of enablers namely strategy and capacity planning, collaboration and coordination among stakeholders, government support and policy formulation, etc., for the resilient humanitarian supply chain. The HSCMEs were identified through the literature review and brainstorming session conducted with the expert panel. This study analyzed the identified humanitarian supply chain management enablers (HSCMEs) with the help of ISM approach. Table 28.1 detailed the list of enablers.

Methodology

ISM is a technique to develop hierarchical relationship among variables, which represent graphically, the framework of the system. ISM is an established approach for identifying relationships among specific variables and structured them into a systematic model [14, 15]. ISM presents the establishment of the contextual relationships among identified variables. It is a modeling technique that analyzed the impact of one variable on other variables. ISM methodology is interpretive as the experts' judgment decides whether and how the identified variables are associated. Yadav and Barve [7] applied ISM approach to study enablers in HSCM. The ISM technique consists of the following steps:

1. To identify the variables through brainstorming, survey, expert opinion, literature review, etc.
2. Develop a contextual relationship of variables with respect to each variable which is to be examined.
3. Prepare a structural self-interaction matrix (SSIM) of variables, which represents pair-wise comparison between variables.

Using experts' opinion "contextual relationships between identified enablers, say i and j , are developed. Symbols are used to identify the type of relationship that exists between two variables under examinations." The notations are explained as follows:

- (a) V —variable " i " needs to be addressed before variable " j "
 - (b) A for the relation from variable j to variable i and not in both directions
 - (c) X —both variables " i " and " j " need to be addressed at the same time and
 - (d) 0 (zero), if the relation between the two variables i and j does not exist
4. The next step is to establish an initial reachability matrix from the SSIM, and apply the concept of transitivity principle. If a variable " i " leads to a variable " j " and " j " leads to a variable " k "; then as per the principle of transitivity, variable " i " is linked to variable " k ".
 - (a) If "entry (i, j) in SSIM = ' V ', enter element (i, j) as '1' and (j, i) as '0' in initial reachability matrix".
 - (b) If "the (i, j) entry in SSIM is A , then the (i, j) entry in the reachability matrix becomes 0 and the (j, i) entry becomes 1".
 - (c) If "entry (i, j) in SSIM = ' X ', enter element (i, j) as '1' and (j, i) as '1' in initial reachability matrix".
 - (d) If "the (i, j) entry in SSIM is 0, then the (i, j) entry in the reachability matrix becomes 0 and the (j, i) entry becomes 0".
 5. The next step is partition of level and development of framework for ISM.
 6. Directed graph (DIGRAPH) is plotted based on the relationships given above in the reachability matrix, and remove transitive links.

Analysis and Result

SSIM is formed based on pairwise comparison of each HSCME (Table 28.2). Initial reachability matrix (IRM) is developed by converting SSIM into binary matrix (Table 28.3). Substitution rule is mentioned above for the four symbols of SSIM (*V*, *A*, *X*, and *O*) to 1 and 0 s. Transitivity rule is applied to convert the initial reachability matrix (IRM) into final reachability matrix (FRM) (Table 28.4). Reachability set and antecedent set are achieved for each HSCME (Table 28.5) from the final reachability matrix (FRM). ISM structure model is represented in Fig. 28.1. The bottom level of ISM model considered HSCMEs that are most critical factors among all HSCMEs in the HSCM implementation. This study reveals that “strategic planning,” “capacity planning” and “financial planning” are the most influencing HSCMEs that drive other HSCMEs for achieving the ultimate goal. Strategic planning, capacity planning and financial planning help in providing humanitarian assistance to the affected victims in the disaster relief operations. In this study, the HSCME at the top level is “Food and water delivery.” Top-level enablers having high dependence power while driving power is minimum. Need assessment facilitates humanitarian logisticians to realize the impact of a disaster and ways through which the logistics services are to be provided. Donor plays an important role in humanitarian logistics system by providing fund to the relief agencies.

Conclusion

The aim of this study is to identify HSCMEs and to analyze the relationship between HSCMEs using ISM model that would help in successful HSCM implementation in the emergency management and disaster relief operations. Coordination and collaboration of humanitarian stakeholders result in effective and efficient HSCM implementation, which leads to quickly respond to affected victims in the disaster prone areas. It is not possible for the individual humanitarian actor to make disaster relief operation successful. Proper implementation of strategic planning helps to mitigate disaster losses.

This study helps to the academicians, managers and policymaker to implement HSCM with proper planning to supplies relief items in the affected areas and saves human lives. This study can be extended in the future by considering real-case study of disaster. This study limited to identifying less number of enablers, in practical implications, more number of enablers that may help to implement effective HSCM implementation. Also, developed ISM model can be statistically validated using structural equation modeling (SEM).

Table 28.3 Initial reachability matrix for HSCMEs

	HSCME1	HSCME2	HSCME3	HSCME4	HSCME5	HSCME6	HSCME7	HSCME8	HSCME9	HSCME10	HSCME11	HSCME12
HSCME1	1	0	0	0	0	0	1	0	0	0	0	0
HSCME2	0	1	0	0	1	0	0	1	1	0	0	0
HSCME3	0	1	1	0	1	0	0	0	1	1	0	0
HSCME4	0	0	1	1	0	0	0	1	1	0	0	0
HSCME5	0	0	0	0	0	0	0	1	0	0	0	0
HSCME6	0	0	0	0	1	0	1	0	0	0	0	0
HSCME7	0	0	0	1	0	1	0	1	0	0	0	0
HSCME8	0	0	0	0	1	0	0	1	0	0	0	0
HSCME9	0	0	0	0	0	0	1	1	1	0	0	0
HSCME10	0	1	1	0	0	0	0	1	1	1	0	0
HSCME11	1	0	0	0	1	0	0	1	0	0	1	0
HSCME12	0	1	1	0	1	1	0	1	0	1	1	0

Table 28.4 Final reachability matrix for HSCMEs

	HSCME12	HSCME11	HSCME10	HSCME9	HSCME8	HSCME7	HSCME6	HSCME5	HSCME4	HSCME3	HSCME2	HSCME1
HSCME1	1	0	0	0	0	1	0	1	0	0	1	0
HSCME2	0	1	0	1	1	0	0	1*	0	0	0	0
HSCME3	0	1	1	1	0	0	0	1	0	0	0	0
HSCME4	0	0	0	1*	1	0	0	0	0	1	0	0
HSCME5	0	0	0	0	1	0	0	0	0	0	0	0
HSCME6	0	0	0	0	0	1	0	1	0	0	0	0
HSCME7	0	0	0	0	1	0	1	0	1*	0	0	0
HSCME8	0	0	0	0	1	0	0	1	0	0	1	0
HSCME9	0	0	0	0	1	1	0	0	1	1	0	0
HSCME10	0	1	1	1	1	0	0	0	0	1	0	0
HSCME11	1	0	0	0	1	0	0	1	0	0	1	0
HSCME12	0	1	1	0	1	0	1	1	0	0	0	1

*Transitivity

Table 28.5 Partition and levels of the HSCMEs

HSCMEs Code	Reachability set	Antecedent set	Common set	Level
HSCME1	1, 6, 8, 11	1, 2, 3, 4, 6, 7, 8, 9, 10, 11, 12	1, 6, 8, 11	II
HSCME2	2, 3, 4, 10	2, 3, 4, 7, 9, 10, 12	2, 3, 4, 10	III
HSCME3	2, 3, 4, 10	2, 3, 4, 7, 9, 10, 12	2, 3, 4, 10	III
HSCME4	2, 3, 4, 10	2, 3, 4, 7, 9, 10, 12	2, 3, 4, 10	III
HSCME5	5	1, 2, 3, 4, 5, 6, 7, 8, 9, 10, 11, 12	5	I
HSCME6	1, 6, 8, 11	1, 2, 3, 4, 5, 6, 7, 8, 9, 10, 11, 12	1, 6, 8, 11	II
HSCME7	7, 9, 12	7, 9, 12	7, 9, 12	IV
HSCME8	1, 6, 8, 11	1, 2, 3, 4, 6, 7, 8, 9, 10, 11, 12	1, 6, 8, 11	II
HSCME9	7, 9, 12	7, 9, 12	7, 9, 12	IV
HSCME10	2, 3, 4, 10	2, 3, 4, 7, 9, 10, 12	2, 3, 4, 10	III
HSCME11	1, 6, 8, 11	1, 2, 3, 4, 6, 7, 8, 9, 10, 11, 12	1, 6, 8, 11	II
HSCME12	7, 9, 12	7, 9, 12	7, 9, 12	IV

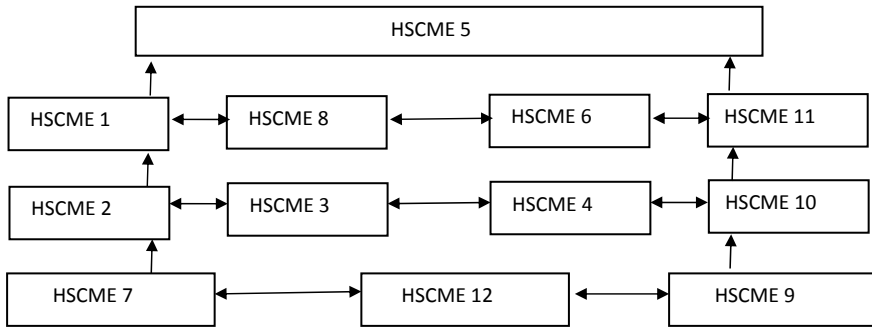


Fig. 28.1 ISM structure model for HSCMEs

References

1. Thomas AS, Kopczak LR (2005) From logistics to supply chain management: the path forward in the humanitarian sector. *Fritz Institute* 15:1–15
2. Van Wassenhove LN (2006) Humanitarian aid logistics: supply chain management in high gear. *J Oper Res Soc* 57(5):475–489
3. Oloruntoba R (2010) An analysis of the Cyclone Larry emergency relief chain: some key success factors. *Int J Prod Econ* 126(1):85–101
4. Pettit S, Beresford A (2009) Critical success factors in the context of humanitarian aid supply chains. *Int J Phys Distrib Logistics Manage* 39(6):450–468
5. Zhou Q, Huang W, Zhang Y (2011) Identifying critical success factors in emergency management using a fuzzy DEMATEL method. *Saf Sci* 49(2):243–252
6. Li Y, Hu Y, Zhang X, Deng Y, Mahadevan S (2014) An evidential DEMATEL method to identify critical success factors in emergency management. *Appl Soft Comput* 22:504–510
7. Yadav DK, Barve A (2015) Analysis of critical success factors of humanitarian supply chain: an application of interpretive structural modeling. *Int J Disaster Risk Reduction* 12:213–225

8. Oloruntoba R, Gray R (2009) Customer service in emergency relief chains. *Int J Phys Distrib Manage* 39(6):486–505
9. Vaillancourt A (2016) A theoretical framework for consolidation in humanitarian logistics. *J Humanitarian Logistics Supply Chain Manage* 6(1):2–23
10. Tatham P, Spens K, (2011). Towards a humanitarian logistics knowledge management system. *Disaster Prev Manage: An Int J* 20(1):6–26
11. Singh RK, Gupta A, Gunasekaran A (2018) Analysing the interaction of factors for resilient humanitarian supply chain. *Int J Prod Res* 56(21):6809–6827
12. Gunasekaran A, Ngai EW (2003) The successful management of a small logistics company. *Int J Phys Distrib Logistics Manage* 33(9):825–842
13. Pettit SJ, Beresford AK (2005) Emergency relief logistics: an evaluation of military, non-military and composite response models. *Int J Logistics: Res Appl* 8(4):313–331
14. Warfield JN (1974) Developing subsystem matrices in structural modeling. *IEEE Trans Syst Man Cybern* 1:74–80
15. Sage A (1977) Interpretive structural modeling: methodology for large-scale systems, pp 91–164